Development of 3D high-resolution imaging of complex devices by the correlation of ToF-SIMS and AFM

Maiglid Andreina Moreno Villavicencio

▶ **To cite this version:**

Maiglid Andreina Moreno Villavicencio. Development of 3D high-resolution imaging of complex devices by the correlation of ToF-SIMS and AFM. Electronics. Université de Lyon, 2019. English. NNT : 2019LYSEI122 . tel-02902102

HAL Id: tel-02902102
https://theses.hal.science/tel-02902102

Submitted on 17 Jul 2020

HAL is a multi-disciplinary open access archive for the deposit and dissemination of scientific research documents, whether they are published or not. The documents may come from teaching and research institutions in France or abroad, or from public or private research centers.

L'archive ouverte pluridisciplinaire **HAL**, est destinée au dépôt et à la diffusion de documents scientifiques de niveau recherche, publiés ou non, émanant des établissements d'enseignement et de recherche français ou étrangers, des laboratoires publics ou privés.

N°d'ordre NNT : 2019LYSEI122

THÈSE DE DOCTORAT DE L'UNIVERSITÉ DE LYON

Opérée au sein de

INSA Lyon

Ecole Doctorale N° ED160

Électronique, Électrotechnique et Automatique

Spécialité de doctorat :

Micro et nano technologies

Soutenue publiquement le 03 / 12 / 2019 par :

Maiglid Andreina Moreno Villavicencio

Développement de l'imagerie 3D haute résolution par ToF-SIMS et AFM de dispositifs avancés

---

Devant le jury composé de

Leonard, Didier	PU - Université Claude Bernard Lyon 1	Président
Galtayries, Anouk	MC - Chimie ParisTech	Rapporteure
Conard, Thierry	Ingénieur de recherche - IMEC	Rapporteur
Valle, Nathalie	Ingénieur de recherche - LIST	Examinatrice
Fearn, Sarah	Chargée de recherche - Imperial College	Examinatrice

Gautier, Brice	PU	INSA Lyon	Directeur de thèse
Barnes, Jean-Paul	Dr. Ingénieur de recherche	CEA	Encadrant de thèse
Chevalier, Nicolas	Dr. Ingénieur de recherche	CEA	Encadrant de thèse

Cette thèse est accessible à l'adresse : http://theses.insa-lyon.fr/publication/2019LYSEI121/these.pdf
© [M.A. Moreno Villavicencio], [2019], INSA Lyon, tous droits réservés

Cette thèse est accessible à l'adresse : http://theses.insa-lyon.fr/publication/2019LYSEI121/these.pdf
© [M.A. Moreno Villavicencio], [2019], INSA Lyon, tous droits réservés

UNIVERSITÉ DE LYON

INSA

Département FEDORA – INSA Lyon - Ecoles Doctorales – Quinquennal 2016-2020

SIGLE	ECOLE DOCTORALE	NOM ET COORDONNEES DU RESPONSABLE
CHIMIE	CHIMIE DE LYON http://www.edchimie-lyon.fr Sec. : Renée EL MELHEM Bât. Blaise PASCAL, 3e étage secretariat@edchimie-lyon.fr INSA : R. GOURDON	M. Stéphane DANIELE Institut de recherches sur la catalyse et l'environnement de Lyon IRCELYON-UMR 5256 Équipe CDFA 2 Avenue Albert EINSTEIN 69 626 Villeurbanne CEDEX directeur@edchimie-lyon.fr
E.E.A.	ÉLECTRONIQUE, ÉLECTROTECHNIQUE, AUTOMATIQUE http://edeea.ec-lyon.fr Sec. : M.C. HAVGOUDOUKIAN ecole-doctorale.eea@ec-lyon.fr	M. Gérard SCORLETTI École Centrale de Lyon 36 Avenue Guy DE COLLONGUE 69 134 Écully Tél : 04.72.18.60.97 Fax 04.78.43.37.17 gerard.scorletti@ec-lyon.fr
E2M2	ÉVOLUTION, ÉCOSYSTÈME, MICROBIOLOGIE, MODÉLISATION http://e2m2.universite-lyon.fr Sec. : Sylvie ROBERJOT Bât. Atrium, UCB Lyon 1 Tél : 04.72.44.83.62 INSA : H. CHARLES secretariat.e2m2@univ-lyon1.fr	M. Philippe NORMAND UMR 5557 Lab. d'Ecologie Microbienne Université Claude Bernard Lyon 1 Bâtiment Mendel 43, boulevard du 11 Novembre 1918 69 622 Villeurbanne CEDEX philippe.normand@univ-lyon1.fr
EDISS	INTERDISCIPLINAIRE SCIENCES-SANTÉ http://www.ediss-lyon.fr Sec. : Sylvie ROBERJOT Bât. Atrium, UCB Lyon 1 Tél : 04.72.44.83.62 INSA : M. LAGARDE secretariat.ediss@univ-lyon1.fr	Mme Emmanuelle CANET-SOULAS INSERM U1060, CarMeN lab, Univ. Lyon 1 Bâtiment IMBL 11 Avenue Jean CAPELLE INSA de Lyon 69 621 Villeurbanne Tél : 04.72.68.49.09 Fax : 04.72.68.49.16 emmanuelle.canet@univ-lyon1.fr
INFOMATHS	INFORMATIQUE ET MATHÉMATIQUES http://edinfomaths.universite-lyon.fr Sec. : Renée EL MELHEM Bât. Blaise PASCAL, 3e étage Tél : 04.72.43.80.46 infomaths@univ-lyon1.fr	M. Luca ZAMBONI Bât. Braconnier 43 Boulevard du 11 novembre 1918 69 622 Villeurbanne CEDEX Tél : 04.26.23.45.52 zamboni@maths.univ-lyon1.fr
Matériaux	MATÉRIAUX DE LYON http://ed34.universite-lyon.fr Sec. : Stéphanie CAUVIN Tél : 04.72.43.71.70 Bât. Direction ed.materiaux@insa-lyon.fr	M. Jean-Yves BUFFIÈRE INSA de Lyon MATEIS - Bât. Saint-Exupéry 7 Avenue Jean CAPELLE 69 621 Villeurbanne CEDEX Tél : 04.72.43.71.70 Fax : 04.72.43.85.28 jean-yves.buffiere@insa-lyon.fr
MEGA	MÉCANIQUE, ÉNERGÉTIQUE, GÉNIE CIVIL, ACOUSTIQUE http://edmega.universite-lyon.fr Sec. : Stéphanie CAUVIN Tél : 04.72.43.71.70 Bât. Direction mega@insa-lyon.fr	M. Jocelyn BONJOUR INSA de Lyon Laboratoire CETHIL Bâtiment Sadi-Carnot 9, rue de la Physique 69 621 Villeurbanne CEDEX jocelyn.bonjour@insa-lyon.fr
ScSo	ScSo* http://ed483.univ-lyon2.fr Sec. : Véronique GUICHARD INSA : J.Y. TOUSSAINT Tél : 04.78.69.72.76 veronique.cervantes@univ-lyon2.fr	M. Christian MONTES Université Lyon 2 86 Rue Pasteur 69 365 Lyon CEDEX 07 christian.montes@univ-lyon2.fr

*ScSo : Histoire, Géographie, Aménagement, Urbanisme, Archéologie, Science politique, Sociologie, Anthropologie

Cette thèse est accessible à l'adresse : http://theses.insa-lyon.fr/publication/2019LYSEI121/these.pdf
© [M.A. Moreno Villavicencio], [2019], INSA Lyon, tous droits réservés

Cette thèse est accessible à l'adresse : http://theses.insa-lyon.fr/publication/2019LYSEI121/these.pdf
© [M.A. Moreno Villavicencio], [2019], INSA Lyon, tous droits réservés

RÉSUMÉ

Développement de l'imagerie 3D haute résolution par ToF-SIMS et AFM de dispositifs avancés

La miniaturisation continue et la complexité des dispositifs poussent les techniques existantes de nano-caractérisation à leurs limites. De ce fait, la combinaison de ces techniques apparait être une solution attrayante pour continuer à fournir une caractérisation précise et exacte. Dans le but de dépasser les verrous existants pour l'imagerie chimique 3D haute résolution à l'échelle nanométrique, nous avons concentré nos recherches sur la création d'un protocole combinant la spectrométrie de masse à ions secondaires de temps de vol (ToF-SIMS) avec la microscopie à force atomique (AFM). Ceci permet entre autres de corréler la composition et la visualisation en 3 dimensions avec des cartographies de topographie ou d'autres propriétés locales fournies par l'AFM. Trois principaux résultats sont obtenus grâce à cette méthodologie : la correction d'un ensemble de données ToF-SIMS pour une visualisation 3D sans artefacts, la cartographie du taux de pulvérisation locale permettant de mettre en évidence les effets liés à la rugosité et la présence d'interfaces verticales et la superposition des informations avancées ToF-SIMS et AFM.

Quatre applications de la méthodologie combinée ToF-SIMS et AFM sont abordées dans cette thèse. La procédure de correction des données ToF-SIMS en 3D a été appliquée sur une structure hétérogène GaAs / SiO_2. Les artefacts liés à la pulvérisation, notamment l'effet d'ombrage, ont été étudiés par le biais des cartographies de taux de pulvérisation sur des échantillons avec nano-motifs structurés et non structurés. Enfin, nous avons exploré la combinaison de l'analyse ToF-SIMS avec trois modes avancées de microscopie AFM : piézoélectrique (PFM), capacité (SCM) et conducteur (SSRM). Une première étude a notamment permis d'observer l'évolution et la modification chimique suite à l'application d'une contrainte électrique sur deux films minces piézoélectriques. Une deuxième étude s'est focalisée sur l'impact de l'implantation Ga lors de la préparation d'échantillons par FIB pour voir comment limiter l'effet de l'amorphisation sur la mesure électrique. Les aspects techniques de la méthodologie sont abordés pour chacune de ces applications et les perspectives de cette combinaison sont discutés.

***Mots-Clés**: AFM – ToF-SIMS – caractérisation chimique 3D – PFM – SCM – SSRM corrélation et combinaison de techniques – reconstruction et visualisation 3D – effets d'ombrage – cartographie de vitesse de pulvérisation – overlay ToF-SIMS et AFM.*

Cette thèse est accessible à l'adresse : http://theses.insa-lyon.fr/publication/2019LYSEI121/these.pdf
© [M.A. Moreno Villavicencio], [2019], INSA Lyon, tous droits réservés

Cette thèse est accessible à l'adresse : http://theses.insa-lyon.fr/publication/2019LYSEI121/these.pdf
© [M.A. Moreno Villavicencio], [2019], INSA Lyon, tous droits réservés

ABSTRACT

Development of 3D high-resolution imaging of complex devices by the correlation of ToF-SIMS and AFM

The continuous miniaturization and complexity of devices have pushed existing nano-characterization techniques to their limits. The correlation of techniques has then become an attractive solution to keep providing precise and accurate characterization. With the aim of overcoming the existing barriers for the 3D high-resolution imaging at the nanoscale, we have focused our research on creating a protocol to combine time-of-flight secondary ion mass spectrometry (ToF-SIMS) with atomic force microscopy (AFM). This combination permits the correlation of the composition in 3-dimensions with the maps of topography and other local properties provided by the AFM. Three main results are achieved through this methodology: a topography-corrected 3D ToF-SIMS data set, maps of local sputter rate where the effect of roughness and vertical interfaces are seen and overlays of the ToF-SIMS and AFM advanced information.

The application fields of the ToF-SIMS and AFM combined methodology can be larger than expected. Indeed, four different applications are discussed in this thesis. The procedure to obtain the topography-corrected 3D data sets was applied on a GaAs / SiO_2 patterned structure whose initial topography and composition with materials of different sputter rates create a distortion in the classical 3D chemical visualization. The protocol to generate sputter rate maps was used on samples with structured and non-structured nano-areas in order to study the possible ToF-SIMS sputtering artefacts, especially the geometric shadowing effect. Finally, we have explored the combination of ToF-SIMS analysis with three AFM advanced modes: piezoresponse force microcopy (PFM), scanning capacitance microscopy (SCM) and scanning spreading resistance microscopy (SSRM). Specifically, two main applications were studied: the chemical modification during electrical stress of a piezoelectic thin film and the recovery of initial electrical characteristics of a sample subjected to Ga implantation during FIB preparation. Technical aspects of the methodology are discussed for each application and the perspectives of this combination are given.

***Keywords**: AFM – ToF-SIMS – 3D chemical characterization – PFM – SCM – SSRM – correlation and combination of techniques – 3D reconstruction and visualization – geometric shadowing effect – sputter rate map – ToF-SIMS and AFM overlay.*

Cette thèse est accessible à l'adresse : http://theses.insa-lyon.fr/publication/2019LYSEI121/these.pdf
© [M.A. Moreno Villavicencio], [2019], INSA Lyon, tous droits réservés

Cette thèse est accessible à l'adresse : http://theses.insa-lyon.fr/publication/2019LYSEI121/these.pdf
© [M.A. Moreno Villavicencio], [2019], INSA Lyon, tous droits réservés

CONTENTS

Cette thèse est accessible à l'adresse : http://theses.insa-lyon.fr/publication/2019LYSEI121/these.pdf
© [M.A. Moreno Villavicencio], [2019], INSA Lyon, tous droits réservés

Cette thèse est accessible à l'adresse : http://theses.insa-lyon.fr/publication/2019LYSEI121/these.pdf
© [M.A. Moreno Villavicencio], [2019], INSA Lyon, tous droits réservés

Cette thèse est accessible à l'adresse : http://theses.insa-lyon.fr/publication/2019LYSEI121/these.pdf
© [M.A. Moreno Villavicencio], [2019], INSA Lyon, tous droits réservés

Cette thèse est accessible à l'adresse : http://theses.insa-lyon.fr/publication/2019LYSEI121/these.pdf
© [M.A. Moreno Villavicencio], [2019], INSA Lyon, tous droits réservés

ABBREVIATION INDEX

2D	Two-dimensional
3D	Three-dimensional
AFM	Atomic force microscopy
C-AFM	Conductive-atomic force microscopy
CPD	Contact potential difference
CMOS	Complementary-metal-oxide-semiconductor
DFRT	Dual frequency resonance tracking
EDX	Energy-dispersive X-ray spectroscopy
EELS	Electron-energy-loss spectroscopy
FTIR	Fourier-transform infrared spectroscopy
FWHM	Full width at half maximum
GSI	Gigascale-scale integration
KFM	Kelvin force microscopy
LMIS	Liquid metal ion source
METRO 4-3D	Metrology for future 3D-technologies
MFM	Magnetic force microscopy
MOCVD	Metal organic chemical vapor deposition
MOS	Metal-oxide-semiconductor
MSI	Medium-scale integration
PCA	Principal component analysis
PFM	Piezoresponse force microscopy
PFT	Peak force Tapping
PI Feedback	Proportional-integral feedback system
ROI	Region of interest
SCM	Scanning capacitance microscopy
SEM	Scanning electron microscopy

Cette thèse est accessible à l'adresse : http://theses.insa-lyon.fr/publication/2019LYSEI121/these.pdf
© [M.A. Moreno Villavicencio], [2019], INSA Lyon, tous droits réservés

SIMS	Secondary ion mass spectrometry
SOC	System on a single chip
SSI	Small-scale integration
SSRM	Scanning spreading resistance microscopy
STEM	Scanning transmission electron microscopy
TEM	Transmission electron microscopy
ToF-SIMS	Time-of-flight secondary ion mass spectrometry
XPS	X-ray photoelectron spectroscopy
XRD	X-ray powder diffraction

Cette thèse est accessible à l'adresse : http://theses.insa-lyon.fr/publication/2019LYSEI121/these.pdf
© [M.A. Moreno Villavicencio], [2019], INSA Lyon, tous droits réservés

LIST OF FIGURES

Cette thèse est accessible à l'adresse : http://theses.insa-lyon.fr/publication/2019LYSEI121/these.pdf
© [M.A. Moreno Villavicencio], [2019], INSA Lyon, tous droits réservés

Cette thèse est accessible à l'adresse : http://theses.insa-lyon.fr/publication/2019LYSEI121/these.pdf
© [M.A. Moreno Villavicencio], [2019], INSA Lyon, tous droits réservés

Cette thèse est accessible à l'adresse : http://theses.insa-lyon.fr/publication/2019LYSEI121/these.pdf
© [M.A. Moreno Villavicencio], [2019], INSA Lyon, tous droits réservés

Cette thèse est accessible à l'adresse : http://theses.insa-lyon.fr/publication/2019LYSEI121/these.pdf
© [M.A. Moreno Villavicencio], [2019], INSA Lyon, tous droits réservés

CHAPTER I.
INTRODUCTION TO HIGH RESOLUTION 3D CHEMICAL CHARACTERIZATION OF MICROELECTRONIC DEVICES

This chapter introduces microelectronic technology, its beginning and its challenges. It describes how its development has been important for every field of science and the spread of applications that it has had. The author addresses the importance of reliable characterization instruments that can assure the good performance of micro devices, especially those that can provide chemical information in three dimensions (3D). The pros and cons of using time-of-flight secondary ion mass spectrometry (ToF-SIMS) as a 3D chemical characterization technique are discussed. The chapter presents the atomic force microscopy as a correlative technique to overcome some of the ToF-SIMS limitations. It presents the state-of-the-art of this ToF-SIMS / AFM combination and details its advantages. The chapter concludes with the outline of the information found in this manuscript.

Cette thèse est accessible à l'adresse : http://theses.insa-lyon.fr/publication/2019LYSEI121/these.pdf
© [M.A. Moreno Villavicencio], [2019], INSA Lyon, tous droits réservés

Cette thèse est accessible à l'adresse : http://theses.insa-lyon.fr/publication/2019LYSEI121/these.pdf
© [M.A. Moreno Villavicencio], [2019], INSA Lyon, tous droits réservés

1. MICROELECTRONIC TECHNOLOGY

Microelectronics is the area of technology that uses small elements to manufacture electronic systems. It emerged from the need of less expensive, lighter and smaller electronic devices such as radar, communication and missiles guidance systems.

The evolution of microelectronics is shown in Figure I.1.a. Microtechnology started in 1948 when John Bardeen, William Shockley and Walter Brattain created the first transistor. Three years later, this device would completely replace the electron tubes that electronic systems were using at that time. The transistors were fabricated with semiconductor materials such as germanium and doped monocrystalline silicon. Their size started no bigger than a fingertip and they are now three thousand times smaller than a human hair. They have evolved from lateral dimensions of 10 µm to 45 nm in forty years. Indeed, current production is seeking lateral dimensions down to 7 nm. [1,2]

The reliability of electronic systems, already complex by that time, was not improved by the addition of many small discrete components named transistors. To overcome this issue, in 1959, six of those circuit components were associated as a unit on a single substrate introducing the integrated circuits in the market. Transistors started to be manufactured directly on silicon surface, ten transistors forming the small-scale integration (SSI), one thousand of them in the medium-scale integration (MSI) and soon, ten millions of transistors in a gigascale-scale integration (GSI).

Integrated circuits were created to satisfy the demand of size and weight reduction, as well as a diminution of the number of connections in individual systems. Modern devices are only a few atoms tall and use metal-oxide-semiconductor (MOS) and complementary-metal-oxide-semiconductor (CMOS) technology.

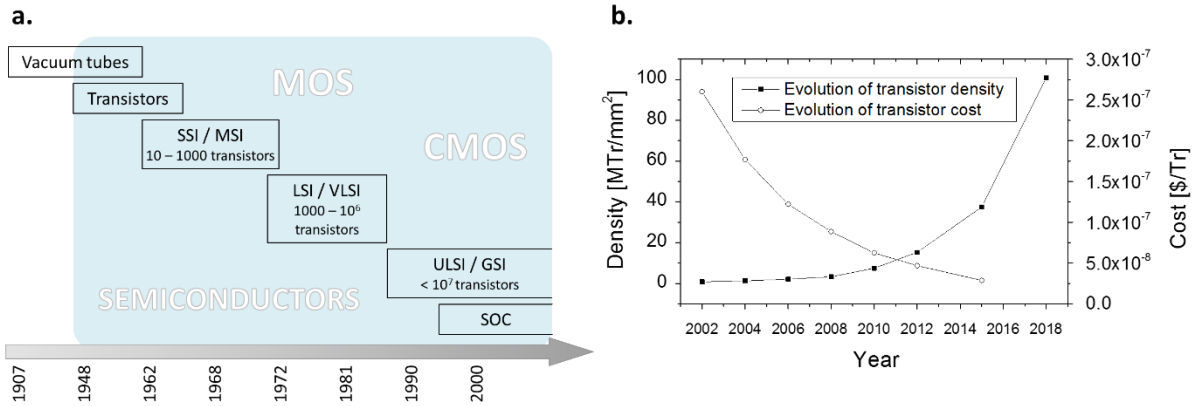

Figure I.1 Evolution of microelectronics (a) and transistor price and density of integrated circuits (b). [3,4]

Cette thèse est accessible à l'adresse : http://theses.insa-lyon.fr/publication/2019LYSEI121/these.pdf
© [M.A. Moreno Villavicencio], [2019], INSA Lyon, tous droits réservés

Some modern electrical devices are not only integrated circuits but also integrated systems; they may have all the components needed by the system on a single chip (SOC) [5]. The wide applications of these powerful integrated circuits created the market of modern electronics: miniaturized, digital and intelligent electronic products with low energy consumption, good quality, reliability and a fair price-performance ratio. Figure I.1.b shows the evolution of transistor price and the density of integrated circuits in the past 20 years. The transistor's price has decreased from 1 to 10^{-7} dollars since 1968. This price reduction is associated to the development of integrated systems with more and smaller transistors. The number of transistors per unit area quadrupled every three years and the price of circuits were reduced by half every 18 months. At the same time, the productivity gains were about 30% every year positioning the electronic industry at the top of the national economy in several countries. [6,7]

The key of the growing market is the investment in innovation to conceive faster, smaller, and more efficient devices; more transistors per area, more functions per area and less cost per function. Electronics started in radio, television and military devices such as weapons, navigation, communications and radar systems. Nowadays, microelectronics is present in the majority of electronic devices. They are found in our offices, in our household goods, in the gadgets that we use to communicate and to entertain us, in the hospitals and in our transportation systems [8]. Bargon [1] illustrated, seven years ago, the applications for microelectronics in every existing market. However, the applications are constantly improved and spread to other markets where consumer demands need to be satisfied: medicine, energy, aerospace, plastics, etc. [6]

These developments came with challenges and complexity. In 1965, Gordon Moore, cofounder of Intel Corporation, the largest semiconductor chip manufacturer, predicted that the semiconductor technology would duplicate its effectiveness every 18 months. Expecting that for 2020, the microelectronic technology will reach a scale of 14 nm. This surprisingly accurate prediction was named "*Moore's law*". [9]

This progress is not only seen in the reduction to nanometer scale but also in the new materials, structures, circuit design, working environment and the evolution of the processing techniques. The precision, quality control and the final product inspection were vital in the improvement of manufacturing. Indeed, the accuracy and reliability of production machines and measuring instruments were decisive factors in the development of the microelectronics industry. [6]

Cette thèse est accessible à l'adresse : http://theses.insa-lyon.fr/publication/2019LYSEI121/these.pdf
© [M.A. Moreno Villavicencio], [2019], INSA Lyon, tous droits réservés

The need for qualitative and quantitative information of nano-devices introduced high quality, reliable and sophisticated characterization techniques. These nanocharacterization techniques allowed to study, throughout the synthesis and processing of nano-devices, the topographical surfaces, morphology, crystal structure, particle size, existing defects and their chemical composition at the nano-scale [10,11]. Furthermore, the continuous fabrication of 3D architectures at a scale where their lateral dimensions have approached their third dimension renders impossible the full comprehension of the system without the analysis of all three dimensions. [12]

Cette thèse est accessible à l'adresse : http://theses.insa-lyon.fr/publication/2019LYSEI121/these.pdf
© [M.A. Moreno Villavicencio], [2019], INSA Lyon, tous droits réservés

Cette thèse est accessible à l'adresse : http://theses.insa-lyon.fr/publication/2019LYSEI121/these.pdf
© [M.A. Moreno Villavicencio], [2019], INSA Lyon, tous droits réservés

2. THREE-DIMENSIONAL CHARACTERIZATION AND CHEMICAL IMAGING

The need for high-resolution chemical and molecular characterization in two and three dimensions has emerged simultaneously in diverse fields of science. The development of chemical imaging in the 70s [13] had an important impact on the optimization of the microstructure for composites materials, on the knowledge of biological structures, on the analysis of mechanical, magnetic and electrical phenomena at small scales, on the functionality of micro and nano devices and on the examination of dopant profiles of microelectronic systems. [14,15]

Figure I.2 presents the most common characterization techniques classified in colors by the information that they provide: imaging techniques in green, physical properties in violet, thickness and density in beige, elemental information in blue and molecular information in red. The utilization of them in physical, material, biological sciences, etc. depends primary on their non-destructive nature, affinity to certain material, spatial resolution and the detection range. [15]

Despite the multiples techniques shown in the graph, only a few of them can determine 3D molecular information or have been adapted to provide 3D chemical imaging. The most used techniques with their limitations are described below.

- Electron tomography: an electron microscopy technique that produces a 3D rendering from two-dimensional (2D) projections of the sample. The object is tilted inside the microscope to obtain a projection of the chemical composition along the electron trajectory. From the 2D projections (typically 1 nm spatial resolution), a reconstruction algorithm creates the 3D matrix of the sample in the real space. Depending on the electron microscopy mode selected to obtain the chemical composition and images [energy-dispersive X-ray spectroscopy (EDX), electron-energy-loss spectroscopy (EELS), electron holography, among others], there are restrictions for the detection of the chemical information and huge challenges when imaging soft materials. Furthermore, electron tomography requires sample preparation to reduce the sample thickness down to a few hundreds of nanometers. [14–16]
- NanoSIMS: uses the principle of dynamic SIMS to obtain elemental and isotopic information with a lateral resolution down to 50 nm. A primary ion beam bombards the surface and the secondary ions are separated using a magnet. The disadvantage of this technique is that only seven different masses can be separated and detected. [17]

Cette thèse est accessible à l'adresse : http://theses.insa-lyon.fr/publication/2019LYSEI121/these.pdf
© [M.A. Moreno Villavicencio], [2019], INSA Lyon, tous droits réservés

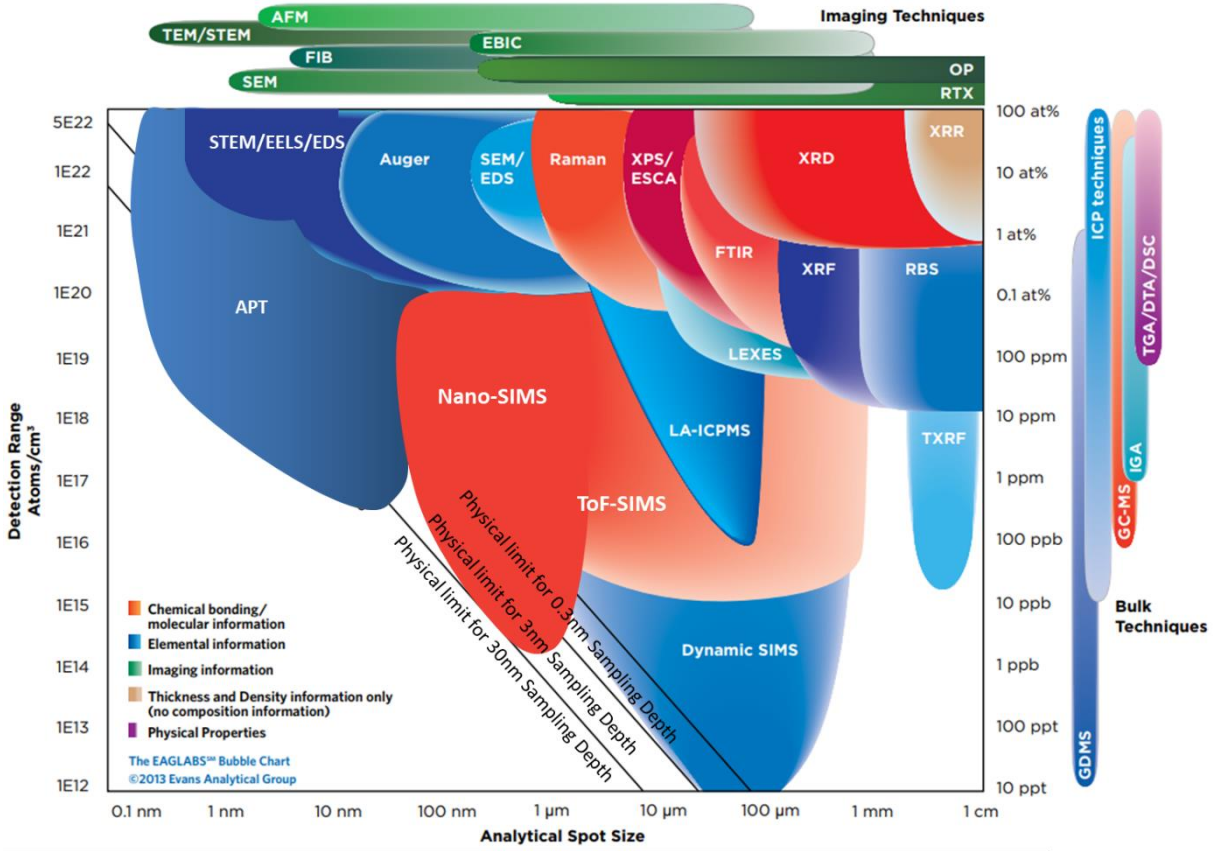

Figure I.2 Analytical resolution vs. detection limit of most common characterization techniques. They are classified in colors depending on the information that they provide. Image extracted from EAG Evans Analytical Group. [16]

- Atom probe tomography: it is a combination of field ion microscopy with a mass spectrometer. It was created to perform chemical measurements and imaging at the atomic scale (down to 0.3 nm in lateral resolution and 0.1 nm in depth resolution). It consists in the evaporation and ionisation of the sample atoms using a pulsed laser. The ions are projected onto a 2D detector where their flight time and x,y localization are registered. Reconstruction algorithms use the x,y localization to obtain 3D visualization of the sample. The main disadvantage of this technique is the sample preparation and thus the low detection range (at the best conditions 5.10^{18} at/cm^3). The sample has to be transformed into a very sharp tip with an end-radius between 10 and 100 nm. [18,19]
- 3D time-of-fight-secondary ion mass spectrometry (ToF-SIMS): it was initially created to image the elemental information of surfaces through the detection of secondary ions sputtered from the sample using a primary ion beam. A second ion beam was integrated to the system in order to remove the already analyzed surface and expose a new one.

Cette thèse est accessible à l'adresse : http://theses.insa-lyon.fr/publication/2019LYSEI121/these.pdf
© [M.A. Moreno Villavicencio], [2019], INSA Lyon, tous droits réservés

A chemical image of the new surface is obtained and an in-depth chemical analysis is performed. The stack of those ToF-SIMS images creates a 3D representation of the sample. This technique does not require sample preparation and its depth resolution can be as good as 1 nm. It has a dynamic range and high mass resolution, up to 10^4 M/ΔM. However, its lateral resolution is only 100 nm.

Additionally, challenges with the 3D reconstruction and the sputtering of inhomogeneous samples remain because the standard ToF-SIMS data reconstruction method does not take into the account the sample topography.

ToF-SIMS is a suitable technique to analyze complex stacks of thin organic and inorganic layers, devices with different compositions, samples with strong topography, patterned structures, among others. It is widely used in the microelectronics, biology, metallurgic and pharmaceutical fields for the identification of contamination, failure analysis, and evaluation of fabrication process and quantification of dopants. [20–22]

However, in microelectronics, the use of a large variety of materials in increasingly complex structures drove this technique to its limit in resolution. For many analytical questions, a combined characterization approach seemed more reliable. Some authors have combined the ToF-SIMS with techniques shown in the top left of the graph in Figure I.2 as a solution to improve the lateral resolution of the chemical imaging. Association of ToF-SIMS with several techniques and novel sample preparation as X-ray powder diffraction (XRD) [23,24], X-ray photoelectron spectroscopy (XPS) [25–27], Fourier-transform infrared spectroscopy (FTIR) [28], scanning electron microscopy (SEM) [29], atom probe tomography [30], and transmission electron microscopy (TEM) [31] are found in the literature. However, the combination of ToF-SIMS with atomic force microscopy (AFM) is found to be the key for the 3D high-resolution imaging of complex microelectronic devices.

2.1. BEYOND THE TOF-SIMS CHALLENGES BY ITS COMBINATION WITH THE ATOMIC FORCE MICROSCOPY

The AFM is largely used to image the surface topography of organic, inorganic and biomaterials. Topographical maps are created using the interaction force between a nanometric tip and the sample surface. The lateral resolution of 10 nm and the depth resolution of 0.1 nm turned the AFM into the instrument most utilized to manipulate and visualize surface properties at the nanoscale.

This technique opens the possibility of compensating the ToF-SIMS lateral resolution and at the same time, contributes the topographical information that is missing in the 3D reconstruction algorithm. Furthermore, the versatility of AFM as a characterization technique through the modification of the tip, allows it to image local properties of the sample. Figure I.3 shows these AFM advanced operation modes.

Cette thèse est accessible à l'adresse : http://theses.insa-lyon.fr/publication/2019LYSEI121/these.pdf
© [M.A. Moreno Villavicencio], [2019], INSA Lyon, tous droits réservés

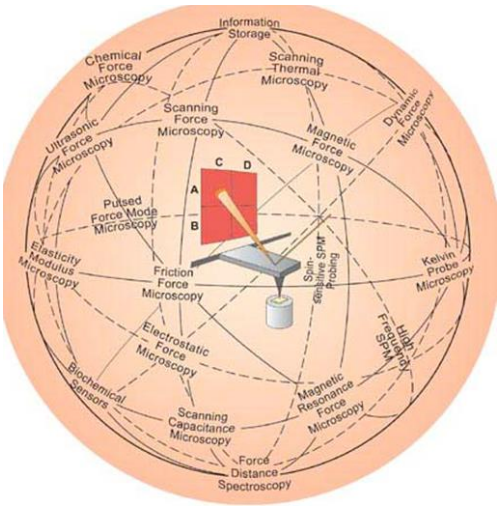

Figure I.3 Advanced AFM operation modes. [35]

The AFM advanced modes have been implemented in the routine characterization of microelectronics since their development in the late 80s. Electrical modes such as scanning capacitance microscopy (SCM) and scanning spreading resistance microscopy (SSRM) are used to image dopant distribution and concentration within semiconductors [32].

Conductive-atomic force microscopy (C-AFM) and Kelvin force microscopy (KFM) measure, respectively, the current between the tip and the sample and the tip-surface contact potential as function of an applied bias within dielectric thin films, dynamic random access memories, etc. [33,34]. Distinct operation modes were also developed to investigate the electromechanical response for piezoelectric films, mechanical response of soft samples and magnetic properties of microdevices. However, none of the existing modes provides molecular or elemental information.

Naturally, the interest of the scientific community on correlating the chemical and the topographical has increased with the years bringing the development of other combined instruments such as AFM with scanning electron microscopes (SEM) or with a NanoSIMS, unique instruments that enable the complementarity of these other techniques [36,37].

Cette thèse est accessible à l'adresse : http://theses.insa-lyon.fr/publication/2019LYSEI121/these.pdf
© [M.A. Moreno Villavicencio], [2019], INSA Lyon, tous droits réservés

3. ToF-SIMS and AFM as a combined approach to characterize microelectronic devices

The ToF-SIMS and AFM have been complementary techniques for more than 20 years in diverse fields of science. They were initially combined to relate surface roughness or morphology to sample composition. This combination has contributed in different ways to the understanding of many phenomena. A few examples are listed below.

- Physics of sputtering: study of inhomogeneity and damage produced by the ToF-SIMS sputtering through the measurement of the surface roughness by AFM [38–40]. Indeed, some authors have compared the damage and the ion-induced topography created by different ToF-SIMS sputtering conditions using AFM analysis in order to set the most suitable conditions for specific analysis [41–43].
- Polymers and organic molecules: study of phase formation, lamellar orientation, molecules aggregation and their distribution into the sample. [44–47]
- Biomolecules and cells chemical imaging: study of biochemical surface patterning, composition of human cells. [48,49]
- Inorganic samples: study of surface contamination or molecule absorption from the environment to metal surfaces, defects existing in interfaces and surfaces of inorganic samples. [50,51]

The research community is attracted by this combination and they are currently using it to advanced characterization of complex samples using diverse operation modes of AFM.

- Conductive-AFM and ToF-SIMS: study the electroforming behavior in resistive switching cells, hysteresis of solar cells. [52,53]
- Piezoresponse force microscopy (PFM) and ToF-SIMS: study of polarization switching in ferroelectric materials. [54,55]
- KFM and ToF-SIMS: correlation of hydrophilic, hydrophobic and charged regions with their chemical composition, study of surface potential and morphology control of organic solar cells. [56,57]
- SCM – SSRM and ToF-SIMS: study of carrier concentration profiles and atomic diffusion within layers. [58,59]
- Chemical modification of AFM tip and ToF-SIMS: study of end groups of molecules present on the sample surface, the determination of any specific recognition of those molecules and their distribution over the surface. [60]

Cette thèse est accessible à l'adresse : http://theses.insa-lyon.fr/publication/2019LYSEI121/these.pdf
© [M.A. Moreno Villavicencio], [2019], INSA Lyon, tous droits réservés

The AFM has also emerged as a solution to overcome the artefacts found in a 3D ToF-SIMS analysis. It is a suitable characterization technique to provide the missing topography to the 3D ToF-SIMS reconstruction. [61,62]

The ToF-SIMS / AFM combination started ex-situ, but an analysis can be time consuming. The sample transfer, the pumping time and the area localization will add about 30 minutes each time a transfer is needed. The duration of a complete analysis depends on the individual time needed to perform common AFM images, common ToF-SIMS depth profiles but also on the transfer time between the two analysis positions. Additionally, the sample transfer needs to be done in a controlled environment to reduce the contamination of the surface.

Arising from the expansion of applications for these two techniques, in 2008 a European project named 3D NanoChemiscope started. Its goal was to develop a combined ToF-SIMS / AFM instrument for the three dimensional chemical analysis of nanostructures. This single ultra-high vacuum instrument would provide information, on the nanoscale, about surface chemistry and surface morphology from the same sample region [63].

The entry of this instrument on the market opened the possibility of performing in-situ analysis with less contamination or surface degradation; the sample remains in the vacuum chamber. The precision of the sample transfer between the instruments is assured by the integrated piezo displacement system allowing analysis to be performed on the same sample area. Additionally, the sample only needs to be pumped down once. However, depending on the AFM operation mode, good quality topographical images under vacuum can take days. Although ex-situ and in-situ methodologies have their advantages and inconveniences both can achieve similar results.

Further investigation of the application fields of combined characterization techniques is being carried out by laboratories around the world. A European project was created in 2016 under the name “Metrology for future 3D-technologies” (METRO 4-3D) in which ten European laboratories studied the applications of correlative characterization techniques in semiconductor 3D-structures and devices [64]. Part of the work in this manuscript was performed as part of this European programme and it has received funding from the European Union’s Horizon 2020 research and innovation programme under grant agreement No 688225.

This thesis project aims the development of a combined ToF-SIMS / AFM methodology that allows a correlation of the chemical and topographical information of advanced devices. It studies several applications of this combination while answering current challenges that the individual techniques present. The project was held at the NanoCharacterization Platform of CEA Grenoble. However, it benefited from the in-situ ToF-SIMS / AFM instrument located at IMEC in Belgium and the data treatment knowledge of the EMPA group located in Switzerland.

Cette thèse est accessible à l'adresse : http://theses.insa-lyon.fr/publication/2019LYSEI121/these.pdf
© [M.A. Moreno Villavicencio], [2019], INSA Lyon, tous droits réservés

4. THESIS OUTLINE

CHAPTER II of this thesis project presents in detail a combined ToF-SIMS and AFM methodology that can be used in the microelectronic field. The methodology comprises AFM topographical images, crater depth measurements and sequences of ToF-SIMS images, all acquired on the same area of the sample. The principle is to perform AFM images and crater depth measurements every time an interface is detected in the ToF-SIMS depth-profile. These intermediate AFM images can be used to estimate the sample surface topography and roughness at different points of the depth profile, matching each value to their corresponding chemical element at that depth. In the case where AFM advanced operation modes are used, a combination of three types of information is possible: chemical, topographical and the property provided by the advanced mode. In addition, the intermediate AFM images allow the calculation of pixel-per-pixel sputter rates and provide further knowledge about the sputtering behavior of 3D systems. [65,66].

CHAPTER III describes the process to correct the 3D ToF-SIMS visualization of a GaAs / SiO_2 heterogeneous sample using the established ToF-SIMS and AFM combined methodology. The initial topography of the sample and the high difference of sputter rates between the GaAs and the SiO_2 creates a distortion of the ToF-SIMS data set when performing a classical 3D visualization. In the same way, local sputter rate maps of the analyzed area were calculated and the lateral variation of sputter rates was analyzed using the AFM topographical profiles. Moreover, overlay of the chemical elements over topographical surfaces allowed the correlation of the chemical composition with surface roughness and morphology.

The ToF-SIMS and AFM procedure to obtain local sputter rate maps was used to study the artefacts found when performing ToF-SIMS analysis of nano-structures. CHAPTER IV starts analyzing the optimization of the analysis conditions when sputtering nano-patterns. Specifically, the influence of the primary energy and beam orientation on sputter yield, sample roughness, lateral and depth resolution and topography evolution. It introduces the term geometric shadowing effect that was sequentially studied for an AlN / GaN heterostructure with cracks on all over the surface.

Finally, three AFM advanced operation modes are introduced in CHAPTER V. They are piezoresponse force microscopy (PFM), scanning capacitance microscopy (SCM) and scanning spreading resistance microscopy (SSRM). Specific protocols for the experiments are described. The chapter starts with the combination of PFM with ToF-SIMS. It was used to analyze the chemical modification produced during electrical stress of piezoelectric thin films. The chemical effect of the contact of the AFM tip with the surface is also investigated.

Cette thèse est accessible à l'adresse : http://theses.insa-lyon.fr/publication/2019LYSEI121/these.pdf
© [M.A. Moreno Villavicencio], [2019], INSA Lyon, tous droits réservés

Secondly, the results obtained through the combination of ToF-SIMS with AFM electrical modes such as SCM and SSRM are presented. The ToF-SIMS sputtering was used to remove from an n-p-doped sample the gallium implantation from FIB preparation and thus, recover the initial electrical characteristics.

The thesis manuscript ends with the general conclusions of the different sub-projects and the perspectives of this combined ToF-SIMS and AFM methodology.

Cette thèse est accessible à l'adresse : http://theses.insa-lyon.fr/publication/2019LYSEI121/these.pdf
© [M.A. Moreno Villavicencio], [2019], INSA Lyon, tous droits réservés

5. CONCLUSIONS

This chapter presents the motivations behind this project and concludes with the thesis outline.

The development of microelectronics brought the necessity of having reliable three dimensional characterization techniques at the nanoscale. Both chemical and morphological information is required to control the processing of microelectronic devices. Many existing characterization techniques are at the limits of their capacities when faced with the increasing complexity of new devices. The combination of techniques may be a solution to exceed those limits.

The ToF-SIMS was described as a powerful 3D chemical characterization technique. It has high detection range, provides chemical maps of the detected secondary ions and the analysis can be performed in-depth. However, the lateral resolution of 100 nm and the lack of consideration of the sample topography when analyzing a sample are seen as a limitation for the characterization of microdevices. The AFM was identified as a characterization technique that could resolve the ToF-SIMS limitations. Indeed, the AFM provides maps of surface topography with a lateral resolution of 10 nm, and the possibility of using advanced operation modes of the AFM to analyze other local properties of the sample exists.

The AFM and ToF-SIMS have been used ex-situ as complementary techniques for many years. Some of the applications of this combined ToF-SIMS and AFM methodology are listed. This combination has been of recent interest for many research groups and an in-situ ToF-SIMS and AFM instrument is currently on the market. There are advantages and inconveniences working in-situ and ex-situ but if they are considered, the results are comparable.

Cette thèse est accessible à l'adresse : http://theses.insa-lyon.fr/publication/2019LYSEI121/these.pdf
© [M.A. Moreno Villavicencio], [2019], INSA Lyon, tous droits réservés

Cette thèse est accessible à l'adresse : http://theses.insa-lyon.fr/publication/2019LYSEI121/these.pdf
© [M.A. Moreno Villavicencio], [2019], INSA Lyon, tous droits réservés

CHAPTER II.

TOF-SIMS AND AFM AS INDIVIDUAL CHARACTERIZATION TECHNIQUES AND THEIR COMBINED PROTOCOL

In this second chapter, the working principle of the time-of-flight secondary ion mass spectrometry (ToF-SIMS) and the atomic force microscopy (AFM) are introduced. The operation modes that were used during the development of this thesis project are also addressed. Secondly, the complementarity of these techniques is demonstrated through the development of a combined ToF-SIMS / AFM protocol and a fully description of the protocol is presented. Lastly, the instruments employed to perform the ex-situ and the in-situ ToF-SIMS / AFM combined methodology are described.

Cette thèse est accessible à l'adresse : http://theses.insa-lyon.fr/publication/2019LYSEI121/these.pdf
© [M.A. Moreno Villavicencio], [2019], INSA Lyon, tous droits réservés

Cette thèse est accessible à l'adresse : http://theses.insa-lyon.fr/publication/2019LYSEI121/these.pdf
© [M.A. Moreno Villavicencio], [2019], INSA Lyon, tous droits réservés

1. TIME-OF-FLIGHT SECONDARY ION MASS SPECTROMETRY

The mass spectrometry uses the principle of mass to charge (m/z) of ions demonstrated by Joseph John Thomson in 1886. The secondary ion mass spectrometry (SIMS) studies the secondary ions emitted from a surface (< 0.5 nm depth) to determine their mass-to-charge ratio and to obtain the functional groups, elemental and molecular composition of the analyzed sample. SIMS is a destructive characterization technique; the impact of the primary ions damages the sample surface and the near vicinity (up to 500 µm away due to redeposition). [67,68]

1.1. GENERAL PRINCIPLE

The secondary ion emission is achieved by bombarding the sample surface with a primary ion beam of sufficient energy to produce a process known as sputtering [69]. The primary ions collide with the solid, some of them with enough energy to break the superficial bonds and to eject some molecules or atoms from the surface. The extracted atoms can be neutral, positively or negatively charged. The charged particles are accelerated by an electric field at a fixed voltage (U). They enter into a field free drift tube of length (L) where a time-of-flight analyzer measures the time-of-flight (t_{TOF}) that the ions require to reach the detector. Their m/z is calculated from their t_{TOF} (Eq. II.1) under two assumptions: the energy supplied to the ions by the electric field is transformed into kinetic energy and gravity or other external forces do not affect the ion flight. Hereby, lighter ions arrive faster than heavier ions at the detector. [70]

$$t_{TOF\,[s]} = \frac{L}{v} = \frac{L}{\sqrt{2.e.U}}\sqrt{\frac{m}{z}} \qquad \textit{Eq. II.1} \quad \textit{[71]}$$

Initially, the ToF-SIMS was a technique for surface analysis, the so-called static SIMS. For this, the number of primary ions or primary ion dose (I_p) needs to be lower than 10^{13} ions/cm^2 [21,70,72]. However, if higher doses are used, the ToF-SIMS can perform dynamic SIMS analysis. The most common mode is the depth-profiling. Here, two primary beams are required: the analysis and the sputter beam (see the diagram in Figure II.1.a). The analysis beam analyzes the surface; the sputter beam then removes the already analyzed surface thus digging into the sample. This cycle is repeated many times to obtain a depth profile [73]. The analysis and the sputtering can be done by the same ion gun in the single beam mode or by different guns in the dual-beam mode [74]. The ToF-SIMS depth-profiling dual beam mode can be performed in non-interlaced or interlaced mode.

Cette thèse est accessible à l'adresse : http://theses.insa-lyon.fr/publication/2019LYSEI121/these.pdf
© [M.A. Moreno Villavicencio], [2019], INSA Lyon, tous droits réservés

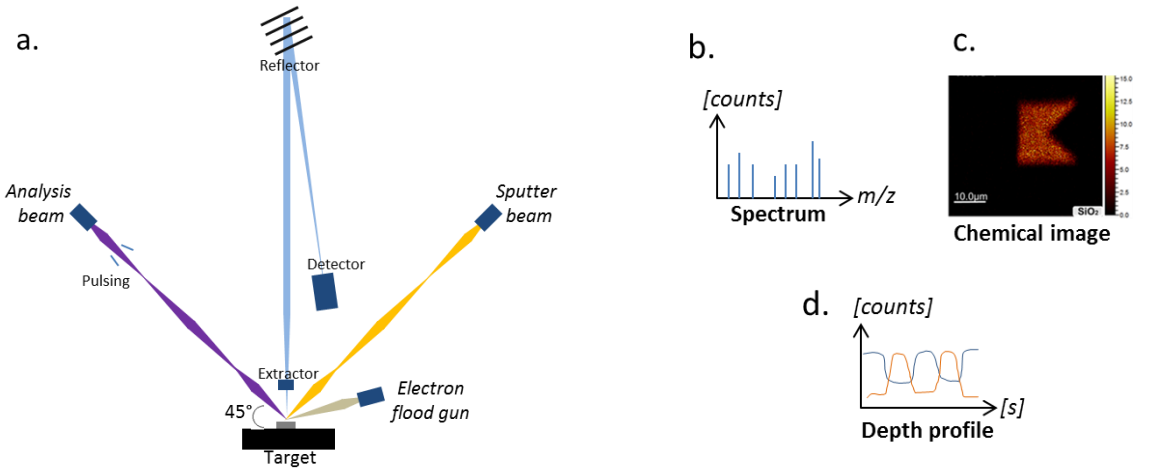

Figure II.1 *a. Schematic of the ToF-SIMS dual beam instrument. Information provided by the detected secondary ions: b. mass spectrum, c. chemical image for each ion and d. depth profile of secondary ion intensities.*

In the non-interlaced mode, the analysis and the sputter phase are separated. The analysis beam scans the entire area, the secondary ions are detected, and lastly the sputter beam sputters the surface. There is a pause time before repeating the cycle where a low energy electron gun, better-known as a "flood gun", neutralizes the surface charges [70,72,75]. In the interlaced mode, the analysis beam analyzes a pixel, the sputter beam sputters that pixel and then the flood gun neutralizes the surface charges. The extraction field is switched off to assure that only the secondary ions emitted by the analysis beam enter to the flight tube. The analysis time for a given depth analyzed is shorter than using non-interlaced mode. [74,76]

Besides the ToF-SIMS depth-profiling, the in-depth chemical information can be obtained by the FIB / ToF-SIMS imaging and the bevel crater approach (Figure II.2.b and c respectively).

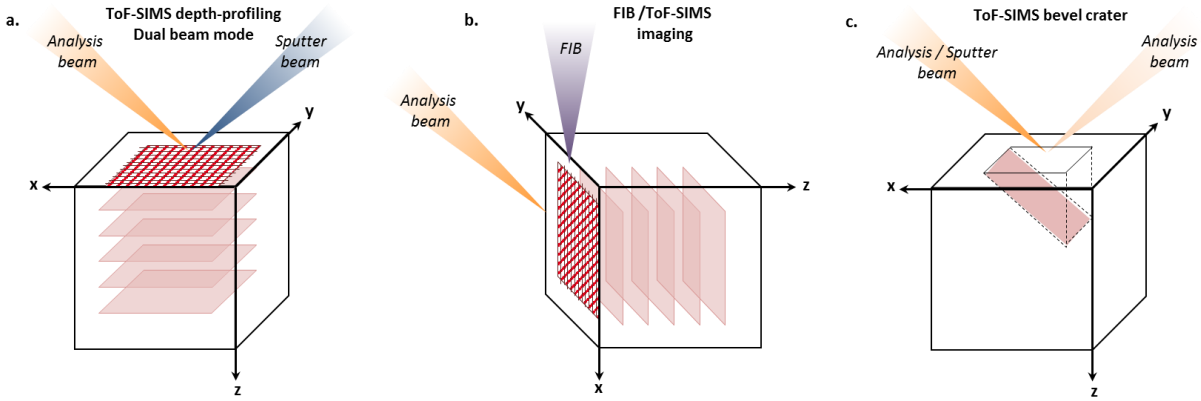

Figure II.2 *Schematic of the a. ToF-SIMS depth-profiling dual beam mode, b. FIB / ToF-SIMS imaging and c. ToF-SIMS bevel crater.*

Cette thèse est accessible à l'adresse : http://theses.insa-lyon.fr/publication/2019LYSEI121/these.pdf
© [M.A. Moreno Villavicencio], [2019], INSA Lyon, tous droits réservés

The FIB / ToF-SIMS approach is suitable to analyze the 2D planes perpendicular to the top of the sample surface, contrary to the depth-profiling where the analyzed 2D planes are the one parallel to the sample surface [77]. The third approach consists on creating a bevel crater instead of a flat crater. The ion beam is used to mill the surface in a bevel shaped crater by varying the dose from 0 to 100% from one side of the crater to the other. This method allows a rapid surface study of the generated cross-section and is especially useful on thin multi-layers structures as the bevel introduces a magnification factor. [78]

The ToF-SIMS analysis beam scans areas from a few μm^2 to several hundred of μm^2 with a pixel resolution between 2 x 2 pixels and 2048 x 2048 pixels. From each pixel, a mass spectrum such as the one in Figure II.1.b is collected. From each scan, 2D images such as those shown in Figure II.1.c are produced. Moreover, from each 3D analysis the previous results are collected as a function of the sputter time (t). From them, a depth profile as shown in Figure II.1.d and a 3D visualization are generated.

- Mass spectrum: one mass spectrum is collected per pixel representing the number of detected secondary ions (intensity) as a function of their m/z ratio. Two important characteristics of the spectra are their mass resolution of up to $M/\Delta M > 10^4$ and their mass range of 10 kDaltons which enables the detection of polymers, isotopes, ions, among others [70,79]. The pulsing width of the primary beam influences the mass resolution of the spectra; shorter the pulse is, higher is the mass resolution. However, this last one is also affected by other factors such as the dead time of the detector, the sample topography or roughness and the correction of the secondary ion energy distribution [70,74].
- 2D ToF-SIMS images: they are obtained by locating the secondary ion intensity of every m/z specie at the pixel from where it was sputtered. The lateral resolution can go down to 100 nm and it depends mainly on the interaction volume that is related to the diameter of the primary beam. The smaller this is, the higher is the lateral resolution [70,80]. Aberrations of the 2D images are commonly found because the ToF-SIMS neglects the sample topography when performing an analysis. Concrete examples will be given in 0.
- Depth profile: it represents the intensity of each m/z specie as a function of the sample depth or sputter time. The ToF-SIMS may achieve a depth resolution down to 1 nm depending on the accumulation of the sputtering damage and the sample roughness. It is influenced by the sputter beam energy, current, angle, sample morphology, among others [81,82]. Information about its calculation can be found in [73,83,84].
- 3D visualization: it is generated by stacking the ToF-SIMS images. However, the aberrations in the ToF-SIMS images propagate themselves to the 3D visualization.

Cette thèse est accessible à l'adresse : http://theses.insa-lyon.fr/publication/2019LYSEI121/these.pdf
© [M.A. Moreno Villavicencio], [2019], INSA Lyon, tous droits réservés

The third dimension of the volume corresponds to the sputter time. This can be transformed into a depth (z) scale using the sputter rate (S_R) [nm/s], Eq. II.2.

$$z[nm] = S_R . t \qquad \textit{Eq. II.2} \quad \textit{[73]}$$

1.1.1. SPUTTER RATE CALCULATION

The sputter rate refers to the velocity at which the atoms are extracted from the sample. It changes vertically, in the depth-profile, and horizontally, from pixel to pixel, product of the damage accumulation on the sample surface and the non-homogeneous sputtering [69,85–87]. The sputter rate depends on the mechanism of energy transfer between the primary ions and the sample. Thus, its value relies upon the material nature, the sample topography and the setting of the primary beam. It can be calculated by [88]:

- depth-profiling a sample with well-known depth dimensions to determine the needed time to sputter a specific depth.
- measuring the depth of the crater created during the analysis with another technique and then use the Eq. II.2 to calculate the sputter rate.
- using the sputter yield (Sy) which is linked to the sputter rate (S_R) by the relation of Eq. II.3. The equation includes the molar mass (M) of the material present in the sample, the primary ion beam current (I), the sample density (ρ), the Avogadro number (N_A), the electron charge (e) and the surface area hit by the primary ions (A).

$$S_R[nm/s] = \frac{M . I . S_y}{\rho . N_A . e . A} \qquad \textit{Eq. II.3} \quad \textit{[73]}$$

The sputter yield is the number of secondary particles of a given specie (neutrals or charged) that were extracted from the surface per impact of primary ion. The sputter yield is affected by the sample topography, roughness and the analysis conditions. It is enhanced when the primary beam hits the surface at glancing angle [83] and it is directly proportional to the ion current, the primary energy and the mass of the primary ions. However, the opposite effect is seen when the mass of the primary ions is excessively increased or the beam energy is higher than 30 keV. In this case, there is a deep penetration of the primary ions producing their implantation at a large depth. Thus, collisions are not shallow enough to cause the ejection of atoms. [72,89] The theoretical values for the elements of the periodic table depending on the energy and angle of the primary beam can be calculated following the empirical formula developed by Yamamura *et al*. [90–92]. However, an experimental value can be obtained from Eq. II.4 where ρ_a is the atomic density, A is the surface area hit by the primary ions, z is the sputtered depth and I_p is the primary ion dose.

Cette thèse est accessible à l'adresse : http://theses.insa-lyon.fr/publication/2019LYSEI121/these.pdf
© [M.A. Moreno Villavicencio], [2019], INSA Lyon, tous droits réservés

$$S_y = \frac{\rho_a . A . z}{I_p} \qquad \textit{Eq. II.4} \quad \textit{[72,74]}$$

The ion dose corresponds to the number of primary ions per unit of area. It is calculated following the Eq. II.5 or the ToF-SIMS IONTOF software *SurfaceLab 6*.

$$I_P[ion/m^2] = \frac{I . t}{e . A} \qquad \textit{Eq. II.5} \quad \textit{[93]}$$

1.2. ION-SOLID INTERACTIONS

The collision of a primary ion accelerated to several keV with a surface is mainly led by elastic interactions between the primary ions and atoms from the surface. From the moment a primary ion strikes the surface, the energy from the ion is transferred to the sample. If the primary ion energy is higher than the surface bonding energy, the sputtering of atoms or molecules from the first 5 Å of the sample occurs. Sputtering-induced damages as dislocations, vacancies, stress, strain, atom implantation, recoil or cascade mixing are then produced in the following nanometers. After this damaged area, the maximum penetration of the primary ions is found. [69,84,94]

Three elastic collision models can explain this distribution in the sample [95,96]:

- Knock-on: two-body collision regime. The primary ion hits the surface; its energy is transferred to an atom of the sample. The atom has now enough energy to displace itself deeper in the sample or to be sputtered. This occurs for primary energy less than 1 keV.
- Linear cascade: the energy transferred to the superficial atom is sufficiently high that it can collide with other atoms and transfer them enough energy for them to displace as well. Sputtering can occur if the cascade approaches the surface.
- Spike: the energy transferred to the atoms of the second collision causes them to collide with other atoms increasing the density of moving atoms. No sputtering is produced because the collisions are deep in the sample.

After the collision, low energy electrons, photons, neutrals and charged particles are emitted. These last one are the so-called secondary ions. They may be formed by, for example, the dissociation of M_xO_y and M_xCs_y compounds created after a reaction of remaining Cs^+ or O_2^+ primary ions with M metallic atoms of the sample [72,97]. The oxygen keeps the negative charge as it is more electronegative and the M^+ fragment is formed. In the opposite case, cesium can behave as an electron donor due to its low electronegativity creating fragments of Cs^+ and M^-.

Cette thèse est accessible à l'adresse : http://theses.insa-lyon.fr/publication/2019LYSEI121/these.pdf
© [M.A. Moreno Villavicencio], [2019], INSA Lyon, tous droits réservés

This example relates the nature of the primary ion beam with the sputtering yield of a specific species [21,79,98]. The ionization theories vary depending on the nature of the matrix and differ in when and how the charges are created. At the moment there is not a formal explanation of the ionization process. However, it is possible to find some of the proposed models in the literature: nascent ion molecule model, desorption ionization model, the bond breaking model, electron tunneling model [21,94].

Along the entire process, the surface is constantly changing. The recoil implantation that corresponds to the displacement of one atom of the sample within the sample creates defects. The cascade produces layer mixing. The generated impurities, ion implantation, atomic mixing, surface roughness produce non-homogeneous sputtering, causing local changes in the sputtering yield and with it the diminution of the depth resolution. [96] This phenomenon of local sputtering may also lead to the development of the surface topography, better-known as ion induced topography. The generated morphology usually starts with etch pits and it can evolved into ripples, pits, facets, etc. depending on the sputtering conditions and the sample nature [41,85,96,99].

1.3. TIME-OF-FLIGHT MASS ANALYZER

The secondary ions are attracted to the analyzer using the voltage set by the extractor. Inside the 2 m flight tube, the ions are focused by a lens toward the detector. The ions reach the reflector (see Figure II.1.a) and their trajectory length is modified according to the ion energy. The higher the energy, the deeper the ion will enter into the reflector increasing his path before being redirected to the detector by an electrostatic field. Any extra energy that atoms from the same nature may have is compensated with a longer flight-path. Thus, ions of same nature will arrive at the same time to detector. The time-of-flight is calculated per secondary ion using the time spent between the pulsing of the analysis beam and its arrival to the detector. [21,70]

The number of detected secondary ions of species *m,* known as secondary ion intensity (I_m), is calculated with the following relation:

$$I_m = n.\, I_{p.} S_m.\, {P_m}^{+/-}.\, C_m \qquad \textit{Eq. II.6} \quad \textit{[100]}$$

The relation includes the surface concentration of the element *m* (C_m), the probability of that element to be ionized either positive or negative (P_m), the sputter yield of *m* particles (S_m), the primary ion dose (I_p) and the transmission efficiency of the instrument toward the detector (*n)*, 90 – 95 % for the instrument we have used (ToF-SIMS V $_{\text{ION-TOF}}$).

Cette thèse est accessible à l'adresse : http://theses.insa-lyon.fr/publication/2019LYSEI121/these.pdf
© [M.A. Moreno Villavicencio], [2019], INSA Lyon, tous droits réservés

1.4. INSTRUMENTAL SETUP

1.4.1. ANALYSIS BEAM

The analysis beam is a low current (less than some pA) high energy pulsed beam. Generally, a liquid metal ion source (LMIS) is used. The beam can be formed by atomic ions or metal clusters: Bi_x^+, Ga^+, Au_x^+ and In^+ are some of them. The bismuth is the most common due to the wide range of primary ion species that it produces (Bi^+, Bi^{++}, Bi_3^+, Bi_3^{++}, Bi_5^+, Bi_7^+). A suitable analysis gun should produce the highest secondary emission with the smallest beam size. Empirically, it has been shown that the increase of projectile mass increases secondary ion emission. However, this trend can be reversed due to the lower velocity of heavier clusters as in the case of Bi_5^+. [84,93]

The ion source consists of two electrical contacts set on an insulating base. Those contacts are the support of a heater filament where a needle and a reservoir coated with the metal are mounted. A high negative potential is applied from an extractor located close to the tip of the needle. The needle is heated and due to the negative potential the electrons of the metal goes backwards while the positive metal ions move toward the tip creating a cone and starting the ion emission. [74,84,101]

The ions are accelerated to an energy that is typically between 15 keV and 30 keV. Electrostatic lenses focus the beam and a Wien filter (flight time filter) separates the ions by their mass. Electric and magnetic fields accelerate the atoms in order for them to be separated according to their velocity. Only the required type of ions goes through the filter to reach an aperture that gives final size of the beam. [96,101]

The mass resolution is defined by the pulse width, the shorter the pulse, the higher the mass resolution. However, a short pulse width reduces the secondary ion intensities and thus the signal-to-noise-ratio of the ToF-SIMS images. [79,93,102,103] Following these constraints, diverse operation modes are possible:

- Bunched mode: suitable for high mass resolution analysis. It applies a pulse of about 600 ps with high current (more than 500 primary ions per pulse).
- Collimated mode: suitable for high lateral resolution analysis. The aperture defines the beam diameter, about 100 nm. Long pulse to guarantee a high signal-to-noise-ratio by increasing secondary ion intensity.
- Burst mode (patented by IONTOF): good compromise between the mass and the lateral resolution. The pulse time is about 1.5 ns with a current of 100 primary ions. Several pulse repetitions in one cycle are done in order to sum the secondary ion intensities obtained at each time. This way, the pulse is short enough to have 5000 $M/\Delta M$ mass resolution and the beam is small enough to have 250 nm spatial resolution.

Cette thèse est accessible à l'adresse : http://theses.insa-lyon.fr/publication/2019LYSEI121/these.pdf
© [M.A. Moreno Villavicencio], [2019], INSA Lyon, tous droits réservés

The analysis beam should sputter an insignificant depth compared to the entire sputtered depth, a fraction less than 0.01. To achieve this value, the dose ratio between sputter beam and analysis beam should be in the rage of 600 up to 1000 [45].

1.4.2. SPUTTER BEAM

The sputter beam is used for 3D ToF-SIMS analysis. It is a DC, low energy (from 100 eV to a few keV), high current beam (up to several hundred nA). A high primary energy may fragment the molecules causing the loss of chemical information; a low primary energy (less than 500 eV) creates ion deposition and collision mixing on the surface. A compromise between fragmentation and depth resolution should be found.

C_{60}+, SF_5+, Ar_x^+, O_2^+, Cs^+, Xe^+ are the most frequent ions for sputtering and they are used as atomic ions or as clusters. It is also possible, but not common, to use some of the primary ions on the list for analysis and sputtering. The selection of the sputter ions depends on the sample nature. The organic molecules are likely to be fragmented under a strong impact of the primary ions and then the chemical information can be missed [80]. Argon clusters sources were developed to sputter polymeric matrices reducing the damage and fragmentation without losing secondary ion intensity. The energy of a single ion depends on the number of atoms in the cluster. Extensive information about ToF-SIMS analysis on organic materials can be found in those references[[45,74,104,105].

The beam formation is different. The Cs^+ ions are formed during the evaporation of a Cs metal or compound; the vapor flows towards a porous plug where it diffuses. They are then extracted and accelerated. On the other hand, the noble gas and oxygen beams are formed by electron impact ion sources. In this case, electrons are accelerated through an aperture where they collide with the gas molecules to produce the ions. References [21,74,96] give more information about this principle. The analysis area should be 9 times smaller and centered with the sputtered area to avoid the edge effects [45,79].

The chemical information provided by the ToF-SIMS characterization technique can be combined with other physical properties to obtain a better understanding of the sample.

Cette thèse est accessible à l'adresse : http://theses.insa-lyon.fr/publication/2019LYSEI121/these.pdf
© [M.A. Moreno Villavicencio], [2019], INSA Lyon, tous droits réservés

2. ATOMIC FORCE MICROSCOPY

The atomic force microscopy (AFM) was created in 1986 by Binnig, Quate and Gerber [106] to overcome the main limitation of the scanning tunnelling microscopy, the surface imaging of exclusively conductive samples. Its principle is based on the detection of interaction forces between the sample surface and a tip located a few nanometers above on a flexible cantilever. Those interaction forces are assumed to represent the surface topography.

2.1. GENERAL PRINCIPLE

The interaction forces between the tip and the sample surface vary with the tip-sample distance. Figure II.3 describes this variation and illustrates the three existing regimes: (i) no interaction force when the tip is far away from the surface, (ii) the attractive regime when the tip approaches itself toward the sample surface and, (iii) the repulsive regime when the tip is in contact with the sample. [107]

Different nature of forces are found within each regime. In the attractive regime, long and short-range forces in the range of pN to nN are detected [108]:

- Electrostatic force: long-range force produced by a non-zero potential difference between the tip and the sample. This force is always present for conductive or semi-conductive samples and tips.
- Magnetic force: long-range force obtained by the utilization of magnetic tips to locally measure magnetic properties of the sample.
- Van der Waals force: long-range force due to the variation in the local electric dipole between the atoms of the tip and the sample.
- Capillarity force: short-range force produced by the deposition of water molecules from the air in the sample or in the tip surface. A water meniscus between the sample and the tip is formed when they are close enough. This force can be reduced when working inside a glove box with controlled oxygen and H_2O levels.

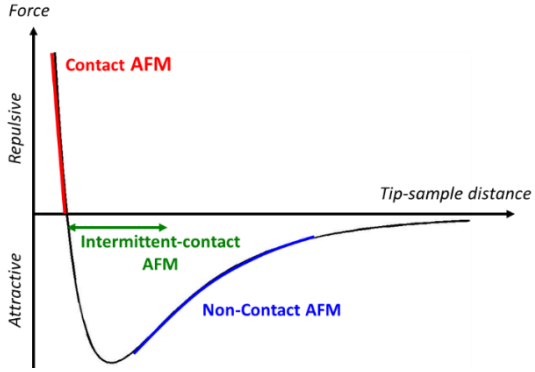

Figure II.3

Force – distance curve. Three regimes: attractive, repulsive and no forces. Three AFM operation modes are represented in the curve: the contact mode in the repulsive regime, the non-contact mode in the attractive regime and the intermittent-contact that includes the repulsive to the attractive mode.

Cette thèse est accessible à l'adresse : http://theses.insa-lyon.fr/publication/2019LYSEI121/these.pdf
© [M.A. Moreno Villavicencio], [2019], INSA Lyon, tous droits réservés

The repulsive regime is dominated by the Pauli exclusion principle. It depends on the tip apex and the penetration of this one in the sample. The detected forces can be controlled by the cantilever geometry and nature, but in general, they have values of about 100 nN.

There is a different AFM operation mode associated to each regime. They are identified with different colours in the curve of Figure II.3:

- Contact mode: the tip is in contact with the sample while scanning. The analysis is consequently carried out in the repulsive regime (red part of the curve).
- Non-contact mode: the tip never touches the sample; it scans the surface in the attractive regime (blue part of the curve).
- Intermittent-contact mode: the tip traverses the attractive and repulsive regimes while scanning the sample (green part of the curve).

2.1.1. AFM EXPERIMENTAL SETUP

Figure II.4 shows the schematic of the AFM general principle used by all operation modes.

A laser beam hits the end of the cantilever; its reflection reaches the center of a photodiode (0,0). The tip starts scanning the surface in the *x-y* plane, analyzing the number of points required by the user. Each point is called a pixel. The interaction force between the tip and the sample changes with the surface topography displacing the reflection of the laser at the photodiode. The photodiode determines the vertical displacement of the laser, called output signal, and sends it to the proportional-integral feedback system. This compares the detected value with a fixed set point. The set point corresponds to a property that allows to detect the modification of the interaction forces. It can be the amplitude or the frequency of the cantilever when this one is oscillating or the applied force when the tip is in contact with the surface.

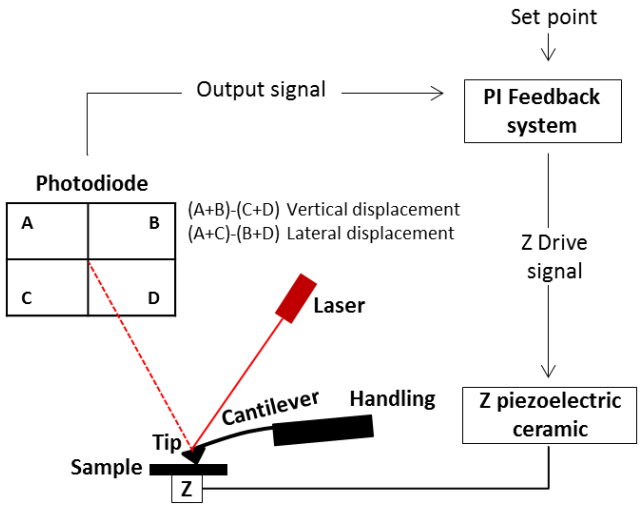

Figure II.4

Schematic of the AFM principle and components: the four-quadrant photodiode to measure the cantilever deflection with the laser beam deviation, the feedback system which gives the z drive signal to the piezoelectric in order to restore the value to the set point.

Cette thèse est accessible à l'adresse : http://theses.insa-lyon.fr/publication/2019LYSEI121/these.pdf
© [M.A. Moreno Villavicencio], [2019], INSA Lyon, tous droits réservés

The feedback system determines the vertical distance, z-drive signal, that needs to be applied to the sample in order to restore the set point value. This signal is sent to the ceramic piezo-electric that vertically moves the AFM probe or the sample stage to adjust the tip-sample distance that will restore the set point value. It is possible to install a motion sensor to measure the executed displacement and to compare it with the command signal. [109]

The z-drive signal and the executed displacement measured by the motion sensor as a function of the pixel position create respectively two images representative of the sample topography. In a well-calibrated AFM, the z sensor image should be the same as the height image, indicating that the executed displacement is the same as the commanded.

2.1.1.1. CANTILEVER

In the AFM setup, the tip is located at the extremity of a sub-millimeter cantilever, which is itself attached to a millimeter substrate for an easier handling. The size and the stiffness of the cantilever (k) influence its response to external forces. The cantilever is studied following the spring model, which is lead by Eq. II.7. F refers to the field force in newton that the cantilever is feeling and Δz corresponds to the cantilever deflection in volts caused by the mentioned field force.

$$F\,[N] = k\Delta_z \qquad \textit{Eq. II.7} \quad \textit{[110]}$$

The spring constant of the cantilever is defined by its geometry. The required stiffness is determined by the analysis conditions. For fluid conditions, spring constant in the range of 0.4 – 1.2 N/m are commonly used. A softer cantilever may cause sample adhesion provoking a non-accurate topography map, while a stiffer cantilever increases the risk of permanent sample damage due to high deformation. For air conditions, the cantilever spring constant can be up to 50 N/m when analyzing hard samples.

The cantilever as a clamped beam has a characteristic vibration mode, which is linked to its resonant frequency (f_0). This one corresponds to the frequency where the oscillation amplitude of the system is the highest. The cantilever amplitude when oscillating at this frequency is highly sensible to small external forces. The free resonant frequency is measured oscillating the cantilever without interaction of forces and its value depends on the cantilever mass and spring constant. The resonant frequency of the cantilever is required with the quality factor (Q) to determine the maximum scan rate for an AFM analysis. [111]

The quality factor refers to an energy loss and defines the number of oscillations executed before the cantilever stops vibrating. It is calculated dividing the resonant frequency by the full width at half maximum (FWHM) (Δf) of the oscillation peak.

Cette thèse est accessible à l'adresse : http://theses.insa-lyon.fr/publication/2019LYSEI121/these.pdf
© [M.A. Moreno Villavicencio], [2019], INSA Lyon, tous droits réservés

Its value, influenced by the environmental conditions of the analysis, is between 10^2 and 10^3 when working in air and up to 10^4 in vacuum conditions. [112]

2.2. AFM SCANNING MODES

The AFM was initially created to measure the sample topography. Three principal operation modes were developed: contact mode, intermittent contact and non-contact mode. Only the first two were used in this thesis project and are introduced below. The tips employed were commonly silicon or silicon nitride tips. Nowadays, the AFM is used to measure not only the topography but also local mechanical, electrical or magnetic properties. These applications require specific tips that are commercially available (conductive, high or low stiffness, magnetic).

2.2.1. CONTACT MODE

This is the first AFM mode designed to measure the sample topography. It works in the repulsive regime because the tip is in contact with the sample surface during the scanning (red part of the curve in Figure II.3). The repulsive force is measured by the cantilever deflection.

While the tip scans the surface, the initial cantilever deflection may be modified due to an approach or withdrawal from the sample because of the topography. An alteration of the cantilever deflection causes a vertical displacement of the laser in the photodiode. This shift is quantified by subtracting the voltages of the first upper half of the photodiode (A+B) from the voltages of the lower half (C+B). The obtained value is compared with the initial deflection, set as set point. The feedback commands the vertical movement needed to restore the deflection set point value. [109,113]

Very high-resolution images are rapidly obtained using AFM contact mode. However, the contact of the tip with the sample can damage the sample surface in the same way that the tip deteriorates itself. For this reason, cantilevers with a spring constant lower than 1 N/m are recommended. [114]

The principle of the contact mode is mainly employed when performing electrical conductivity measurement as for example, the scanning capacitance microscopy (SCM), the scanning spreading resistance microscopy (SSRM) and the piezoresponse force microscopy (PFM).

Cette thèse est accessible à l'adresse : http://theses.insa-lyon.fr/publication/2019LYSEI121/these.pdf
© [M.A. Moreno Villavicencio], [2019], INSA Lyon, tous droits réservés

2.2.2. INTERMITTENT CONTACT OR TAPPING MODE

This is an AFM dynamic mode. At every oscillation, the tip traverses the attractive regime, enters to the repulsive regime, touches the sample and returns to the attractive regime while withdrawing (Figure II.3). Hence, the name intermittent contact.

The cantilever oscillates in a simple harmonic motion at a frequency 5 to 10% lower than its free resonant frequency. The oscillation frequency (f_{set}) may vary from 10 kHz to 500 kHz with an amplitude (A_{set}) that can go up to 100 nm. The oscillation is mechanically induced by the application of a voltage to a piezoelectric located close to the probe.

A difference in the topography while the tip is scanning the surface causes a shift in the initial resonance curve (blue curve, Figure II.5). Following Eq. II.8, an alteration in the gradient of interaction forces causes a shift to the left when the tip is in the attractive regime (green curve) and in the same way, the curve is shifted to the right in the repulsive regime (red curve) [115]. These shifts in the resonance curve modify the oscillation amplitude of the cantilever at the f_{set}. For every pixel, the photodiode detects the oscillation signal; the lock-in amplifier amplifies the signal and extracts the amplitude and the phase of the detected oscillation [116]. The output amplitude is compared with the initial oscillation amplitude A_{set}, defined as set point, and the feedback determines the vertical displacement needed to restore this value.

The time needed by the system to detect a change in the oscillation amplitude is called the characteristic time (τ). This value defines the minimum time that should be spent analyzing one pixel. It depends on the quality factor of the probe and its natural frequency (Eq. II.9). It is of the order of some milliseconds when working in air and some seconds when working in vacuum. From this, a 1024 x 1024 pixels image under vacuum conditions may take up to 1 month while in air it can be done within 1 hour.

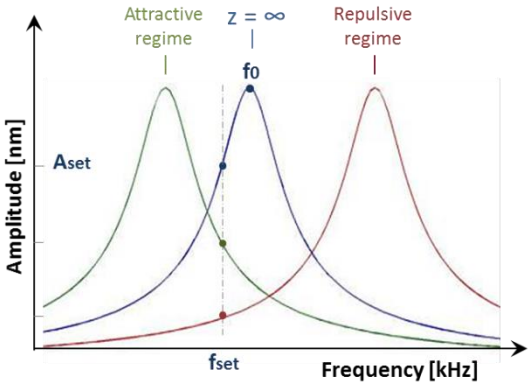

Figure II.5

Resonance curve for a single harmonic oscillator in a non-interaction regime (blue curve), in an attractive regime (green curve) and in a repulsive regime (red curve).

$$\Delta f \approx -\frac{f_0}{2k}\frac{\partial F}{\partial z} \qquad \textit{Eq. II.8} \quad [112]$$

Cette thèse est accessible à l'adresse : http://theses.insa-lyon.fr/publication/2019LYSEI121/these.pdf
© [M.A. Moreno Villavicencio], [2019], INSA Lyon, tous droits réservés

$$\tau\,[s] = \frac{2Q}{f_0} \qquad \textit{Eq. II.9} \quad \textit{[117]}$$

The vertical resolution of the tapping mode can go down to 0.1 nm. It depends on the piezoelectric displacement but even more on the thermal noise reduction [118].

The Tapping mode provides images of height, amplitude error and phase. The first one corresponds to the image of the sample topography. The amplitude error, also called feedback signal error, is the difference between the detected amplitude and the set point value. The third information is the phase image, which shows the phase difference with respect to the excitation signal.

A typical cantilever for tapping mode has a spring constant between 1 and 100 N/m and a tip radius smaller than 20 nm. The probes used in this project were:

- Silicon probe with aluminium reflex coating on the detector side of the cantilever (TAP300Al-G from Budget Sensors). The nominal spring constant is 40 N/m and the nominal resonant frequency is 300 kHz. The nominal tip radius is smaller than 10 nm.
- Silicon probe with aluminium reflective coating on the backside of the cantilever (OTESPA-R3 from Bruker). The nominal spring constant is 26 N/m and the nominal resonant frequency is 300 kHz. The tip has a nominal radius of 7 nm.

2.2.3. SCANNING CAPACITANCE MICROSCOPY

The scanning capacitance microscopy (SCM) relies on the measurement of local depletion capacitance to provide local free carrier concentration. The SCM uses the principle of C-V measurement on MOS capacitors to provide qualitative information on the doping region of semiconductor materials. The MOS system is created by the contact of a conductive AFM tip with a semiconductor that has a thin oxide layer on the surface. [119]

The C-V curve and the schematic behavior of an n-type semiconductor when the voltage is applied through the metal layer is in Figure II.6 (blue curve). The application of a high positive voltage creates an accumulation of negative charges below the oxide (Figure II.6.a). The capacitance of the system is the capacitance of the oxide layer. By the time the voltage is ramped toward less positive values, the accumulation is reduced, a depletion in the top of the semiconductor is produced, Figure II.6.b. The capacitance of the system decreases because it depends now on the capacitance of the oxide and the capacitance in depletion. Consecutively, an application of a high negative voltage at low frequency will create an inversion layer under the oxide, Figure II.6.c. In case where the high negative voltage is applied at high frequency, as for the SCM, the semiconductor stays in depletion.

Cette thèse est accessible à l'adresse : http://theses.insa-lyon.fr/publication/2019LYSEI121/these.pdf
© [M.A. Moreno Villavicencio], [2019], INSA Lyon, tous droits réservés

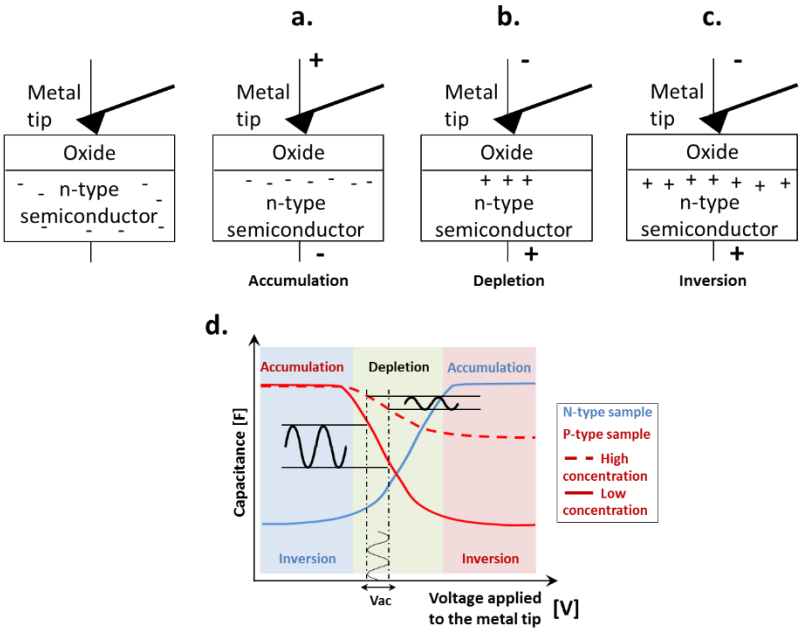

Figure II.6 *MOS capacitor system. Schematic behaviour when a voltage is applied to the metal layer for an n-type semiconductor: a. accumulation, b. depletion and c. inversion. d. C-V curves for n-type doped semiconductor in blue, p-type low-doped semiconductor in continuous red and highly doped p-type semiconductor in dashed red.*

The capacitance in depletion depends on the thickness of the depleted region, which is in turn related to the doping concentration of the semiconductor. This effect is seen in the C-V curve, Figure II.6.d, for a p-type semiconductor. The thickness of the depletion layer produced with low doping concentration is higher than the one produced with high doping concentration samples. This causes that the variation in the capacitance from accumulation to inversion in a low-doped sample is higher. [120]

The SCM measures the dC/dV in the depletion regime. Two voltages applied to the sample are used for this: a continuous voltage (DC) and an alternating voltage (AC) in the 20 to 150 kHz range. Those voltages cause the alternate attraction and repulsion of the carriers beneath the tip. It originates a depletion region dependant on the local carrier concentration and a variation of the system capacitance around the fixed DC bias. The detection of this capacitance variation relies on the connection of the probe, in contact with the sample, to a resonant circuit excited by an ultra-high frequency oscillator. The frequency and amplitude of this resonant circuit change with the variation of the capacitance between the tip and the sample. A lock-in amplifier extracts the new amplitude and phase at the same frequency of the applied AC voltage to determine the capacitance variation ΔC from the C-V curve. [121]

Cette thèse est accessible à l'adresse : http://theses.insa-lyon.fr/publication/2019LYSEI121/these.pdf
© [M.A. Moreno Villavicencio], [2019], INSA Lyon, tous droits réservés

The amplitude of the detected signal provides information about the carrier concentration in the sample. The difference in the output signal amplitude between a highly and a slightly doped semiconductor when the same alternating voltage (V_{ac}) is applied is seen in Figure II.6.d. A high carrier concentration produces small amplitude signal, while a low carrier concentration produces a high amplitude signal. In the other hand, since the C-V curve for an n-type sample is 180 degrees out-phase from the p-type C-V curve, the phase of the output signal indicates the sign of the charge carriers present in the sample. [122]

The SCM operation mode provides maps of the dC/dV amplitude, phase, as well as a map of the sample topography. This latter is measured at the same time as the capacitance variation following the contact mode principle detailed before. For this, the initial cantilever deflection is used as the set point.

Soft cantilevers with spring constant between 1 and 5 N/m are commonly used in SCM to avoid damage of the oxide layer. The applied forces are lower than 100 nN. The probe used in this project was a:

- Conductive platinum silicide probe with aluminium reflective coating on the backside of the cantilever (SCM-PTSI from Bruker). The nominal spring constant is 2.8 N/m and the nominal resonant frequency is 75 kHz. The nominal tip radius is 15 nm.

2.2.4. SCANNING SPREADING RESISTANCE MICROSCOPY

The scanning spreading resistance microscopy (SSRM) provides information about the carrier distribution and concentration in doped materials. It measures the local spreading resistance when the tip is in ohmic contact with the sample. With silicon, the ohmic contact is achieved by an elevated contact-force, between 1 and 10 µN. The goal is to penetrate the native oxide of the sample and to assure a stable electrical contact for the SSRM measurement. [123]

A DC voltage is applied between the sample and a conductive tip, typically between -1 V and 1 V. A logarithmic current amplifier measures the current that passes through the sample, commonly between 10 pA a 100 µA. The measured current is used to calculate resistance values, from 10^4 Ω to 100 GΩ corresponding to doping concentrations from 10^{14} to 10^{21} atoms/cm^3. Further information about this calculation is given in [111].

The SSRM operation mode provides a topographical map using the contact-mode principle with the initial cantilever deflection as feedback set point, as well as a map with the values corresponding to the logarithm of the local resistance. The spreading resistance (R) is related to the local resistivity (ρ) by the tip radius a.

Cette thèse est accessible à l'adresse : http://theses.insa-lyon.fr/publication/2019LYSEI121/these.pdf
© [M.A. Moreno Villavicencio], [2019], INSA Lyon, tous droits réservés

$$R = \frac{\rho}{4a} \qquad \textit{Eq. II.10} \quad \textit{[120]}$$

The main disadvantage of the SSRM mode is the damage created in the sample and tip by the elevated contact force. In case where the contact force needs to be reduced, the DC voltage should be increased to maintain a proper signal detection. [124] The cantilever recommended for SSRM measurements are stiff with a spring constant between 5 N/m and 50 N/m.

Diamond-coated silicon tips or metal-coated tips with a radius between 20 and 50 nm are commonly used. The tip resistivity should be lower than 10^{-3} Ω.cm to guarantee the detection of the doping concentration range previously mentioned [111].

The probe used in this project to perform the SSRM mode was:

- Conductive diamond probe doped with boron. The probe has a gold reflective coating on the backside of the cantilever (AD-40-AS from Bruker). The nominal spring constant is 40 N/m. The nominal tip radius is 10 nm.

2.2.5. PIEZORESPONSE FORCE MICROSCOPY

Piezoresponse force microscopy (PFM) uses the inverse piezoelectric effect to study ferroelectric domains. The piezoelectric effect describes the relationship between the deformation (or stress) and the variation of electric charges that some materials have. The appearance of a dielectric polarization under mechanical stress is known as direct piezoelectric effect. On the other hand, the deformation of the material when it is exposed to an electric field is known as inverse piezoelectric effect.

The deformation of the ferroelectric material, expansion or contraction in the vertical direction, depends on the orientation, parallel or antiparallel, of the electric field with the material polarization. Illustration of this behavior is shown in Figure II.7 a and b respectively. Other cases, such as horizontal displacement due to a polarization oriented perpendicular to the electric field or with specific angle exist and can be reviewed in the reference [125].

The PFM consists on the application of a modulated driving voltage between the tip and the sample when they are in contact. The voltage of the driving signal should be less than the coercive voltage of the material so as not to polarize it. The driving frequency can be set at the contact resonant frequency that commonly is 4.4 times higher than the free natural frequency in air. The application of the modulated voltage induces the contraction and the expansion of the sample at the frequency of the AC bias.

Cette thèse est accessible à l'adresse : http://theses.insa-lyon.fr/publication/2019LYSEI121/these.pdf
© [M.A. Moreno Villavicencio], [2019], INSA Lyon, tous droits réservés

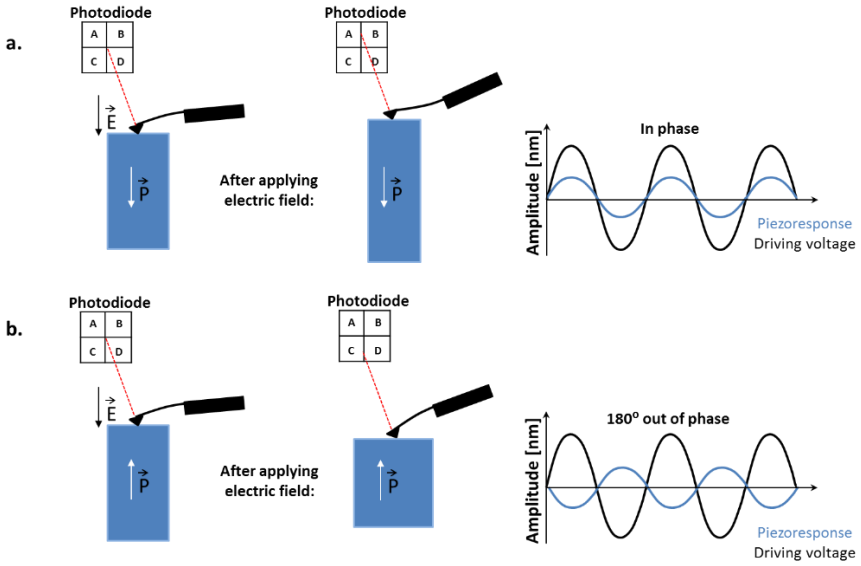

Figure II.7 *Schematic of piezoelectric behavior under electric field. a. Piezoelectric domains with polarization parallel to the electric field cause the expansion of the material and a piezoresponse with 0-degree phase deviation with the driving voltage. b. Piezoelectric domains with polarization antiparallel to the electric field cause contraction of the material and a 180 degrees phase deviation with the driving voltage.*

The photodiode detects the oscillation of the cantilever and the signal is sent to the lock-in amplifier that extracts the amplitude and phase of the signal.

The PFM provides maps of the local phase and amplitude as well as the topography measured using the contact mode principle. The amplitude of the signal may refer to the local expansion coefficient of the piezoelectric material while its phase may indicate the local orientation of the polarization. A polarization parallel to the electric field produces a signal with the same phase than the driving oscillation, Figure II.7.a. On the other hand, a polarization antiparallel to the electric field causes a signal 180^{o} out of phase with the driving signal, Figure II.7.b. [126]

The contact resonant frequency may change while scanning because it is dependent on the interaction with the material that is in contact with the tip. In order to maintain the driving signal at the contact resonant frequency, the dual frequency resonance tracking (DFRT) technique was used. It monitors the local resonant frequency and keeps the driving signal at that value. Additional information about the DFRT is given in reference [127].

The PFM is widely used to study the formation and the reversal of the polarization of ferroelectric materials in real time. This is possible through the manipulation of piezoelectric domains by the application of a DC bias higher than the coercive voltage.

Cette thèse est accessible à l'adresse : http://theses.insa-lyon.fr/publication/2019LYSEI121/these.pdf
© [M.A. Moreno Villavicencio], [2019], INSA Lyon, tous droits réservés

Domains of any shape can be “written” with a nanometric resolution using the AFM tip in contact with the sample. The tip scans the desired surface while the DC voltage is applied. The evolution of the domains can be then studied.

The cantilever stiffness for the PFM needs to counteract the external electrostatic forces that can affect the cantilever oscillation and at the same time assure a proper electrical contact. Spring constants higher than 1 N/m and contact forces in the range of 10 to 1000 nN are recommended. [128]

The probes used in this project to perform the PFM mode were:

- Conductive platinum silicide probe with aluminium reflective coating on the backside of the cantilever (SCM-PTSI from Bruker). The nominal spring constant is 2.8 N/m and the nominal resonant frequency is 75 kHz. The nominal tip radius is 15 nm.
- Conductive single crystal diamond probe with gold reflective coating on the backside of the cantilever (AD-2.8-AS from Bruker). The nominal spring constant is 2.8 N/m and the nominal resonant frequency is 65 kHz. The nominal tip radius is 10 nm.

Here concludes the description of the working principle of ToF-SIMS and AFM as characterization techniques. These two powerful and complementary techniques were combined following the protocol detailed below.

Cette thèse est accessible à l'adresse : http://theses.insa-lyon.fr/publication/2019LYSEI121/these.pdf
© [M.A. Moreno Villavicencio], [2019], INSA Lyon, tous droits réservés

Cette thèse est accessible à l'adresse : http://theses.insa-lyon.fr/publication/2019LYSEI121/these.pdf
© [M.A. Moreno Villavicencio], [2019], INSA Lyon, tous droits réservés

3. DESCRIPTION OF THE INSTRUMENTS

3.1. IN-SITU TOF-SIMS / AFM INSTRUMENT

The in-situ ToF-SIMS / AFM instrument, in Figure II.8.a, is the product of the 3D NanoChemiscope European project and it is currently commercialized by IONTOF GmbH. The one used for this thesis project is located at IMEC in Belgium. Two techniques are performed in the same chamber under high-vacuum conditions (10^{-9} mbar for the main analysis chamber and 10^{-6} mbar in the load-lock chamber). As they cannot be done simultaneously, a XYZRT-piezo transfer system, shown in Figure II.8.b, displaces the sample stage between the ion gun of the ToF-SIMS and the AFM probe head within a submicron resolution. The sample stage is adapted to be tilted and rotated if needed. [129]

The ToF-SIMS in the combined instrument is a ToF-SIMS 5 from IONTOF GmbH, Figure II.8.a right side of the chamber. It has three ion guns, LMIS for analysis, the cluster / FIB column with Ar cluster source and recently added O cluster source, and the sputter gun. The instrument can be used for 2D and 3D analysis. It enables the dual beam mode using either large clusters suitable for organic materials or monoatomic sources for the inorganic materials. Two important characteristics are that the instrument allows the heating and the cooling of the sample and that the sample holder can be rotated during the analysis.

The AFM is located in the left part of the chamber, Figure II.8.a. It is suited to provide the topographic information needed in a 3D ToF-SIMS analysis.

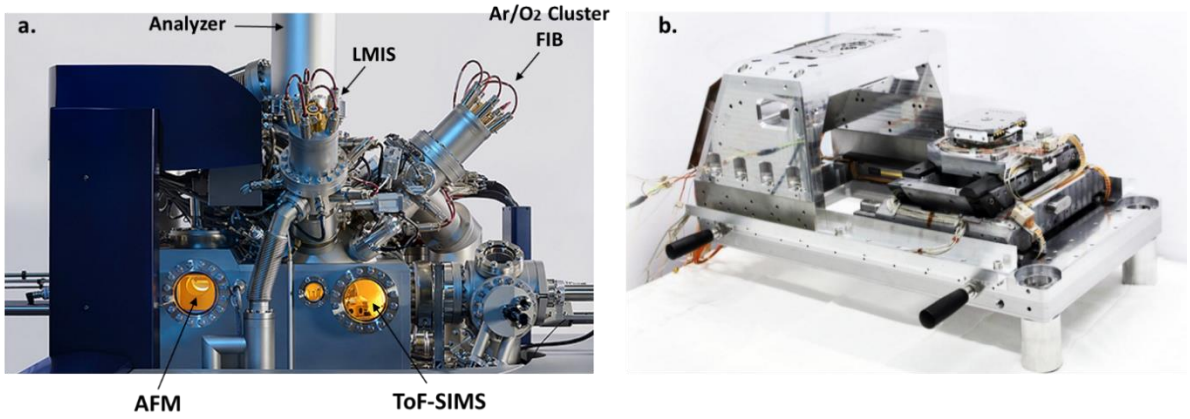

Figure II.8 *a. Combined ToF-SIMS / AFM in-situ instrument. AFM is located in the left of the chamber while ToF-SIMS is in the right. The ToF-SIMS counts with LMIS, cluster and FIB gun and the sputter gun located 180 in the opposite site of the LMIS. The sample transfer between the AFM and the ToF-SIMS chamber is done with the b. XYZRT-piezo transfer system.*

Cette thèse est accessible à l'adresse : http://theses.insa-lyon.fr/publication/2019LYSEI121/these.pdf
© [M.A. Moreno Villavicencio], [2019], INSA Lyon, tous droits réservés

However, non-topographic modes such as magnetic force microscopy (MFM), kelvin probe force microscopy (KPFM); conductive AFM can be also performed. Its maximum field of view is 80 x 80 x 10 μm^3 but a surface profiler mode allows the measurement of 800 µm in a one-dimensional scan. This latter mode stitches AFM scans adapting the AFM field of view to measure the depth of ToF-SIMS large craters.

3.2. EX-SITU TOF-SIMS / AFM INSTRUMENTATION

The ex-situ results that will be presented here were performed at the NanoCharacterization Platform of CEA Grenoble. They were obtained using a ToF-SIMS 5 from 2005 and a ToF-SIMS 5 2013 commercialized by IONTOF. In general, both ToF-SIMS have the same characteristics as the one in the in-situ instrument, however the ToF-SIMS 5 from 2005 does not have an argon cluster gun and the ToF-SIMS 5 from 2013, Figure II.9.a, has a glove box under nitrogen to load the samples.

Furthermore, the AFM analysis were performed on an AFM Dimension Icon from Bruker which is in a nitrogen-filled glove box (MBraun) with controlled H_2O and O_2 levels around 3 ppm, Figure II.9.b. The maximum analysis field of view is about 80 x 80 μm^2. An optical microscope is integrated within the AFM to facilitate area localization and visualize the cantilever. The sample is set on a plate where small air ducts can aspirate the sample in order to keep it immobile. The whole instrument is placed on a vibration isolation platform to reduce the noise produced by external activities. Specific SCM, SSRM and PFM modules are implemented to the AFM head for these operation modes. The AFM does not have the stitching scans mode as for the in-situ instrument. For this reason, the depths of ToF-SIMS craters were measured using optical or stylus surface profilometry.

The 3D Plu neox optical profilometer by Sensofar with a magnification between 20X and 50X was used to measure the crater depths, Figure II.9.c. This instrument can work in both the confocal mode and the interferometer mode, both with a sub-micron resolution. The first one is based on a visible light focused on an object's surface and a detector captures its reflection. On the other hand, the interferometer mode captures the shift between a reference beam reflected at a mirror and the beam that arrives to the object's surface. More information about the different modes in the reference [130].The main disadvantage of this technique is its sensitivity to the sample reflection, in other words, it is not reliable for transparent samples. For challenging sample, the utilization of a stylus profilometer is recommended. It has a similar principle as the AFM contact mode with a resolution down to a few angstroms.

Cette thèse est accessible à l'adresse : http://theses.insa-lyon.fr/publication/2019LYSEI121/these.pdf
© [M.A. Moreno Villavicencio], [2019], INSA Lyon, tous droits réservés

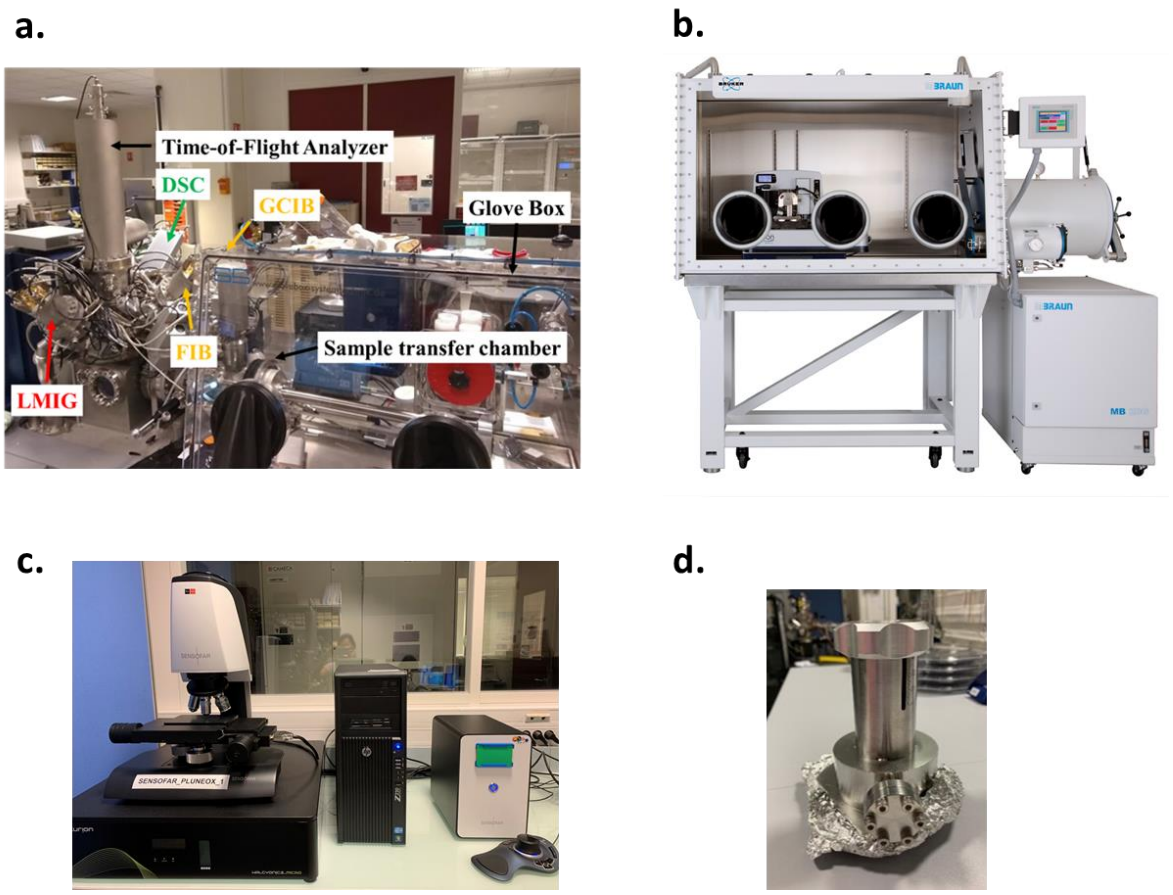

Figure II.9 *Instruments for the ex-situ approach. a. ToF-SIMS 5 from IONTOF with the analysis, sputter and cluster / FIB gun. The sample loading is done inside a glove box. b. AFM Dimension Icon from Bruker inside an MBraun glove box. c. 3D Plu neox optical profilometer by Sensofar. d. Sample transfer vessel.*

The sample transfer between the instruments is done using a nitrogen-filled transfer vessel, Figure II.9.d. This is expected to decrease the surface contamination. In order to localize the same analyzed region in both instrument, reference marks are made in the case where the region is not optically visible. The field of views of both analyses should be about the double of the pattern size to guarantee that the desired area is inside.

Cette thèse est accessible à l'adresse : http://theses.insa-lyon.fr/publication/2019LYSEI121/these.pdf
© [M.A. Moreno Villavicencio], [2019], INSA Lyon, tous droits réservés

Cette thèse est accessible à l'adresse : http://theses.insa-lyon.fr/publication/2019LYSEI121/these.pdf
© [M.A. Moreno Villavicencio], [2019], INSA Lyon, tous droits réservés

4. COMBINED TOF-SIMS AND AFM METHODOLOGY

The combined ToF-SIMS and AFM methodology presented here consists of four main stages: (i) sample preparation, (ii) cyclical ToF-SIMS / AFM / profilometer analysis, (iii) raw data processing and (iv) advanced data processing. Figure II.10 shows a schematic of these stages with their subdivisions.

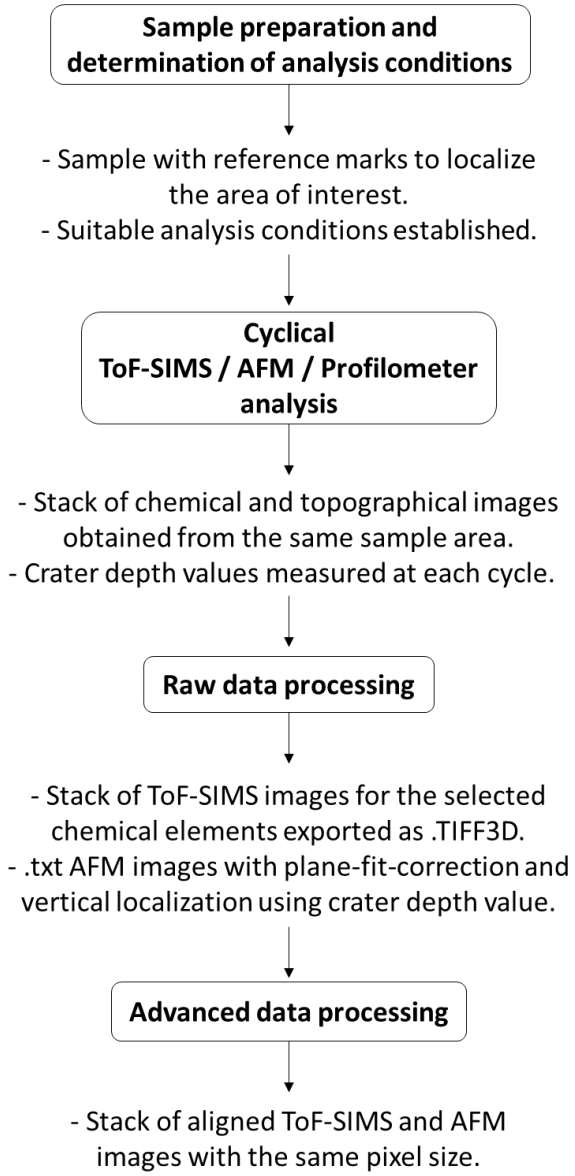

Figure II.10 Schematic of the ToF-SIMS and AFM combined methodology.

The goal of this methodology is to (i) create an overlay of the chemical information over topographical surfaces, (ii) map the local sputter rate of the analyzed area and (iii) produce a topography-corrected 3D ToF-SIMS data set. For this, ToF-SIMS and AFM images from the same sample region are needed.

Reference marks of the to-be-analyzed area are made in the sample preparation step. Here the suitable ToF-SIMS and AFM analysis conditions for the specific sample are determined.

For the experimental section, that can be done ex-situ or in-situ, a cyclical ToF-SIMS / AFM / Profilometer analysis was established. The sample topography and the crater depth are measured at the beginning, at the end and every time an interface is visualized in the ToF-SIMS depth-profile. The several interruptions of the ToF-SIMS analysis bring issues such as sample reposition, area localization and sample transfer between the instruments. These challenges are taken into consideration.

Cette thèse est accessible à l'adresse : http://theses.insa-lyon.fr/publication/2019LYSEI121/these.pdf
© [M.A. Moreno Villavicencio], [2019], INSA Lyon, tous droits réservés

Once the data is obtained, there is a raw data processing step where mass calibration and peak selection are done for the ToF-SIMS spectra and plane fit correction for the AFM images. The AFM images are vertically localized using the corresponding crater depth value. The data is exported as .TIFF3D for ToF-SIMS images and as .txt for AFM images.

Then the exported data requires then an advanced processing where the ToF-SIMS and AFM images are resized in order to obtain the same pixel size and consequently the entire data set is aligned in order to correct the reposition issues of the experimental section. This processing is done using ImageJ from NIH and MATLAB.

A detailed description of each stage is presented below.

4.1. SAMPLE PREPARATION AND PREVIOUS ANALYSIS

Some restrictions in the sample size may exist depending on the sample holder used in ToF-SIMS and AFM. In the same way, the size of the transfer vessel needs to be considered in case that the methodology is done ex-situ. Either way, a sample cleavage can be done when the sample does not meet the size requirements.

In the case where there is a specific area to be analyzed, it can be previously identified using an optical microscope. Any defect or pattern close to the area can be used as a reference point for the localization. In case of a homogenous surface, visible marks on the sample surface can be done using, for example, the sputter beam in a selected raster shape.

A ToF-SIMS high mass resolution depth-profile is recommended when the sample to be analyzed is unknown. It allows the identification of layer and characteristic secondary ions, the settings of analysis conditions, such as primary energy and nature, and high mass resolution ToF-SIMS spectra of the sample.

4.2. CYCLICAL TOF-SIMS / AFM / PROFILOMETER ANALYSIS

The analysis conditions depend on the sample to be analyzed. However, here are some points to take into account:

- A high lateral resolution ToF-SIMS analysis is suitable to obtain good quality ToF-SIMS images. Keep in mind that the lateral resolution of the ToF-SIMS is about 150 nm. Patterns smaller than this size are not seen in the ToF-SIMS images.
- The ToF-SIMS and AFM images have a high difference in lateral resolution. The ratio of ToF-SIMS and AFM pixel size should be an integer number to facilitate in the future the image resizing.
- The area to be analyzed at every step of the procedure should be the same or with the least possible variation.

Cette thèse est accessible à l'adresse : http://theses.insa-lyon.fr/publication/2019LYSEI121/these.pdf
© [M.A. Moreno Villavicencio], [2019], INSA Lyon, tous droits réservés

- The analysis area in the field of view should be bigger than the desired area. Due to the sample reposition, the field of view may slightly vary. By choosing a bigger field of view, it is possible to ensure that the desired area will always be in it.

The procedure for the cyclical ToF-SIMS / AFM / profilometer analysis is the following:

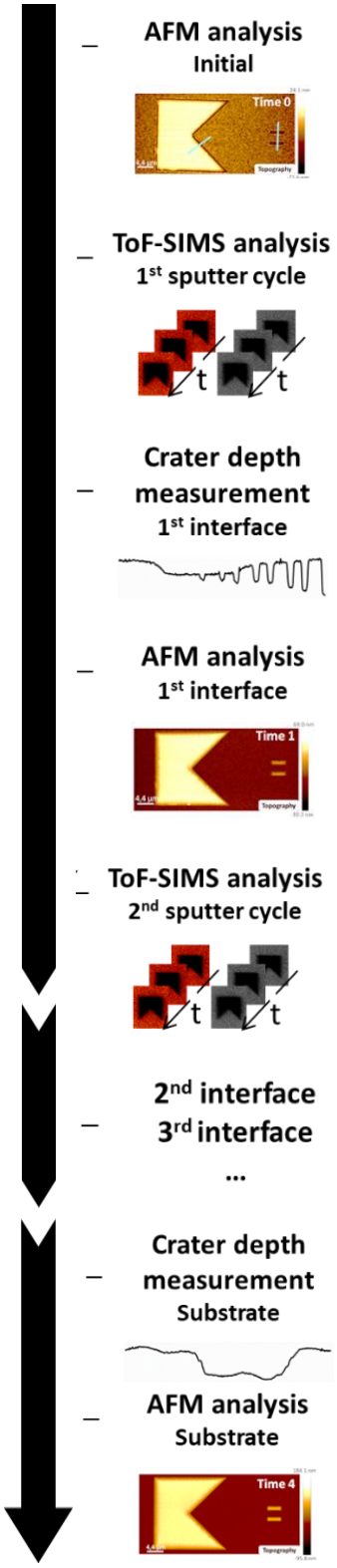

(1) An AFM image is taken to obtain the initial topography of the surface.

(2) The acquisition of successive 2D ToF-SIMS images during sputtering is started. The depth-profile is stopped when the first interface is detected. This defines the first sputter cycle. The interface can be set as the point when the curve intensity decreases to 50 % of its maximal value.

(3) The depth of the crater created by the ToF-SIMS sputtering is measured using AFM with a large scanner, optical or mechanical profilometer or an AFM with surface profiler mode in case of working in the in-situ instrument.

(4) An AFM topographical image of this first interface is captured.

(5) The ToF-SIMS depth analysis is continued and it is stopped when the second interface of the sample is detected in the depth-profile. This determines the second sputter cycle.

(6) Steps 3 and 4 are repeated every time an interface is detected in the ToF-SIMS depth-profile until the substrate is reached everywhere in the analyzed field of view.

(7) Measurement of the final depth of the sputtered crater.

(8) Final AFM topographical image of the substrate is performed.

Cette thèse est accessible à l'adresse : http://theses.insa-lyon.fr/publication/2019LYSEI121/these.pdf
© [M.A. Moreno Villavicencio], [2019], INSA Lyon, tous droits réservés

The main limitation of this cyclical ToF-SIMS / AFM methodology is that the number of AFM scans in-between depends on the existing layers of the sample. However, it is an optimized protocol for structures with 2 or 3 horizontal interfaces. It can be carried out in-situ or ex-situ with no modifications of the procedure.

The data obtained at the end of this experimental procedure are: sequences of 2D images per ToF-SIMS sputter cycle; initial, final and one AFM image and crater depth measurement per interface of the sample.

4.3. RAW DATA TREATMENT

4.3.1. ToF-SIMS RAW DATA

The schematic of ToF-SIMS raw data processing is shown in Figure II.11. Four main steps are required: mass calibration, peak selection, export data and stack creation.

The first action is the mass calibration and it should be done for the spectrum of each sputter cycle. Some well-defined ion peaks, that can be unambiguously identified, are used to set the spectrum peaks at the correct *m/z* values. From a ToF-SIMS analysis, over ten thousand peaks can be obtained. Some of them with useful information but others with nothing to explore. It is recommended to set a minimum intensity value and select the peaks whose intensities are higher than that or to manually select the specific ions that want to be visualized in the representation.

The 2D ToF-SIMS images corresponding to the sequences of the selected peaks can be exported in two different formats: TIFF and ASCII (x,y,I).

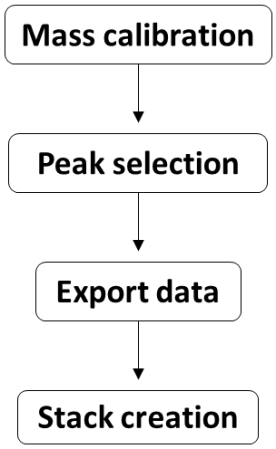

Figure II.11

Schematic of the ToF-SIMS raw data processing.

The individual .TIFF images are 2D matrices with a (x,y) size corresponding to the number of pixels used in the ToF-SIMS analysis and with the secondary ion intensity obtained for each pixel. TIFF images can be imported into the ImageJ software as a sequence of images in order to create the stack of images per chemical element. Those 3D stacks are then exported again as .TIFF format. In the ASCII format, all images are saved in the same .txt file as columns: image, x, y, intensity. The difference between the mentioned formats is the normalization of the intensity. In the TIFF images the intensity values are in the range between 0 and 255 while the ASCII images have the real measured counts per pixel.

Cette thèse est accessible à l'adresse : http://theses.insa-lyon.fr/publication/2019LYSEI121/these.pdf
© [M.A. Moreno Villavicencio], [2019], INSA Lyon, tous droits réservés

The normalization is automatically made by the software and individually per image. This is important to keep in mind when reconstructing the topography-corrected depth-profile because original intensity counts should be calculated when working with .TIFF format.

4.3.2. PROFILOMETER RAW DATA

Depending on the equipment used to measure the crater depth, a profile line or a surface map is obtained. The schematic of the raw data processing is in Figure II.12. It consists of three steps: plane fit correction, profile line extraction and depth measurement.

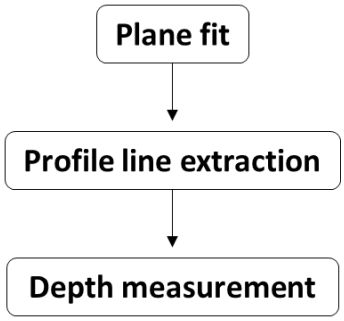

Figure II.12

Schematic of the profilometer raw data processing.

A plane fit is performed to correctly identify the bottom of the crater, keeping in mind that this one is not always flat and homogeneous.

A profile line is extracted from the surface map to measure then the crater depth.

The crater depth measurement should be done from the non-sputtered surface until the bottom of the crater, always measuring in the approximate same position at the bottom in case it has strong relief or patterns.

4.3.3. AFM RAW DATA

The AFM raw data processing includes three main steps: the plane fit correction, the localization of the topography in the corresponding depth of the sample and the export of data in the .txt format. A diagram is shown in Figure II.13.a.

The plane fit is a challenging step when the sample does not have a known flat surface to take as a reference. Commonly, the *polynomial plane fit* and the *flatten* functions are used. In the first one, the software calculates a polynomial for the selected image and then subtracts it from the image. The degree of the polynomial can vary from 0 to 6. The 1st, 2nd and 3rd degree will remove a tilt, a curve or an S-shape respectively. This is recommended when a flat surface can be chosen as a reference for the polynomial detection. On the other hand, for samples with several features over a perfectly flat base, the *flatten* command is recommended. It determines a polynomial fit per line and subtracts it from the line. The degree of the polynomial goes from 0 to 6 in the same way as for *plane fit*. This action modifies the data and may change the overall perception of the image.

Cette thèse est accessible à l'adresse : http://theses.insa-lyon.fr/publication/2019LYSEI121/these.pdf
© [M.A. Moreno Villavicencio], [2019], INSA Lyon, tous droits réservés

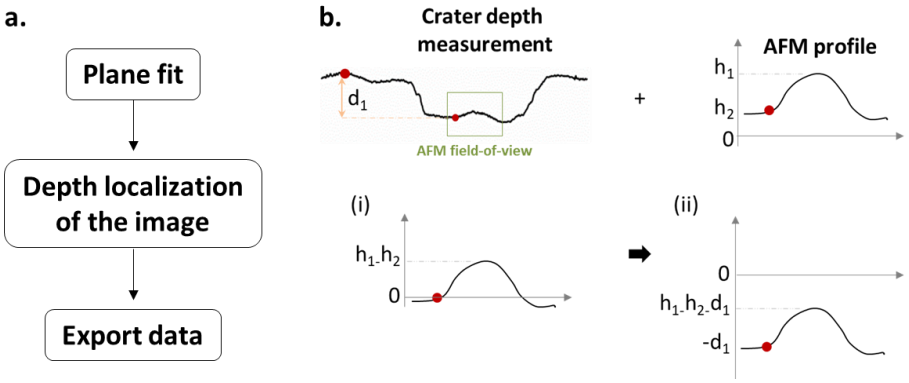

Figure II.13 Schematic of the AFM raw data processing (a) and the displacement in depth of AFM profiles (b).

Once the best fit for the image is found, the topographical surfaces should be located at the depth from where they were obtained. This process consists of (i) setting the approximate area from where the crater depth was measured to z=0. This area is represented as a red point in the schematic shown in Figure II.13.b and (ii) the measured crater depth, d_1, is subtracted from the corresponding AFM image using for example, the *Image Math* command.

The AFM images are exported in ASCII format providing a file with the height obtained per data point in length units. The data can be presented in columns or in a 2D matrix whose size is the number of pixels in (x,y).

4.4. ADVANCED DATA PROCESSING

For this stage, MATLAB and ImageJ software are used. The procedure for the processing of the 2D data is comparable to the protocol exposed by Jung *et al.* [62]. Two algorithms were developed for a semi-automatic process of advanced data processing. The first one converts the chemical and the topographical images to the same pixel size while the second corresponds to the alignment of those treated images.

In order to process the data, the files should be imported as matrices to the selected programming software, MATLAB in our case. Functions to import .txt and .TIFF files already exist. Matrices have pixel dimensions when they are in 2D and voxel dimensions when they are in 3D. The ToF-SIMS images saved as 3D stacks in .TIFF are read as sequences of 2D matrices per chemical element, forming what is known as 3D matrices. The first two dimensions correspond to the pixels' dimensions as for the individual 2D images and the third dimension corresponds to the number of ToF-SIMS images in the stack. On the other hand, the ToF-SIMS data saved as .txt file is read as a table. For every image, a 2D matrix should be formed assigning the (x,y) dimensions in pixel. The 2D matrix is stored in the third dimension of a general 3D matrix that represents the stack per chemical image.

Cette thèse est accessible à l'adresse : http://theses.insa-lyon.fr/publication/2019LYSEI121/these.pdf
© [M.A. Moreno Villavicencio], [2019], INSA Lyon, tous droits réservés

The AFM images are imported the same way as for the ToF-SIMS images converting the columns into 2D matrices with the number of pixels in (x,y).

4.4.1. PIXEL SIZE CORRECTION OF 2D TOF-SIMS AND AFM IMAGES

In a proper data correlation, the analyzed area enclosed in one specific pixel of an AFM image should be the same as in one ToF-SIMS pixel. The pixel size is calculated dividing the length of the analyzed area by the number of pixels set during the analysis. Due to the difference in lateral resolution of the AFM and the ToF-SIMS (down to a factor of 15), the pixel size between them may be different up to a factor of 10. Therefore, they need to be matched.

There are two options: (i) transform the ToF-SIMS resolution to the one of AFM, (ii) conserve the ToF-SIMS resolution and modify the AFM images. As the topographical information provided in the AFM images includes measurement of the surface roughness, transforming them to the resolution of ToF-SIMS means loosing that information. This option is not recommended when the user considers that loosing this information can be critical, as for the overlay of the ToF-SIMS images over the topographical surfaces. On the other hand, after the 3D ToF-SIMS data set correction the user may need the original values of the ToF-SIMS study for further analysis, in this case modifying this data is not recommended. It is important to remark that this is a user choice.

The pixel size correction consists of the three steps shown in the schematic of Figure II.14. The data resizing requires the calculation of the pixel size factor that will be used. It is determined by dividing the AFM pixel size by the ToF-SIMS pixel size when converting the AFM images to the ToF-SIMS resolution or by dividing the ToF-SIMS pixel size by the AFM pixel size in the opposite case.

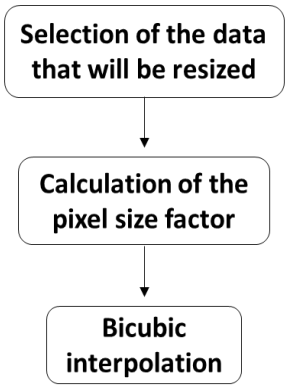

Figure II.14 Schematic of the pixel size correction.

The pixel size correction is done using *imresize* MATLAB function, which increases or decreases the pixel size. It lets the user choose the mathematic method to do it. In our case, the *bicubic* method is used. It consists of a weighted average of pixels in the nearest 4-by-4 neighborhood.

The reduction in the pixel size means an increment of the number of pixels in the image. Moreover, the increase in the pixel size is related to a reduction of the number of pixels in the image. To modify the number of pixels, the *bicubic* method uses either interpolation in the first case or binning in the second case.

Cette thèse est accessible à l'adresse : http://theses.insa-lyon.fr/publication/2019LYSEI121/these.pdf
© [M.A. Moreno Villavicencio], [2019], INSA Lyon, tous droits réservés

This *bicubic* interpolation is used in commercial image editing programs because it preserves well the fine details of images. It may create some distortion at the interfaces with strong transitions and at the edges due to the lack of neighbors. Furthermore, binning the image may create aliasing effects due to the pixel reduction.

4.4.2. ALIGNMENT OF ToF-SIMS AND AFM IMAGES

The data alignment consists of three steps: (i) alignment of AFM data set, (ii) alignment of ToF-SIMS data set and (iii) alignment of AFM and ToF-SIMS data set with each other. The schematic is seen in Figure II.15.

(i) Alignment of ToF-SIMS images: when in-depth ToF-SIMS analysis is being performed, there are slight shifts in the 2D images resulting in misaligned stacks of ToF-SIMS images. The proper translation and rotation found per chemical image of a single stack can automatically be applied to the images of the other stacks.

(ii) Alignment of AFM images: the field of view when performing the AFM images are not the same at every time of the methodology. The proper translation and rotation is found per image in order to align all the topographical set.

(iii) Alignment of ToF-SIMS and AFM images: since the goal is to correlate both data sets, the alignment of AFM and ToF-SIMS stacks with each other is needed. This is done by using one AFM image and one single stack of ToF-SIMS images. The calculated translation and possible rotation for the selected data set are automatically applied to the rest of the AFM images or ToF-SIMS stacks.

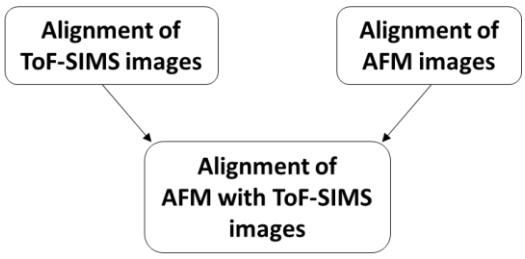

Figure II.15
Schematic of the alignment process.

An alignment code using MATLAB functions was written. It is based on the 2D normalized cross-correlation algorithm from the image processing toolbox, *normxcorr2* function. It determines the most suitable translation (shift in x, and y direction) and rotation angle to fit each image with a previous selected image of reference.

Here is the description of the settings needed by the code:

(1) Selection of the reference image.

- ToF-SIMS images: it is recommended to take as a reference the sum of the ToF-SIMS images corresponding to the chemical element with the highest intensity.
- AFM images: the AFM image with the highest contrast and least rotation should be chosen.

Cette thèse est accessible à l'adresse : http://theses.insa-lyon.fr/publication/2019LYSEI121/these.pdf
© [M.A. Moreno Villavicencio], [2019], INSA Lyon, tous droits réservés

- ToF-SIMS and AFM images: it is recommended to take one AFM image because they normally have a higher contrast.

(2) Establishing a range for the rotation angles: this is a user choice and depends on how misaligned the images are. The angles are given in degrees, counter clockwise when they are positive and clockwise when they are negative.

(3) Selection of the image or images that will be aligned with the reference.

- ToF-SIMS images: every image of the selected single stack is compared and aligned with the image of reference. The determined translation and rotation per image in the stack are applied to the images of the other stacks too. This is valid because the images of all elements at a specific depth are obtained from the same ToF-SIMS field of view.
- AFM images: every AFM image is individually aligned with the one chosen as a reference.
- ToF-SIMS and AFM images: the sum of the ToF-SIMS images existing in the selected ToF-SIMS stack will be compared with the AFM image set as a reference. The calculated translation and rotation are applied to all the ToF-SIMS images of that specific stack and then to the ToF-SIMS images of the other stacks.

The comparison and alignment of the images with the image of reference consist of four sections:

(1) The image to align is rotated, using *imrotate* MATLAB function, at one of the angles given in the rotation range. For that specific angle, the *normxcorr2* translates the image to every possible x and y pixel in order to superpose it with the image of reference. For every x, y pixel the function determines a number of compatibility with the reference image (higher the number is, better is the correlation of images). Once all the (x,y) positions are tested by the function, the highest compatibility number for that specific angle is saved together with the corresponding (x,y) translation in a table similar to the one in Figure II.16.

Rotation range = [a : z]

Angle	Highest compatibility (normxcorr2)	Corresponding *x* translation	Corresponding *y* translation
a			
.			
.			
z			

Figure II.16

Table of compatibility created using normalized-cross-correlation.

This action is repeated for every angle set in the rotation range saving every time the highest compatibility number and the corresponding (x, y) translation that needs to be applied.

Cette thèse est accessible à l'adresse : http://theses.insa-lyon.fr/publication/2019LYSEI121/these.pdf
© [M.A. Moreno Villavicencio], [2019], INSA Lyon, tous droits réservés

(2) From the column where the highest compatibility numbers per angle are, the program selects the highest one with the corresponding angle and (x,y) translation. The program tags those values as the ones that need to be applied to the image in order to obtain the maximal correlation with the reference image.

(3) This process is done for all the images in order to rotate them and translate them following their proper values calculated by the program. This alignment process can be done several times until the obtained proper translation and rotation for every image are zero, assuring that for every image there is a 100% correlation with the reference image. At this stage, blank pixels may appear in the images after rotation and translation in order to conserve the initial number of pixels.

(4) All the images, AFM and ToF-SIMS, are cropped to delete the created blank pixels.

This is not a straightforward process because the contrast of the ToF-SIMS images may not be enough to compare the images. In case where this problem is present, other treatments can be done to the images as erosion, dilation or both. The idea is to automatically fill the blank spaces in the ToF-SIMS images to enhance the contrast. There is also the possibility of using a “find edge” function to identify patterns in the images that can help with the correlation. Those are solutions to a semi-automatic alignment process. But in cases where the results are not as expected, manual alignment can be done [62]. For this, the user selects points in the reference image and identify the same points in the image to be aligned. The program can automatically find the best translation and rotation to superpose those points. However, these marks should be done in every image and it can be time consuming when applied to stacks of many ToF-SIMS images.

Cette thèse est accessible à l'adresse : http://theses.insa-lyon.fr/publication/2019LYSEI121/these.pdf
© [M.A. Moreno Villavicencio], [2019], INSA Lyon, tous droits réservés

5. CONCLUSIONS

This chapter presented the ToF-SIMS and the AFM as two complementary characterization techniques. On one hand, topographical maps with lateral resolution down to 10 nm from where no chemical information can be associated. On the other hand, 3D chemical maps that were obtained with no consideration of the sample topography.

The versatility of the AFM as a characterization technique was described. Through SSRM, SCM and PFM advanced operation modes, maps of local properties of the sample, specifically electrical and piezoelectric properties are obtained.

The correlation of these topographical and local properties maps, provided by the AFM, with the chemical maps, provided by the ToF-SIMS, is a solution to overcome the existing challenges of the characterization of complex 3D heterogeneous devices.

A combined ToF-SIMS and AFM methodology was established and described. It comprises four stages: (i) sample preparation, (ii) cyclical ToF-SIMS / AFM / profilometer analysis, (iii) raw data processing and (iv) advanced data treatment. The ToF-SIMS and AFM data set are obtained from the cyclical analysis. It consists on performing an AFM image at the beginning, at the end and every time an interface is detected in the ToF-SIMS depth-profile. It implies several interruptions of the ToF-SIMS analysis, where the sample is transferred to the AFM and the profilometer in order to measure the sample topography and the crater depth.

This methodology was carried out in-situ using the 3D Nanochemiscope instrument and ex-situ using classical ToF-SIMS V from ION-TOF and AFM Dimension Icon from Bruker.

The following chapters are focused on presenting some of the applications and results that can be obtained using this combined ToF-SIMS / AFM methodology.

Cette thèse est accessible à l'adresse : http://theses.insa-lyon.fr/publication/2019LYSEI121/these.pdf
© [M.A. Moreno Villavicencio], [2019], INSA Lyon, tous droits réservés

Cette thèse est accessible à l'adresse : http://theses.insa-lyon.fr/publication/2019LYSEI121/these.pdf
© [M.A. Moreno Villavicencio], [2019], INSA Lyon, tous droits réservés

CHAPTER III.
COMBINED TOF-SIMS AND AFM PROTOCOL FOR A TOPOGRAPHY-CORRECTED 3D CHEMICAL VISUALIZATION AND DEPTH-PROFILES

This chapter introduces the current challenges in the interpretation of the ToF-SIMS 3D data sets, specifically for the 3D visualization and the depth-profile. Examples and details of common artefacts will be addressed. The chapter builds on approaches that have been proposed in the literature to overcome this situation and introduces the utilization of a combined ToF-SIMS / AFM protocol as a solution. Finally, the combined protocol applied both ex-situ and in-situ on a 3D heterogeneous sample is presented.

Cette thèse est accessible à l'adresse : http://theses.insa-lyon.fr/publication/2019LYSEI121/these.pdf
© [M.A. Moreno Villavicencio], [2019], INSA Lyon, tous droits réservés

Cette thèse est accessible à l'adresse : http://theses.insa-lyon.fr/publication/2019LYSEI121/these.pdf
© [M.A. Moreno Villavicencio], [2019], INSA Lyon, tous droits réservés

1. 2D ToF-SIMS IMAGES AND THE 3D VISUALIZATION

The ToF-SIMS generates successions of two-dimensional images during the sputtering. A 2D chemical image per m/z detected is obtained at each depth. However, the ToF-SIMS is a chemical characterization technique with no topographical information.

1.1. CHALLENGES AND ARTEFACTS

When a 2D ToF-SIMS image is acquired, no reliable information of the surface topography is recorded although the surface topography influences the image formation. It creates a 2D chemical image supposing a flat surface (Figure III.1.e). For this reason, the interpretation of the 2D images is not straightforward for samples with superficial topography.

The different artefacts created by the topography are shown in Figure III.1 [74,83,131] using as an example, a sphere of material A upon a substrate of material B. The primary ions come from the right with an inclination of 45 degrees. It starts analyzing the pixel 1 detecting the secondary ions from the surface. In the pixel 2, the substrate is sputtered but the right side of the sphere retains the secondary ions and they cannot reach the detector (green area in Figure III.1.c). The analysis continues with the pixels 3 and 4. Since the angle between the beam and the surface is no longer 45°, the sputter yield changes. This is seen in the ToF-SIMS images as a contrast variation (point a and b). In pixel 4, the primary beam should also hit the substrate. The sphere behaves as a barrier and the area below the sphere is never detected (red area in Figure III.1.c). For this reason, the secondary ions, located in the pixel 4 of the chemical image, will come from the sphere, rather than the substrate, thus distorting the shape of the sphere in the chemical image (Figure III.1.a). More information about geometrical shadowing, distortion and sputter yield enhancement can be found in [132].

Another aberration increased by the topography is the heterogeneous redeposition of the secondary ions from the substrate over the sphere. The ions will then be detected from the pixels corresponding to the sphere and not from the substrate. Added to this, depending on the nature of the sphere and the substrate, the lines of electric field for secondary ion extraction change [83]. The trajectories of the secondary ions coming from the sides of the sphere may be sufficiently modified that the analyser no longer transmits them. The lack of secondary ion detection from the sphere edges creates a contrast of intensity in the chemical image (Figure III.1.d). Moreover, the overlay of the ToF-SIMS images corresponding to the ion A (detected from the sphere) and the ion B (detected from the substrate) gives the idea of a flat surface. Consequently, neither the ToF-SIMS images nor the depth-profiles of samples with initial topography correspond to real surface.

Cette thèse est accessible à l'adresse : http://theses.insa-lyon.fr/publication/2019LYSEI121/these.pdf
© [M.A. Moreno Villavicencio], [2019], INSA Lyon, tous droits réservés

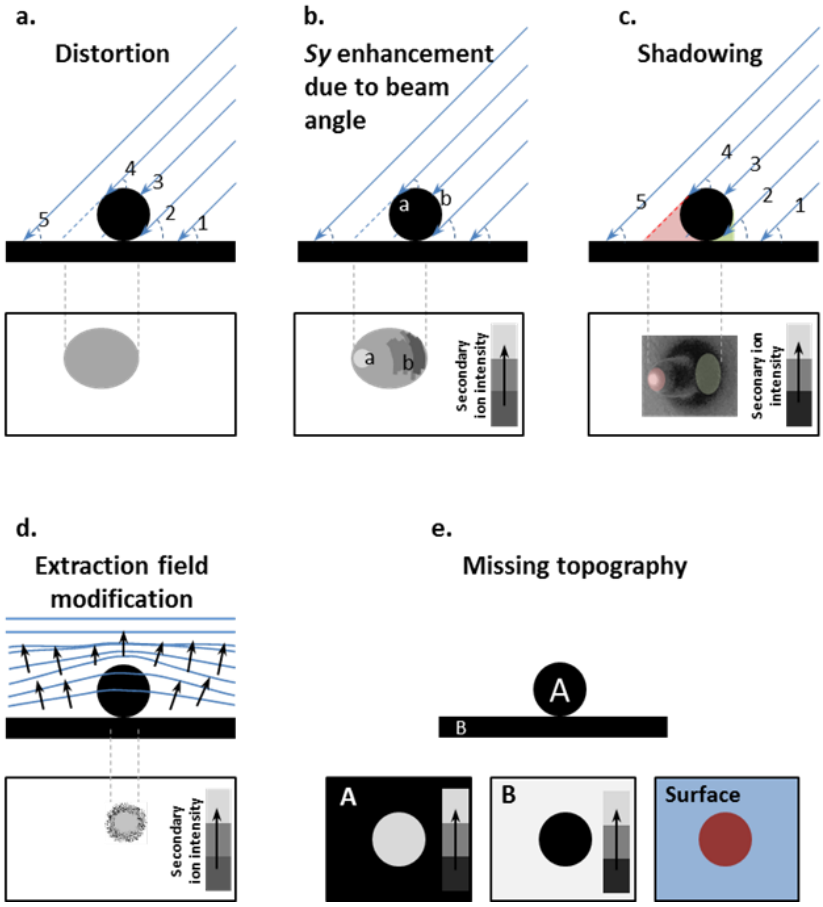

Figure III.1

Aberrations of ToF-SIMS images created by the sample topography. a. Image distortion due to beam inclination. b. Enhancement of the sputtering yield (Sy) depending on the angle of the primary beam hitting the surface. c. Shadowing effect due to the barrier created by the same sample topography that prevent the secondary ions from entering the analyzer. d. Shadowing created by the deformation of the extraction field and e. Missing topography in the 2D images.

Similarly, there is the case where topography changes during the sputtering due to the difference in sputter rate of the materials present in the sample. The ToF-SIMS images during the in-depth profile always assume a flat surface. They will now have the aberrations due to the initial topography plus the topography that is being developed [133,134].

Figure III.2 shows the distortion of the 3D visualization and depth-profiles created by stacking 2D images that do not include the topographical information. It explains the process for two samples composed of three different materials A, B and C.

The first sample has an initial topography. The three materials are sputtered at the same rate. At the surface t_0, the ToF-SIMS identifies the materials A and B. The sputtering starts and at t_1 the layers of materials A and B are still detected. The sputtering is continued and at t_2 the B layer is completely sputtered. At this moment, material A and C are detected. Sputtering is continued until the A layer is completely sputtered at t_3. Only substrate C is detected from the entire analysis area.

A similar situation can be encountered when depth-profiling a sample with flat surface but this time the sputter rate of material B is higher than material A. Both materials are detected from the surface at t_0.

Cette thèse est accessible à l'adresse : http://theses.insa-lyon.fr/publication/2019LYSEI121/these.pdf
© [M.A. Moreno Villavicencio], [2019], INSA Lyon, tous droits réservés

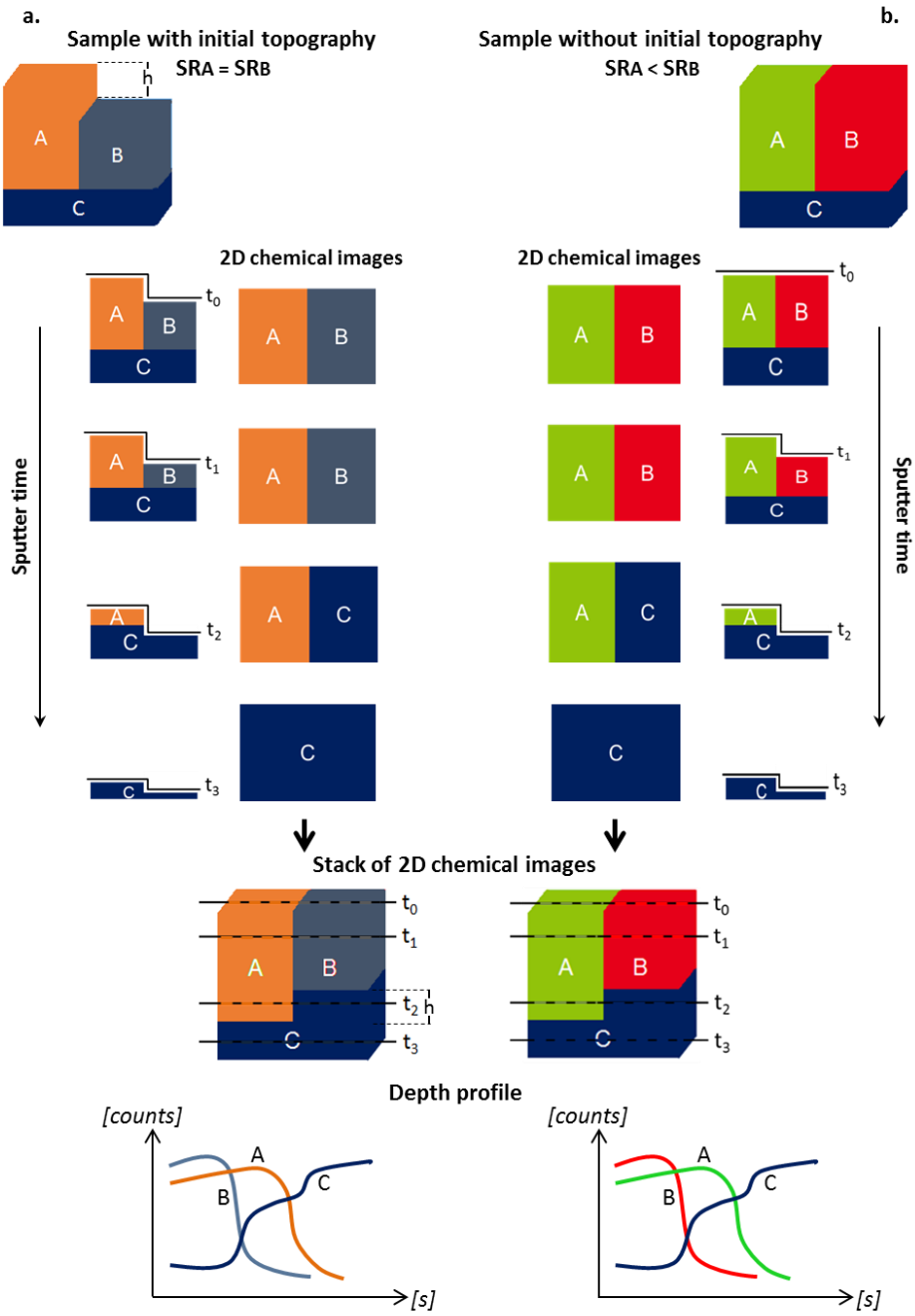

Figure III.2 Distortion of 3D visualization when stacking 2D ToF-SIMS images of samples with initial topography or with the topography developed throughout the sputter time (t_0, t_1, t_2, t_3…) due to difference of sputter rate of materials.

Sputtering starts and the B layer is sputtered faster; it is completely removed at t_2 where the substrate C and material A are detected in the field-of-view. The A layer is completely sputtered at t_3 and the ions from the substrate C are detected from all the fields of view.

Cette thèse est accessible à l'adresse : http://theses.insa-lyon.fr/publication/2019LYSEI121/these.pdf
© [M.A. Moreno Villavicencio], [2019], INSA Lyon, tous droits réservés

For both samples, the 3D visualization when stacking the 2D images does not represent the real samples shown in the top Figure III.2. No initial topography is seen in the sample on the left and a deformation of the flat interface with the substrate is seen in both visualizations. Indeed, the topography not only distorts the ToF-SIMS images but also the sample depth profile. In both cases, the A and B intensities are detected from the beginning and the difference in sputter rate can create the illusion of a thinner B layer.

In order to obtain an accurate 3D chemical reconstruction and depth profile of the sample, the dimensions of the sputtered volume must be known. The lateral dimensions are given by the field-of-view and the height depends on the transformation of the sputter time into sputtered depth using the sputtering rate. In a heterogeneous sample as those in the example, a sputter rate should be separately calculated for materials A, B and C. Consequently, establishing a depth scale that is correct over the entire volume is challenging.

1.2. SOLUTIONS AND APPROACHES

Over the years, ideas have emerged in order to correct the 3D ToF-SIMS visualization. The most practical method is to utilize a flat surface, interface or substrate of the sample as a reference establishing it as a z=0 to shift the ToF-SIMS images (Figure III.3.a) [135–137]. Furthermore, this reference can also be a profile of the initial topography of the sample measured in advance by other characterization technique (Figure III.3.b) [138,139]. This procedures are automatically done by the IONTOF data treatment software SurfaceLab and have been largely used especially for organic cells [135,140]. Nevertheless, the visualizations obtained through these procedures do not always include the real depth of the sample. The conversion of sputter time into sputter depth requires the calculation of the sputter rate, which may be different for every existing material in the sample.

A new approach came out to create a 3D ToF-SIMS reconstruction with the real depths. This procedure includes the measurement of the topography before and after the ToF-SIMS analysis together with the depth of the crater created during the sputtering. From these, the volume of the sputtered sample can be delimited (Figure III.3.c). The pixels of the ToF-SIMS images will be introduced within the volume per column doing an interpolation along the depth in order to fill up all the volume [134,141]. Nevertheless, interpolating the chemical intensities along the depth assumes a homogenous sputter rate, which is not the case for 3D heterogeneous or multi-stack structures. The depth of the layers will not be accurate even when the depth of the entire volume is correct.

The aforementioned reconstruction methods do not take into account the lateral and vertical variations in sputter rates producing an incorrect 3D ToF-SIMS visualization.

Cette thèse est accessible à l'adresse : http://theses.insa-lyon.fr/publication/2019LYSEI121/these.pdf
© [M.A. Moreno Villavicencio], [2019], INSA Lyon, tous droits réservés

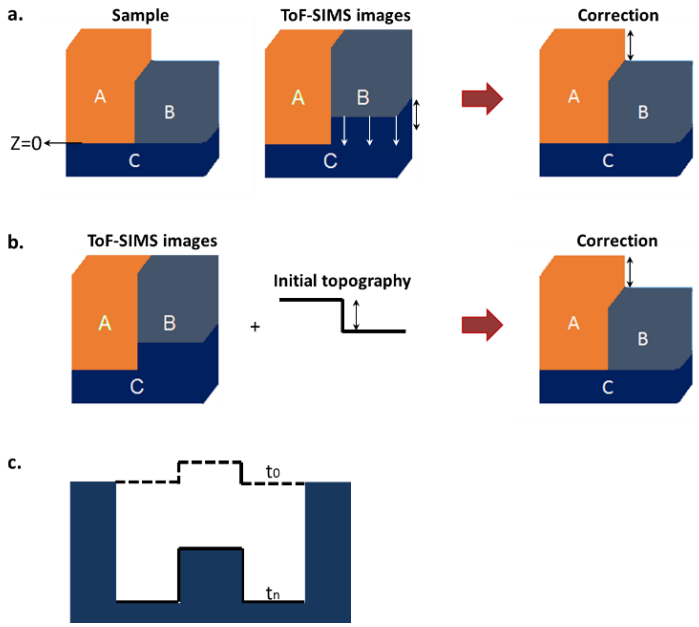

Figure III.3

Approaches to correct the 3D ToF-SIMS data visualization. a. Establishing a flat substrate a z=0 to shift the ToF-SIMS images. b. Utilizing a previously measured surface topography profile to shift the ToF-SIMS images. c. Creating the sputtered volume with an initial and final surface topography profile and the sputtered depth of the sample to introduce the chemical ions.

However, one reconstruction methodology integrates AFM measurement with sputtering simulation in order to predict the behavior of the sample throughout the ToF-SIMS analysis and determine the sputter rate of every existing material. This protocol can be found in [142].

We have adapted those methodologies to create a new protocol that allows the topography-corrected 3D ToF-SIMS visualization for multilayer samples by calculating a pixel-per-pixel sputter rate for every existing layer.

Cette thèse est accessible à l'adresse : http://theses.insa-lyon.fr/publication/2019LYSEI121/these.pdf
© [M.A. Moreno Villavicencio], [2019], INSA Lyon, tous droits réservés

Cette thèse est accessible à l'adresse : http://theses.insa-lyon.fr/publication/2019LYSEI121/these.pdf
© [M.A. Moreno Villavicencio], [2019], INSA Lyon, tous droits réservés

2. PROPOSED TOF-SIMS AND AFM COMBINED METHODOLOGY TO CORRECT THE 3D TOF-SIMS VISUALIZATIONS AND DEPTH-PROFILES

The proposed methodology comprises:

- The experimental section previously detailed in CHAPTER II.4.2. In this phase, the ToF-SIMS, AFM and profilometer analysis are performed. This procedure can take several hours and it mainly depends on the number of times that the ToF-SIMS analysis is stopped.
- The data processing detailed in CHAPTER II.4.3 and 4.4. This includes the treatment of the raw data, the export, the pixel size correction and the alignment of the data. The writing of the code took about 3 months. The code running can be performed now in a few hours.
- The results section. The full description of this stage is presented below. It includes the procedure to obtain an overlay of the ToF-SIMS chemical information on the AFM topographical surfaces, maps with the local sputter rate of the analyzed area and the visualization of the topography-corrected ToF-SIMS 3D data set.

A concise version of this methodology can be found in the Journal of Vacuum Science & Technology B 36, 03F122 (2018) [143].

An illustration of the procedure detailed afterwards will be given for the data given in Figure III.4. It consists of two ToF-SIMS sputter cycles with two ToF-SIMS images within each. The ToF-SIMS images correspond to three elements I, II and III visualized in blue, red and green respectively. The non-corrected 3D visualization for each element and for the sample is shown. The data set includes also three AFM images. They were taken at the beginning, at the end and at the interface between the two sputter cycles. It can be assumed that the raw data processing steps have been already applied to the data set.

Cette thèse est accessible à l'adresse : http://theses.insa-lyon.fr/publication/2019LYSEI121/these.pdf
© [M.A. Moreno Villavicencio], [2019], INSA Lyon, tous droits réservés

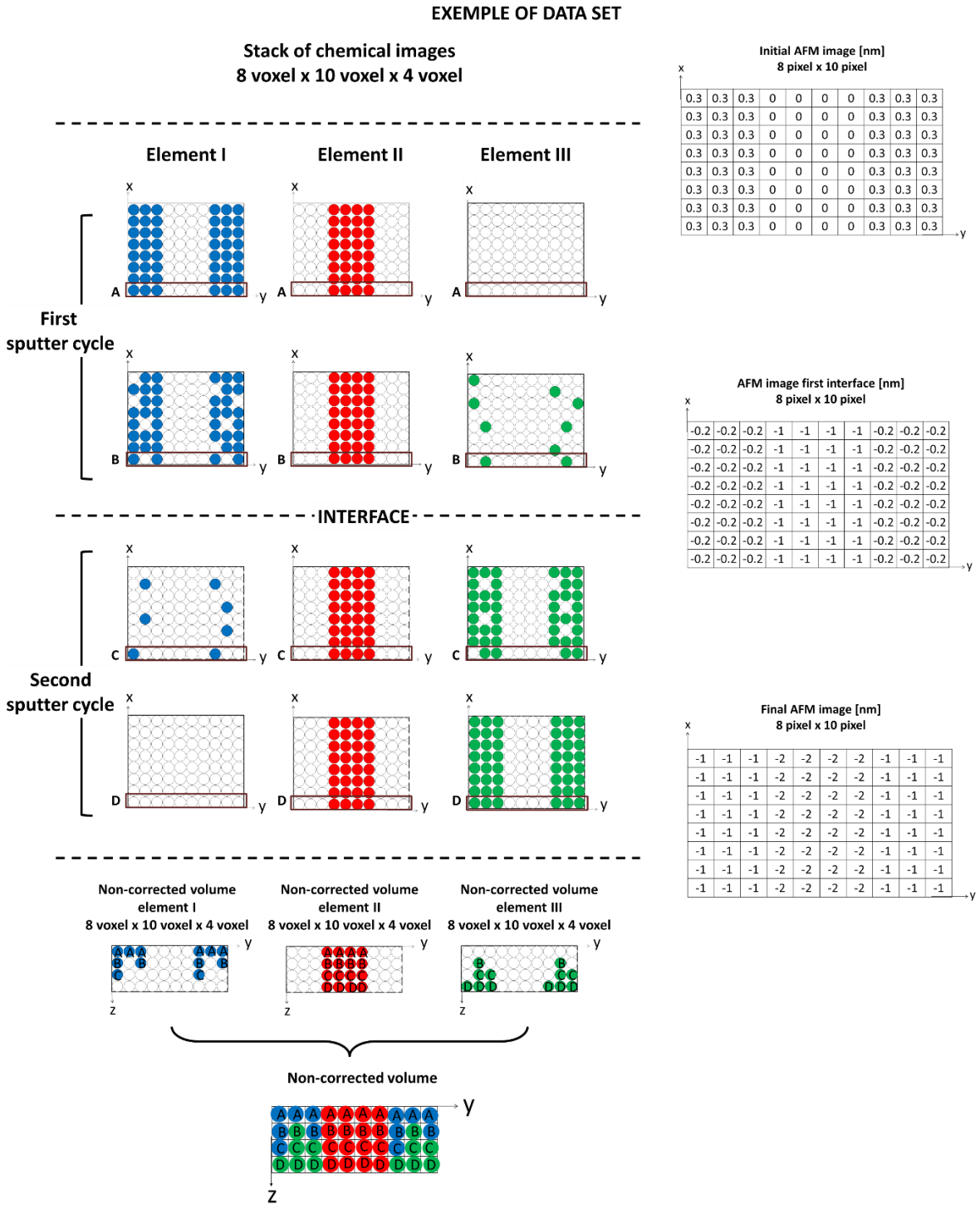

Figure III.4 Exemplary ToF-SIMS and AFM data set, as well as the non-corrected visualization created by stacking the ToF-SIMS images.

Cette thèse est accessible à l'adresse : http://theses.insa-lyon.fr/publication/2019LYSEI121/these.pdf
© [M.A. Moreno Villavicencio], [2019], INSA Lyon, tous droits réservés

2.1. OVERLAY OF THE CHEMICAL INFORMATION OVER TOPOGRAPHICAL SURFACES

A ToF-SIMS / AFM overlay enables the correlation of local composition with surface roughness and morphology. The AFM image is displayed as a topographical surface on which each chemical element is represented as a different color [47,144,145]. The schematic of the overlay procedure is presented in Figure III.5. It can be detailed as follows:

(1) Selection of the ToF-SIMS images per element that correspond to each of the topographical images. It is recommended to use the sum of a few ToF-SIMS images to increase the signal-to-noise-ratio. The number of summed ToF-SIMS images depend on the depth that they represent; normally three to five is sufficient.

(2) The voxel size of the 3D matrices that will form the topographical surfaces is set. The voxel size in x,y correspond to the pixel size of the AFM images. However, the voxel size in z depends on the vertical resolution of the AFM images that is normally 0.1 nm. Consequently, it is possible to set the depth of one voxel as 0.1 nm.

(3) The AFM matrices are then divided by the voxel depth value (i.e. 0.1 nm). It will provide the number of voxels that correspond to each topographical value, in other words an AFM image with the topography in voxels. The results are rounded down when it is not an integer.

(4) If some of the topographical values in voxels are negative, the entire matrix is rescaled to the positive scale starting from 1. Depending on the programming software that is being used the 3rd dimension of a matrix starts from the bottom of the volume or from the top. Since MATLAB starts counting a 3D matrix from the top but the zero of our volume is at the bottom, the matrices with the number of voxels per topographical value need to be inverted. To do this, all the AFM images will be subtracted from its maximum topographical voxel value and the added +1.

(5) Creation of one empty 3D matrix per chemical element that want to be overlaid. Their 2D dimensions are the same as for the topographical surface that should be the same as for the ToF-SIMS images if a good crop was performed in the alignment stage. While their 3D dimension corresponds to the maximum topographical value in voxel, found in the AFM matrices.

(6) Creation of a topographical surface per chemical element. The intensity of every (x,y) pixel in the chemical image is relocated along the depth-axis of one of the empty volume using the topographical value in voxel indicated in the same (x,y) pixel of the corresponding AFM topographical surface. This procedure is repeated in a new empty matrix for every chemical element to be overlaid.

Cette thèse est accessible à l'adresse : http://theses.insa-lyon.fr/publication/2019LYSEI121/these.pdf
© [M.A. Moreno Villavicencio], [2019], INSA Lyon, tous droits réservés

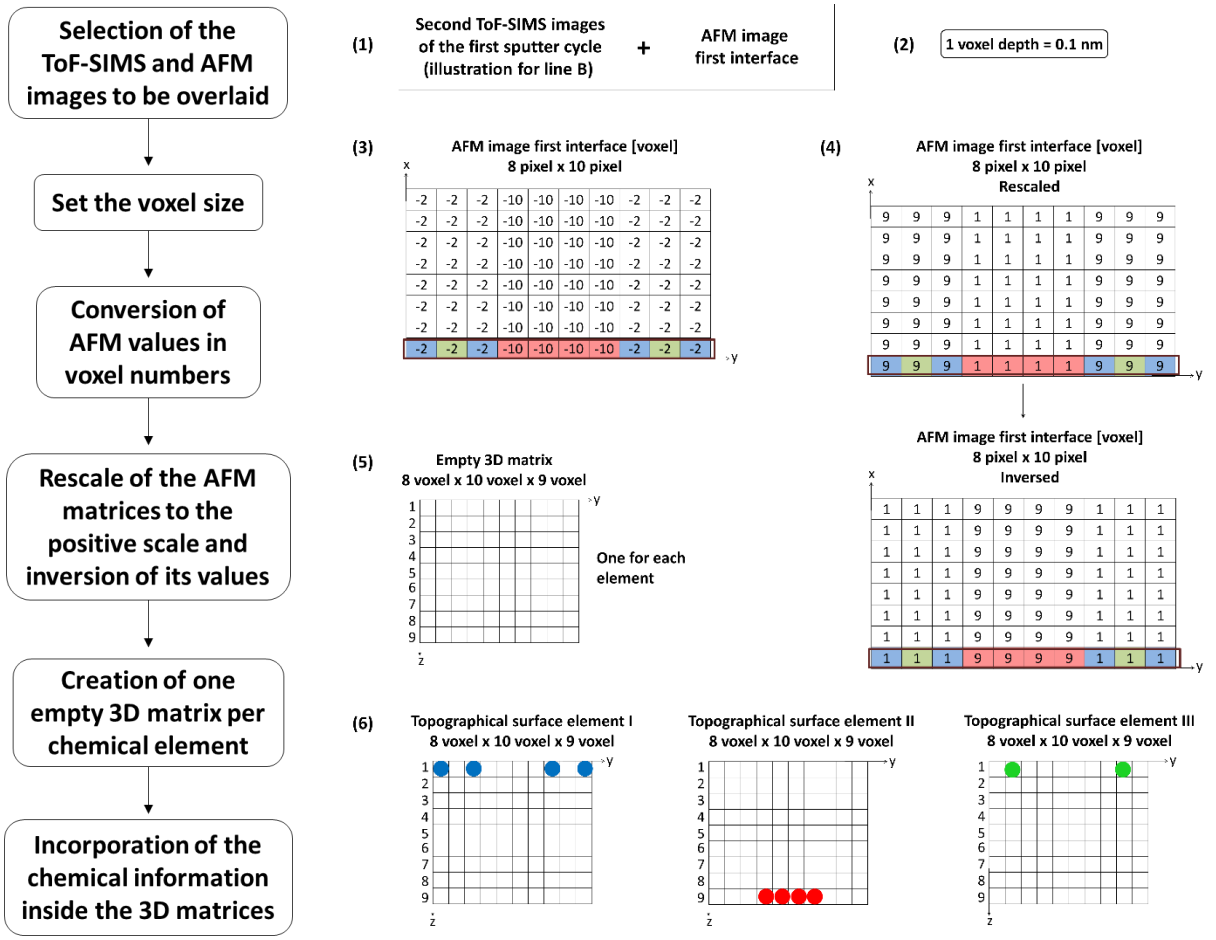

Figure III.5 Schematic of the overlay procedure. Illustration of filling up the empty topographical surfaces with the chemical information of the (1,y) line.

Figure III.5 illustrates the overlay of the AFM image of the first interface with the last ToF-SIMS images of the first sputter cycle. The procedure shows the filling of the empty topographical surfaces with the chemical elements of the line B corresponding to the (1,y) coordinates.

2.2. CALCULATION OF SPUTTER RATE MAPS

A similar approach to the one presented in Wucher *et al.*[22] for the pixel-per-pixel sputter rate calculation is applied. However, intermediate AFM images make this novel methodology suitable for multilayer patterned structures, such as those found in semiconductor technology. The 2D sputter rate map is calculated using the AFM images captured before and after a sputter cycle as well as the corresponding crater depth and sputter time. Figure III.6 shows a schematic of the procedure to obtain sputter rate maps in [nm/s], [nm/chemical image], [voxel/chemical image] for one sputter cycle. It should be repeated for the other sputter cycles.

Cette thèse est accessible à l'adresse : http://theses.insa-lyon.fr/publication/2019LYSEI121/these.pdf
© [M.A. Moreno Villavicencio], [2019], INSA Lyon, tous droits réservés

(1) Pixel-per-pixel sputter depth calculation. A new 2D matrix is created with the difference between the top and the bottom AFM images. If the raw images were already offset using the crater depth measurement (see section CHAPTER II.4.3.3), this subtraction corresponds to the sputtered depth for that sputter cycle.

(2) Sputter rate map [nm/s]. The resulting 2D sputtered depth matrix is then divided by the sputter time of that sputter cycle to obtain the sputter rate map in nm/s.

(3) Sputter rate map [nm/chemical image]. Dividing the sputtered depth by the number of ToF-SIMS images obtained in that sputter cycle, a sputter rate map corresponding to the depth sputtered to produce the pixel of one chemical image is calculated.

(4) Sputter rate map [voxel/chemical image]. The sputter rate maps [nm/chemical image] have the information of how many nm correspond to the depth of one chemical image. By using the voxel depth set by the user, it is possible to calculate pixel-per-pixel how many voxels correspond to the depth of one chemical image.

Nevertheless, the sputter rate mapping approach requires straight vertical and horizontal interfaces in the sample because it assumes a constant pixel-per-pixel sputter yield along the depth within one sputter cycle.

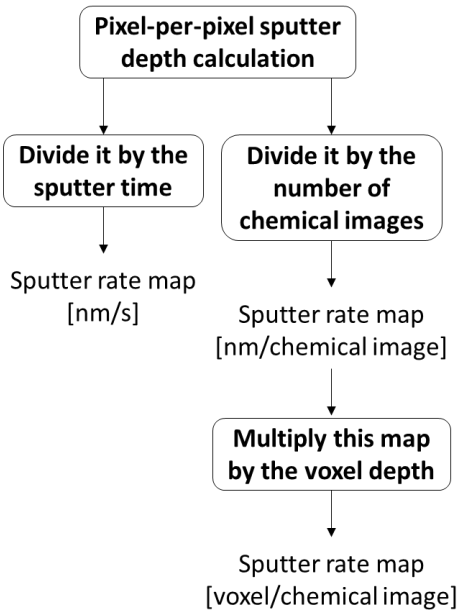

Figure III.6 Schematic of sputter rate maps.

Having these assumptions in mind, this sputter rate mapping opens the door to further investigation of the sample behavior during the sputtering and its relationship with the analysis conditions.

The calculation of the sputter rate map per sputter cycle using the exemplary data set is in Figure III.7. Since there is not a given value for the sputter time, it has been considered as t.

Cette thèse est accessible à l'adresse : http://theses.insa-lyon.fr/publication/2019LYSEI121/these.pdf
© [M.A. Moreno Villavicencio], [2019], INSA Lyon, tous droits réservés

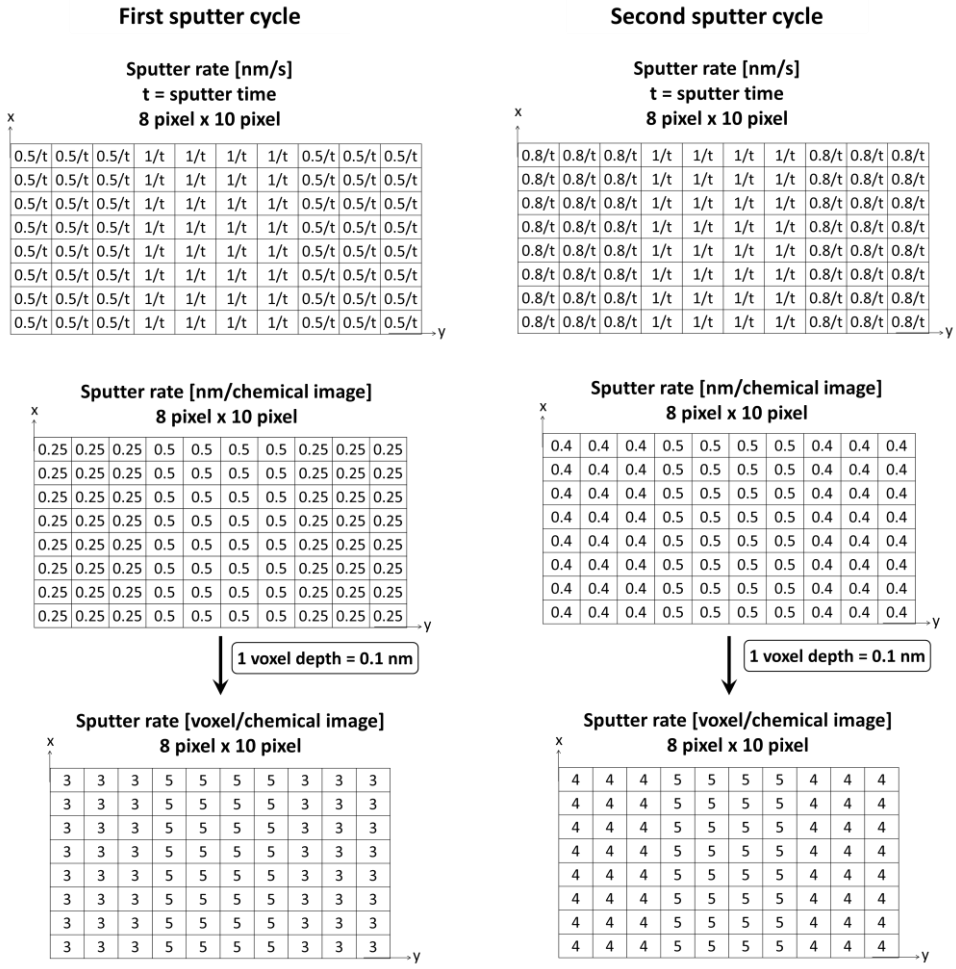

Figure III.7 Calculation of sputter rate maps for the example data set.

2.3. TOPOGRAPHY-CORRECTED 3D CHEMICAL VISUALIZATION

The goal of this methodology is to create a rendered-volume view of the reconstructed ToF-SIMS images topographically corrected with the AFM. The procedure is listed in Figure III.8 and consists of:

(1) Creation of the volume and sub-volumes defined by each sputter cycle. This is actually made when subtracting the measured crater depths to the corresponding AFM images in the AFM raw data processing. A sputtered volume per sputter cycle was created, all of them within the entire sputtered volume. The entire volume is delimited by the initial and final AFM, t_0 and t_n, while each sub-volume is delimited by AFM images acquired before and after a sputter cycle. Each sub-volume provides a framework into which the secondary ion intensities can be placed.

Cette thèse est accessible à l'adresse : http://theses.insa-lyon.fr/publication/2019LYSEI121/these.pdf
© [M.A. Moreno Villavicencio], [2019], INSA Lyon, tous droits réservés

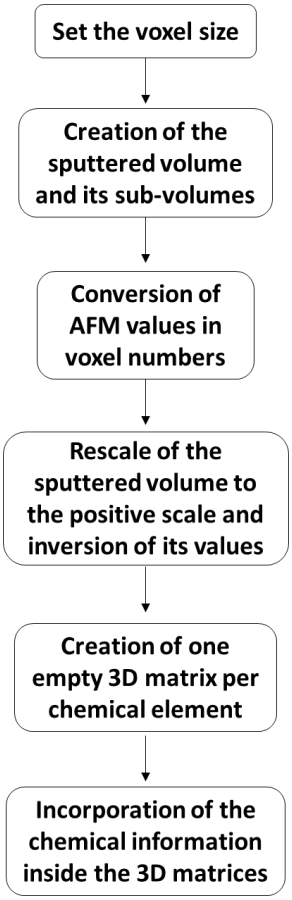

Figure III.8
Schematic to correct 3D ToF-SIMS data set.

(2) Determine the AFM topographical image in voxel values using the selected voxel depth. The value should be rounded to obtain integer numbers. This step is detailed in the overlay ToF-SIMS / AFM procedure.

(3) The topographical information in voxels should be rescaled to the positive scale starting from 1. This time the rescale is not individually done for each image but the entire volume formed with the AFM images is shifted. In order to do this, the final AFM image is needed. Its maximum negative value is determined and its absolute value +1 is added to all the AFM images. Since MATLAB starts counting a 3D matrix from the top but the zero of our volume is at the bottom, the topographical values in voxel need to be inverted as for the overlay ToF-SIMS / AFM. All the AFM images are subtracted from the maximum topographical value of the volume, corresponding to the initial AFM image and then added +1.

(4) Creation of empty volume per chemical element. As for the topographical surfaces in the overlay of the chemical over the topographical information, the volume should have the dimensions of the 2D chemical and topographical images. The third dimension of this volume corresponds to the maximum topographical value of the initial AFM image [voxel].

(5) Filling up the empty volumes with the chemical intensities per chemical element. This is done per chemical element and per sub-volume of sputter cycle. A schematic of the relocation of the ToF-SIMS images intensity within the reconstructed volume is shown in Figure III.9. The relocation of the intensities found in the stack of ToF-SIMS images is made per columns delimited by the (x,y) pixels. The filling starts from the top along the z-axis, 3rd dimension, of the volume. The (x,y) position of the intensity in the empty volume is the same as for the raw data. However, the location in the z-axis is defined by the topographical value indicated in the same (x,y) position of the AFM top image [voxel] for the corresponding sub-volume. The sputter rate value [voxel/chemical image] found in the map for the same (x,y) position indicates the number of voxels in the 3rd dimension that corresponds to that chemical intensity.

Cette thèse est accessible à l'adresse : http://theses.insa-lyon.fr/publication/2019LYSEI121/these.pdf
© [M.A. Moreno Villavicencio], [2019], INSA Lyon, tous droits réservés

This number is the same for all the chemical intensities located in the same (x,y) pixel within the same sputter cycle without distinction of chemical element.
This procedure is done for the chemical intensity located at (x,y,1), corresponding to the first chemical image of the ToF-SIMS stack. Since the volume is filled up per (x,y) columns, the second ToF-SIMS intensity (x,y,2) is located in the 3rd dimension of the empty volume using the AFM value, the sputter rate [voxel/ chemical image] value and its position in the chemical stack z. The position of the chemical intensity within the empty volume follows the algorithm [x, y, AFM(x, y) + (z-1) * SR(x, y)].
This procedure continues going down in the stack of ToF-SIMS images and it is repeated for every (x,y) position, and for every stack of chemical element until every sub-volume of sputter cycle is filled up.

By applying the same chemical intensity in the number of voxels indicated by the sputter rate map, we assume that the intensity of that chemical element is the same along the depth of that sputtered scan. This is not entirely true when approaching an interface. For this reason, instead of applying the same intensity in all the voxels, there is also the possibility of relocating the intensity in the first voxel and interpolate the chemical intensity in the voxels in-between. However, this is kept as a user choice. The final result is a 3D matrix per chemical element with the same two dimensions as for the aligned 2D chemical and AFM images and a 3rd dimension corresponding to the total sputtered depth converted in voxels.

Figure III.9 illustrates the procedure to reconstruct the chemical volume. The process counts with three AFM images with topographical values in voxel units, two ToF-SIMS sputter cycles with two ToF-SIMS images in each, and one sputter rate map per sputter cycle. The procedure is described for one pixel line (1,y) of the ToF-SIMS images (A, B, C and D). It is done per column of pixels. Here is the description for the (1,1,z) column : the intensity in the corresponding position of the first chemical image (A line) is located at the depth indicated at (1,1) position of the AFM image, 1st voxel. The value at (1,1) in the sputter rate map for the 1st sputter cycle indicates the number of voxels that this intensity should occupy within the volume, 3 voxels. The relocation of the (1,1) intensity of the second chemical image (B line) starts in the reconstructed volume where the first finishes. It occupies the same number of voxels as for the first one because they are in the same sputter cycle. For the second sputter cycle, the (1,1) intensity in the 3rd chemical image (line C) is located following the depth indicated in the (1,1) AFM image of the first interface, 6th voxel and it occupies 4 voxels along the depth (sputter rate map 2nd sputter cycle (1,1) position). The intensity of the line D is then located where the previous one finishes. It occupies the same number of voxels as the first image of the 2nd sputter cycle. The corrected volume per chemical element and their superposition are found in the image.

Cette thèse est accessible à l'adresse : http://theses.insa-lyon.fr/publication/2019LYSEI121/these.pdf
© [M.A. Moreno Villavicencio], [2019], INSA Lyon, tous droits réservés

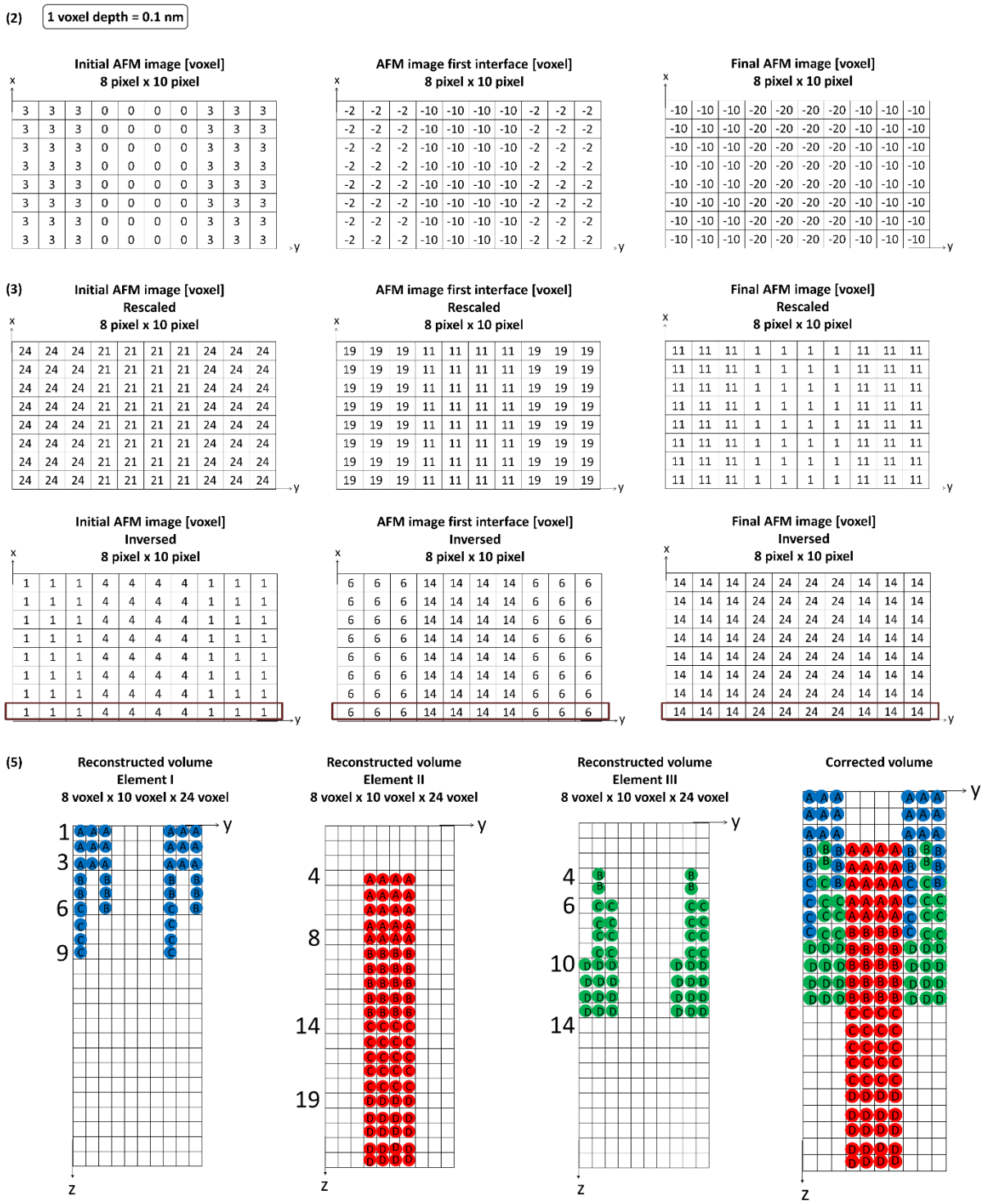

Figure III.9 Schematic of the relocation of the ToF-SIMS images intensities within the reconstructed volume of each element.

Another approach for the reconstruction of a topography-corrected volume is using a general sputter rate per chemical element instead of sputter rate maps. In this case, it is assumed that the sputter rate does not change with the depth nor in the same 2D plane.

Cette thèse est accessible à l'adresse : http://theses.insa-lyon.fr/publication/2019LYSEI121/these.pdf
© [M.A. Moreno Villavicencio], [2019], INSA Lyon, tous droits réservés

This approach is suitable when the number of layers in the sample makes the combined methodology too long. The procedure is similar to the previously mentioned, with slight differences:

(1) The sputter rate [nm/s] is converted to [nm/chemical image] using the sputter time per data point. It is then transformed to [voxel/chemical image] with the voxel depth set by the user.

The sputter rate [voxel/chemical image] indicates, as in the case before, the number of voxels corresponding to one chemical intensity. Since there is no sputter rate map, this is a constant value for all the intensities of the same chemical element.

(2) Average of sputter rates [voxel/chemical image]. Different chemical elements are present in the same (x,y,z) position. The value that defines the number of voxels that will occupy all the chemical intensities present in that position is determined by the average of the sputter rate of the present chemical elements. Every (x,y,z) position may have then different sputter rates. Contrary to the previous approach where there was a common sputter rate along the *z* axis.
(3) The chemical intensities are relocated in the corrected-volume per (x,y) columns following the previous procedure and the average of sputter rates calculated before.

Differences between the real sample and the reconstructed volume may be found. This approach does not take into account the sample behaviour throughout the sputtering creating a theoretical volume instead of a realistic one.

Once the topography-corrected volumes per chemical element are created, the ToF-SIMS depth-profile can be extracted. The chemical intensities per chemical element are averaged in the 2D plane, the resulting value per 2D plane of the volume is saved in a table. It is important to outline that the real chemical intensities were lost if the ToF-SIMS images were exported as .TIFF. In order to obtain the real counts per pixel, the images should be exported as .txt format.

2.4. RESULTS AND THEIR 3D VISUALIZATION

The resulting matrices can be exported as .TIFF format. They are then read by AVIZO visualization software from Thermo Scientific™ allowing the final 3D visualization of the results.

- Overlay ToF-SIMS and AFM: there is one surface topography per overlaid chemical element. Since they are in the format of 3D matrices they are exported as .TIFF 3D.

Cette thèse est accessible à l'adresse : http://theses.insa-lyon.fr/publication/2019LYSEI121/these.pdf
© [M.A. Moreno Villavicencio], [2019], INSA Lyon, tous droits réservés

They are imported to AVIZO, which superposes every 3D matrix because they have the same dimensions. The voxel size in length units are given for the three dimensions and a different color per surface topography is set in order to obtain different colors per chemical element. These matrices enable the intensity change within the same chemical element to be visualized through the chosen color bar per chemical element.

- Sputter rate maps: they are 2D matrices that can be exported as .TIFF format and opened in a basic program to read images. In our case, SPIP, that is a classical software to treat AFM images, was used. It is recommended to set a color bar that highlights the sputter rate differences within the map.
- Topography-corrected chemical volumes: there is a 3D matrix per chemical element that is exported as .TIFF 3D. The importation in AVIZO is done in the same way as for the overlay: the voxel size in length units is set and a different color per chemical element is chosen.
- Topography-corrected ToF-SIMS depth profile: the columns of data, one per chemical element, can be exported as .txt and be read by any graphing software. All the chemical elements should be plotted in the same graph.

AVIZO software allows the user to see orthogonal views, slice the volumes, perform rotation, dimension settings, personalize the visualization of the data, the exportation of the data as images and recording videos while performing any of the mentioned actions.

Cette thèse est accessible à l'adresse : http://theses.insa-lyon.fr/publication/2019LYSEI121/these.pdf
© [M.A. Moreno Villavicencio], [2019], INSA Lyon, tous droits réservés

Cette thèse est accessible à l'adresse : http://theses.insa-lyon.fr/publication/2019LYSEI121/these.pdf
© [M.A. Moreno Villavicencio], [2019], INSA Lyon, tous droits réservés

3. ToF-SIMS / AFM combined methodology applied on a GaAs / SiO_2 patterned structure

The capability of the previously mentioned ToF-SIMS / AFM combined methodology was demonstrated ex-situ and in-situ on an inorganic 3D structure. The ex-situ protocol was carried out at CEA whilst the in-situ methodology was performed at IMEC.

3.1. Sample description

The sample was a GaAs based structure supplied by LTM/CNRS laboratory. The GaAs layer was selectively grown by metal organic chemical vapor deposition (MOCVD) in SiO_2 cavities on a (100) oriented 300 mm silicon substrate. More details about the growth are given in the reference [146].

Figure III.10.a shows a scanning transmission electron microscopy (STEM) image of the sample. The SiO_2 cavities were obtained using standard electron beam lithography and plasma etching. To ensure good selectively growth of the GaAs, the substrate was pre-cleaned by SiConi^{TM} etching, which allows the native oxide to be removed from the bottom of the cavities. This pre-epi cleaning resulted in an isotropic etching of SiO_2 and thus a lateral etching of SiO_2 barriers. This has lead to the appearance of a step in the silicon substrate, 9 nm in height, visible at the bottom of the cavity. The SiO_2 layer had a thickness of about 167 nm and the GaAs layer had a non-constant thickness dependent on the deposition time. [82]

The analyzed area was a 20 µm wide SiO_2 pattern named *pacman* structure, an optical top-view is shown in Figure III.10.b. The AFM imaging of the *pacman* structure revealed a step of 14 nm between the GaAs layer and SiO_2. The size of the *pacman* structure facilitated the optical localization in both instruments.

The initial topography of this structure and the 9 nm step in the silicon substrate made the classical 3D ToF-SIMS reconstruction challenging.

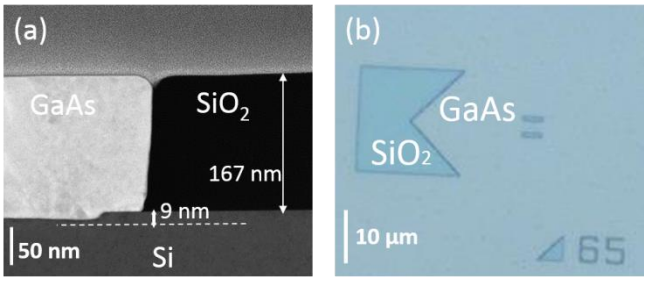

Figure III.10

a. Cross-sectional STEM image of the GaAs layer grown in a SiO_2 cavity. b. Top view optical image of the pacman structure (20 µm x 20 µm).

Cette thèse est accessible à l'adresse : http://theses.insa-lyon.fr/publication/2019LYSEI121/these.pdf
© [M.A. Moreno Villavicencio], [2019], INSA Lyon, tous droits réservés

There was no flat substrate or surface that could be used as a reference to shift the ToF-SIMS images. In addition to this, the existence of two materials with different sputter rates would have created a 3D visualization with a non-accurate layer thickness.

3.2. ANALYSIS CONDITIONS

ToF-SIMS experiments were performed using a ToF-SIMS V instrument from ION-TOF GmbH. Bi_3^{++} primary ions were used with an incident energy of 50 keV (0.1 nA) in the Bi-BA-Image mode. This primary beam was rastered over a 50 x 50 μm^2 area with 256 x 256 $pixels^2$ scan resolution. A Cs^+ sputter beam at 500 eV energy (31 nA) was used as raster over a 250 x 250 μm^2 area. Spectra were obtained in negative, non-interlaced mode using an electron beam (20 eV) for charge compensation. Using a cycle time of 50 µs, the cycle of acquisition was 40 frames and 10 s sputtering with 10 s pause time between two acquisitions.

The AFM images were obtained with an AFM Dimension Icon from Bruker, which is in a nitrogen-filled glove box (MBraun), with H_2O and O_2 contents below 3 ppm. All measurements were performed in Tapping mode with standard silicon cantilever (TAP300Al-G from Budget Sensors) with a nominal spring constant of 40 N/m. A typical 22 x 44 μm^2 area with a 512 x 1024 $pixels^2$ resolution was analyzed.

The crater depth after ToF-SIMS depth profiling was measured by optical surface profilometry (3D Plu neox by Sensofar) in confocal mode. The values provided in this thesis have a precision of ± 5 nm.

3.3. EXPERIMENTAL SECTION

The sample was previously studied in an optical microscopy in order to localize the *pacman* pattern and identify reference points to easily identify it in both instruments.

A complete ToF-SIMS depth profile exposed two interfaces in the sample, GaAs with the Si substrate and the SiO_2 with the Si substrate. From this, a cyclical ToF-SIMS / AFM / profilometer methodology consisting of adding AFM images and crater depth measurements to a classical ToF-SIMS depth profile every time an interface was detected was structured. Figure III.11 illustrates the methodology when it was applied on the aforementioned GaAs based structure. Values are given from that experiment; but the protocol can be applied to other samples.

(1) Initial state, t_0: initial surface topography was imaged and a step h_o of 14 nm between the SiO_2 and GaAs was detected.
(2) The depth profile started, defining the first sputter cycle. After 920 s of sputtering, at the first interface (GaAs / Si), the ToF-SIMS analysis was stopped.

Cette thèse est accessible à l'adresse : http://theses.insa-lyon.fr/publication/2019LYSEI121/these.pdf
© [M.A. Moreno Villavicencio], [2019], INSA Lyon, tous droits réservés

(3) First interface, t_1: an AFM image was captured, the topography had increased to 108 nm since the initial time. The crater depth was measured to be 160 nm.

(4) The second ToF-SIMS sputter cycle was performed until the detection of the SiO_2 / Si interface at 2350 s.

(5) Second interface, t_2: the topography and the crater depth were measured. The topography was similar to that captured at t_1, 119 nm. The crater depth was 295 nm.

(6) Third sputter cycle was run until 2710 s at which point the substrate was detected in the entire analysis area.

(7) Final state, t_3: the AFM image revealed that at the end of the sputter process the initial step h_o evolved to 119 nm, h_3. The final crater had a depth d_3 of 356 nm.

The methodology was performed ex-situ and the transfer between instruments was made using a nitrogen-filled sample transfer vessel (overpressure of 10 mbar).

The data obtained from this cyclical analysis includes:

- Four AFM images with a pixel size of 43 nm (t_0, t_1, t_2 and t_3).
- Three sputter cycles with stacks of ToF-SIMS images in each of them. The 1st sputter cycle had 92 ToF-SIMS images in the stack, the 2nd had 136 ToF-SIMS images and the 3rd had 36 ToF-SIMS images. There was one stack per chemical element. Every chemical image had a pixel size of 198 nm.
- Three crater depth values (d_1, d_2 and d_3) were calculated by measuring the height difference between the GaAs sputtered and non-sputtered surface.

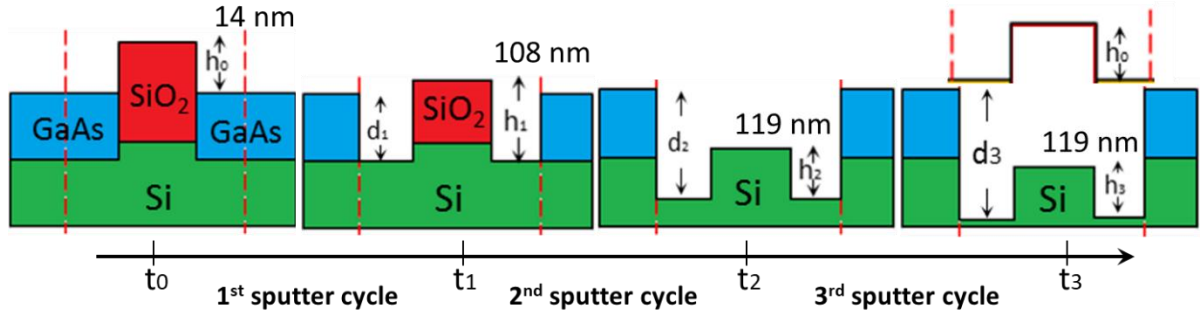

Figure III.11 Illustration of the evolution of the sample during the combined ToF-SIMS / AFM methodology on a GaAs based sample. The times correspond to the initial state (t_0), the first interface (GaAs / Si, t_1), the second interface (SiO_2 / Si, t_2), and the end of sputtering (deeper in Si substrate, t_3). The crater depth evolution is denoted d and the topography step h. An AFM scan was performed at each time.

Cette thèse est accessible à l'adresse : http://theses.insa-lyon.fr/publication/2019LYSEI121/these.pdf
© [M.A. Moreno Villavicencio], [2019], INSA Lyon, tous droits réservés

3.4. DATA PROCESSING

The raw data was treated following the procedure described in CHAPTER II.4.3. The ToF-SIMS images representing the secondary ions SiO_2^-, $GaAs^-$ and Si^- were exported in TIFF and the AFM images in txt format. The sequences of ToF-SIMS images were opened in ImageJ where they were stacked per chemical element. The data was imported to MATLAB were the advanced data processing was performed. A schematic of the successive steps for the advance data processing is shown in Figure III.12.

The difference in pixel size between the AFM and the ToF-SIMS images was up to a factor of 4.6. Since the overlay of the chemical information over the topographical surfaces can outline the relationship between the morphology and the composition of the surface, we decided to perform this step keeping the lateral resolution of the AFM. An interpolation of the ToF-SIMS images was performed. The ToF-SIMS images went from 256 x 256 pixels to 1183 x 1183 pixels, (Figure III.13.a).

On the other hand, we have decided that the topography-corrected 3D ToF-SIMS volume would have the original chemical data furnished by the analysis. For this, the AFM images were binned from 512 x 1024 pixels to 111 x 222 pixels (Figure III.13.b), in order to preserve the pixel size of the ToF-SIMS images.

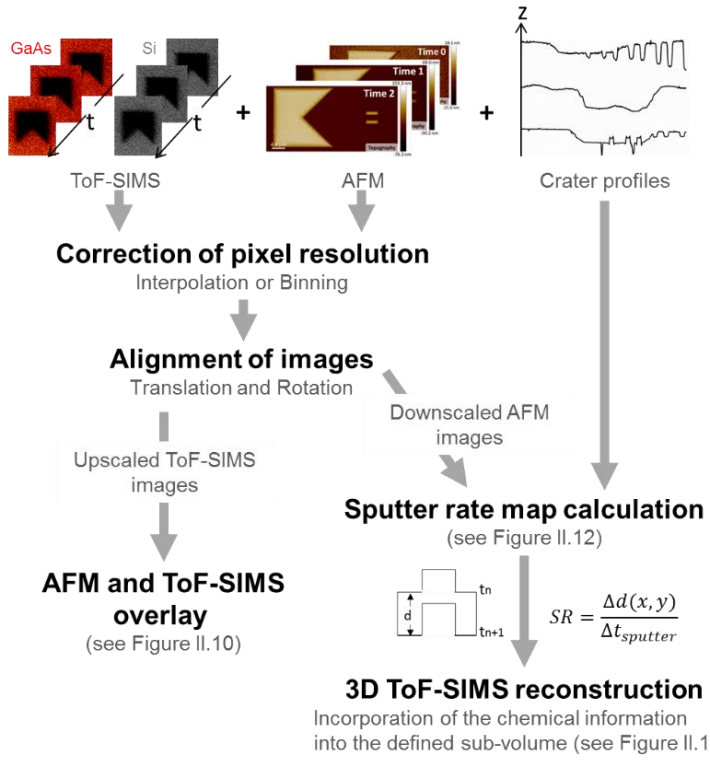

Figure III.12

Schematics of the data processing steps to achieve a topography-corrected 3D ToF-SIMS reconstruction and an AFM / ToF-SIMS overlay starting from ToF-SIMS and AFM images and crater depths.

Cette thèse est accessible à l'adresse : http://theses.insa-lyon.fr/publication/2019LYSEI121/these.pdf
© [M.A. Moreno Villavicencio], [2019], INSA Lyon, tous droits réservés

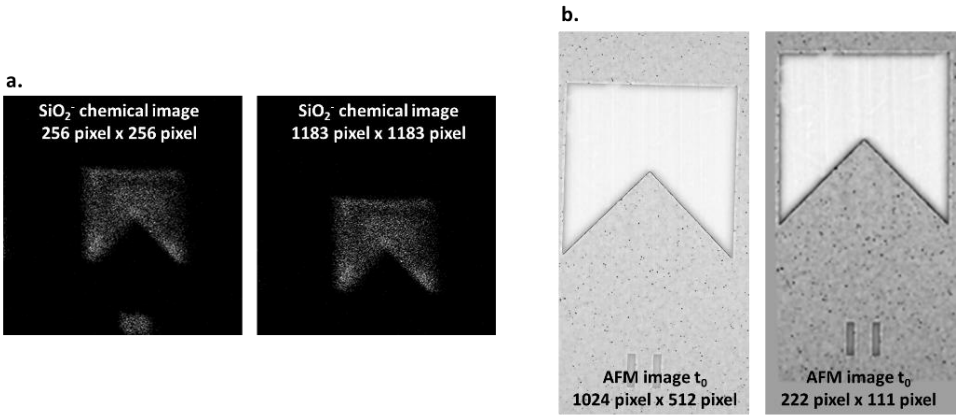

Figure III.13 Resizing the AFM and the ToF-SIMS images to obtain the same pixel size. a. An interpolation between the pixels is needed when the pixel size of an image has to be reduced. In the opposite case b. A binning of pixels is done when the pixel size should be increased.

The increment of the contrast seen between the original and the binned image is product of the amplification of the AFM values by the binning of pixels. This influences an incorrect surface roughness interpretation seen as the emerging of many dark points in the binned image. If the roughness were measured from the last one, the value would be higher than the one measured from an AFM image captured using the same number of pixels as the binned image (222 pixels x 111 pixels).

The alignment procedure was performed on the stacks of ToF-SIMS images. Each chemical image was compared with the sum of the images corresponding to SiO_2^- ions. In the case where shifts were still present, the sum of the already aligned SiO_2^- images was used as the new reference image to repeat the alignment process. The alignment cycle was stopped when the translation found for each image was 0. The Figure III.14.a shows the orthogonal views of the non-corrected stack of ToF-SIMS images, SiO_2^- stack in red, $GaAs^-$ in blue and the Si^- coming only from the substrate in green. The Si^- images obtained before reaching the GaAs / Si interface were removed to avoid confusion in the visualization. Selection of O_2^- ions instead of SiO_2^- could have also avoid the superposition of Si signal coming from the SiO_2 layer and the substrate.

The calculated pixel translation in *y* for one (x,y) position is plotted as a function of the ToF-SIMS images, Figure III.14.b. The ToF-SIMS images were slightly shifted within the same sputter cycle due to the heating of sample when sputtering or the lack of fixation of the sample in the holder. This shift was up to 20 pixels, corresponding to almost 4 µm. In addition to this, there is a shift due to the reposition of the sample between sputter cycles. This one went up to 40 pixels, corresponding to almost 8 µm of precision when repositioning the sample between the instruments.

Cette thèse est accessible à l'adresse : http://theses.insa-lyon.fr/publication/2019LYSEI121/these.pdf
© [M.A. Moreno Villavicencio], [2019], INSA Lyon, tous droits réservés

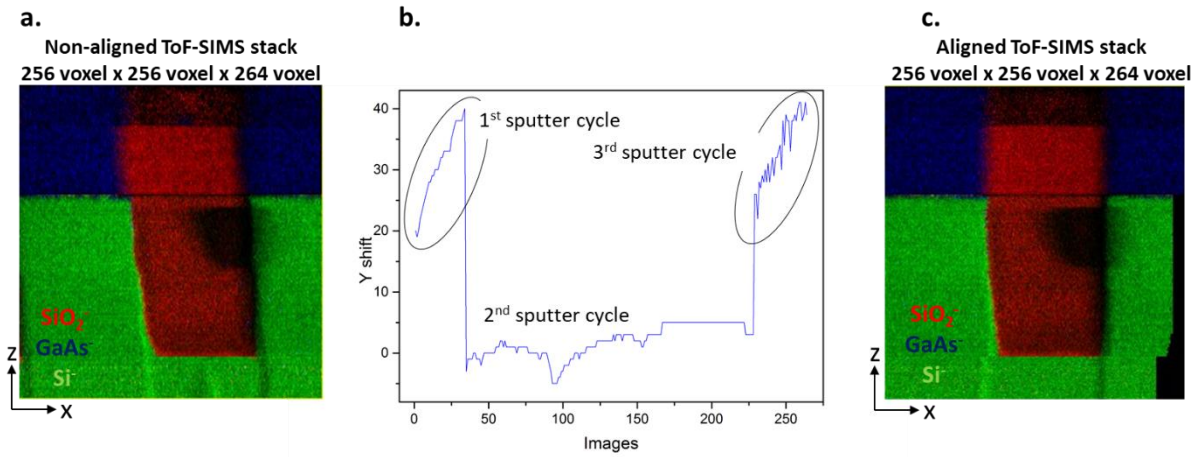

Figure III.14 Stack of ToF-SIMS images: SiO_2^- stack in red, $GaAs^-$ in blue and the Si^- from the substrate in green. a. Non aligned stack. b. Shifts determined for the y direction of one specific (x,y) position along the ToF-SIMS images of the stack. c. Aligned stack.

Once the (x,y) translation and rotation were applied to all the ToF-SIMS images empty pixels appeared in the edges where the chemical image was shifted from, Figure III.14.c.

The same alignment procedure was done for the topographical images using as a reference the one of t_3 due to a high contrast in the image. Once the AFM and ToF-SIMS images were aligned together, the empty pixels were cropped out. This procedure was done twice, once to align the ToF-SIMS images (256 x 256 pixels) with AFM images (222 x 111 pixels) and then to align the ToF-SIMS images (1183 x 1183 pixels) with the topographical images (1024 x 512 pixels).

3.5. RESULTS OF THE EX-SITU METHODOLOGY

3.5.1. TOF-SIMS AND AFM OVERLAY

The ToF-SIMS images corresponding to each AFM surface were selected: the first five ToF-SIMS images of the stack for the initial AFM surface, a representative depth of a few nanometers. The last five ToF-SIMS images before reaching the interface and the first five after the interface for the overlay of each interface. Moreover, the last five ToF-SIMS images for the final topography.

The ToF-SIMS and AFM overlay obtained at four different times are in Figure III.15.a-d. They correspond respectively to the initial surface (t_0), the GaAs / Si interface (t_1), the SiO_2 / Si interface (t_2) and the final surface state (t_3). Each color represents a chemical element or material: red for the SiO_2, blue for the GaAs and green for the Si. The images display the distribution of those specific ions in the analyzed area.

Cette thèse est accessible à l'adresse : http://theses.insa-lyon.fr/publication/2019LYSEI121/these.pdf
© [M.A. Moreno Villavicencio], [2019], INSA Lyon, tous droits réservés

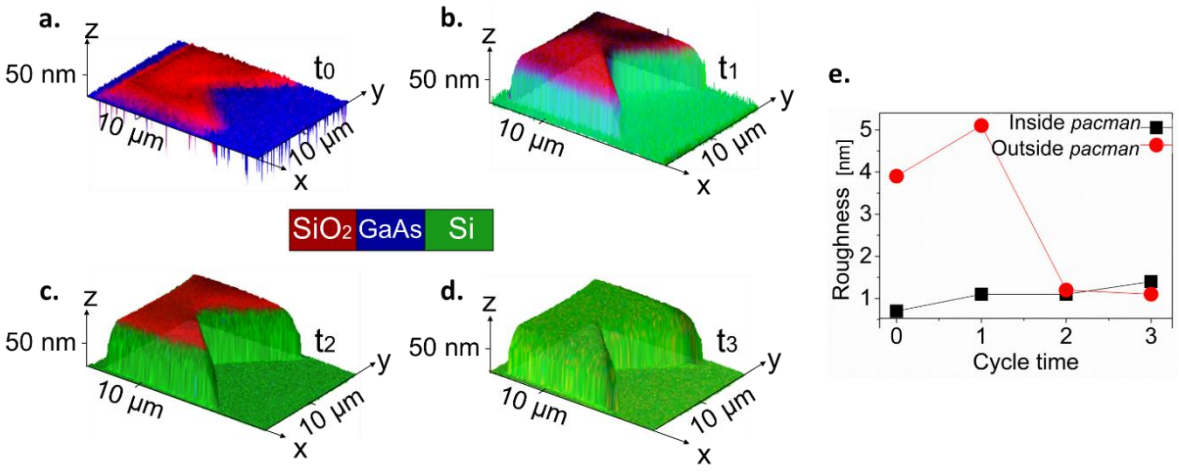

Figure III.15 *a-d. AFM and ToF-SIMS overlay for each cycle stage; initial state t_0, first interface (GaAs / Si) t_1, second interface (SiO_2 / Si) t_2, and at the end of sputter (deeper in the Si substrate) t_3, respectively. The colors represent the chemical composition of that area, red, blue and green for the SiO_2, GaAs and Si respectively. e. Roughness evolution at the areas "inside pacman" structure (black curve) and "outside pacman" structure (red curve) while sputter cycles t_0, t_1, t_2 and t_3.*

Color mixture illustrates the existence of more than one element at the interfaces, traces of $GaAs^-$ and SiO_2^- ions on the Si substrate surface at the first t_1 and second interface t_2.

There are two main pieces of information that could be extracted from these overlays. The first one is the evolution of the topography and its relationship with the chemical information. The elevation of the *pacman* SiO_2 structure with respect to the rest of the surface was 14.8 nm, 108.6 nm, 119.1 nm and 119.7 nm for t_0, t_1, t_2, and t_3 respectively. The initial topography visible in the STEM image Figure III.10 largely increased during the first sputter cycle (from t_0 to t_1) because of the sputter rate difference between the GaAs and the SiO_2. However, the height of this step seemed to stay stable for the next sputter cycles, meaning a similar sputter rate for Si substrate and SiO_2.

As the lateral resolution of the AFM images was preserved, a second piece of information could be extracted from the overlays, the surface roughness. The values obtained after each sputter cycle when the roughness was measured inside and outside the *pacman* structure are shown in the Figure III.15.e. In the initial state, the GaAs roughness was five times greater than the SiO_2 surface; it is visible in the overlay image at time t_0 as holes in the GaAs surface, blue color. In the present case, this relatively large surface roughness was due to the presence of antiphase boundaries in the GaAs layer, characteristic defects related to the growth of a polar material on a non-polar substrate [147].

Cette thèse est accessible à l'adresse : http://theses.insa-lyon.fr/publication/2019LYSEI121/these.pdf
© [M.A. Moreno Villavicencio], [2019], INSA Lyon, tous droits réservés

It has recently been shown that this type of defects can be completely eliminated by a specific preparation of the Si surface in order to obtain a well ordered network of biatomic steps even on a nominally (100)-oriented Si substrate. [147] The surface roughness slightly increased during the first sputter cycle, especially on the GaAs area. The non-homogeneous sputtering, the bombarding of primary ions toward the surface, the existence of defects on the surface may increase the roughness in the surface. More about the materials behavior during the sputtering is explained in the next chapter. Once the substrate was reached in the entire analysis area, the measured roughness values were in the same range. From this, it is possible to say that roughness values can provide the idea of only one material is present on the surface.

The AFM profiles provided further information about the influence of the sputtering conditions on the topography. Those profiles can be seen in Figure III.16. For each AFM image three sections were made on the edges of the *pacman* structure, they correspond to the black lines with number *1*, *2* and *3* in the AFM image initial state (Figure III.16.a). Those sections were located at 0, 90 and 45 degrees with respect to the sputter beam orientation (represented with green arrows in the AFM image). Figure III.16.b-d show the sections extracted from the four AFM images corresponding to the orientation *1*, *2* and *3*, respectively.

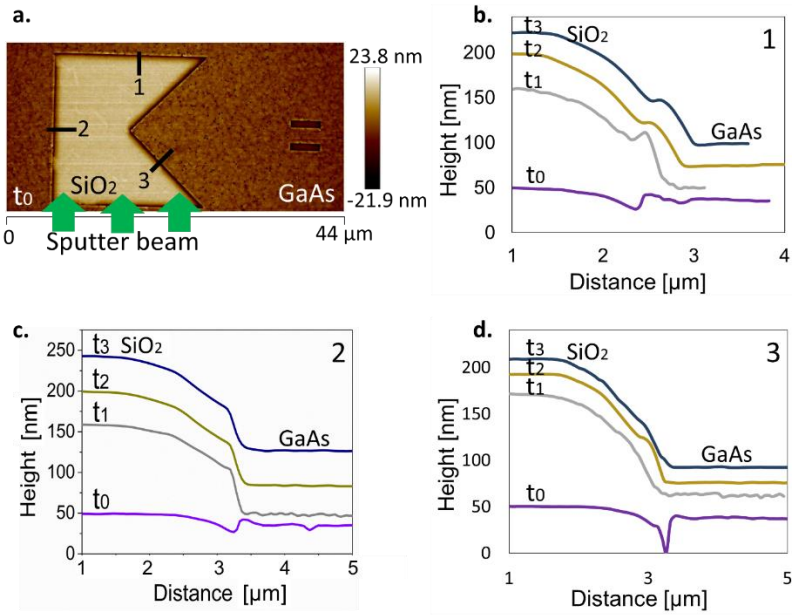

Figure III.16 *Topography profiles of AFM image sections. a. AFM image at t_0. Sections (1, 2 and 3) are shown with black lines. They correspond respectively to parallel (b, Line 1), perpendicular (c, Line 2) and 45-degree orientation to the sputter beam (d, Line 3). The three sections were made for each cycle time; initial state t_0, first interface (GaAs / Si) t_1, second interface (SiO_2 / Si) t_2, and end of sputter (deep in Si substrate) t_3 are shown in color purple, gray, gold and blue respectively*

Cette thèse est accessible à l'adresse : http://theses.insa-lyon.fr/publication/2019LYSEI121/these.pdf
© [M.A. Moreno Villavicencio], [2019], INSA Lyon, tous droits réservés

The profiles from t_0 to t_3 evidenced the eight times increment in the surface topography that was seen in the overlay due to the sputter rate difference. Lateral sputtering in the *pacman* structure was visible in the profiles. A shadowing effect due to the perpendicular orientation of the sputter beam was seen in the section *1*, Figure III.16.b.

The ripple found along the GaAs surface at the edge of the SiO_2 / GaAs vertical interface at t_0 profiles lost its shape throughout the sputtering when it was parallel to the sputter beam Figure III.16.c. Further information about the influence of the sputter beam orientation will be provided in the next chapter.

3.5.2. MAPPING THE SPUTTER RATES OF THE ANALYZED AREA

The procedure to calculate sputter rate maps detailed in section 0 was followed. Three different sputter rate maps were obtained, one per sputter cycle. However, to have an idea of sputter rate values for the materials present in the sample, the sputter rate map for the first and the second sputter cycle were sufficient (Figure III.17.b and c, respectively). Those sputter rates maps have the lateral resolution of the AFM. The images outlined the pixel-per-pixel dependence of the sputter rate values.

Figure III.17.a shows an orthogonal view of the volume created when the AFM images were offset in the raw data treatment procedure. The offset was done using the value of the corresponding crater depth: 160 nm for the AFM 1st interface t_1 (represented in the figure with a gray surface), 295 nm for the AFM 2nd interface t_2 (gold surface in the figure), and 356 nm for the final AFM, seen as a blue surface in the figure. The initial and the final AFM image, surfaces in purple and blue respectively, delimited the entire sputtered volume. Indeed, the intermediate AFM images delimited the sub-volumes corresponding to the sputtered sample per sputter cycle (seen as (1), (2) and (3) in the Figure III.17.a).

Note that the surfaces defined by the AFM appear to overlap in the 3D representation due to lateral differences in sputter rate. At t_1, the GaAs / Si interface was reached at 160 nm whilst the SiO_2 layer had only been sputtered 60 nm. The step in the Si substrate that is shown in the STEM image, Figure III.10, was visible at around 160 nm of sputtering with the overlap of t_1 and t_2 topographies.

As expected for the first sputter cycle, the GaAs sputter rate was almost 2.5 times that of SiO_2. A histogram of this map shows two defined peaks of sputter rate values, belonging to each material. SiO_2 at 0.07 +/- 0.01 nm/s and GaAs at 0.17 +/- 0.01 nm/s (Figure III.17.b). The roughness of the sample surface causes a spreading of sputter rate values and since the GaAs roughness is about 5 times greater than the SiO_2, it resulted in an increase by a factor of 3.3 of the full width at half-maximum value.

Cette thèse est accessible à l'adresse : http://theses.insa-lyon.fr/publication/2019LYSEI121/these.pdf
© [M.A. Moreno Villavicencio], [2019], INSA Lyon, tous droits réservés

The sputter rate map corresponding to the second sputter cycle shows close sputter rate values for Si and SiO_2 areas. The histogram in Figure III.17.c presents a wide peak where sputter rate values of 0.07 +/- 0.01 nm/s and 0.08 +/- 0.01 nm/s were respectively extracted for SiO_2 and Si. The SiO_2 sputter rate value of the second cycle coincided with the sputter rate obtained during the first cycle for the SiO_2. The Si sputter rate value was confirmed by sputtering a silicon reference sample with the same analysis conditions. It lead to a sputter rate of 0.08 nm/s. The sputter rate alteration due to the GaAs roughness was still visible in this second cycle.

Sputter rates could also be estimated using the layer depths provided by the STEM image (Figure III.10) and the ToF-SIMS sputter time. The determined values for GaAs and SiO_2 coincided with the sputter rate values given by the histograms. GaAs, SiO_2 and Si sputter yield were determined using the Eq. II.4. The calculated values were 2.5, 1.5 and 1.5 atoms/ion for GaAs, SiO_2 and Si respectively. The 1.6 GaAs / SiO_2 sputter yield ratio was compared with the 1.7 ratio calculated in the reference [148] using Ar, 500 eV at normal incidence as sputter beam. Seah *et al.* plot the SiO_2 / Si sputter rates (nm/s) ratio for different energies using Ar sputter beam at normal incidence, the values were always close to 1 whatever the energy used. However, Py [101] obtained a sputter rate ratio of 1.35 for SiO_2 / Si using Cs^+, 500 eV at 45°.

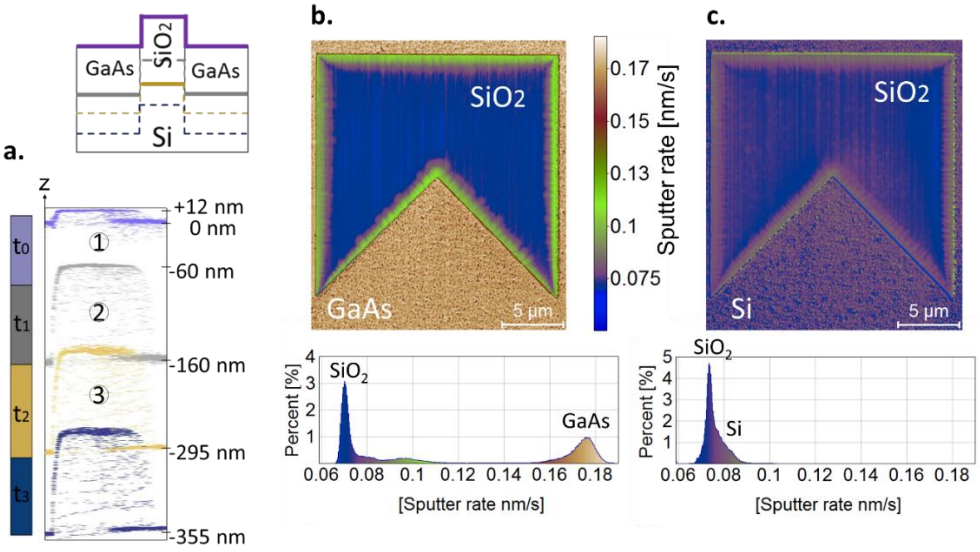

Figure III.17 *a. XZ view of the total sputtered volume of the sample delimited by the AFM images. Initial, final and intermediate sample topographies (t_0, t_1, t_2 and t_3) define the sub-volumes. The AFM topographies are shown as iso-surface in colors purple, gray, gold and blue respectively. Sputter rate map [nm/s] for b. 1st sputter cycle, and c. 2nd sputter cycle. For each map, the corresponding histogram displays the distribution of the sputter rate. The same color bar is used for both maps.*

Cette thèse est accessible à l'adresse : http://theses.insa-lyon.fr/publication/2019LYSEI121/these.pdf
© [M.A. Moreno Villavicencio], [2019], INSA Lyon, tous droits réservés

The vertical interfaces of the *pacman* structure in both maps showed different sputter rate values compared to those found at the surface outside and inside the pattern. Because of the initial topography, ion beam orientation, and the high difference in sputter rate of the materials separated by the interface, the sputtering on those regions was not the same as for the rest of the surface. The effect of vertical and horizontal interfaces, their widths and roughness in the sputtering have been largely studied [149,150] and this methodology is a window for a deeper analysis of the sputtering process.

3.5.3. TOPOGRAPHY-CORRECTED 3D TOF-SIMS VISUALIZATION AND DEPTH-PROFILE

The non-corrected stack of aligned ToF-SIMS images corresponding to SiO_2, GaAs and Si ions in red, blue and green respectively is shown in Figure III.18.a. Color discontinuity in the SiO_2 layer was due to surface charging. The SiO_2 pattern width started to be reduced when the sputtering was approaching to the SiO_2 / Si interface; this was due to a non-homogeneous ToF-SIMS sputtering in the horizontal planes, creating a deformation of the ToF-SIMS images when the end of the layer was getting closer.

The presented cross section view does not resemble to the STEM image of Figure III.10 nor to the schematic sample representation in Figure III.11. The basic ToF-SIMS reconstruction method assumed the top and the bottom of the volume as flat. The initial h_o of 14 nm between the SiO_2 pattern and the GaAs surface did not exist in this 3D visualization. At the same time, the GaAs / Si and SiO_2 / Si interfaces did not correspond to expectations (SiO_2 / Si interface higher than GaAs / Si by 9 nm). In this visualization, it was not possible to establish a voxel depth because it depends on the material sputter rates, which were not calculated.

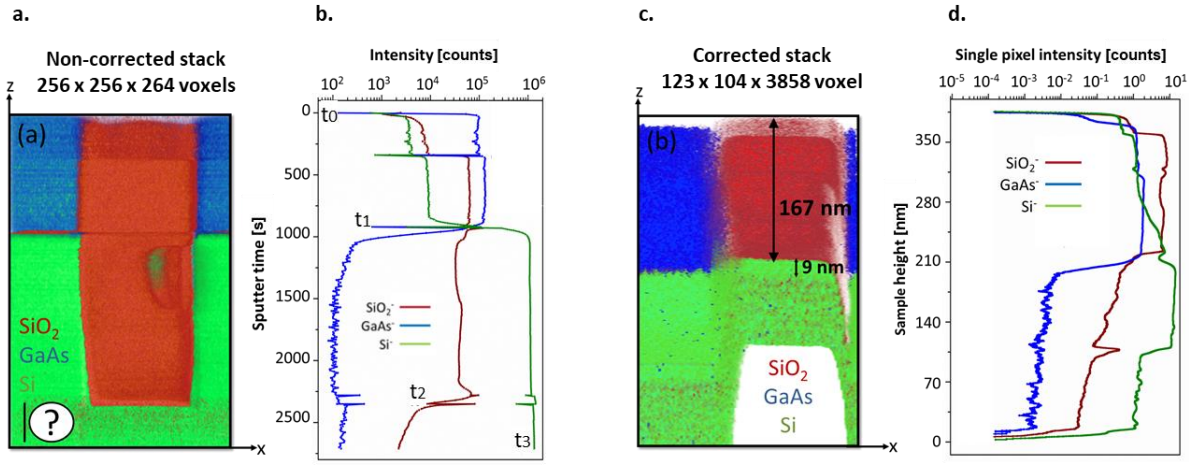

Figure III.18 *Stack of ToF-SIMS images (Si, SiO_2 and GaAs in green, red and blue, respectively). a. Front view of the non-corrected 3D volume. Z scale is not corrected. b. Raw ToF-SIMS depth-profile. c. Front view of the corrected 3D volume and d. Corrected ToF-SIMS depth-profile of Si-, SiO_2- and GaAs- secondary ions for the GaAs structure.*

Cette thèse est accessible à l'adresse : http://theses.insa-lyon.fr/publication/2019LYSEI121/these.pdf
© [M.A. Moreno Villavicencio], [2019], INSA Lyon, tous droits réservés

Figure III.18.c is a cross section of the corrected 3D chemical volume, which takes into account the initial and final sample topography. The voxel size was set at 0.1 nm that corresponds to the vertical resolution of the AFM. The empty hole observable under the silicon layer was a direct consequence of the sputter rate difference between the GaAs and the SiO_2. The initial topography of 14 nm evolved to 119 nm topography. The 167 nm SiO_2 layer and the 9 nm step between GaAs / Si and SiO_2 / Si interfaces, seen in the STEM image, were now visible.

The 3D results depend on the 2D data processing; a good chemical visualization is influenced by the alignment of the ToF-SIMS images and the topographical correction relies on the accurate correlation between the chemical stack and the 2D AFM images. Even though the alignments had an accuracy of some microns, the edge effect was shown in Figure III.18 where the edge of *pacman* structure was distorted and went down in the silicon substrate. The charge compensation issue in the SiO_2 layer and the surface oxidation when ToF-SIMS analysis was stopped were visible for both images.

The raw ToF-SIMS depth-profile and the depth-profile using the topography-corrected 3D data are shown in Figure III.18 b and d, respectively. We chose $GaAs^-$, SiO_2^- and Si^- as characteristic ions for the GaAs, SiO_2 and Si layers, respectively. Some discontinuities in the intensity curves of Figure III.18.b were visible probably due to oxidation, contamination and/or surface modification induced during the sample transfer between the instruments. The effect was insignificant compared to the sputtered depth. However, it has to be taken into account in the case where ToF-SIMS analysis has to be stopped several times or when analyzed layers are too thin.

The depth-profile corresponding to the corrected volume was made with the intensity of every voxel in z for every (x,y) column and the sample height once the sputter time was accurately converted into depth. It was not possible to identify t_1 and t_2 in the same way as for the non-corrected depth-profile because the interfaces were properly localized. The $GaAs^-$ intensity started to increase after the one of the SiO_2 evidencing the initial topography of 14 nm observed between the SiO_2 and GaAs surface. The signal was kept constant during 154 nm when the GaAs / Si interface started to appear. Regarding the SiO_2^- intensity, we could notice a gradually increase probably due to the charging effect. Its interface with the substrate was reached before the GaAs / Si one, corresponding to the 9 nm step between both interfaces observed on the STEM image (Figure III.10). As the Si^- ion was also characteristic of the SiO_2 layer, we observe a non-zero intensity since the beginning. Its maximum value was reached after the GaAs was completely sputtered. The drop of Si^- ion intensity at the end was due to the hole in the substrate observed in the section of the corrected visualization (Figure

Cette thèse est accessible à l'adresse : http://theses.insa-lyon.fr/publication/2019LYSEI121/these.pdf
© [M.A. Moreno Villavicencio], [2019], INSA Lyon, tous droits réservés

III.18.c). With this 2D ToF-SIMS profile real layer depths could be measured and confirmed with STEM measurements.

3.6. RESULTS OF THE IN-SITU TOF-SIMS AND AFM COMBINED METHODOLOGY

The ToF-SIMS / AFM combined methodology was applied on the same sample using the 3D NanoChemiscope in-situ instrument. The used instrument is located at IMEC in Belgium, one of the members of the METRO 4-3D European project.

ToF-SIMS experiments were performed using a ToF-SIMS V instrument from ION-TOF GmbH. Bi_1 primary ions were used with an incident energy of 30 keV in the fast imaging mode. This primary beam was rastered over a 50 x 50 μm^2 area with 256 x 256 $pixels^2$ scan resolution. A Cs^+ sputter beam at 1 keV energy was used as raster over a 200 x 200 μm^2 area. Spectra were obtained in negative, non-interlaced mode using an electron beam (20 eV) for charge compensation. Using a cycle time of 45 µs, the cycle of acquisition was 3 frames and 2 s sputtering with 1 s pause time between two acquisitions.

The AFM images were performed in contact mode with standard silicon cantilever (PPP-NCLR from Nanosensors) with a nominal spring constant of 48 N/m. A typical 40 x 40 μm^2 area with a 256 x 256 $pixels^2$ resolution was analyzed. The crater depths were not measured due to an instrumental problem at the time of acquisition. In normal operation, the in-situ instrument allows crater depth to be measured in-situ using the AFM tip.

The cyclical methodology was the same as the one applied ex-situ. The ToF-SIMS depth-profile was stopped four times but only two of them were used for the methodology, when the 1st and the 2nd interface GaAs / Si and SiO_2 / Si were detected. AFM images were captured at the beginning, at the end and at each interface.

The ToF-SIMS data was treated using the procedure described in section CHAPTER II.4.3 and the ToF-SIMS images were exported as .TIFF format. They were imported in ImageJ software and stacked per chemical element. In Figure III.19.a the superposition of the stack of SiO_2^- in red, $GaAs^-$ in blue and Si^- in green can be found. It is possible to observe that this non-aligned stack for the in-situ methodology is less misaligned than the non-aligned stack for the ex-situ methodology in Figure III.14.a. This is due to the utilization of the transfer system for the reposition of the sample between the instruments when the analysis is done in-situ.

The raw ToF-SIMS depth profile in Figure III.19.b was comparable with the one obtained in the ex-situ methodology, Figure III.18.b. In both graphs it was observable that the time needed to sputter the SiO_2 layer was the double of the one needed for the GaAs layer. This difference in the sputter time created the distortion of the ToF-SIMS images, giving the false idea that the SiO_2 layer was deeper than the GaAs when the reality was the opposite.

Cette thèse est accessible à l'adresse : http://theses.insa-lyon.fr/publication/2019LYSEI121/these.pdf
© [M.A. Moreno Villavicencio], [2019], INSA Lyon, tous droits réservés

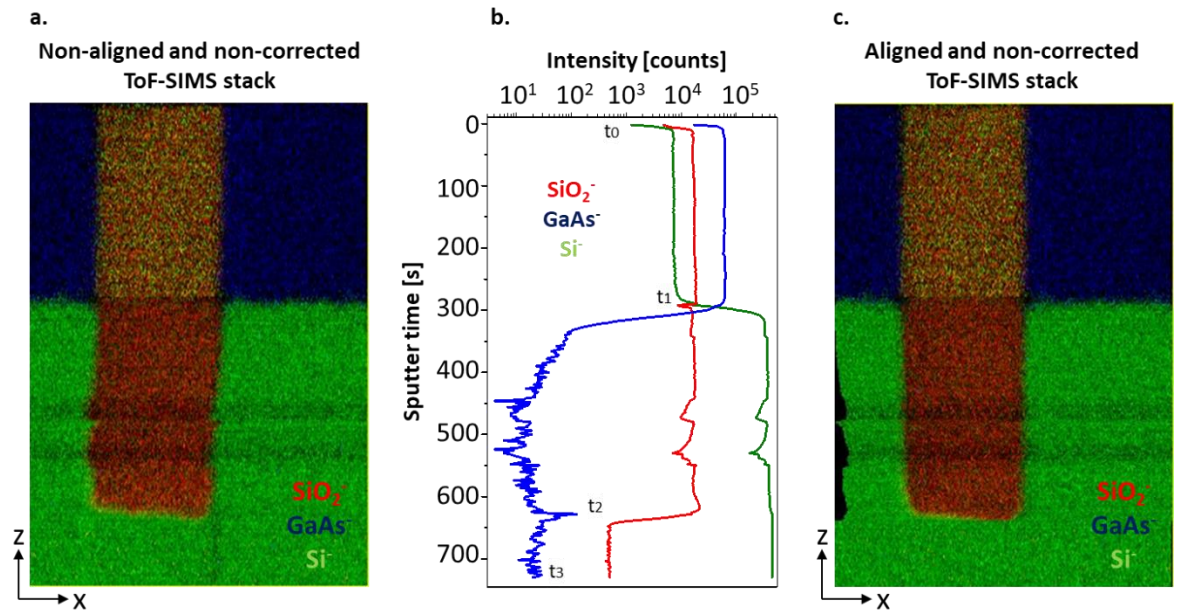

Figure III.19 *Stack of ToF-SIMS images (Si, SiO_2 and GaAs in green, red and blue, respectively). a. Front view of the non-corrected and non-aligned 3D ToF-SIMS volume. b. Raw ToF-SIMS depth-profile. c. Front view of the non-corrected aligned 3D ToF-SIMS volume.*

The oxidation and/or contamination of the sample was produced every time the ToF-SIMS analysis was stopped and the sample was transferred. It is visible in the ToF-SIMS images as a darker line in the ToF-SIMS stack but also in the depth-profile as peak in the intensity curves. Those peaks were more visible in the depth-profile of the ex-situ methodology but they were also present when it was done in-situ.

The AFM images were exported as .txt and their plane fit was done in SPIP software. However, since there were no measurements of the crater depth, the images could not been offset. The AFM images showed an initial and a final topography of 6 nm and 95 nm respectively. For the topography correction the pixel size of the ToF-SIMS images were preserved but the AFM images were binned. The ToF-SIMS stacks went through the semi-automatic alignment procedure producing the new ToF-SIMS stack of the Figure III.19.c. Once they were aligned with the AFM images, they were cropped to 205 x 205 pixels.

It was not possible to produce sputter rate maps per sputter cycle because there was no measurement of crater depths in this particular data set. However, the procedure for the topography-correction using a general sputter rate per chemical element was used. The sputter rates were calculated with the depth of the GaAs and SiO_2 layers given by the STEM image, Figure III.10, and the corresponding sputter time per layer giving values of 0.54 nm/s and 0.27 nm/s respectively.

Cette thèse est accessible à l'adresse : http://theses.insa-lyon.fr/publication/2019LYSEI121/these.pdf
© [M.A. Moreno Villavicencio], [2019], INSA Lyon, tous droits réservés

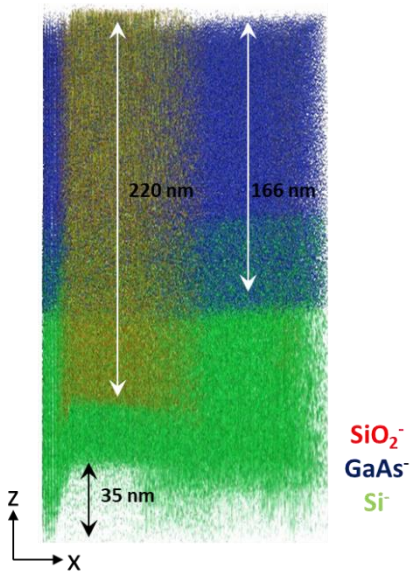

Figure III.20

Front view of the topography-corrected stack of ToF-SIMS images (Si, SiO_2 and GaAs in green, red and blue, respectively) using a common sputter rate per material.

The sputter rate for the Si substrate was calculated using a reference sample of silicon and analyzing it with the same analysis conditions. The obtained value was 0.37 nm/s. The voxel depth was set at 0.1 nm, which correspond to the vertical resolution of AFM images. The topography-corrected 3D ToF-SIMS visualization using a common sputter rate per element is in Figure III.20.

Figure III.20. shows the initial topography of 6 nm measured by the AFM. However, the visualization shows a final topography of 35 nm. The silicon was also detected from the SiO_2 layer. In the case where the Si and the SiO_2 were detected from the same pixel, the algorithm calculates an average of their sputter rates. In the case where materials of different sputter rate are being analyzed, this averaging can introduce distortions in the visualization. This explains the lack of the 9 nm step between the SiO_2 and the GaAs interfaces and that the apparent depth of SiO_2 (220 nm) instead of the real 167 nm. On the other hand, the GaAs layer shows the real depth of 166 nm because its pixels were not mixed with another selected element.

In order to perform this approach only the initial AFM image is needed. It is a fast procedure to obtain a more realistic 3D visualization of the analyzed sample and it is recommended when the system to be analyzed has numerous layers and executing an AFM image at each interface becomes a tedious procedure.

Cette thèse est accessible à l'adresse : http://theses.insa-lyon.fr/publication/2019LYSEI121/these.pdf
© [M.A. Moreno Villavicencio], [2019], INSA Lyon, tous droits réservés

Cette thèse est accessible à l'adresse : http://theses.insa-lyon.fr/publication/2019LYSEI121/these.pdf
© [M.A. Moreno Villavicencio], [2019], INSA Lyon, tous droits réservés

4. CONCLUSIONS

A ToF-SIMS / AFM combined methodology was successfully established to achieve a topography-corrected ToF-SIMS data set. It consists of an experimental section, a data treatment procedure and the visualization of the results. Through this protocol, it was possible to create a 3D visualization of the correlation of the topographical and chemical information. The surface roughness and evolution of topography during sputtering was also studied.

The methodology was tested ex-situ and in-situ on a selectively grown GaAs / SiO_2 patterned structure. The initial topography of the structure, the presence of different materials and the non-flat substrate generated a challenge for the ToF-SIMS 3D standard reconstruction.

During the in-situ and ex-situ measurements, the sample could be repositioned between the instruments with an accuracy of some microns. The advantage of the in-situ measurements is that less oxygen is absorbed on the surface and thus the profile is more continuous when the TOF-SIMS measurement is restarted. The pixel size of the dataset was upscaled or downscaled in order to obtain the same pixel size for the AFM and the ToF-SIMS images. They were then aligned using the semi-automatic MATLAB script detailed in the methodology. The AFM images were used to determine the sputter rate of present elements in order to correct the depth scale of the ToF-SIMS chemical stack and adjust the topography distortion in 3D visualization.

The two different approaches were applied for the correction of the 3D ToF-SIMS data set, the pixel-per-pixel sputter rate maps and the assumption of a general sputter rate per chemical element. In both cases, the 3D visualization resulted in similar images with the proper depth scale.

The AFM not only provides morphological information but local mechanical, electric and magnetic properties. This brings the possibility of an extension of our methodology into other fields that will be seen in the next chapters.

Cette thèse est accessible à l'adresse : http://theses.insa-lyon.fr/publication/2019LYSEI121/these.pdf
© [M.A. Moreno Villavicencio], [2019], INSA Lyon, tous droits réservés

Cette thèse est accessible à l'adresse : http://theses.insa-lyon.fr/publication/2019LYSEI121/these.pdf
© [M.A. Moreno Villavicencio], [2019], INSA Lyon, tous droits réservés

CHAPTER IV.
STUDYING THE SPUTTERING PHENOMENON OF NANOSTRUCTURES WITH TOF-SIMS AND AFM

This chapter presents the challenges when performing ToF-SIMS analysis on nanostructures. This includes analysis of nano-patterned surfaces or nano-defects that the sample may have. The combined ToF-SIMS / AFM methodology is used to illustrate the influence of the primary energy and beam orientation on the sputtering process, specifically on the sputtering yield, the lateral resolution and the topography evolution of vertical interfaces. The “geometric shadowing effect” is investigated. The chapter continues with a concrete example of problems related to the sputtering phenomenon at the nanoscale. The presented example exposes the inaccurate conclusions that the ToF-SIMS analysis may bring if the artefacts explained before are not taken into account. It also shows the utility of the AFM images to demonstrate and counteract these artefacts.

Cette thèse est accessible à l'adresse : http://theses.insa-lyon.fr/publication/2019LYSEI121/these.pdf
© [M.A. Moreno Villavicencio], [2019], INSA Lyon, tous droits réservés

Cette thèse est accessible à l'adresse : http://theses.insa-lyon.fr/publication/2019LYSEI121/these.pdf
© [M.A. Moreno Villavicencio], [2019], INSA Lyon, tous droits réservés

1. WHAT REALLY HAPPENS DURING SPUTTERING AND ANALYSIS OF NANOSTRUCTURES?

The collection of the chemical information of nanostructures is not always assured. The limitations in terms of lateral resolution and non-homogeneous sputtering are the main challenges. The typical ToF-SIMS lateral resolution is between 100 nm and a few microns. The highest resolution ToF-SIMS mode allows a lateral resolution down to 50 nm but adjusting the settings to achieve this resolution is time consuming. Thus, any chemical composition variations at length scales smaller than this resolution are not resolved.

Beside the lateral resolution, the sputtering phenomenon varies with sample composition and analysis conditions. The species of primary ions [151], angle [152,153], energy and orientation of the sputter beam as well as the impact of surface roughness and initial topography have been largely studied. From those investigations, phenomena such as ion-beam induced topography [154,155] and the artefacts listed in Figure III.1 such as extraction field modification and locally enhanced sputtering yield were detected.

The mentioned artefacts in combination with the lack of consideration of topography by the ToF-SIMS causes important distortions and shadowing issues in the ToF-SIMS images when analyzing nanostructures (Figure III.1). The observable shadowing is due to the loss of the chemical information from the dark areas. This effect tends to increase for samples with strong topography because the extraction field lines may be modified or the topography may act as a geometrical barrier [156]. For both situations, multivariate image analysis strategies have been developed as a post-analysis solution to determine the chemical information hidden in the shadows [157]. The study of deformation of extraction field lines was possible through simulations [132]. Moreover, a reduction of the shadowing was found when the extraction voltage was modified, the extraction delay was increased and when the ion beam orientation was optimized [158].

In this first part of the chapter, we have used the combined ToF-SIMS / AFM protocol, detailed in CHAPTER II, to demonstrate and minimize the effect of primary energy and primary ion beam orientation in the sputtering of 3D heterogeneous samples with initial topography and nano-patterns of different sizes.

Cette thèse est accessible à l'adresse : http://theses.insa-lyon.fr/publication/2019LYSEI121/these.pdf
© [M.A. Moreno Villavicencio], [2019], INSA Lyon, tous droits réservés

1.1. IMPACT OF THE PRIMARY ENERGY ON SPUTTER YIELD, ROUGHNESS AND DEPTH RESOLUTION

1.1.1. SAMPLE DESCRIPTION AND EXPERIMENTAL PROTOCOL

The analyzed sample was the GaAs / SiO_2 patterned structure detailed in CHAPTER III 3.1 Sample description : the SiO_2 *"squares"* patterned area shown in Figure IV.1 was selected for this study. It corresponds to five SiO_2 closed patterns with GaAs confined inside. The width of the confined GaAs goes from 250 nm up to 1.2 µm. The initial surface is not homogeneous, defects such as dislocations are seen. The initial topography between the patterns and the surface is about 40 nm but it varies within the same regions due to the non-controlled growth of GaAs. However, the SiO_2 patterns have a constant depth of about 167 nm.

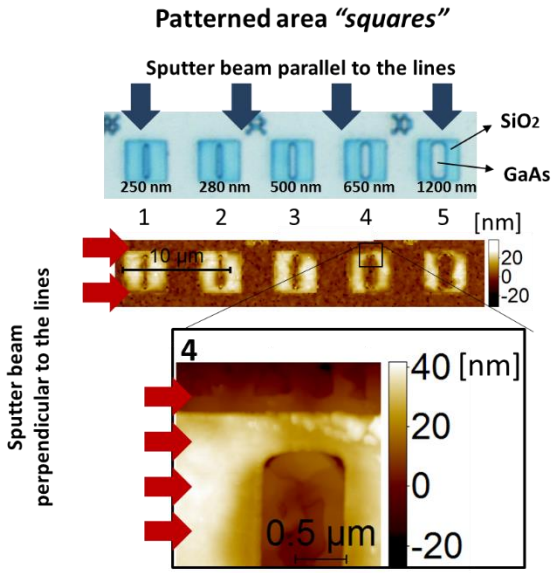

Figure IV.1

Optical and initial AFM images of the "squares" patterns, SiO_2 patterns with GaAs confined inside them. The blue arrows correspond to the parallel orientation of the sputter beam with respect to the patterns. The red arrows correspond to the perpendicular orientation of the sputter beam with respect to the patterns. The GaAs width goes from 250 nm up to 1200 nm and they are numbered from 1 to 5. An AFM image of the pattern number 4 is shown.

The region was analyzed ex-situ as followed:

(1) Initial AFM image of the region of interest.
(2) ToF-SIMS depth-profile until detecting the first interface, GaAs / Si.
(3) Crater depth measurement.
(4) Final AFM image.

Ex-situ analysis:

They were performed using Cs^+ as sputter beam at three different energies: 250 eV (8 nA), 500 eV (31 nA) and 2 keV (125 nA). The crater size was 250 x 250 µm^2. The analysis beam was Bi_3^{++} (50 keV, 0.1 nA) in the Bi-BA-image mode.

Cette thèse est accessible à l'adresse : http://theses.insa-lyon.fr/publication/2019LYSEI121/these.pdf
© [M.A. Moreno Villavicencio], [2019], INSA Lyon, tous droits réservés

It was rastered over a 50 x 50 μm^2 area with 512 x 512 pixels. Spectra were obtained in negative, non-interlaced mode using an electron beam (20 eV) for charge compensation and a cycle time of 50 µs.

Each study was carried out in two different beam orientations: parallel and perpendicular to the SiO_2 pattern (sputter beam coming in the direction of the blue and red arrows, Figure IV.1, respectively). For the 2 keV sputter energy, the methodology was additionally performed with 360° sample rotation.

The AFM images were obtained in Tapping mode. A standard silicon cantilever (TAP300Al-G from Budget Sensors) with a nominal spring constant of 40 N/m was used. Two different images were captured: one of the entire pattern area (35 x 23 μm^2 with 512 x 336 pixels) and a 2 x 2 μm^2 (128 x 128 pixel) image of the fourth pattern (Figure IV.1) and images of regions outside the Bi raster area of 20 x 10 μm^2 with 512 x 256 pixel resolution. The crater depth was measured by optical surface profilometry (3D Plu neox by Sensofar) in confocal mode.

1.1.2. RESULTS

The impact of the primary ions on the sample surface involves elastic collisions that can be explained with the three models previously detailed (CHAPTER II.1.2): knock-on, linear cascade and spike. The sputtering process requires that the energy transferred to the surface in the collision is enough to break the atomic bonds. The influence of the primary energy in the sputtering process is shown in Figure IV.2.a, b and c.

The *squares* patterned area was sputtered until the GaAs / Si interface with the primary beam oriented perpendicular to the patterns. Figure IV.2.a illustrates the ToF-SIMS depth-profiles at primary energies of 250 eV (green curve), 500 eV (blue curve) and 2 keV (black curve). If the interface is considered where the GaAs and Si curves cross, the primary ion dose needed to sputter the sample until the first interface was three times higher at 250 eV than at 500 keV, and six times higher at 250 eV than at 2 keV. The ion dose depends directly on the ion current, which is influenced by the primary ion energy. From the ion dose values and the crater depth measurements, the sputter yield for each energy was calculated. Error bars were calculated using the precision of the ToF-SIMS current measurement and the depth resolution of the optical profilometer. The sputter yield is proportional to the primary energy but not necessarily in a linear fashion [159–161]. This proportionality is seen in Figure IV.2.b where the sputter yield of GaAs indicates that this layer was sputtered 9 times faster at 2 keV than at 250 eV and 2.5 times faster than at 500 eV. Indeed, in contrast to the depth profiles at 250 eV and 500 eV where the GaAs signal is constant enough to identify a well-defined GaAs layer and interface, the profile obtained at 2 keV showed a rapid diminution of the GaAs intensity because of the elevated sputter rate at this primary energy.

Cette thèse est accessible à l'adresse : http://theses.insa-lyon.fr/publication/2019LYSEI121/these.pdf
© [M.A. Moreno Villavicencio], [2019], INSA Lyon, tous droits réservés

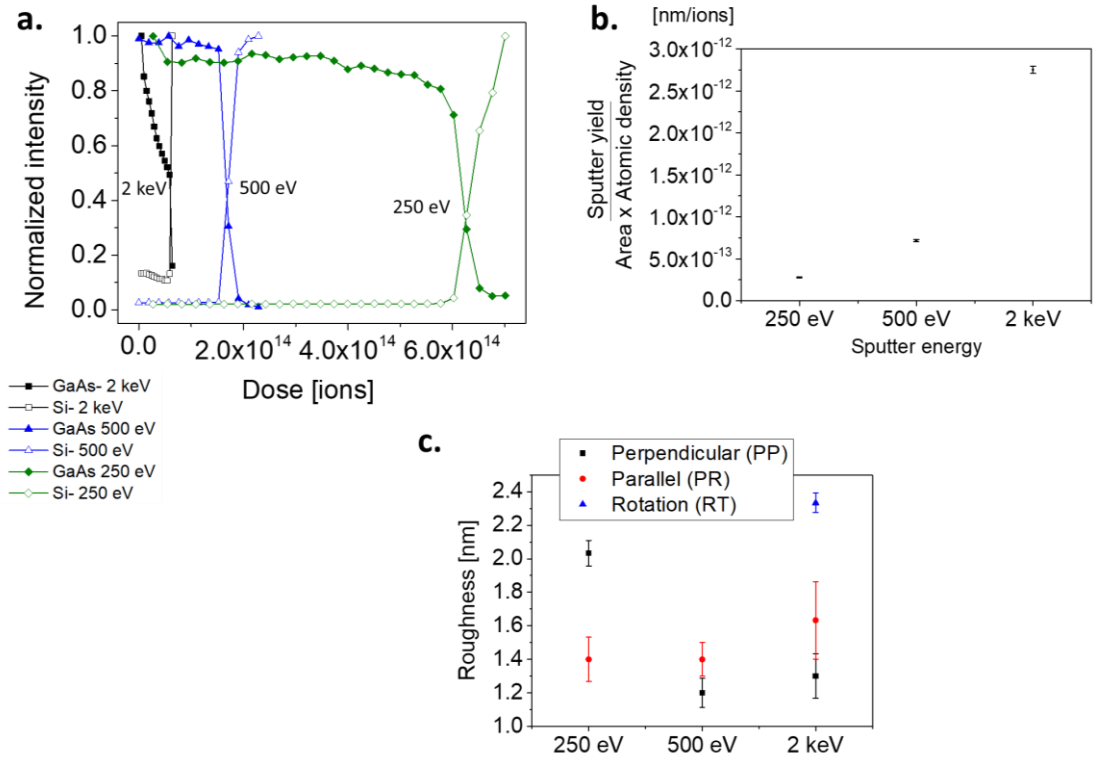

Figure IV.2 *Influence of the primary energy on the sputter yield and surface roughness. a. ToF-SIMS depth-profile until the first interface GaAs / Si at 2 keV (in black), 500 eV (in blue) and 250 eV (in green). The sputter beam was aligned parallel to the patterns of the sample. b. Sputter yield as a function of the sputter energy calculated with the ion dose of the depth profiles. c. Roughness of the surface at the first interface GaAs / Si after sputtering at 250 eV, 500 eV and 2 keV when the beam was oriented parallel (PR), perpendicular (PP) and when the sample was rotating (RT).*

The surface roughness values of the GaAs surface measured after ToF-SIMS sputtering at 250 eV, 500 eV and 2 keV are shown in Figure IV.2.c. The primary beam was oriented perpendicular (PP, black curve), parallel (PR, red curve) and fast rotation (RT, blue curve). The surface roughness measured for a primary beam oriented parallel to the patterns is comparable for the three energies. For 500 eV and 2 keV the roughness values at perpendicular and parallel orientation were comparable. Gorbenko *et al.* [162] found that the effect of the ion beam orientation on the ion-beam-induced morphology was minimized with a parallel alignment of the ion beam to pattern lines when sputtering with O_2^+ but as in our case, no improvement was seen for Cs^+ sputtering at high energy.

The efficiency of 250 eV primary beam has been questioned to sputter inorganic materials. The energy may not be high enough to remove the analyzed surface, causing bismuth accumulation and in turn an elevated surface roughness [97].

Cette thèse est accessible à l'adresse : http://theses.insa-lyon.fr/publication/2019LYSEI121/these.pdf
© [M.A. Moreno Villavicencio], [2019], INSA Lyon, tous droits réservés

The values presented in the graph were compared with roughness measured at areas of the crater with no contribution of bismuth. The roughness was found to be similar at every orientation and energy except for the perpendicular orientation at 250 eV where the roughness was measured at 1.6 nm instead of 2.1 nm. At this orientation, the roughness of the analyzed area at 250 eV is 50 % higher than at 500 eV and 2 keV. An absolute explanation of this behavior is difficult to provide. A hypothesis is that the shadowing effect in the perpendicular orientation inhibits a homogeneous sputtering thus, a higher number of bismuth ions may be implanted in the surface and they may not be completely removed by the sputter beam. The bismuth accumulation creates then an elevated surface roughness. On the other hand, the beam at low energy is more instable and not necessary in a round shape. The orientation change may cause a difference of the angle at which the beam hits the surface, thus influencing in the roughness formation.

Diverse studies have demonstrated the negative impact of the surface roughness on: (i) sputtering yield [163] and (ii) topography evolution [164]. In order to dismiss these unwanted phenomena, some research groups have proposed the rotation of the sample while sputtering [41,165,166]. Their results were promising in the reduction of the topography induced by the sputtering, in the improvement of the depth resolution and in the homogenization of the sputtering yield. Despite the results found in the literature, the roughness value when rotating the *squares* sample at 2 keV was almost double compared with single ion beam orientation. This effect, also seen by Gorbenko [82] may be due to the high reactivity of Cs^+ ions on the surface forming agglomerations. More information about the Cs^+ aggregates found in our experiments is addressed in the appendix A. Another possible explanation for the high roughness could arise from a non-homogenous sputtering during the rotation. The pattern to be analyzed should be located exactly at the axis of rotation and this is not a straightforward procedure when analyzing nano-patterns.

The variation of the primary energy affected the sputter yield, the roughness and the depth resolution. The 2 keV energy improved the sputter yield and the surface roughness. The 250 eV primary beam produced the lowest sputter yield and the highest surface roughness if the rotation results are excluded. Finally, primary beams with energies of 500 eV showed the best compromise between the damage and the material removal of this inorganic sample.

The sputtering yield and surface roughness are not the only parameters to consider when analyzing nano-structures. The lateral resolution, shadowing effect and interface deformation should also be optimized.

Cette thèse est accessible à l'adresse : http://theses.insa-lyon.fr/publication/2019LYSEI121/these.pdf
© [M.A. Moreno Villavicencio], [2019], INSA Lyon, tous droits réservés

1.2. IMPACT OF THE PRIMARY BEAM ORIENTATION ON THE LATERAL RESOLUTION, SHADOWING EFFECT AND TOPOGRAPHY EVOLUTION OF THE VERTICAL INTERFACES

1.2.1. SAMPLE DESCRIPTION AND EXPERIMENTAL PROTOCOL

For this section, two patterned areas were analyzed from the same GaAs / SiO_2 patterned structure detailed in CHAPTER III 3.1 Sample description: they correspond to the *squares* area previously described and the *lines* area of Figure IV.3. This last patterned area consists of SiO_2 "infinite" (300 µm) lines of about 100 nm wide separated 120 nm between them. These dimensions cannot be seen in the initial image due to the inhomogeneous growth of the GaAs between and over the lines. These lines are hard to see at the beginning because of the irregular topography that the dislocations and the GaAs growth created.

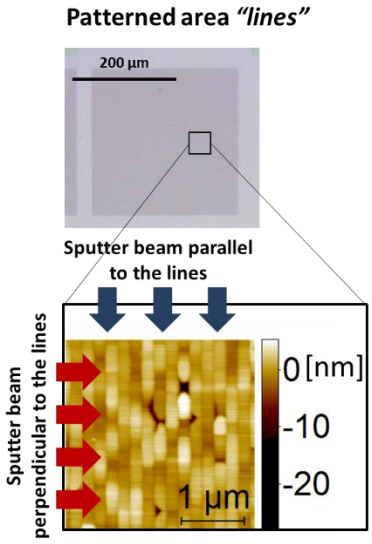

Figure IV.3

Optical and AFM initial images of the analyzed area, SiO_2 lines of about 100 nm separated by 120 nm wide GaAs. The blue arrows correspond to the parallel orientation of the sputter beam with respect to the patterns. The red arrows correspond to the perpendicular orientation of the sputter beam with respect to the patterns.

The optical and AFM initial images of this area are shown in Figure IV.3. It was analyzed ex-situ as followed:

(1) Initial AFM image of the region of interest.
(2) ToF-SIMS bevel crater where the substrate and the top layer of GaAs and SiO_2 are simultaneously exposed.
(3) ToF-SIMS high-resolution 2D analysis.
(4) Crater depth measurement.
(5) Final AFM image.

This area was analyzed through the bevel crater approach. A bevel crater was created with the sputter beam parallel and perpendicular to the lines. The Cs^+ (1 keV, 62 nA) ion beam was rastered over an area of 300 x 300 μm^2 with 128 x 128 pixels. The dose varied from 0% to 100% from right to left.

Cette thèse est accessible à l'adresse : http://theses.insa-lyon.fr/publication/2019LYSEI121/these.pdf
© [M.A. Moreno Villavicencio], [2019], INSA Lyon, tous droits réservés

The milling duration was 3.41 s using two milling passes per scan and a dwell time per pixel of 9 ms. A 2D analysis over 5 x 5 μm^2 (1024 x 1024 pixels) of the crater surface was then performed using Bi_3^{++} (60 keV) in the imaging ultimate mode.

AFM images of 7 x 7 μm^2 with 512 x 512 pixels were obtained in Tapping mode. A standard silicon cantilever (OTESPA – R3 from Bruker) with a nominal spring constant of 26 N/m was used. The images were performed scanning at 0 and 90 degrees to study the tip convolution.

1.2.2. RESULTS

The spatial resolution of ToF-SIMS is vital to guarantee a proper analysis of nano-patterns. A linescan of an abrupt feature in a chemical image can be used to measure the lateral resolution. Figure IV.4.a presents the overlay of the ToF-SIMS images corresponding to SiO_2^- (in green) and $GaAs^-$ (in red). They were obtained during the sputtering of the "*squares*" area at 2 keV. The existing patterns were numbered from 1 to 5 starting from the narrowest confined GaAs.

Figure IV.4.b shows the line scans with the normalized intensity of the ToF-SIMS images that correspond to the oxygen ion, characteristic ion of the SiO_2 layer. The ToF-SIMS images were obtained after sputtering the sample with the ion beam oriented perpendicular (PP), parallel (PR) and with 360° rotation (RT). The five patterns are numbered in the profiles.

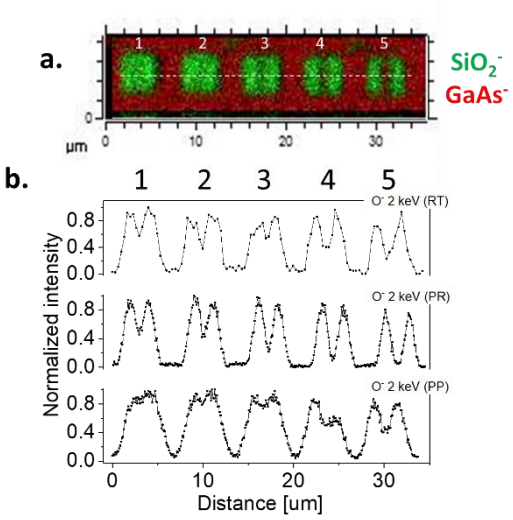

c. Length of the GaAs confined in SiO_2 patterns measured by:

	1	2	3	4	5
AFM ± 137 nm	250 nm	280 nm	500 nm	650 nm	1200 nm
ToF-SIMS Linescan (RT) ± 195 nm	800 nm	770 nm	760 nm	1570 nm	1390 nm
ToF-SIMS Linescan (PR) ± 195 nm	840 nm	800 nm	680 nm	1140 nm	1220 nm
ToF-SIMS Linescan (PP) ± 195 nm	-	650 nm	1060 nm	500 nm	1160 nm

Figure IV.4

Influence of the primary beam orientation on the lateral resolution of ToF-SIMS imaging. a. Overlay of the sum of five ToF-SIMS images corresponding to SiO_2 and GaAs, in green and red respectively. They were obtained after depth-profiling the "squares" area until the GaAs / Si interface at 2 keV. b. ToF-SIMS line scans corresponding to the white section shown in the ToF-SIMS images. The line scans were obtained from the analysis performed with the primary beam parallel (PR) and perpendicular (PP) to the patterns. c. Length of the GaAs confined inside the SiO_2 patterns measured from the AFM profile and ToF-SIMS line scans.

Cette thèse est accessible à l'adresse : http://theses.insa-lyon.fr/publication/2019LYSEI121/these.pdf
© [M.A. Moreno Villavicencio], [2019], INSA Lyon, tous droits réservés

When the ion beam was oriented perpendicular to the SiO_2 patterns, the oxygen was detected inside the confined area of patterns 1 to 3, instead of detecting the GaAs characteristic ions. The topography of the patterns acted as a geometrical barrier inhibiting the impact of the primary ions inside the confined material. For the wider confined GaAs areas (patterns 4 and 5), the barrier was not sufficient to block the primary ions and there was a slight diminution of the oxygen signal coming from the GaAs regions inside the patterns. The geometrical constraint decreased for the ion beam in the parallel orientation. When the sample was rotated in order to determine any improvement on the sputtering of confined regions, there was a diminution of oxygen signal in the confined areas within the SiO_2 patterns but less defined than that for parallel orientation.

The lateral resolution was calculated to be about 450 nm, 800 nm and 1000 nm for parallel, rotation and perpendicular orientation respectively. The values were obtained using the line scan option of SurfaceLab. The widths of the confined GaAs areas were estimated from the line scans for each orientation. The error associated to each measurement corresponds to the twice the pixel size of the image. They were then compared in Figure IV.4.c with the widths measured by AFM. The values obtained from pattern 5 corresponded, for all orientations, to about 85 % of the one measured by the AFM. This confined area was 1200 nm wide, being the only one bigger than the lateral resolution measured for each analysis conditions. The values measured for the other patterns gave an overestimation of the width because of the limitation in lateral resolution.

The lack of lateral resolution in the perpendicular orientation was a result of the shadowing effect. The barrier caused by the topography inhibited the sputtering. AFM profiles were a suitable tool to compare the sputtered depths along the confined and the bulk surfaces. Figure IV.5.a compares the topography profiles of the *squares* area after sputtering at 250 eV with the ion beam perpendicular (PP, in black) and parallel (PR, in black). The sputtered depth for each confined area was calculated using the depth of the blue point as a reference. This point is located at a non-confined area, thus its sputtering is not limited by the shadowing effect. Figure IV.5.b presents the obtained values. The sputtered depth values and their respective error bars were obtained using the histogram of AFM data and the FWHM of its peak values, respectively. The number of data points within the narrower confined areas were not sufficient to provide an accurate FWHM value, this is the reason why the error bars for patterns 1 and 2 are larger.

The intensification of the shadowing effect with the perpendicular orientation meant that the final depths of the narrower confined GaAs areas in patterns 1 and 2 were not the same as in the rest of confined area or as in the bulk. This difference is seen in the black AFM profile in Figure IV.5.a but also when comparing the relative sputtered depth values. There was a lack of about 10 – 15 nm of sputtering inside the patterns 1 and 2 compared to the reference point.

Cette thèse est accessible à l'adresse : http://theses.insa-lyon.fr/publication/2019LYSEI121/these.pdf
© [M.A. Moreno Villavicencio], [2019], INSA Lyon, tous droits réservés

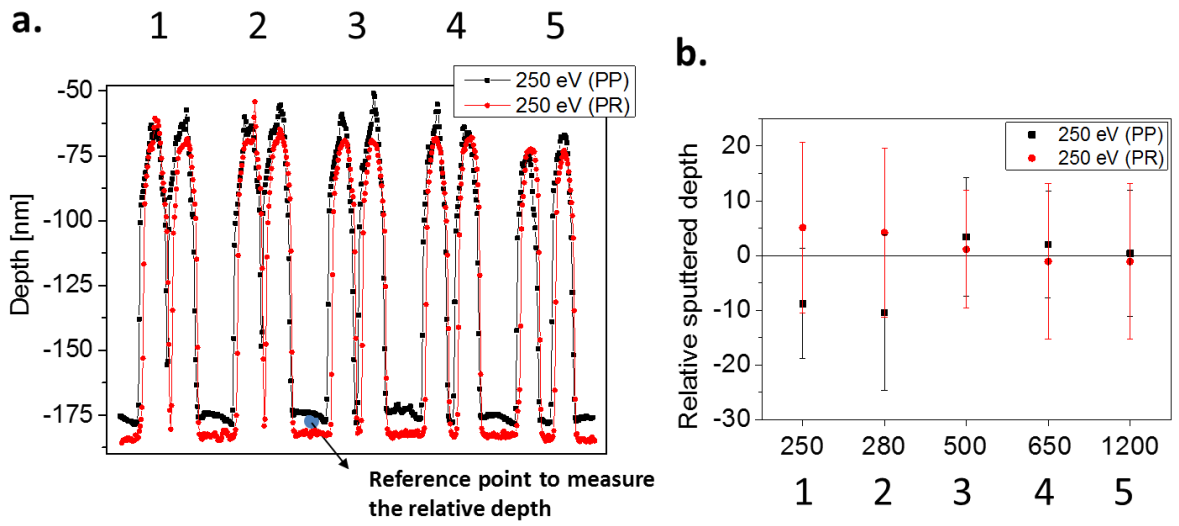

Figure IV.5 *Influence of the beam orientation on the sputtering rate of the sample. a. AFM profiles were extracted from the white section shown in Figure IV.4a for the ToF-SIMS linescans. The measurements were done after ToF-SIMS analysis with 250 eV as primary energy and two beam orientations, perpendicular and parallel to the sample patterns (black and red curve respectively). b. Sputtered depth values of the confined areas using the depth of the blue point of the AFM profiles as reference.*

The critical size for the shadowing effect in perpendicular orientation was set at 500 nm because the sputtering of the confined areas wider than that number was not delayed or affected. Simulations need to be done in order to calculate the theoretical value of the critical size. Moreover, the following factors should be considered:

(i) The primary beam has an angle of 45 degrees meaning that the shadow length would be at least the height of the barrier.

(ii) The shadow dimension changes during the sputtering because of the topography evolution.

(iii) The sputter barrier increases faster because the GaAs is sputtered twice faster than the SiO_2. This expands the shadowing effect.

The ion beam oriented parallel to the patterns line did not cause any difference in the depths of the confined areas. Recommendations of orienting the ion beam parallel to pattern lines to reduce the geometric shadowing and the deformation of the extraction lines were exposed in [158].

The ion beam orientation not only produced a delay in the sputtering but also modified the vertical interfaces of the sample. This effect was studied with the AFM profiles after (i) depth-profiling the *"squares"* area at 500 eV and (ii) creating a bevel crater of the *lines* area.

Cette thèse est accessible à l'adresse : http://theses.insa-lyon.fr/publication/2019LYSEI121/these.pdf
© [M.A. Moreno Villavicencio], [2019], INSA Lyon, tous droits réservés

The profiles of Figure IV.6.a correspond to the red section shown in the AFM image, pattern number 4. They were obtained after sputtering the *squares* area with parallel (PR in red) and perpendicular (PP in black) orientation. Stewart and Thompson describe in [167] a theoretical model to predict the modification of the topography by the variation of the incident angle. The predictions were based on the maximum sputtering yield, which is in turn dependent on the angle of incidence. This model gets more complex when the analyzed sample is heterogeneous; two factors need to be considered: the variation of incidence angle due to the topography and the material dependant sputter yield.

For perpendicular orientation, the variation of incident angle along and between the vertical interfaces of the patterns modified the local sputtering yield. There is also the fact that the ion beam did not bombard the left interface in its totality because it is located in the shadow of the protruding material. The difficulty of predicting the topography evolution because of those phenomena precluded the alignment of parallel and perpendicular profiles to quantify their variation.

However, remarkable differences are seen: (i) for parallel orientation the bottom of the profiles that correspond to the confined GaAs area is wider; (ii) for perpendicular orientation the right interface, receiving directly the impact of the primary ions, is less inclined than the left interface.

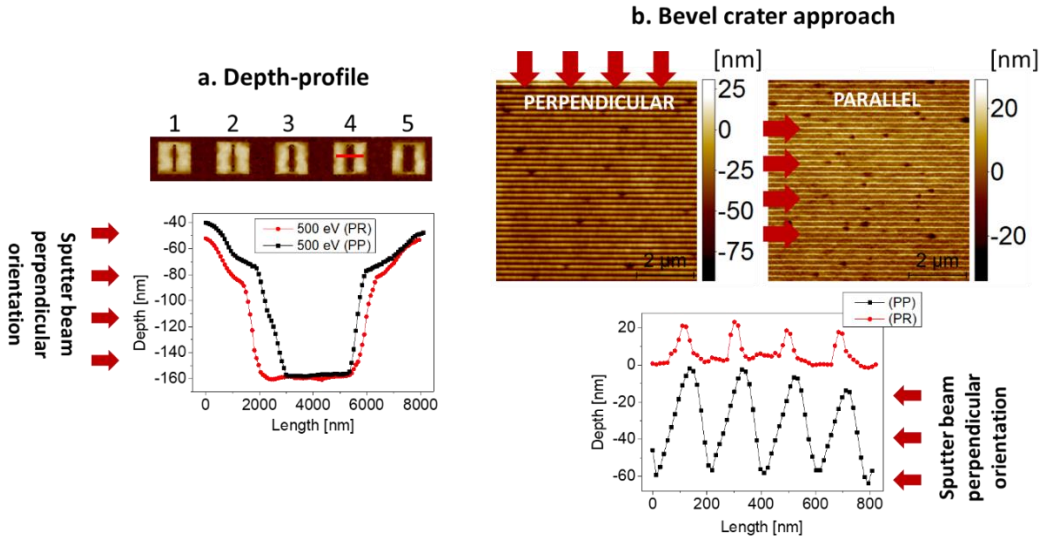

Figure IV.6 *Influence of the primary beam orientation on the topography evolution at the interfaces. a. AFM profiles of the red line section obtained after depth-profiling the sample with the primary beam oriented perpendicular and parallel to the patterns, black and red curve respectively. b. AFM profiles of four pattern lines obtained after sputtering the sample with the bevel crater approach using the sputter beam perpendicular and parallel to the lines, shown in black and red respectively. The red arrows indicate the position from which the sputter beam came.*

Cette thèse est accessible à l'adresse : http://theses.insa-lyon.fr/publication/2019LYSEI121/these.pdf
© [M.A. Moreno Villavicencio], [2019], INSA Lyon, tous droits réservés

The slopes for right and left interfaces are about 0.12 for parallel orientation while for perpendicular orientation are 0.15 and 0.07 respectively. Sigmund [168] highlighted the apparition of grooves around the bottom of elevations, as the one in the bottom left for the parallel orientation. The formation of those grooves arose from the tendency of areas near the valley to be sputtered faster than the top.

The topography evolution of vertical interfaces was also noticed when performing the bevel crater approach. The bevel crater was created with the dose varying along the line orientation to ignore the sputter yield enhancement, which is a product of the ion dose variation. The AFM profiles obtained after sputtering the *lines* area with the ion beam perpendicular and parallel to the SiO_2 lines are in Figure IV.6.b as black and red curves, respectively. The sputtered depths are different between the profiles because they depend on the part of the bevel crater from where they were extracted. For the perpendicular orientation, part of the left interfaces were under the shades of the incident angle and vertical interfaces with non-similar inclinations were produced. Slopes of 0.87 and 0.59 for the right and left interface of the lines were measured. In contrast, the vertical interfaces of the SiO_2 lines showed a similar inclination of 1.09 of slope when the ion beam was oriented parallel to them. The GaAs surface between the lines is observable uniquely for the parallel orientation. The profiles of the perpendicular orientation provided the wrong idea of continuous line patterns.

It is important to specify that the tip geometry does not interfere with dimensions measured from the AFM topography profiles. Profiles captured using zero and 90° degrees scan angles were compared to confirm this. Those profiles together with further explanation of this phenomenon can be seen in the appendix A.2 Tip convolution.

It was shown so far that the sputtering of defined nano-patterns could be optimized by the ion beam orientation and the sputtering energy. However, how can we interpret the sputtering artefacts when there are no defined nano-patterns but non-homogeneous nano-defects?

Cette thèse est accessible à l'adresse : http://theses.insa-lyon.fr/publication/2019LYSEI121/these.pdf
© [M.A. Moreno Villavicencio], [2019], INSA Lyon, tous droits réservés

Cette thèse est accessible à l'adresse : http://theses.insa-lyon.fr/publication/2019LYSEI121/these.pdf
© [M.A. Moreno Villavicencio], [2019], INSA Lyon, tous droits réservés

2. CHEMICAL ANALYSIS OF NON-STRUCTURED NANO-AREAS

The artefacts found in the sputtering of nano-patterns may lead to an incorrect interpretation of the obtained 3D ToF-SIMS data. Furthermore, the problem is more accurate for non-structured nano-areas where the analysis conditions cannot be optimized to reduce these artefacts. In these cases, AFM can be used as a tool to study the existence of data distortion and avoid wrong conclusions about the sample. We propose to illustrate this effect using an AlN / GaN heterostructure. Experiments were carried out ex-situ at CEA.

2.1. SAMPLE DESCRIPTION AND PRELIMINARY ANALYSIS

An AlN / GaN heterostructure was grown by MOCVD on a single 200 mm silicon (1 1 1) wafer. A 10-nm-passivation layer of SiN was grown in-situ over the AlGaN layers to protect the surface from degradation and to stabilize them. The thickness of the AlGaN layers were 1.6 µm for the GaN and about 25 nm for the AlN. A schematic of the sample is shown in Figure IV.7.a. More information about the fabrication process can be found in [169].

The top view optical image of the sample in Figure IV.7.b showed cracks in the entire SiN surface. The formation of these cracks is assumed to be due to the AlN thickness. The 20 nm-layer exceeds the critical thickness that avoids dislocations forming. Indeed, it is probable that the high lattice mismatch between AlN and GaN (2.4 % [170]) was counteracted by the relaxation of the material through the crack formation. It is also possible that a thermal phenomenon could participate in the origin of the cracks.

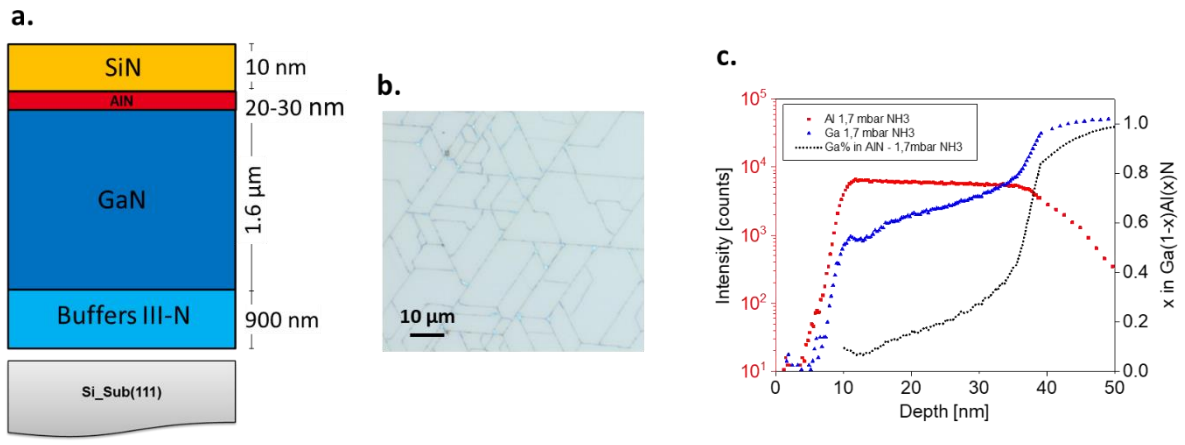

Figure IV.7 *a. Schematic and b. top view optical image of the AlN / GaN heterostructure. c. Previous SIMS depth-profile of the sample, extracted from [169].*

Cette thèse est accessible à l'adresse : http://theses.insa-lyon.fr/publication/2019LYSEI121/these.pdf
© [M.A. Moreno Villavicencio], [2019], INSA Lyon, tous droits réservés

The sample was depth-profiled using standard SIMS. The obtained depth profiles are shown in Figure IV.7.c [169]. The profiles show an increment of gallium and aluminum intensities after respectively 5 nm and 7 nm of sputtering. No defined AlN / GaN interface is seen at the expected depth of about 35 nm. The presence of gallium within the AlN layer implied an unexpected gallium diffusion of about 30 nm.

The origin of this diffusion was unknown and the cracks of the sample hampered further analysis of the SIMS depth-profile. In fact, the presence of gallium within the AlN layer could mean a simple detection of gallium merely through the cracks giving a wrong impression of gallium diffusion. The need of high-resolution chemical imaging from where the chemical information at the grains and at the cracks could be separated emerged. Advanced chemical characterization was required to provide a proper conclusion.

2.2. ADVANCED CHARACTERIZATION OF NANO-CRACKS

The sample was depth-profiled using ToF-SIMS ultimate imaging mode from where high-resolution ToF-SIMS images were obtained. An area of 50 µm x 50 µm of the sample was analyzed using Bi_3^{++} at 60 keV (0.4 nA). The scanned area consisted on 512 x 512 pixels that were impacted using 30 shots per pixel. A 1 keV (56 nA) Cs^+ sputter beam was rastered over an area of 300 µm x 300 µm to remove the already analyzed surface. The analysis was performed in non-interlaced mode using 50 µs cycle time, 1 analysis frame, 20 s of sputtering and 10 s of pause time.

Through the creation of two regions-of-interest (ROI) corresponding respectively to pixels extracted from the cracks and from the grains, the chemical information detected at the cracks and at the grains could be segmented. The analysis of the cracks was limited by the lateral resolution. Indeed, the size of cracks is smaller than the beam. Thus, there may be a contribution of the signal from the grains in the ROI corresponding to the cracks. The depth-profiles of these ROIs are in Figure IV.8.a as a continuous line for the grains and dashed line for the cracks. The SiN^-, AlN^- and $^{71}GaN^-$ ions were chosen to represent the three upper layers of the sample. The low mass resolution of the imaging mode created an interference of the m/z = 83 and m/z = 85 corresponding to $^{69}GaN^-$ and $^{71}GaN^-$ with the peaks of Si_2Al^- and Si_3H^- respectively. For each ROI, the SiN^-, AlN^- and $^{71}GaN^-$ are respectively traced in yellow, red and blue.

The profiles show two interfaces, the SiN / AlN reached after 100 s of sputtering and the AlN / GaN reached after 420 s of sputtering. The unexpected high intensity of $^{71}GaN^-$ in the SiN layer is due to the influence of Si_3H^- ions in that peak, explaining the behavior of that part of the curve being the same as the one observed for SiN^-. Once the first interface was reached and the contribution of Si_3H^- ions was insignificant, the intensity of detected 71GaN^- increased showing a gradient of gallium within the AlN layer.

Cette thèse est accessible à l'adresse : http://theses.insa-lyon.fr/publication/2019LYSEI121/these.pdf
© [M.A. Moreno Villavicencio], [2019], INSA Lyon, tous droits réservés

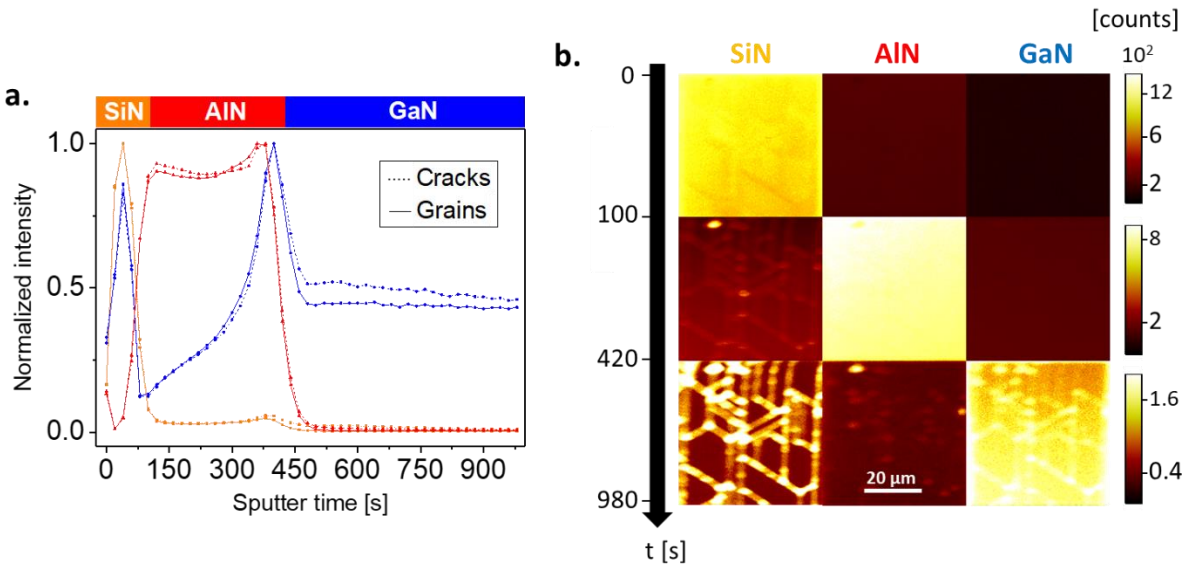

Figure IV.8 *High lateral resolution 3D ToF-SIMS analysis of the AlN / GaN heterostructure. a. ToF-SIMS depth-profile of the cracks and the grains with SiN^-, AlN^- and $^{71}GaN^-$ ions in yellow, red and blue respectively. They were obtained after 983 s of sputtering with Cs 1 keV. b. Evolution in time of the ToF-SIMS images corresponding to SiN^-, AlN^- and $^{71}GaN^-$ ions. They represent an area of 50 x 50 µm² (512 x 512 pixels) analyzed with Bi_3^{++} 60 keV. The images were 4 x 4 binned to enhance the intensity.*

The gallium diffusion previously detected by the SIMS analysis is confirmed at the grains and at the cracks. Further investigation of the depth-profiles revealed a slight delay of the curves representing the cracks. Indeed, at the cracks the signal of SiN^- never decreased to zero, the GaN^- diffusion was slightly shifted to the right and once the GaN layer was reached, the $^{71}GaN^-$ intensity was higher than at the grains. Considering the artefacts when sputtering nano-structures the possibility of a geometric shadowing effect influencing the delay of the intensities in the depth-profile emerged.

Figure IV.8.b shows the evolution in time of the ToF-SIMS images corresponding to SiN^-, AlN^- and $^{71}GaN^-$ ions. The image shown per ion represents the sum of all the images obtained for that ion in the corresponding sputter time range. The time ranges correspond to the sputter time needed to reach the interfaces, 100 s for the SiN / AlN and 420 s for the AlN / GaN. The images have been four-pixel-binned in order to increase their contrast and they have the same color bar per sputter time range to facilitate the comparison.

The first sputter range, from 0 to 100 s, corresponds to the sputtering of the SiN layer. The SiN^- image shows the cracks in a darker contrast. The gallium diffusion within the AlN layer is seen in the second sputter range, from 100 s to 420 s. The $^{71}GaN^-$ image is not entirely black. The chemical image of the AlN^- has the highest intensity but SiN^- ions are still detected from the cracks.

Cette thèse est accessible à l'adresse : http://theses.insa-lyon.fr/publication/2019LYSEI121/these.pdf
© [M.A. Moreno Villavicencio], [2019], INSA Lyon, tous droits réservés

Once the AlN layer is completely sputtered at 420 s, the chemical image corresponding to $^{71}GaN^-$ shows the highest intensity. At this moment, secondary ions of SiN^-, AlN^- and $^{71}GaN^-$ are detected from the cracks. This fact together with the low SiN^- intensity coming from the cracks in the first sputter range made us consider a geometric shadowing effect affecting the sputtering at the cracks.

A 3D chemical visualization of the sample is shown in Figure IV.9. This visualization was created by stacking the obtained ToF-SIMS images without any correction of the initial or evolved topography. It represents the SiN, AlN and GaN layers in yellow, red and blue respectively. Contemplating exclusively this 3D chemical visualization, the ToF-SIMS analysis lead to the conclusion of cracks going deeper in the GaAs layer and that SiN and AlN filled them. This fact is better seen in Figure IV.9.b where the cross section allows to visualize only the GaN layer with the GaN ions in blue and SiN ions in yellow.

However, an accurate interpretation of the depth profile and ToF-SIMS images of this AlN / GaN heterostructure requires some considerations:

- The lateral resolution of this ToF-SIMS analysis, determined at several tens of nanometers, does not assure a proper detection of the chemical information at the cracks. Indeed, the separation of the cracks and the grains in two different ROIs was not a straightforward procedure and thus, the reliability of the depth profile is not certain.
- In the same way, three layers of different materials may signify three different sputter rates not taken into account in the depth profile observed in Figure IV.8.

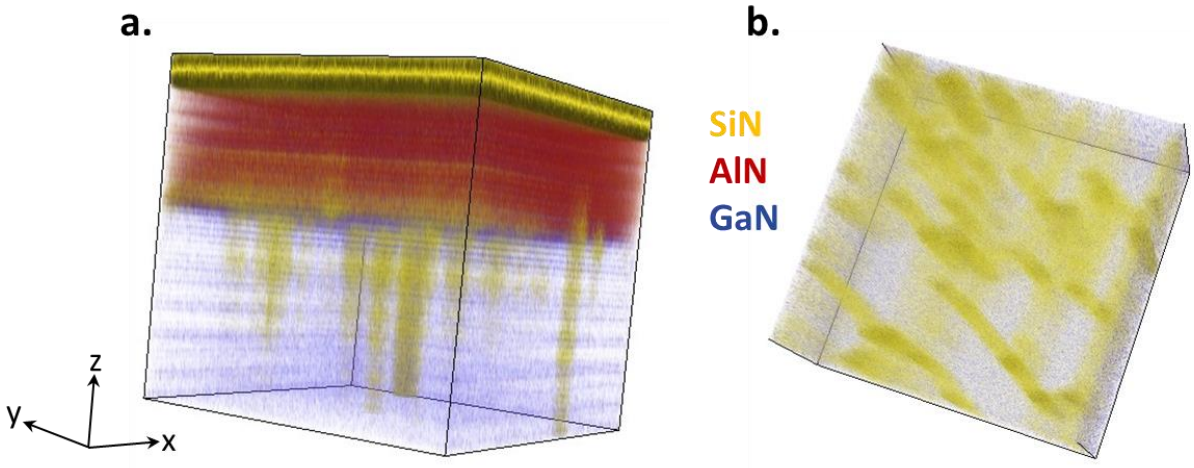

Figure IV.9 *a. 3D non-corrected visualization of the ToF-SIMS data. The SiN^-, AlN^- and $^{71}GaN^-$ ions are shown in yellow, red and blue respectively. The dimensions of the visualization do not correspond to the real one of the sample. b. Cross section in the xy plane at the GaN layer.*

Cette thèse est accessible à l'adresse : http://theses.insa-lyon.fr/publication/2019LYSEI121/these.pdf
© [M.A. Moreno Villavicencio], [2019], INSA Lyon, tous droits réservés

- The existence of nano-cracks in the surface of the sample produces a non-homogeneous sputtering that can be aggravated with the existence of artefacts as geometric shadowing effect.

The study of these factors with other characterization techniques, especially the AFM, would help with the interpretation of the ToF-SIMS data and an accurate conclusion about the sample can be given.

The ToF-SIMS and AFM combined methodology was used to confirm the existence of a geometric shadowing effect in order to provide an accurate conclusion about the sample. In addition, the information provided by the AFM was used to determine the geometry of the cracks, their thickness and orientation, as well as their evolution with the sputtering.

2.2.1. EXPERIMENTAL PROTOCOL AND ANALYSIS CONDITIONS

The protocol established to study the cracks geometry and their evolution during the sputtering consisted in two stages:

(1) Creating a ToF-SIMS bevel crater where the three layers are exposed.
(2) Performing an AFM image at three different areas of the crater corresponding respectively to the SiN layer, AlN layer and GaN layer.

The bevel crater was created with the Cs^+ sputter beam (1 keV, 56 nA). It was rastered over an area of 400 x 400 μm^2 with 128 x 128 pixels. The dose varied from 0% to 100% from right to left. The milling duration was 6 min using 1 milling pass per scan and a dwell time per pixel of 44 ms.

The AFM images were obtained with an AFM Dimension Icon from Bruker, which is in a nitrogen-filled glove box (MBraun), with H_2O and O_2 contents below 3 ppm. All measurements were performed in Tapping mode with standard silicon cantilever (OTESPA – R3 from Bruker) with a nominal spring constant of 26 N/m. A typical 7 x 7 μm^2 area with a 512 x 512 pixels was analyzed.

With the goal of studying the topography evolution of the cracks after a long sputter time, an extra ToF-SIMS sputtering was performed. The Cs^+ (1 keV, 48 nA) sputter beam was rastered over an area of 200 x 200 μm^2 for several minutes. An AFM image of the bottom of the crater was performed with the same conditions as for the bevel crater images.

Cette thèse est accessible à l'adresse : http://theses.insa-lyon.fr/publication/2019LYSEI121/these.pdf
© [M.A. Moreno Villavicencio], [2019], INSA Lyon, tous droits réservés

2.2.2. RESULTS

Figure IV.10.a, b and c show the AFM images taken from areas of the crater corresponding to the SiN, AlN and GaN layers respectively. The exact depths from where the images were acquired are unknown. However, a ToF-SIMS image of the entire crater confirmed that the three layers were exposed to the surface. The cracks are seen in every AFM image, their width and length varied with the sample depth. The same color bar was used for the three images to allow an easier comparison.

The cracks present in the sample before sputtering showed a round edge. Figure IV.11.a shows the AFM initial image. This round shape of the cracks suggested that the material was cracked before the SiN deposition and that, during the deposition, some SiN entered inside the cracks filling them inhomogeneously. This theory would explain the width evolution of the cracks from 30 - 60 nm in the SiN layer to 80 - 130 nm in the GaN. As well as the length of the cracks increasing from 5 - 15 nm up to 30 nm after sputtering deeper in the sample. However, the depth of the crack presented in Figure IV.10 is not truthful. In fact, the depth can be larger than the represented because the tip did not reach the bottom of the crack.

Figure IV.11.b shows the AFM image captured deeper in the GaN layer after the sample was sputtered for a few minutes using classical depth profile. Same color bar was used for both AFM images.

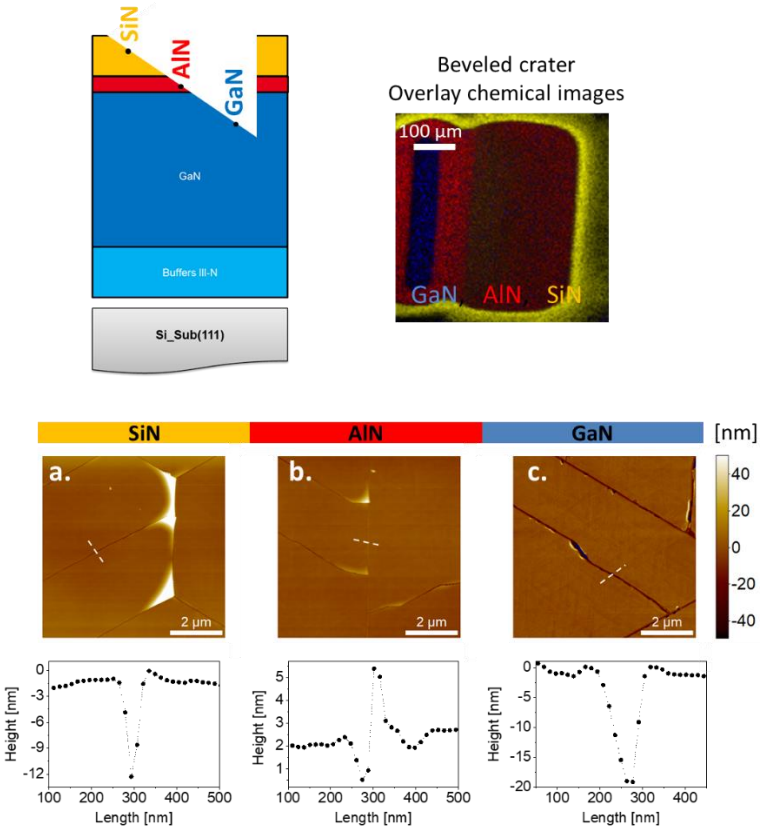

Figure IV.10

AFM topographical images captured in areas of the beveled crater that correspond to the a. SiN layer, b. AlN layer and c. GaN layer. The magnification was calculated at about 10^4. The scan size was 7 x 7 μm^2 with 512 x 512 pixels. The topographical profiles correspond to the cross section of the white dashed line shown in the AFM images.

Cette thèse est accessible à l'adresse : http://theses.insa-lyon.fr/publication/2019LYSEI121/these.pdf
© [M.A. Moreno Villavicencio], [2019], INSA Lyon, tous droits réservés

The pink areas seen in the image are areas where the detected topography was over 1 micron. The topography of the cracks evolved during the sputtering producing bumps in the surface, the topography was inversed. This phenomenon implies the existence of a geometric shadowing effect hampering the sputtering inside the cracks. The ToF-SIMS started analyzing the sample; the SiN was detected from the grains and from the cracks but with less intensity. In fact, because of the crack's width the geometric shadowing effect produced a diminution of the sputter yield at the cracks that is seen as a lower intensity in the ToF-SIMS images, Figure IV.8.b. The analysis continued and the SiN was completely sputtered from the grains. However, since the sputtering at the cracks was delayed, the SiN was still detected from them. This difference in sputter yield modified the edges of the cracks creating small bumps such as the one shown in Figure IV.10.a and b. When the AlN layer was completely sputtered at the grains, the ToF-SIMS images of SiN and AlN showed a remaining intensity coming from the cracks. This revealed the delay in the sputtering at these nano-areas. As the difference in the sputtering yield continued, the grains were sputtered more than the cracks. Consequently, by the time the bottoms of the cracks were reached, the topography of the cracks was inversed as can be seen in Figure IV.11.b.

Studying the profiles of the crack in Figure IV.10.c, we have noticed that the vertical interfaces show the same topography-modification effect explained in the previous part of the chapter. The sputter beam bombards the sample from the left side creating a higher slope in the vertical interface of the right. This is the product of a complete exposition of the right interface to the sputter beam and a geometric shadowing blocking the normal sputtering of the left interface.

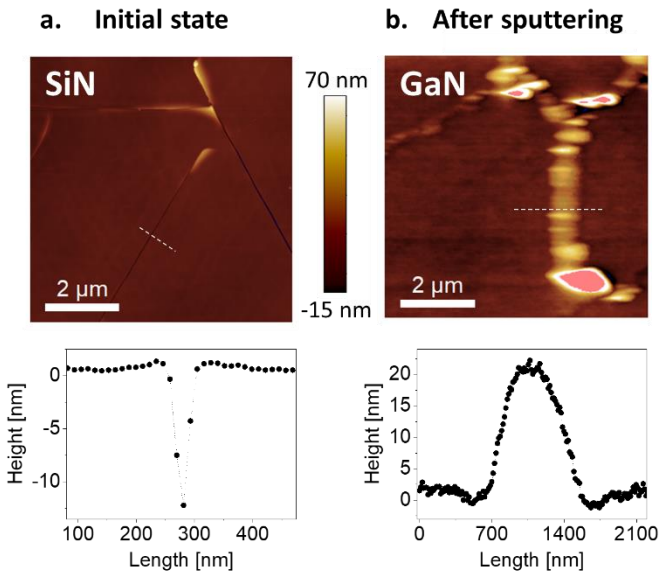

Figure IV.11

AFM images and profiles of the cross section (white dashed line) captured a. initial state before ToF-SIMS sputtering and b. at the GaN layer after ToF-SIMS sputtering. Images do not correspond to the same area.

Cette thèse est accessible à l'adresse : http://theses.insa-lyon.fr/publication/2019LYSEI121/these.pdf
© [M.A. Moreno Villavicencio], [2019], INSA Lyon, tous droits réservés

STEM images and EDX analyses were carried out on a sample with the same composition and dimensions as the one detailed before but fabricated with a different NH_3 pressure. Superficial cracks were also visible in this second sample with the difference that the initial widths are less than 20 nm. The STEM image in Figure IV.12.a shows the cracks from the GaN layer to the surface. A slight cavity of the SiN layer at the areas where the cracks are is also seen. It confirms the filling of the cracks with SiN, being consistent with the information extracted from the AFM profiles and ToF-SIMS images.

The SiN entering inside the cracks during the deposition is also confirmed with the EDX silicon image. Figure IV.12.b shows the EDX images corresponding to silicon, nitrogen and gallium respectively. It is seen that the interface AlN / SiN is not straight. Indeed, at the areas where the cracks are, the chemical image of silicon creates the idea of a diffusion within the AlN layer.

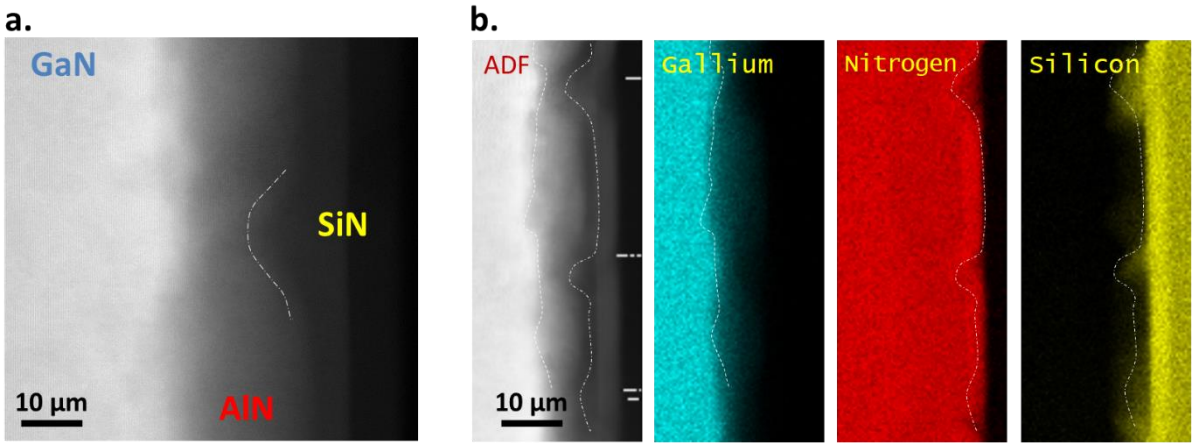

Figure IV.12 a. STEM and b. EDX images of a SiN / AlN / GaN structure with the same dimensions as the previously detailed sample but fabricated at a different NH_3 pressure.

Cette thèse est accessible à l'adresse : http://theses.insa-lyon.fr/publication/2019LYSEI121/these.pdf
© [M.A. Moreno Villavicencio], [2019], INSA Lyon, tous droits réservés

3. CONCLUSIONS

The existence of diverse artefacts as ion-induced topography and shadowing effect when performing ToF-SIMS analysis of nanostructures was confirmed. The importance of considering them at the time of providing a conclusion about the analyzed sample was demonstrated. The ToF-SIMS and AFM combined methodology was used to study the artefacts produced by sputtering nano-patterned-areas and to optimize the analysis conditions in order to reduce them. A concrete example of a classical misinterpretation of ToF-SIMS data was exposed and it was shown how the ToF-SIMS and AFM combination helps to identify it.

The first part of the chapter discussed the influence of the primary energy and ion beam orientation on sputter yield, surface roughness, depth and lateral resolution, topography evolution and shadowing effect. The optimization of these two analysis conditions was found to be important in the reduction of unwanted results. The most convenient primary energy and beam orientation to sputter a GaAs / SiO_2 patterned sample were determined. A low primary energy considerable decreased the sputter yield. In the other extreme, a high primary energy showed the highest sputter yield. An important influence of the ion beam orientation on the sample roughness was found at 250 eV. A compromise between the increase of surface roughness and the diminution of sputter yield was found with a primary energy of 500 eV. Moreover, orienting the ion beam parallel to the patterns and lines showed a reduction of the shadowing effect and a symmetry in the vertical interfaces of the patterns.

The influence of the geometric shadowing in the accuracy of a depth-profile and ToF-SIMS images was demonstrated. Indeed, when analyzing nano-patterned-areas, the lateral resolution of ToF-SIMS proved to be a limitation that can be overcome using the AFM profiles. Moreover, the AFM was validated as a tool to understand the sputtering of the sample and the sample evolution during the analysis.

Cette thèse est accessible à l'adresse : http://theses.insa-lyon.fr/publication/2019LYSEI121/these.pdf
© [M.A. Moreno Villavicencio], [2019], INSA Lyon, tous droits réservés

Cette thèse est accessible à l'adresse : http://theses.insa-lyon.fr/publication/2019LYSEI121/these.pdf
© [M.A. Moreno Villavicencio], [2019], INSA Lyon, tous droits réservés

CHAPTER V.
COMBINING TOF-SIMS WITH AFM ELECTRICAL MODES

This chapter expands the classical ToF-SIMS and AFM methodology with the utilization of AFM advanced operation modes. The adapted methodology was used for two different applications. The first application consisted of studying the chemical modification of ferroelectric samples after they were locally polarized with the AFM tip. This research was based on combining piezoresponse force microscopy (PFM) with ToF-SIMS analysis. The chapter illustrates the results obtained for two samples: ferroelectric $BaTiO_3$ and non-ferroelectric $LaAlO_3$. The second part of the chapter presents a new application; the recovery of electrical properties of doped structures through the removal of gallium implantation caused by the FIB during the sample preparation step. For this study, the ToF-SIMS was combined with scanning capacitance microscopy (SCM) and scanning spreading resistance microscopy (SSRM). At the end, the establishment of a protocol that can be incorporated to the classical FIB sample preparation routine emerges as a perspective.

Cette thèse est accessible à l'adresse : http://theses.insa-lyon.fr/publication/2019LYSEI121/these.pdf
© [M.A. Moreno Villavicencio], [2019], INSA Lyon, tous droits réservés

Cette thèse est accessible à l'adresse : http://theses.insa-lyon.fr/publication/2019LYSEI121/these.pdf
© [M.A. Moreno Villavicencio], [2019], INSA Lyon, tous droits réservés

1. ToF-SIMS with advanced AFM operation modes. Is it a novel combination?

The versatility of AFM as characterization technique allows determining not only topographical information but also local properties such as mechanical, electrical, magnetic, piezoelectric. This information is provided through maps of the scanned area with a lateral resolution at the nanoscale (commonly higher than 50 nm). The scientific community firstly thought in correlating the ToF-SIMS chemical information with the classical topographical information of the AFM. Inorganic, organic, hybrid and biological samples were characterized by these two techniques with the aim of providing solid and accurate conclusions. Examples of these studies can be seen in CHAPTER I.3.

The development of AFM advanced operation modes opened the possibility of adding a new property to the existing correlation. Thus, the ex-situ ToF-SIMS and AFM combination continued characterizing samples in an extended manner. It can be found in the literature cases where the ToF-SIMS has been used together with AFM modes such as SSRM, c-AFM, SCM, PFM, Peak Force Tapping®, etc. CHAPTER I.3 listed some of them. They were used as complementary techniques where the analyzed area was not the same in both instruments. However, the launch of the in-situ ToF-SIMS / SPM instrument promoted the correlation of these techniques easily analyzing the same area of the sample. Multiple applications have appeared from it.

The results shown in this chapter were obtained following the combined AFM / ToF-SIMS cyclical analysis previously detailed. We combined the ToF-SIMS with AFM advanced operation modes, specifically the PFM, KFM, SSRM and SCM, for two different applications. The analyses correspond to the same sample area allowing a proper correlation. In this first part of the chapter, we studied the chemical change of ferroelectric samples after local polarization with the AFM tip.

Cette thèse est accessible à l'adresse : http://theses.insa-lyon.fr/publication/2019LYSEI121/these.pdf
© [M.A. Moreno Villavicencio], [2019], INSA Lyon, tous droits réservés

Cette thèse est accessible à l'adresse : http://theses.insa-lyon.fr/publication/2019LYSEI121/these.pdf
© [M.A. Moreno Villavicencio], [2019], INSA Lyon, tous droits réservés

2. ToF-SIMS AND PFM COMBINED METHODOLOGY TO STUDY THE CHEMICAL MODIFICATION OF PIEZOELECTRIC SAMPLES AFTER LOCAL POLARIZATION

Piezoelectric materials have the capacity to generate electric charge when subjected to mechanical energy solicitation. They are widely used as actuators [171], transducer, frequency control [172], ultrasonic receiver [173], etc. The piezoelectric family also includes the ferroelectric materials, which have spontaneous polarization in one or more directions that can be reversed through the application of an external electric field. They are of interest for memory, display and modulator applications [174]. All ferroelectrics are piezoelectric but not all piezoelectrics are ferroelectric [128].

The use of these materials for electric components increased in the last century. Their size reduction has brought the need to understand and control their properties at the nanoscale. To study the ferroelectric effect at the nanoscale, a conductive AFM tip can be used to apply a bias higher than the coercive voltage of the sample. It would induce, in a ferroelectric sample, a permanent alignment of the polarization in the direction of the electric field. This process is known as "*writing*" local domains. [175]

We have applied the combined ToF-SIMS and PFM methodology in an attempt to detect an eventual chemical modification at the nanoscale after the writing process. Experiments were carried out ex-situ at CEA. Two samples have been analyzed, one ferroelectric and one non-ferroelectric: $BaTiO_3$ (BTO), and $LaAlO_3$ (LAO) respectively.

2.1. EXPERIMENTAL PROTOCOL AND ANALYSIS CONDITIONS

The methodology consisted of writing local domains for each sample using the AFM tip and consequently, analyzing the polarized area by ToF-SIMS to detect any chemical modification. The analyses were performed ex-situ and the transfer of the sample between the instruments was done in air. The general protocol followed for all the samples was:

(1) Writing local squares domains by contact AFM mode. The same bias was applied for positive and negative voltages over two different regions of the sample. The writing conditions were the same for both polarizations.
(2) PFM analysis on each written square.
(3) 3D ToF-SIMS analysis of the sample without sputtering.

The specific analysis conditions will be given afterwards for each sample.

Cette thèse est accessible à l'adresse : http://theses.insa-lyon.fr/publication/2019LYSEI121/these.pdf
© [M.A. Moreno Villavicencio], [2019], INSA Lyon, tous droits réservés

2.1.1. $LaAlO_3$ (LAO) PIEZOELECTRIC SAMPLE

There are several studies in the literature of non-ferroelectric samples showing well-defined and convincing PFM signal [176–178]. Figure V.1 compares the PFM phase images captured after DC bias application in ferroelectric and non-ferroelectric samples. Ievlev et al. [54] studied the polarization switching process of a $PbZr_{0.2}Ti_{0.8}O_3$ (PZT) / $SrRuO_3$ ferroelectric sample. Figure V.1.a shows the PFM phase image captured after voltages of ± 4 V were applied to that sample creating artificially written domains. Borowiak et al. performed a similar procedure this time on LAO non-ferroelectric sample. Figure V.1.b illustrates the PFM image captured after application of DC ± 5 V bias.

Nonambiguous PFM phase images are shown for both samples. The regions scanned with a positive bias show 180° phase shift compared to the areas where negative voltage was applied. The same comparison of PFM signal of ferroelectric and non-ferroelectric samples was performed by Guan *et al.* [179]. They obtained unambiguous phase images for BTO, PVDF and Al_2O_3 structures after applying a DC voltage with the AFM tip. The PFM signal of the LAO sample was confirmed to disappear after less than an hour but the reason of the ferroelectric-like phase image is still unknown. Hypotheses have emerged to explain this behavior: ionic mobility in the bulk as redistribution of oxygen vacancies, field-induced charge injection and structural distortions at the interfaces [180].

In order to investigate these hypotheses, we studied the same LAO sample as Borowiak *et al.* It consisted of 3 nm thick of amorphous $LaAlO_3$ (LAO) grown on a silicon substrate using molecular beam epitaxy (Figure V.2.a). The deposition of the first nanometer was done whilst limiting the oxygen pressure to conserve the LAO / Si interface without oxide formation. The remaining two nanometers were deposited under 2 x 10^{-6} Torr of oxygen pressure. More information about the fabrication of the sample is found in [181].

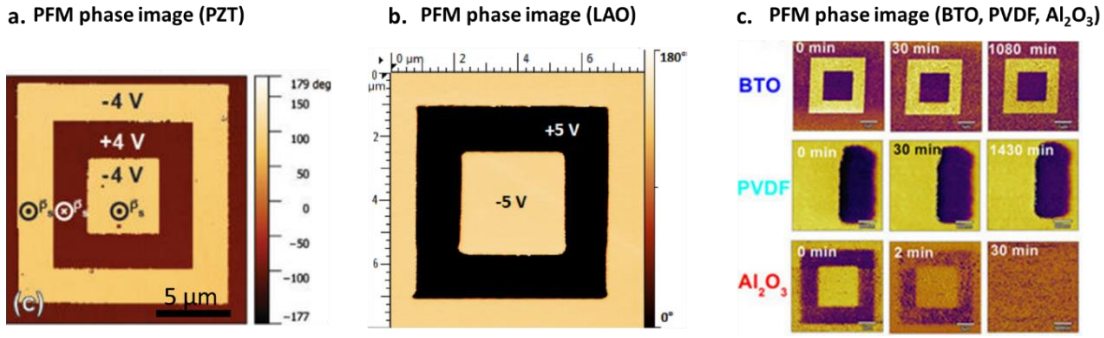

Figure V.1 *PFM phase image of PZT (a) ferroelectric sample (extracted from [54]) and LAO (b) non-ferroelectric sample (extracted from [176]) right after application of a DC bias using the AFM tip. c. PFM phase images as a function of time after applied field captured for BTO, PVDF and Al_2O_3* samples (extracted from *[179]*)

Cette thèse est accessible à l'adresse : http://theses.insa-lyon.fr/publication/2019LYSEI121/these.pdf
© [M.A. Moreno Villavicencio], [2019], INSA Lyon, tous droits réservés

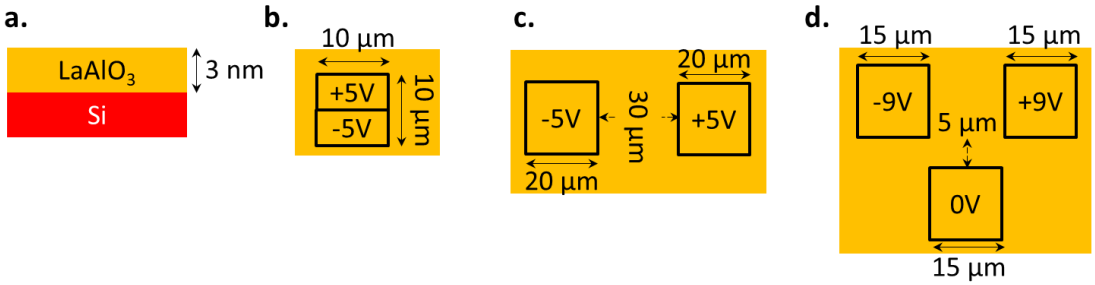

Figure V.2 Schematic of amorphous LAO structure a. Schematic of the sample surface after local polarization in the first (b), second (c) and third (d) analysis.

Since charge injection is one of the theories that may explain a possible ferroelectric-like PFM signal, KFM scans were added to the ToF-SIMS / PFM routine to discard or confirm the existence of such charges and the lifetime of the perceived signal. Kelvin force microscopy is used to detect the electrostatic forces between the tip and the sample surface. It produces maps of the local contact potential different, which can be related to the presence of superficial charge. More information about this technique can be found in [182].

Three analysis were performed on the LAO sample using the combined ToF-SIMS and KFM / PFM methodology. Their schematics are shown in Figure V.2.b, c and d respectively. The first analysis was performed to determine the lifetime of the signal read by the KFM. The second and the third were carried out with the goal of detecting surface charges through KFM analysis and determining any chemical modification after polarization. The protocol was similar, but the writing conditions varied.

2.1.1.1. FIRST ANALYSIS – DETERMINING LIFETIME OF SUPERFICIAL CHARGES

(1) Domains were written in contact AFM mode with a contact force of about 95 nN and a tip velocity of 16 µm/s. Tip bias of ± 5 V were applied over a 10 µm square (256 pixels) as the schematic in Figure V.2.b

(2) KFM analysis was performed several times for two days after the writing process. The scan size for the lifetime study varied from 20 µm x 2 µm (128 pixels x 13 pixels) for the first image to 30 µm x 30 µm (128 pixels) for the last image. This was to avoid a discharge of the surface caused by the tip scanning the entire area.

Cette thèse est accessible à l'adresse : http://theses.insa-lyon.fr/publication/2019LYSEI121/these.pdf
© [M.A. Moreno Villavicencio], [2019], INSA Lyon, tous droits réservés

2.1.1.2. SECOND ANALYSIS – DETECTING ANY CHEMICAL MODIFICATION WITH TOF-SIMS

NEGATIVE POLARIZATION

(1) Domains were written in contact AFM mode with a contact force of about 95 nN and a tip velocity of 16 µm/s. Tip bias of ± 5 V were applied over two squares of 20 µm x 20 µm (512 x 512 pixels). The configuration of the domains is in Figure V.2.b.
(2) KFM images of the written domains were captured. For the first analysis, the scan size was 40 µm x 5 µm (256 x 32 pixels). The tip velocity was set at 40 µm/s and the drive amplitude at 5000 mV.
(3) 3D ToF-SIMS analysis was performed on the sample for almost 17 hours in negative mode. A primary beam of Bi_3^{++} (60 keV, 0.8 nA) was rastered over an area of 100 µm x 100 µm (1024 x 1024 pixels). The cycle time was set at 70 µs. No sputter beam was used.

2.1.1.3. THIRD ANALYSIS – DETECTING ANY CHEMICAL MODIFICATION WITH TOF-SIMS

POSITIVE POLARIZATION

(1) Domains were written in contact AFM mode with a contact force of about 150 nN and a tip velocity of 12.2 µm/s. Sample bias of ± 9 V were applied over two squares of 15 µm x 15 µm with 1024 lines each. The configuration of the domains is in Figure V.2.d.
(2) PFM analysis was performed on each written square. An area of 20 µm x 2 µm (1024 x 102 pixels) was scanned with an AC bias of 5 V. The resonant frequency in contact was measured at 335 kHz. Same tip velocity and contact force as for the writing process were used.
(3) KFM images of the written domains were acquired. The same scan size as for the PFM images was maintained. The tip velocity was set at 40 µm/s and the drive amplitude at 5000 mV.
(4) 3D ToF-SIMS analysis was performed on the sample for over 55 hours in positive mode. A primary beam of Bi_3^{++} (60 keV, 0.8 nA) was rastered over an area of 75.73 µm x 75.73 µm (2048 x 2048 pixels). The cycle time was set at 110 µs. No sputter beam was used.

2.1.2. $BaTiO_3$ (BTO) FERROELECTRIC SAMPLE

The sample was provided by Florencio Sanchez from the Institut de Ciència de Materials de Barcelona (ICMAB-CSIC) in Barcelona (Spain). It consisted of a 10 nm $LaNiO_3$ electrode deposited on a $SrTiO_3$ substrate. Consequently, a 100 nm $BaTiO_3$ (BTO) top layer grown on top of the deposition. The schematic of the sample is seen in Figure IV.1.a.

Cette thèse est accessible à l'adresse : http://theses.insa-lyon.fr/publication/2019LYSEI121/these.pdf
© [M.A. Moreno Villavicencio], [2019], INSA Lyon, tous droits réservés

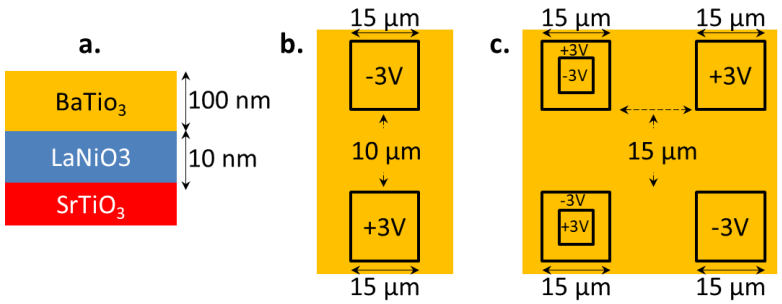

Figure V.3

(a) Schematic of the BTO structure. Sample surface after local polarization for the first (b) and second analysis (c).

The BTO is part of the perovskite family and has been largely studied since 1950s [183]. It can be switched between two polarization states through the application of a DC voltage or a mechanical force, a typical PFM phase image for this sample is shown in Figure V.1.c.

A first ToF-SIMS and PFM combined analysis was carried out to optimize the protocol and the analysis conditions. Its configuration is shown in Figure V.3.b.

2.1.2.1. FIRST ANALYSIS – OPTIMIZATION OF THE PROTOCOL

(1) Domains were written in contact AFM mode with a contact force of about 95 nN and a tip velocity of 20.9 µm/s. Sample bias of ± 3 V were applied over two squares of 15 µm x 15 µm (1024 pixels). The configuration of the domains is in Figure V.3.b.

(2) The PFM analysis for the first configuration was performed over an area of 50 µm x 50 µm (1024 x 102 pixels) with an AC bias of + 500 mV applied to the sample. The contact force was about 150 nN.

(3) The ToF-SIMS imaging mode was selected to chemically analyze in-depth the sample. A primary beam of Bi_3^{++} (60 keV, 0.36 nA) was rastered over an area of 70 µm x 70 µm (1024 x 1024 pixels). The cycle time was set at 70 µs. No sputter beam was used. The depth profile was acquired for over 15 hours in negative mode.

2.1.2.2. SECOND ANALYSIS – DETERMINING ANY CHEMICAL MODIFICATION

(1) Domains were written in contact AFM mode with a contact force of about 95 nN and a tip velocity of 30.5 µm/s. Sample bias of ± 3 V were applied over four squares of 15 µm x 15 µm (1024 pixels). Two smaller squares of 7.5 µm x 7.5 µm (512 pixels) were written inside of two of the former squares with the opposite polarization. The same tip velocity was maintained. The configuration of the domains is shown in Figure V.3.c.

(2) The PFM analysis was performed over an area of 60 µm x 60 µm (1024 x 102 pixels) with an AC bias of + 250 mV applied to the sample. The contact force was about 255 nN.

(3) The sample was analyzed in-depth using ToF-SIMS imaging mode. A primary beam of Bi_3^{++} (60 keV, 0.4 nA) was rastered over an area of 120 µm x 120 µm (512 x 512 pixels).

Cette thèse est accessible à l'adresse : http://theses.insa-lyon.fr/publication/2019LYSEI121/these.pdf
© [M.A. Moreno Villavicencio], [2019], INSA Lyon, tous droits réservés

The cycle time was set at 70 µs. No sputter beam was used for 20 minutes and then, a depth-profile in non interlaced (analyze 15 frames, sputter 1 frame, 1 s pause) was performed using Cs^+ 500 eV to sputter a surface of 500 µm x 500 µm. The depth profile was acquired for over 17 hours in negative mode.

2.2. RESULTS OF THE NON-FERROELECTRIC LAO SAMPLE

Interesting results were obtained for the lifetime of KFM signal in the LAO non-ferroelectric sample. Images shown in Figure V.4. were acquired 0 (a), 3.5 (b), 25 (c) and 51 (d) hours after the DC bias was locally applied to the AFM tip while this one was scanning the LAO surface. The surface potential image obtained immediately after domain writing showed a lower CPD for the second half of the square corresponding to the area where the negative voltage was applied. The rest of the images did not conserve this contrast change probably due to the charge dispersion during time. Bark *et al.* [177] observed the decay of the PFM and electrostatic force microscopy signals after tens of minutes and 3 hours respectively. The KFM images that we obtained showed a potential contrast after 51 h.

The KFM potential images corresponding to the second analysis are in Figure V.5.a. They have shown a lighter contrast in both written areas indicating a higher contact potential difference (CPD) than the original surface. This was not the expected behavior because the application of a negative and a positive voltage through the AFM tip would respectively imply a lower and higher CPD than the measured at the original surface. The superficial charges may have inhibited a proper electrical contact between the tip and the surface. Thus, a proper conclusion about these preliminary KFM results was not possible.

ToF-SIMS images corresponding to the total ion sum, O_2 and C are shown in Figure V.5.b. Chemical contrasts at the written squares and at the areas where the KFM measurements were performed were seen in the ToF-SIMS images. The arrows number 1 and 2 point respectively at the tip engagement point and at the area seen in the KFM images. The 40 µm KFM image started with an aspect ratio of 1 before the scan size was reduced to 40 x 5 μm^2, the arrow number 3 indicates the edge of that initial scan size. At these mentioned areas, points 1 and 3 especially, the intensity of O_2 and C was higher. These results suggest a chemical modification produced by the tip-surface contact no matter the applied voltage. Hypotheses such as the removal of surface contamination with the AFM tip during scanning or traces from the tip left behind when scanning could be considered. The combined protocol was adapted for the following experiments in order to dismiss this effect in the polarized areas but at the same time to explain the chemical difference.

Cette thèse est accessible à l'adresse : http://theses.insa-lyon.fr/publication/2019LYSEI121/these.pdf
© [M.A. Moreno Villavicencio], [2019], INSA Lyon, tous droits réservés

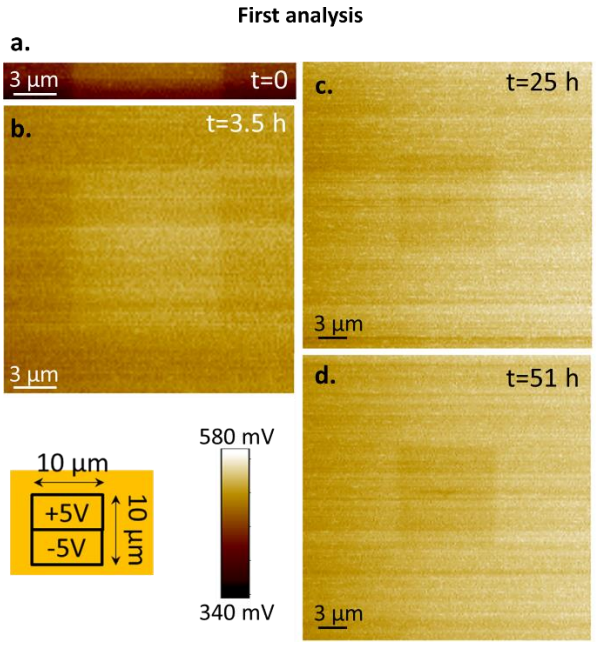

Figure V.4

KFM images obtained after 0 (a), 3.5 (b), 25 (c) and 51 (d) hours the application of ± 5 V DC bias. Same color bar was used. Note that (c-d) has lower magnification.

The coming PFM scans were not performed over the entire areas but only a few lines per written square were acquired. In the same way, a new step was included. The tip would scan an area of the sample under the same dimensions as the written areas, but no voltage was applied.

The preliminary results obtained from the third analysis are shown in Figure V.6. This time, the complete ToF-SIMS / PFM / KFM combined protocol was applied. An additional AFM scan in contact mode was performed without bias application over an area with the same dimensions as for the written domains. The PFM amplitude and phase images of the written domains are seen in Figure V.6.a and b respectively. The stripes seen in those images are probably due to the existing charges inhibiting the electrical contact between the tip and the sample during the analysis. A non-expected contrast in the PFM phase image is seen when a bias of 9 V was applied to the sample. Indeed, polarization does not normally occur at non-ferroelectric samples.

Through the combined ToF-SIMS / KFM / PFM methodology, the existing hypothesis of this ferroelectric-like behavior can be studied and discarded. As for the second analysis, the existence of charge injection was confirmed with the KFM potential images (Figure V.6.c). This time the CPD variation is consistent with the signal of the applied bias. The ToF-SIMS images were then used to demonstrate a chemical modification of the scanned areas. The contrast seen in the ToF-SIMS images corresponding to the sum of LaO^+ and total ions (Figure V.6.d) identifies the three squares scanned by the AFM.

Cette thèse est accessible à l'adresse : http://theses.insa-lyon.fr/publication/2019LYSEI121/these.pdf
© [M.A. Moreno Villavicencio], [2019], INSA Lyon, tous droits réservés

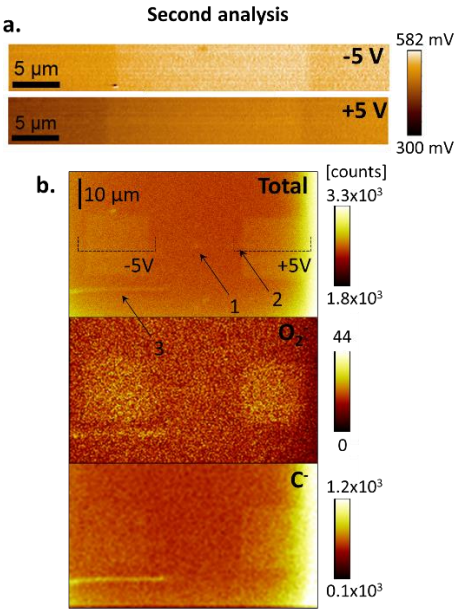

Figure V.5

Results of the second analysis of the LAO sample: potential KFM images for ± 5 V DC bias (a). Same color bar was used. ToF-SIMS images (b) corresponding to the total ion sum, O_2^- and C^-. The images are binned using 4 pixels. Two rectangles enclosed the areas analyzed by the KFM and three arrows indicates the traces left by those measurements.

It confirms a chemical modification influenced already by the tip contact. No signal was detected in the PFM analysis performed on the 0 V area. This suggests that there is no mechanical induced switching-like behaviour produced by an internal field generated by the tip-sample contact. Since the expected chemical modification is small, the interpretation of the ToF-SIMS images is not a straightforward procedure. Principal component analysis (PCA) was carried out on the data from the second and the third analysis. Both depth profiles were divided into three ranges: from data point 1 to 50, 190 to 240 and 426 to 476. For each, three ROIs corresponding to the +5 V, -5 V squares and the area where the tip never scanned (reference area) were delimited. In order to obtain a more accurate PCA analysis, three sets of data were extracted from each ROIs.

The PCA finds the direction where the data has the highest variance [184]. The result is the data organized according to their projection in the found directions. This is known as scores. Figure V.7.a, b and c show the scores obtained for the first, second and third range respectively. Every point in the plot represents one ROI data set. The scores have grouped the data according to the area where they were extracted from. Furthermore, they located the data corresponding to the – 5 V square close to x = 0. It means that observing at the x-direction the major variance was found between the points extracted from the + 5 V square and the reference data.

The PCA provides also the value of such variance in the corresponding direction. It is known as loadings. Figure V.7. d, e and f show the loadings per range of the x-direction. The peaks located at the positive area in the loadings are the more abundant of the points located in the positive x-axis of the scores. In the same way, the negative loadings refer to the peaks found in majority at the points located in the negative x-axis of the scores.

Cette thèse est accessible à l'adresse : http://theses.insa-lyon.fr/publication/2019LYSEI121/these.pdf
© [M.A. Moreno Villavicencio], [2019], INSA Lyon, tous droits réservés

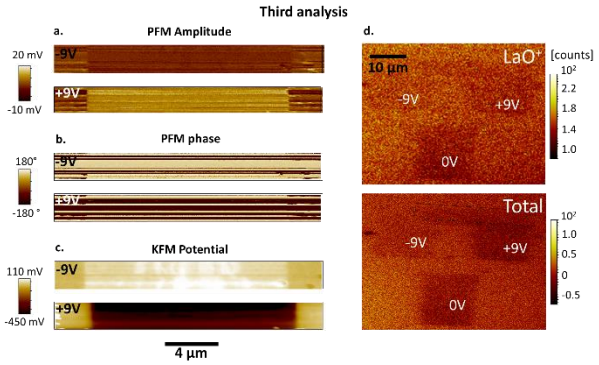

Figure V.6

Results of the third analysis for the LAO sample: PFM amplitude (a), PFM phase (b) and potential KFM (c) images for ± 5 V DC bias. Sum of LaO^+ ToF-SIMS images and total counts (d). ToF-SIMS images are binned by 4 pixels.

To facilitate the recognition, the part of the x-axis corresponding to data of the reference area is indicated in yellow, pink or blue depending on the data point range. Two peaks are found to be characteristic of the reference area during the three ranges, the m/z = 149 and the m/z = 182. They respectively correspond to fragments of phthalate and phosphate, which are well known for representing common organic contamination from plasticizers [185]. This result suggests the tip removes contamination when it scans the surface.

The hypotheses of the PFM signal obtained for this non-ferroelectric sample can be investigated analyzing the ToF-SIMS and AFM data. Field-induced charge injection and ionic mobility in the bulk such as redistribution of oxygen vacancies are the phenomena that we tried to identify.

The surface charging has been related to the dissociation of water molecules into H^+ and OH^- [178] that concludes in a direct charge injection of negative and positive charges when the tip is negatively and positively biased [176,177]. The accumulation of negative and positive charges at the surface would be respectively evidenced in the KFM images as a diminution and an increment of the CPD at those regions. The KFM images of the second analysis are not reliable but the expected CPD behavior is seen in the KFM images of the third analysis. In this case, the application of the bias to the sample results in an accumulation of the opposite charges at the surface. Indeed, the obtained potential KFM images (Figure V.6.c) showed a lower CPD at the positively biased square (+ 9 V) and a higher CPD to the negatively biased area (- 9 V).

The nature of these superficial charges may be determined through the ToF-SIMS analysis. Figure V.8 shows the PCA results of the data extracted exclusively from the ±5 V written areas of the second analysis. The data and peaks corresponding to the negative square is indicated in yellow, pink and blue for an easier visualization. The same three ranges as for the previous analysis was maintained. The score plots suggest a high variance, in the x-direction, between the data from the +5 V and the -5 V squares (Figure V.8.a, b, c). The loadings identified the peaks responsible for such behaviour (Figure V.8.d, e, f).

Cette thèse est accessible à l'adresse : http://theses.insa-lyon.fr/publication/2019LYSEI121/these.pdf
© [M.A. Moreno Villavicencio], [2019], INSA Lyon, tous droits réservés

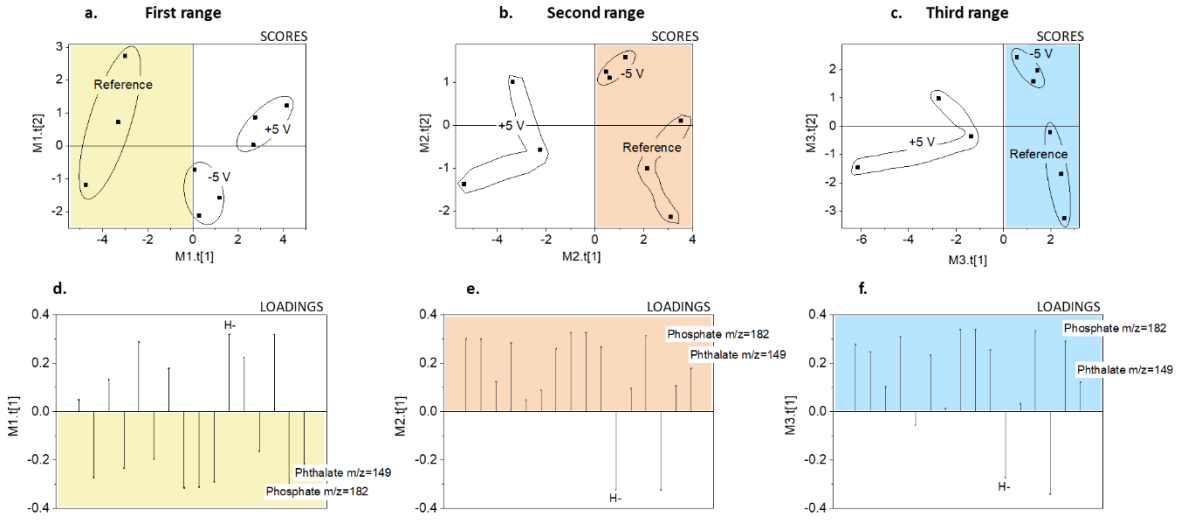

Figure V.7 *PCA scores (a, b, c) and loadings of the x-direction (d, e, f) per range (from data point 1 to 50, 190 to 240 and 426 to 476 respectively). Three data sets were extracted from the ± 5 V squares and a non-scanned area.*

It is important to remember that for this analysis the bias was applied to the tip. Thus, if a dissociation of water molecules was produced (H^+ and OH^-), those free charges would be attracted toward the potential of opposite sign: H^+ ions at the surface if – 5 V are applied while OH^- ions accumulated at the surface biased with + 5 V. However, for all the ranges, the H^+ was detected in a higher proportion at data extracted from the +5 V square while the OH^- was found to be more abundant at points corresponding to the -5 V square. Since the methodology was performed ex-situ, it is not certain that the H and OH ions arise from a pre-existing H_2O layer. Further investigation including a heating step in an in-situ methodology is needed to provide an accurate conclusion.

The ToF-SIMS depth profile can be an important tool in the determination of ionic or oxygen vacancies motion within the sample. However, the detection of this movement is not straightforward due to the small concentrations involved. The suspected migration consists of negatively charged oxygen ions moving towards the anode while the cathode is attracting the positively charged oxygen vacancies. The charges, trapped at those sites, are thought to be responsible for a polarization-like behavior. In our case, a positive bias applied to the tip would imply the migration of negatively charged oxygen ions to the surface. In the opposite case, the application of a negative bias to the AFM tip would produce a migration of oxygen vacancies towards the sample surface. Thus, the oxygen intensity detected at negatively biased areas is expected to be inferior than the one detected at positively biased areas. Unfortunately, the PCA loadings of Figure V.8 are showing a higher concentration of oxygen ions at the data extracted from the -5 V.

Cette thèse est accessible à l'adresse : http://theses.insa-lyon.fr/publication/2019LYSEI121/these.pdf
© [M.A. Moreno Villavicencio], [2019], INSA Lyon, tous droits réservés

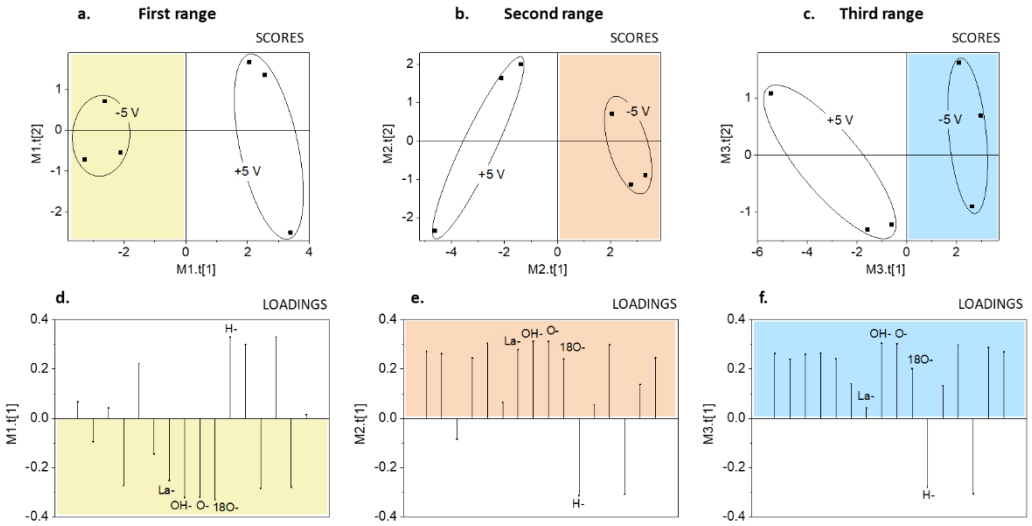

Figure V.8 *Scores (a, b, c) and loadings (d, e, f) obtained when data sets extracted from the ± 5 V squares was analyzed using PCA. The results are shown per range.*

The oxygen vacancies are present in a high concentration in samples fabricated through molecular beam epitaxy as is the case of this LAO structure. The long storage of this sample under room conditions may promote a re-oxidation of the surface modifying the intrinsic oxygen concentration of the sample. This might explain the unexpected oxygen level. However, the topic is still open, and the occurrence of oxygen migration cannot be confirmed.

The PFM signal obtained from non-ferroelectric materials is often attributed to the variation of the molar volume product of ionic migration such as oxygen migration [180]. However, the ToF-SIMS results obtained for the second analysis suggest the ionic migration of lanthanum instead. The positively charged lanthanum ions may be attracted to the negatively biased surface producing a higher concentration of those ions at these areas. This behaviour is shown in PCA loadings of Figure V.8. Indeed, the La^+ peak was found in majority at the – 5 V squares. Since the lanthanum secondary ions are better detected in positive polarity, the ToF-SIMS detection of the third analysis was done in positive mode. Figure V.9.a shows the lanthanum normalized intensity obtained after averaging the three data sets per square. The lanthanum was found in a higher intensity at the surface of the square where + 9 V was applied to the sample. It suggests that effectively, the positively charged lanthanum ions migrate toward the surface where the negative voltage is applied. The ToF-SIMS depth-profile obtained for this analysis is shown in Figure V.9.b. The analysis was stopped three times to optimize the data storage. The discontinuity in the depth profiles coincide with the time when the analysis was stopped. The slightly higher intensity of lanthanum detected at the positive biased area is well noted for at least 28 h of analysis. The intensity detected after this time approaches the one detected for the negatively biased square.

Cette thèse est accessible à l'adresse : http://theses.insa-lyon.fr/publication/2019LYSEI121/these.pdf
© [M.A. Moreno Villavicencio], [2019], INSA Lyon, tous droits réservés

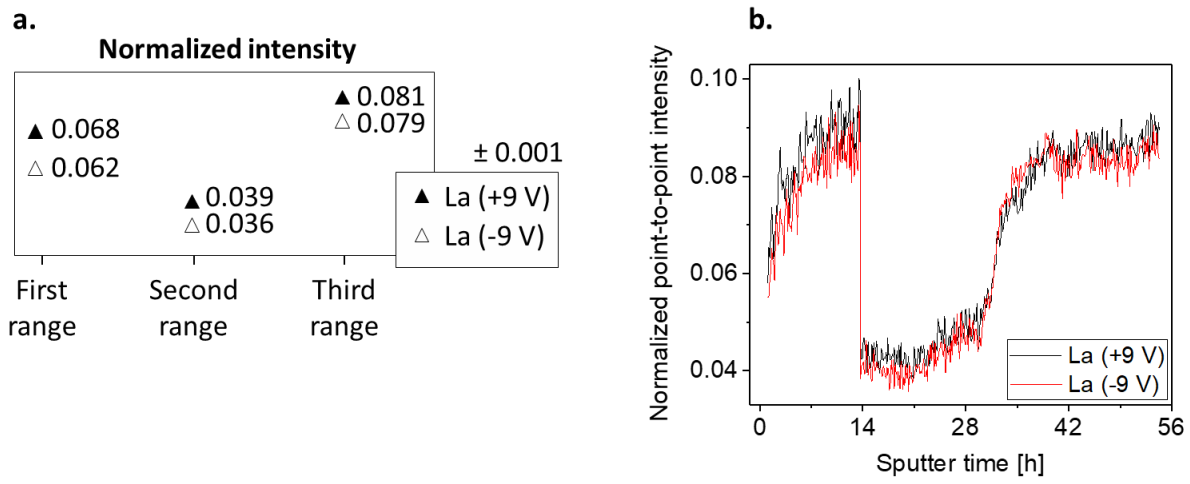

Figure V.9 *a. Lanthanum normalized intensity obtained after averaging three data sets extracted per analysis range. b. depth-profile corresponding to ROIs of the positively and negatively biased area.*

The three hypotheses explaining the PFM signal behaviour were studied. The results obtained for the second analysis led to believe in the contamination removal when the tip scans the sample surface and confirm the existence of charge accumulation at the surface. However, these results are not consistent in the third analysis. The oxygen migration could not be identified in the analyses. Instead, both analyses suggest an ionic migration of positively charged lanthanum ions.

2.3. RESULTS OF THE BTO FERROELECTRIC SAMPLE

The PFM and ToF-SIMS images obtained for the first analysis of the BTO structure are shown in Figure V.10.a, b and c respectively. The contrast seen in the PFM phase image identifies the two polarized areas. However, the difference in phase of the ±3 V domains is not 180° as it should be. The existence of superficial charges might have inhibited the proper electrical contact between the surface and tip. Thus, the PFM images do not correspond to the piezoelectric properties but to the electrostatic force. The ToF-SIMS images were binned by four pixels in order to detect the contrast corresponding to the polarized areas. The two squares can be recognized in the oxygen chemical image (Figure V.10.b). However, there is no evidence of an intensity difference between the +3 V and -3 V squares.

Something similar occurs in the ToF-SIMS images of the second analysis. However, in this case, an unambiguous PFM image was obtained. The regions scanned with a positive voltage (upper square at the right corner) shows a 180° phase shift compared to the region scanned with a negative voltage (bottom square at the right corner). This 180° phase shift decreases for the concentric squares.

Cette thèse est accessible à l'adresse : http://theses.insa-lyon.fr/publication/2019LYSEI121/these.pdf
© [M.A. Moreno Villavicencio], [2019], INSA Lyon, tous droits réservés

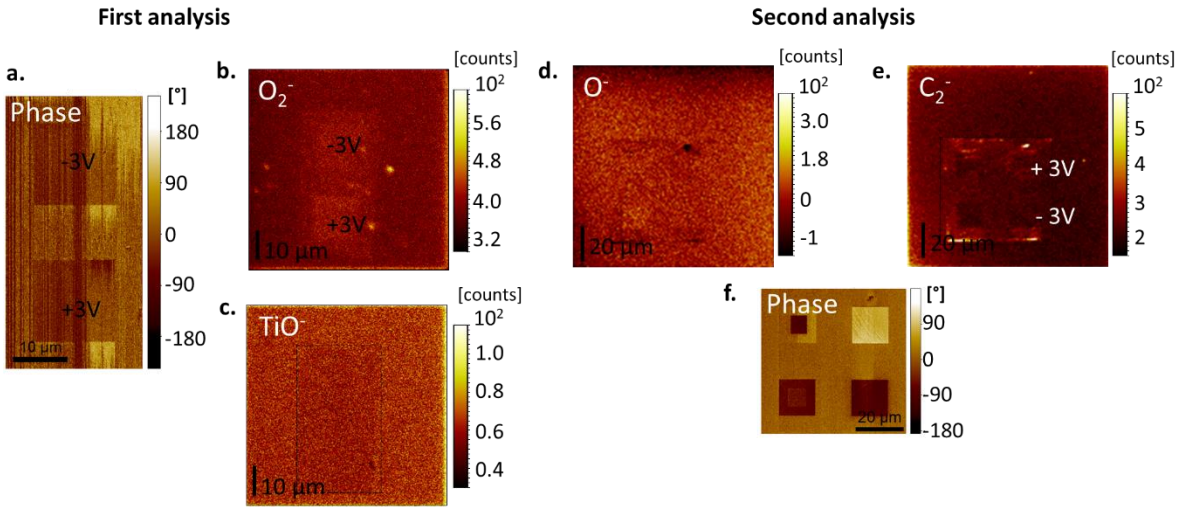

Figure V.10 *Results of the first analysis and second analysis respectively after application of ± 3 V: PFM phase image (a, f), ToF-SIMS images of O_2^- (b) and TiO^- (c) binned 4 x 4 pixels for the first analysis and O^- (d) and C_2^- (e) binned 16 x 16 pixels for the second analysis.*

The regions scanned with a positive voltage, the outer square of the upper left corner and the inner square of the bottom left, did not show the same phase as the big square (4 mV, light color). It is probably that the domain switching was not completed and longer time per pixel was needed.

The sum of the ToF-SIMS images corresponding to O^- and C_2^- are shown in Figure V.10.d and e respectively. The contrast of four squares can be seen in the C_2^- ToF-SIMS images implying that there is less carbon in those areas. However, there is no evidence of the two inner squares as well as no distinction between the areas scanned with positive or negative voltage. The pixel size of the analysis was about 250 nm. The ToF-SIMS images were binned by 16 pixels in order to observe the polarization contrast. This action increases the pixel size up to 2 µm. Detecting chemical change of the 7.5 µm square is thus challenging as there are only 16 to 20 pixels in the square.

As well as for the LAO sample, there is a remarkable contrast in the ToF-SIMS images at the area scanned by the PFM. For the first analysis, this area is enclosed in a dashed square in the TiO^- ToF-SIMS images (Figure V.10.c). The contrast is also seen at the C_2^- chemical image of the second analysis (Figure V.10.e). Further analysis of the data using PCA showed no relationship between this contrast and the peaks corresponding to organic contamination, specifically phthalate m/z = 149 and phosphate m/z = 182. Thus, it cannot be claimed that the AFM tip removed surface contamination during the scanning.

Cette thèse est accessible à l'adresse : http://theses.insa-lyon.fr/publication/2019LYSEI121/these.pdf
© [M.A. Moreno Villavicencio], [2019], INSA Lyon, tous droits réservés

Oxygen vacancies have been considered as major protagonist in the polarization state of $BaTiO_3$. Gómez *et al.* [186] have found a connection between the resistive states and the migration of oxygen vacancies produced by the mechanical switching of a BaTiO3–δ film on silicon. However, no signal of oxygen migration was found in our analysis when a deeper analysis of the chemical modification in the polarized area was done using multivariate analysis (PCA). The study of oxygen migration is not straightforward. The chemical changes are expected to occur at the surface of the sample where there is also the influence of surface contaminants. The fact of performing the analysis ex-situ adds the influence of external oxidation, which needs then to be disassociated from the intrinsic oxygen of the sample.

Moreover, no other ionic migration was detected. The low mass resolution of the imaging mode obstructed the differentiation of titanium related peaks. Even for the isotopes, there was always the contribution of other molecules. The obtained results for the BTO did not allow a proper conclusion to be drawn about the polarization mechanism. In fact, an optimization of the protocol and the analysis conditions is needed. A list with the recommendations to consider for future work is presented below.

2.4. PROPOSITIONS FOR FUTURE WORK

The combined ToF-SIMS / KFM / PFM methodology represents a tool to continue the studies about the switching mechanism of piezoelectric samples. The success of this investigation depends on the optimization of the proposed methodology. Here a list of recommendations for future work:

(1) The surface contamination may affect the written process of the piezoelectrics. Thus, a cleaning step should be considered. Some authors [187] propose sputtering the sample surface with oxygen ions. They have demonstrated that ferroelectric properties are well preserved.

(2) In case where the oxygen movement needs to be detected, it is suitable to perform the analysis in the in-situ ToF-SIMS / SPM instrument. The exposure of the sample to air may influence the oxidation of the surface affecting the interpretation of the oxygen signal.

(3) Compromise between lateral and mass resolutions for the ToF-SIMS spectra is important to consider. The peak interference found at high lateral resolution inhibits a proper PCA analysis. The use of delayed extraction may be an alternative if oxygen ions are not lost.

(4) ToF-SIMS studies need to be carried out in positive and negative polarization to have a proper tracking of the oxygen ions as well as other representative ions.

(5) The chemical modification of the sample due to the AFM analysis needs to be dissociated from the polarization effect. However, since the first one is not entirely understood, this step might not be straightforward.

Cette thèse est accessible à l'adresse : http://theses.insa-lyon.fr/publication/2019LYSEI121/these.pdf
© [M.A. Moreno Villavicencio], [2019], INSA Lyon, tous droits réservés

(6) PCA advanced analysis is recommended not only for the spectra interpretation but also for the ToF-SIMS images. It can be useful to perform PCA analysis directly on the ToF-SIMS images.

The comprehension of the polarization process requires advanced characterization techniques. The methodology used to obtain the results shown in this manuscript are an improvement to the classical one. Theories of chemical modification can be confirmed, and a more profound understanding of piezoelectric materials can be achieved in the future.

Cette thèse est accessible à l'adresse : http://theses.insa-lyon.fr/publication/2019LYSEI121/these.pdf
© [M.A. Moreno Villavicencio], [2019], INSA Lyon, tous droits réservés

Cette thèse est accessible à l'adresse : http://theses.insa-lyon.fr/publication/2019LYSEI121/these.pdf
© [M.A. Moreno Villavicencio], [2019], INSA Lyon, tous droits réservés

3. MEASURING AND RECOVERING ELECTRICAL PROPERTIES OF DOPED SAMPLES WITH TOF-SIMS AND SCM / SSRM

High-resolution characterization techniques are widely used to characterize devices of the microelectronics industry at the nanoscale. The transmission electron microscopy (TEM), scanning electron microscopy (SEM) and atom probe topography (APT) are some examples. The main inconvenient of these techniques is the requirement of specific sample dimensions. Thus, methods of sample preparation were developed, being the focused-ion beam (FIB) the most utilized. This sample preparation tool uses a liquid metal ion source to provide an ion beam, commonly of Ga^+, that is accelerated towards a desired area of the sample surface. The ions bombard the surface and remove the material producing uniformly thick specimens of 20 µm x 5 µm with less than a 100 nm thick in a couple of hours. The FIB spatial accuracy of a few tens of nanometers is valuable when nano-patterned samples wants to be analyzed, precise areas of the sample can be conserved. [188]

For this last characteristic, the CEA together with ST Microelectronics have decided to use the FIB to develop a novel preparation protocol that allows the extraction of a selected area of a wafer that wants to be electrically in-depth characterized. The common method consists of a cleavage of the wafer to expose the cross section of the pattern that needs to be analyzed. However, this is not a straightforward procedure for micro and nano patterns. Indeed, an ultra high precision is needed for the cleavage. For this reason, the proposed protocol includes the extraction of the selected area and the exposure of its cross-section using FIB.

However, even when through the years, this sample preparation process was optimized becoming a popular preparation tool for a wide range of materials such as biological, ceramics, polymers, metals and semiconductors [189], there is an interaction between the primary ions and the surface atoms after the collision. Indeed, artefacts such as redeposition of sputtered atoms, implantation of primary ions and amorphization due to the displacement of sample atoms are unwanted consequences and the main disadvantages of FIB sample preparation tool [190]. Ideas have emerged to reduce the created damage. A low-energy milling and a mechanical polishing of the sample are the most used. However, there is no control about the removed thickness when performing these additional procedures.

Several authors have used Monte Carlo simulations to calculate the damaged depth after sputtering. The implanted ions may influence the formation of unwanted phase and have an impact in the local composition altering the initial properties of the sample as its electronic structure. Studies have been carried out to study the effect of the focused ion beam gallium implantation into silicon, the common component of microelectronic devices.

Cette thèse est accessible à l'adresse : http://theses.insa-lyon.fr/publication/2019LYSEI121/these.pdf
© [M.A. Moreno Villavicencio], [2019], INSA Lyon, tous droits réservés

A relationship between the FIB implantation speed, ion dose and current of the primary beam on the continuous amorphous layer formation and the modification of electrical properties in silicon was investigated by Tamura *et al.* [191]. The detection and quantification of FIB damage was important in the development of this technique. Requiring high lateral resolution for these studies, the AFM and its advanced modes, especially SCM and SSRM, became widely used to determine mapping of the electrical properties of undamaged and damaged samples and quantify the affected areas [192,193].

We have used AFM operation modes to study the modification of electrical properties of the semiconductor samples after gallium implantation due to FIB preparation. We have adapted the combined ToF-SIMS and AFM methodology with the aim of using a controlled ToF-SIMS sputtering to remove the FIB damage and recover the initial properties. The two advanced AFM modes used to electrically characterize the samples were the scanning capacitance microscopy (SCM) and the scanning spreading resistance microscopy (SSRM).

3.1. SAMPLE DESCRIPTION AND PRELIMINARY PROTOCOL

Non-patterned silicon doped samples were used to obtain preliminary results and establish a suitable protocol which was then applied on patterned n-p-silicon samples used for microelectronic devices. The envisioned combined ToF-SIMS / SCM protocol was performed over the same areas of the sample and it included the following steps:

(1) Creation of reference marks using FIB when needed.
(2) FIB gallium implantation over squares of 15 x 15 μm^2 at primary energies of 5 keV, 8 keV, 16 keV and 30 keV. The square size facilitates their visibility in the ToF-SIMS images and the variation of implantation energy allows studying the influence of this one in the electrical properties of the sample.
(3) SCM image of the implanted area.
(4) ToF-SIMS sputtering of the implanted area until the signal of the gallium in the ToF-SIMS images disappears.
(5) SCM image of the sputtered area.

Issues found when performing SCM analysis made us include SSRM measurements at steps number (3) and (5) as well as adding a first step in the protocol consisting on performing initials SCM and SSRM analysis. This will be discussed in the results section.

Cette thèse est accessible à l'adresse : http://theses.insa-lyon.fr/publication/2019LYSEI121/these.pdf
© [M.A. Moreno Villavicencio], [2019], INSA Lyon, tous droits réservés

3.1.1. NON-PATTERNED SAMPLES

3.1.1.1. FIRST ANALYZED SAMPLE – DOPED SILICON

The first analyzed sample consisted of a silicon substrate negatively doped with arsenide at a concentration of 10^{19} atom/cm^3 (Figure V.11.a).

(1) One square that enclosed the implantation area was created as a reference mark. Long lines identifying the corners allowed an easy localization.
(2) Four squares of 15 x 15 µm^2 were implanted with gallium at primary energies of 5 keV (41 pA), 8 keV (70 pA), 16 keV (50 pA) and 30 keV (40 pA) for a time of 26 s, 16 s, 23 s and 30 s respectively. The dose and dwell were maintained at 4.56 pC/ µm^2 and 0.1 µs for all the experiments. The top view image of the sample is in Figure V.11.b.
(3) SCM analyses of 50 x 50 µm^2 (128 pixels x 106 pixels) were performed using contact force of about 51 nN and AC voltage of 2.5 V.
(4) A SSRM analysis were performed over a bigger area of 60 x 60 µm^2 (512 pixels x 512 pixels) with a contact force of about 1.6 µN and a negative DC voltage of -1 V.
(5) Argon clusters of about 1300 atoms were used to sputter 300 x 300 µm^2 of the surface with the implanted area included. A primary energy of 20 keV (2.2 nA) was set. The ToF-SIMS spectrometry mode was used and the gallium intensity was tracked during the sputtering. A Bi_1 beam at 15 keV (1 pA) was rastered over an area of 100 µm x 100 µm (256 x 256 pixels). The analysis was performed in non-interlaced mode using a 100 µs cycle time, 1 analysis frame, 1 sputter frame and 0.5 s of pause time. The analysis was performed with oxygen in the chamber (4.2 x 10^{-6} mbar) to enhance the gallium sputtering yield.

At this moment the cyclical ToF-SIMS / SSRM analysis started. The ToF-SIMS depth profile was stopped every time the ToF-SIMS images showed the end of gallium signal in one of the implanted squares. At this moment, the sample was transferred to the AFM where a SSRM analysis was carried out. The ToF-SIMS analysis was stopped three times: after 112 s, 202 s and 303 s of sputtering. All the SSRM analysis were performed under the same conditions as the initial.

Cette thèse est accessible à l'adresse : http://theses.insa-lyon.fr/publication/2019LYSEI121/these.pdf
© [M.A. Moreno Villavicencio], [2019], INSA Lyon, tous droits réservés

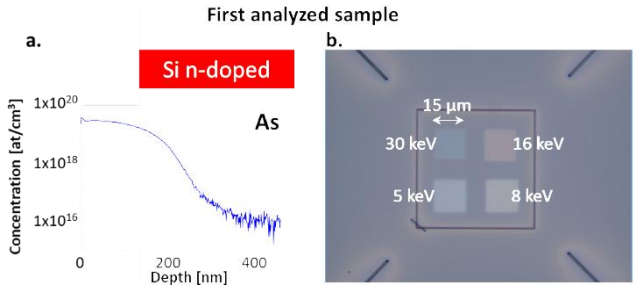

Figure V.11

First analyzed sample: n-doped silicon substrate. a. Doping concentration profile. b. Sample top view after FIB gallium implantation at: 5 keV, 8 keV, 16 keV and 30 keV.

3.1.1.2. SECOND ANALYZED SAMPLE – INTRINSIC 10^{15} at/cm^3 SILICON

The second cyclical analysis was repeated on intrinsic silicon substrates. This time we performed one implantation energy per sample to avoid several transfers between the instruments. The gallium was implanted over 15 x 15 µm^2 squares using primary energies of 8 keV, 16 keV and 30 keV with the same conditions as before. Same reference marks as for the previous implantation were created on the sample. SCM analysis was performed over an area of 25 x 25 µm^2 (512 x 512 pixels) using the same conditions as before but still, no signal was detected. The measurements were repeated using SSRM operation mode. Images of 25 µm^2 were captured for each implanted energy before and after the ToF-SIMS sputtering.

The samples were sputtered over 300 x 300 µm^2 using Ar_{1362} at 20 keV (1.8 nA). Bi_1 at 15 keV (1 pA) was used to analyze an area of 70 µm x 70 µm (256 x 256 pixels). The analysis was performed in non-interlaced mode using a 100 µs cycle time, 1 analysis frame, 1 sputter frame and 0.5 s of pause time. The sputter times were set at 61 s, 95 s and 117 s for the implanted samples at 8 keV, 16 keV and 30 keV respectively.

3.1.2. PATTERNED SAMPLES

Two patterned samples with n and p doped areas were analyzed following the previous detailed protocol. The top view of the analyzed surface before and after gallium implantation are shown in Figure V.12.a, c and b, d respectively.

3.1.2.1. FIRST ANALYZED SAMPLE

The analyzed samples consisted of patterned n-p areas. An additional step consisting of performing an SCM analysis before FIB implantation was added to the protocol. This allowed confirming whether the sample was in suitable conditions for the protocol and at the same time, to have reference data. Since the patterns of the sample were optically visible, no reference mark was needed. The protocol conditions set for the second sample are listed below:

Cette thèse est accessible à l'adresse : http://theses.insa-lyon.fr/publication/2019LYSEI121/these.pdf
© [M.A. Moreno Villavicencio], [2019], INSA Lyon, tous droits réservés

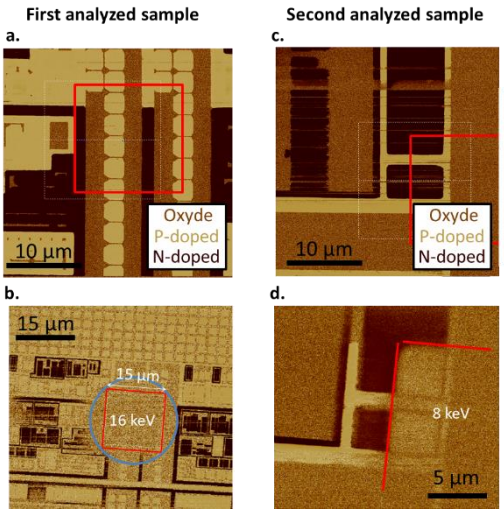

Figure V.12

Description of the two analyzed patterned samples. Top view of the samples before (a, c) and after (b, d) FIB gallium implantation. The images shown correspond to the SCM phase images.

(1) A SCM image of 30 x 30 µm^2 (1024 pixels x 1024 pixels) were captured using an AC voltage of 200 mV. The n-p doped regions as well as the oxide trenches are identified with dark, light and normal brown respectively (Figure V.12.c).

(2) An area of 15 x 15 µm^2 was implanted with gallium during 30 s at 16 keV (50 pA). This area is enclosed in the red square of Figure V.12.d.

(3) A SCM image of 60 x 60 µm^2 (512 pixels x 512 pixels) was captured immediately after the FIB preparation using an AC voltage of 1 V.

(4) Argon clusters of 1021 atoms were used to sputter 500 x 500 µm^2 including the implanted area with an energy of 20 keV (2.1 nA). The ToF-SIMS spectrometry mode was used. A Bi_1 beam at 15 keV (1 pA) was rastered over an area of 40 µm x 40 µm (256 x 256 pixels). The analysis was performed in non-interlaced mode using a 100 µs cycle time, 1 analysis frame, 1 sputter frame and 0.5 s of pause time.

(5) A SCM analysis was performed over an area of 20 x 10 µm^2 (512 pixels x 256 pixels) applying an AC voltage of 1.7 V.

(6) A SSRM image was captured over an area of 35 x 17.5 µm^2 (512 pixels x 256 pixels) applying a DC bias of -1 V.

3.1.2.2. SECOND ANALYZED SAMPLE

An additional SCM image was performed for this data to study the influence of the AFM scan on the loss of SCM signal after implantation.

(1) A SCM image was captured under the same conditions as for the first sample. The n-p doped regions as well as the oxide trenches are identified in the SCM phase image with dark, light and normal brown respectively (Figure V.12.e).

Cette thèse est accessible à l'adresse : http://theses.insa-lyon.fr/publication/2019LYSEI121/these.pdf
© [M.A. Moreno Villavicencio], [2019], INSA Lyon, tous droits réservés

(2) An area of 15 x 15 μm^2 was implanted with gallium during 27 s at 8 keV (50 pA). This area is enclosed in the red square of Figure V.12.f.

(3) A SCM image of 20 x 20 μm^2 (512 pixels x 512 pixels) was captured immediately after the FIB preparation using an AC voltage of 400 mV.

(4) Argon clusters of 1021 atoms were used to sputter 250 x 250 μm^2 with an energy of 20 keV (2.1 nA). The ToF-SIMS spectrometry mode was used and the gallium intensity was tracked during the sputtering. A Bi_1 beam at 15 keV (1 pA) was rastered over an area of 78 µm x 78 µm (256 x 256 pixels). The analysis was performed in non-interlaced mode using a 100 µs cycle time, 1 analysis frame, 1 sputter frame and 0.5 s of pause time.

(5) SCM analysis was performed using the same conditions as for the step (3).

(6) SSRM image was captured over an area of 30 x 15 μm^2 (512 pixels x 256 pixels) applying a DC bias of -1 V.

3.2. RESULTS OF THE NON-PATTERNED SILICON SUBSTRATES

The development of the ToF-SIMS / SCM / SSRM combined protocol started with the study of a highly n-doped silicon substrate after FIB irradiation at different energies. However, the SCM provides high signal for low-doped materials but small signals for damaged and high-doped samples making impossible the distinction of highly doped regions from damaged areas. Indeed, the nonexistent SCM signal detected from this sample was probably due to its elevated concentration of doping (see the capacitance behavior in Figure II.6). SSRM analyses were performed instead.

The SSRM resistance image captured after gallium implantation is shown in Figure V.13.a. The contrast seen between the implanted squares and the non-implanted area indicates a decrease in the resistance of the silicon substrate after FIB irradiation. This confirms the degradation of the electrical properties and defines a damaged area. The FIB preparation also affected the external area near the squares; a diminution of the resistance is seen as well.

We have tested the ToF-SIMS sputtering as an attempt to recover the initial resistance value. The depth-profile was stopped every time an implanted square disappeared on the Ga^+ chemical image (Figure V.13.a). After 112 s, the squares corresponding to energies of 5 keV and 8 keV showed a significant reduction of gallium, which was also seen in the SSRM image as a homogenization of the contrast between those squares and the external area.

The gallium implanted at 16 keV and 30 keV was removed from the sample after 202 s and 303 s of sputtering respectively. At this time, the resistance image showed no evidence of previous electrical damage. The resistance value of the external area near the squares increased smoothly during the sputtering process until achieving a value as the one obtained from the non-affected areas at the beginning.

Cette thèse est accessible à l'adresse : http://theses.insa-lyon.fr/publication/2019LYSEI121/these.pdf
© [M.A. Moreno Villavicencio], [2019], INSA Lyon, tous droits réservés

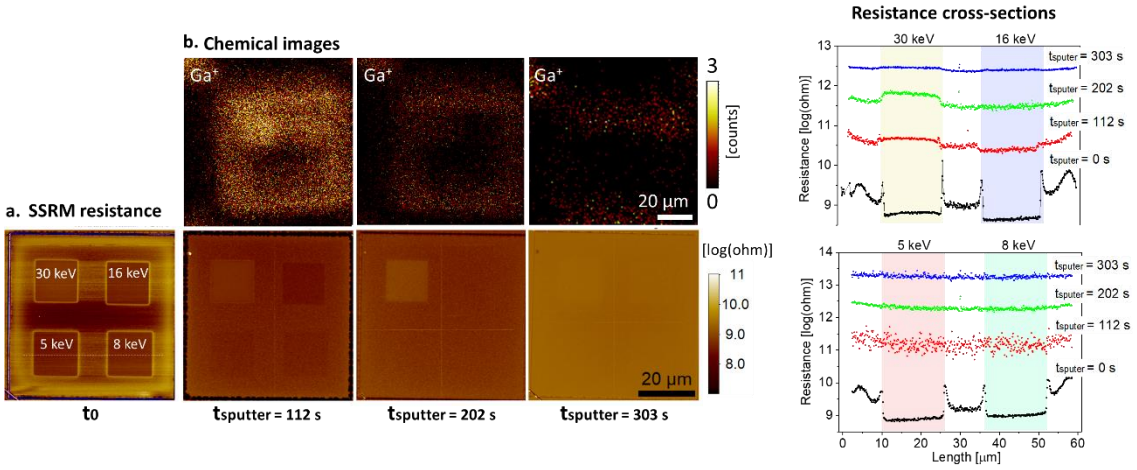

Figure V.13 *Results of the first non-patterned sample. a. SSRM resistance images captured after 0, 112 s, 202 s and 303 s of ToF-SIMS sputtering respectively. b. Sum of last three ToF-SIMS Ga^+ ToF-SIMS images per sputter cycle. The same color bar was set for all the images of a kind. c. Resistance cross-section profiles of the dashed white line shown in the initial resistance image. The areas corresponding to the gallium implantation at 30 keV, 16 keV, 5 keV and 8 keV are highlighted in yellow, blue, pink and green respectively. The resistance profiles are shifted for an easier visualization thus, the resistance values do not correspond to the real measurements.*

The homogenization of the resistance value through the ToF-SIMS sputtering is evidenced in the cross-section profiles obtained from the SSRM images after 303 s (Figure V.13.c). The final difference in the resistance of the irradiated and the non-damaged areas was 0.5 %. The initial profiles showed a swelling at the edges of the implanted area, also seen at the topography profiles of Figure V.14. Spoldi *et al.* [192] explained this phenomenon with the silicon amorphization and the redeposition of the sputtered atoms at the edges of the affected areas.

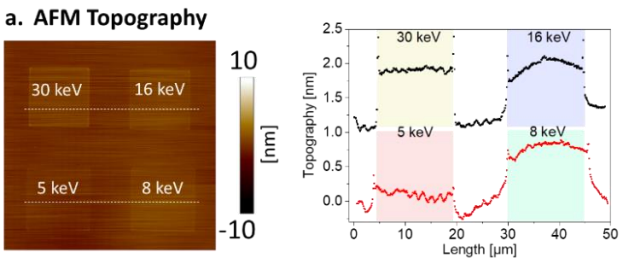

Figure V.14
AFM initial topography and cross sections profiles of the white dashed lines.

The initial AFM topographical image shows a contrast between the implanted areas and the external surface of the sample. However, the created topography does not exceed 1 nm and it seems to be dependent of the FIB primary energy. The modification of the topography has been attributed to the amorphization of the implanted areas.

Cette thèse est accessible à l'adresse : http://theses.insa-lyon.fr/publication/2019LYSEI121/these.pdf
© [M.A. Moreno Villavicencio], [2019], INSA Lyon, tous droits réservés

A slight increment in the topography of the irradiated areas was also found for the second analyzed sample. This time, an intrinsic silicon substrate was used in order to obtain a higher contrast in the SCM images. However, the SCM signal was inexistent at the irradiated and the non-irradiated area. The SCM signal not only depends on the carrier concentration of the sample but also on the existence of a good-quality oxide to form the MOS system with the AFM tip. We sputtered the sample corresponding to implantation energy of 30 keV with Ar clusters for 10 s in an attempt to clean the surface and initiate the formation of a new native oxide. Unfortunately, the SCM signal was still inexistent after the cleaning process and no further explanation could be given. Indeed, no SCM signal was found on other intrinsic silicon samples without FIB irradiation.

The degradation of the samples was studied by SSRM. The initial and final resistance images and cross-section profiles corresponding to the black dashed lines are shown in Figure V.15.a, d, e and f respectively.

The initial resistance values for the areas implanted at 8 keV and 16 keV were comparable. The difference found in the initial resistance measured at the 30 keV sample can be attributed to the cleaning process. Even when clusters of argon have been largely used in organic material because of their reduced induced-damage, the ToF-SIMS sputters superficial atoms and the damage of the sample is not null.

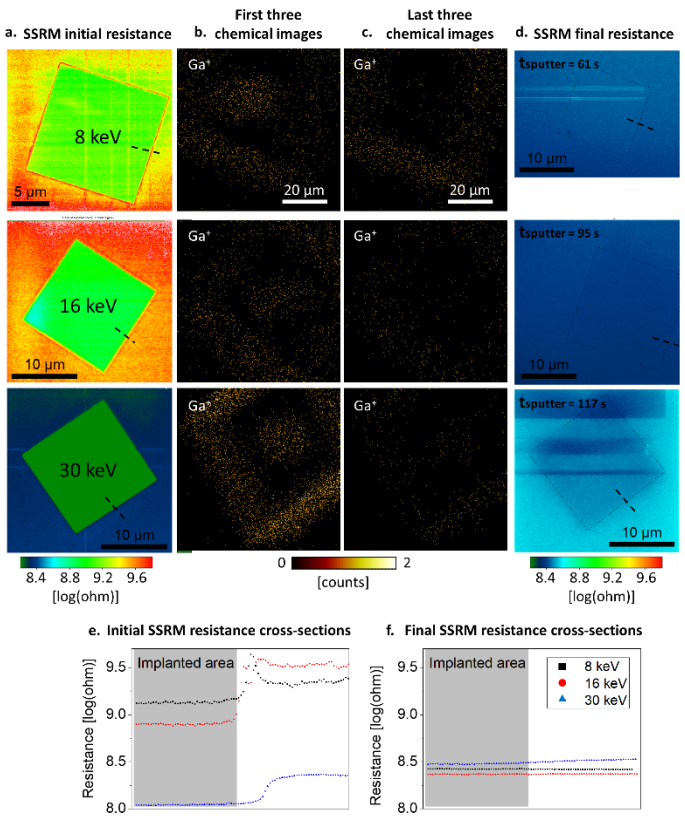

Figure V.15

Results of the second non-patterned sample. a. Initial SSRM resistance images for implantation energies of 8, 16 and 30 keV. Sum of first (b) and last (c) three ToF-SIMS Ga^+ ToF-SIMS images and, d. SSRM resistance images captured after 61, 95 and 117 s of ToF-SIMS sputtering for the corresponding implantation energy. The same color bar was set for all the images of a kind. Initial (e) and final (f) resistance cross-section profiles for implantation energies of 30, 16, and 8 keV (blue, red and black respectively). They correspond to the dashed black line shown in SSRM resistance images.

Cette thèse est accessible à l'adresse : http://theses.insa-lyon.fr/publication/2019LYSEI121/these.pdf
© [M.A. Moreno Villavicencio], [2019], INSA Lyon, tous droits réservés

The gallium removal through ToF-SIMS sputtering was performed. The sum of last three gallium ToF-SIMS images per analysis is seen in Figure V.15.b. The contrast between the irradiated and non-irradiated areas is barely seen at the end of the protocol, the highest difference is seen at 30 keV and it corresponds to a 99.6 % of the final resistance measured at the non-irradiated area. The damage created by the ToF-SIMS sputtering such as amorphization may be the reason why the final resistance values do not correspond to the initial one.

The degradation of the electrical properties of the samples is also seen at the places scanned by the SSRM (lighter and darker areas at the SSRM final images of 8 keV and 30 keV samples respectively). This might be due to the high contact force between the AFM tip and sample, which was calculated at about 1.6 µN.

The ToF-SIMS depth profile as a function of implantation energy is shown in

Figure V.16. It was not possible to convert the sputter time into a depth scale because of problems during the calibration. A delta-layer of bore within a reference sample was used to calibrate but the lack of depth resolution provided non-reasonable depth values.

The silicon intensity was similar for all the samples during the entire analysis. The time needed to remove the gallium signal increased with the implantation energy, which implies that the implantation depth of the gallium is proportional to the primary energy. In fact, Giannuzzi et Stevie [194] have found through simulation models that the created amorphous layer can be roughly assumed as the range of implantation which is in turn approximated to the value of the primary energy of the ion beam.

The obtained results were used to validate a preliminary protocol. However, since the real microelectronic devices are composed of n-p-oxide regions, we explored the future of this combined ToF-SIMS / SCM / SSRM methodology on patterned samples.

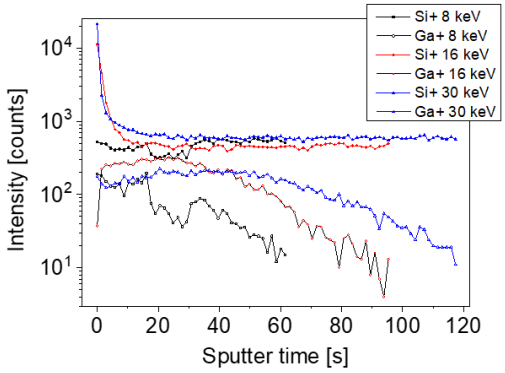

Figure V.16

ToF-SIMS depth profiles of the gallium implanted areas at 30 keV, 16 keV, and 8 keV are in blue, red and black respectively.

Cette thèse est accessible à l'adresse : http://theses.insa-lyon.fr/publication/2019LYSEI121/these.pdf
© [M.A. Moreno Villavicencio], [2019], INSA Lyon, tous droits réservés

3.3. RESULTS OF THE PATTERNED SAMPLES

The combined ToF-SIMS / SCM / SSRM methodology for recovering electrical properties after FIB irradiation was tested on two patterned samples with initial sample topography. A SCM analysis was added to the protocol before gallium implantation to assure an initial SCM signal. The n-p doped areas are well identified for both samples in the initial SCM image (Figure V.17.a and Figure V.18a). The dark brown distinguishes the n-doped patterns while the white or desert sand color the p-doped patterns. The oxide areas are shown in chocolate brown and they correspond to a null SCM signal.

The gallium was implanted in both samples over an area of 15 x 15 μm^2. The irradiated area is easily recognized on the SCM images captured after the implantation (Figure V.17.b and Figure V.18.b). However, the identified damaged area is larger than the implanted region. In fact, it was recorded over the perimeter of 20 µm enclosed by the blue circle in Figure V.17.b. The SCM analysis of the third sample repeated 3 hours after the FIB implantation showed the propagation of the area where the signal is missing. Moreover, the SCM images captured 9 days later showed almost inexistent SCM signal. The previous SCM analyses and the sample storage after them were performed under room conditions; thus, degradation and contamination of the sample were possible. Spoldi *et al.* [192,192] have also remarked this broadening effect and they suggested that interactions of gallium atoms with the superficial atoms may be occurring.

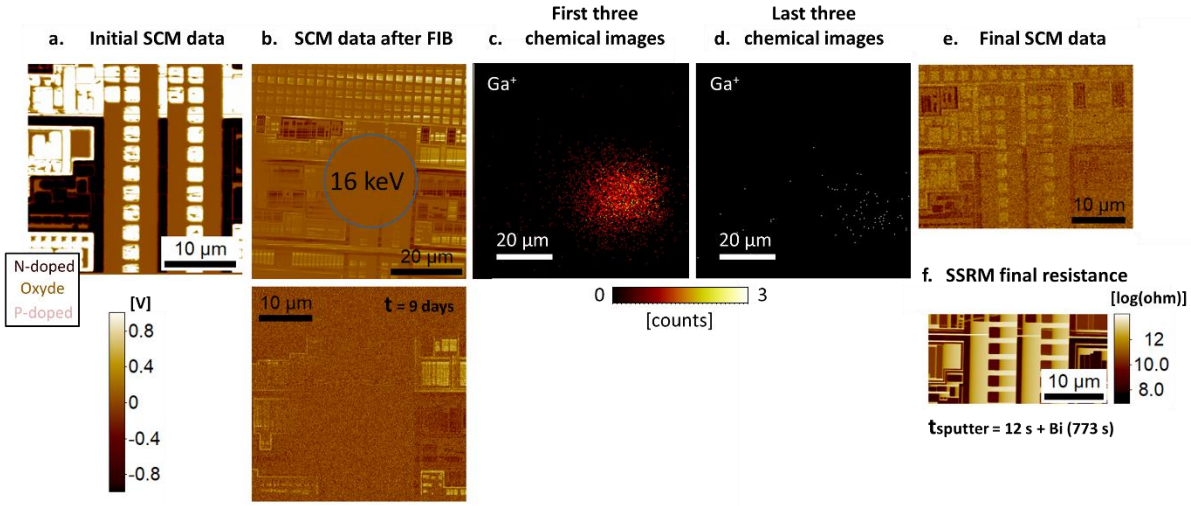

Figure V.17 Results of the first patterned sample. SCM images captured before (a) and after (b) FIB gallium implantation. This last one was repeated 9 days after FIB preparation. c. Sum of last three ToF-SIMS Ga^+ ToF-SIMS images. SCM data (d) and SSRM resistance (e) images captured after 12 s of ToF-SIMS sputtering plus 773 s of surface analysis with Bi_1. The same color bar was set for all the images of a kind.

Cette thèse est accessible à l'adresse : http://theses.insa-lyon.fr/publication/2019LYSEI121/these.pdf
© [M.A. Moreno Villavicencio], [2019], INSA Lyon, tous droits réservés

The samples were sputtered until the gallium disappeared from the gallium chemical image (Figure V.17.c-d and Figure V.18.c). The SCM signal from the implanted area was recovered for the second sample but the intensity of the signal was low (Figure V.17.d). However, no SCM signal was detected for the second sample after sputtering (Figure V.18.e). Two phenomena could have been involved. The first one is the lack of a proper native oxide formation after the sputtering and the second is related to the amorphization and damage created in the sample by the ToF-SIMS bombardment. Both reasons are realistic and they cannot be dismissed. An approach to overcome those factors is to perform a SSRM analysis instead because the high contact force would improve the electrical contact. The final resistance images are shown in Figure V.17.f and Figure V.18.e for the first and second samples respectively. They cannot be compared with initial values to provide a proper conclusion but they are showing a variation in the resistance within p-doped regions for the first sample and oxide regions for the second sample.

Figure V.18.f shows the evolution of the sample topography during the protocol. The height increased after the ToF-SIMS sputtering and the shape of the elevated areas was slightly modified after FIB preparation and the gallium removal. For patterned samples with initial topography, especial consideration of the artefacts found when sputtering nanostructure is needed.

Cette thèse est accessible à l'adresse : http://theses.insa-lyon.fr/publication/2019LYSEI121/these.pdf
© [M.A. Moreno Villavicencio], [2019], INSA Lyon, tous droits réservés

3.4. PROPOSED PROTOCOL FOR FUTURE WORK

Establishing a combined methodology implies a compromise between the limitations of the characterization techniques and the final application that want to be achieved. The preliminary results that have been shown in this manuscript have promoted the improvements of the methodology. A list of the restraints that need to be considered are:

(1) A high SCM signal requires samples with specific characteristics. The signal is inversely proportional to the upper oxide thickness. The need of a proper thin native oxide restraints the utilization of this technique after ToF-SIMS analysis.

(2) The elevated contact force between the AFM tip and the sample during the SSRM analysis may create an additional damage to the surface. This can be dismissed before the ToF-SIMS sputtering because the surface will be removed but it needs to be considered when performing the last step of the protocol, once the device is at the final stage.

(3) The ToF-SIMS sputtering involves collisions within the sample. This can cause unwanted results as ion implantation, roughness development, amorphization, among others.

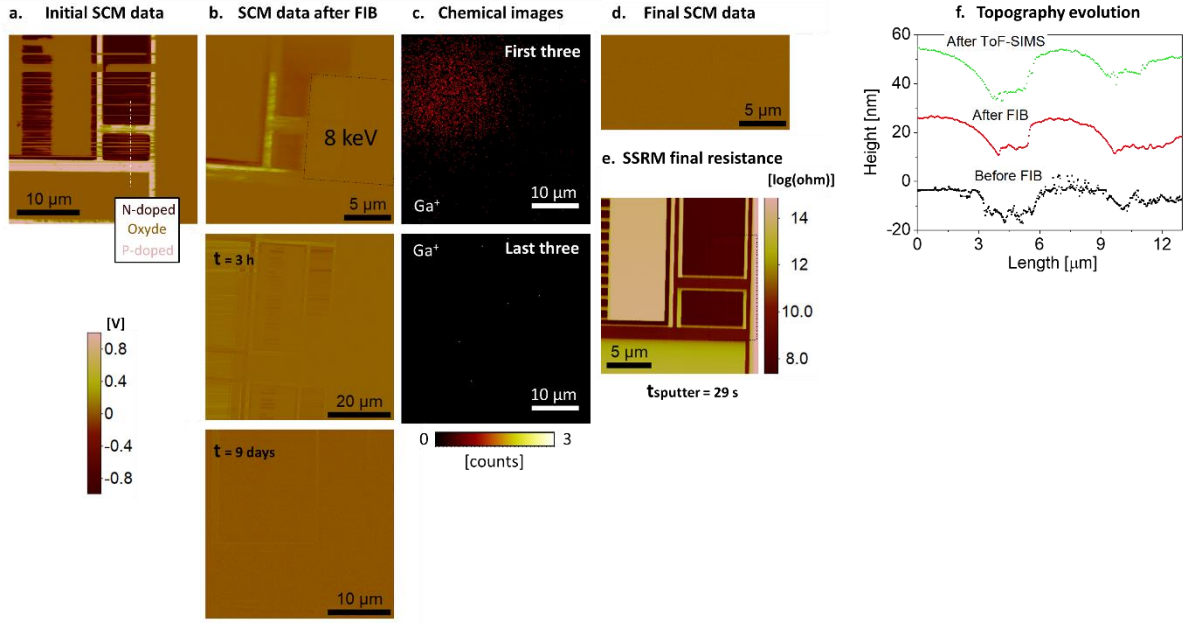

Figure V.18 *Results of the second patterned sample. SCM images captured before (a) and after (b) FIB gallium implantation. This last one was repeated 3 h and 9 days after FIB preparation. c. Sum of last three ToF-SIMS Ga^+ ToF-SIMS images. SCM data (d) and SSRM resistance (e) images captured after 29 s of ToF-SIMS sputtering. The same color bar was set for all the images of a kind. f. AFM topography profile measured before, after FIB preparation and after ToF-SIMS sputtering. They correspond to the dashed white line in the initial SCM image*

Cette thèse est accessible à l'adresse : http://theses.insa-lyon.fr/publication/2019LYSEI121/these.pdf
© [M.A. Moreno Villavicencio], [2019], INSA Lyon, tous droits réservés

A deep study is needed to set the most suitable analysis conditions taking into consideration that they may change for every sample.

(4) The time needed for a FIB / SCM / ToF-SIMS sample preparation protocol needs to be optimized. The utilization of in-situ FIB / ToF-SIMS / AFM instruments can be a good alternative.

After having carried out the combined methodology several times on different samples, the following steps are proposed:

(1) SCM and SSRM analyses of the area to be implanted and an area nearby that will not be affected by the FIB.
(2) FIB gallium implantation.
(3) SCM and SSRM analyses of the implanted area and the area nearby that was previously analyzed.
(4) ToF-SIMS sputtering assuring that both analyzed areas by the SCM and SSRM are inside the crater. The analysis should be stopped once the gallium signal disappears from the Ga^+ chemical image.
(5) SCM and SSRM analyses of the implanted area and the area nearby.

This protocol would allow the initial electrical behaviour of the sample to be compared with the one obtained after implantation and sputtering.

At the same time, the analyses of the properties from the area nearby permit the estimation of the damaged created only by the ToF-SIMS sputtering. This would help to improve the sputtering conditions.

Cette thèse est accessible à l'adresse : http://theses.insa-lyon.fr/publication/2019LYSEI121/these.pdf
© [M.A. Moreno Villavicencio], [2019], INSA Lyon, tous droits réservés

Cette thèse est accessible à l'adresse : http://theses.insa-lyon.fr/publication/2019LYSEI121/these.pdf
© [M.A. Moreno Villavicencio], [2019], INSA Lyon, tous droits réservés

4. CONCLUSIONS

The impact of the ToF-SIMS and AFM combined methodology was successfully demonstrated thanks to the incorporation of AFM advanced operation modes. Its wide range of applications was confirmed. Two different applications were chosen to show the applicability of this methodology to overcome classical characterization.

The first part of this chapter presented a combination of the ToF-SIMS with piezoresponse force microscopy and kelvin force microscopy. It was used as a tool to investigate the chemical changes caused by the poling process in ferroelectric materials. The local polarization of ferroelectric samples using the AFM tip was introduced and the reasons for believing that chemical modification is behind the contrast observed during PFM images were mentioned. The combined ToF-SIMS / PFM methodology was tested on ferroelectric and non-ferroelectric samples. Chemical changes are observed in the ToF-SIMS images after local polarization were discussed, especially the chemical contrast created by the AFM scans when no bias was applied. The hypothesis explaining the PFM signal when polarizing non-ferroelectric samples were discussed and individually studied using ToF-SIMS results and advanced multivariate data analysis. This first part concluded with the perspective of this combined protocol to continue the study of piezoelectric behaviour after local application of a DC voltage.

The second part of this chapter introduced the combination of scanning capacitance microscopy and scanning spreading resistance microscopy with ToF-SIMS to optimize the existing FIB sample preparation protocol. The damages produced by FIB gallium implantation were presented and the electrical degradation of the sample was confirmed through SCM and SSRM analyses. ToF-SIMS sputtering was used to remove the implanted gallium in an attempt to recover the initial electrical properties. The implantation depth was directly proportional to the FIB primary energy. It was corroborated through the ToF-SIMS depth profiles.

The results obtained when this ToF-SIMS / SCM / SSRM combined methodology was tested on patterned and non-patterned samples consisting on n-p doped regions were presented. Diverse issues such as weak SCM signal were encountered. They were attributed to high carrier concentration on the sample or the existence of a thick oxide upper layer. This part of the chapter concluded with suggestions about the optimization of this methodology and the details of the protocol proposed for future work.

Cette thèse est accessible à l'adresse : http://theses.insa-lyon.fr/publication/2019LYSEI121/these.pdf
© [M.A. Moreno Villavicencio], [2019], INSA Lyon, tous droits réservés

Cette thèse est accessible à l'adresse : http://theses.insa-lyon.fr/publication/2019LYSEI121/these.pdf
© [M.A. Moreno Villavicencio], [2019], INSA Lyon, tous droits réservés

FINAL CONCLUSION AND PERSPECTIVES

The development of microelectronic technology came with the miniaturization of the devices. The understanding and study of the efficiency of these devices became only possible through high-resolution chemical analysis of their three dimensions. The ToF-SIMS is a powerful characterization technique that allows 3D chemical characterization with detection limits in the range of parts-per-million. It provides a mass spectrum for each analyzed pixel and its mass resolution of 10^4 M/dM allows the distinction of particles with the same nominal mass. The registered spectra are used to generate ToF-SIMS images from where depth-profiles are extracted. Despite the good performance of the ToF-SIMS, the obtained chemical information has a lateral resolution of 150 nm, which is not sufficient for many analytical problems. The correlation of characterization techniques have emerged to overcome the existing limitations. Indeed, the combination of ToF-SIMS with high lateral resolution characterization techniques have been standing out within the scientific community for the past few years. This thesis manuscript was oriented to the improvement and development of the combination of ToF-SIMS with AFM.

The AFM is a high-resolution characterization technique that was conceived to measure the surface topography through the interaction force between the sample and a nanometric tip located above. Over the years, the AFM principle was adapted to measure not only the topography but also diverse properties of the sample. The AFM currently provides maps of the analyzed area with the topographical, electrical, magnetic, piezoelectric and mechanical information of the sample measured with a lateral resolution of a few nanometers. The combination of these high-resolution maps with the chemical ToF-SIMS information results in a promising improvement of the characterization as it is known.

CHAPTER II presented a combined ToF-SIMS and AFM methodology that includes an experimental section and a data processing stage. The experimental protocol was described as a cyclical ToF-SIMS, AFM and profilometer analysis where the topography and crater depth are measured at the beginning, at the end and every time an interface is detected in the ToF-SIMS depth-profile. The importance of analyzing the same area of the sample at every stage of the protocol was stressed. The second part of the methodology comprised the data processing, which was divided into raw data processing and advanced data treatment. The first one included the plane fit and peak calibration of AFM images and ToF-SIMS spectra respectively, as well as the localization of every topography map at the depth from where it was captured. The advanced data processing section detailed the procedure needed to unify the pixel size of all the data and the process for a proper alignment of the ToF-SIMS and AFM images.

Cette thèse est accessible à l'adresse : http://theses.insa-lyon.fr/publication/2019LYSEI121/these.pdf
© [M.A. Moreno Villavicencio], [2019], INSA Lyon, tous droits réservés

Three main results are obtained from the proposed methodology: (i) a topography-corrected 3D ToF-SIMS visualization, (ii) sputter rate maps of the analyzed area and (iii) overlays of the ToF-SIMS and AFM information. Each of them was used for different applications within the three years of thesis. Chapters three, four and five presented the most promising results.

CHAPTER III introduced the problems found when performing 3D ToF-SIMS analysis of heterogeneous structures with initial topography. The lack of topography consideration in the ToF-SIMS images creates a distortion of the 3D ToF-SIMS data set. The AFM was presented as a tool to correct the data set using the topographical images captured at each interface. The combined ToF-SIMS and AFM methodology was applied on a GaAs / SiO_2 heterostructure whose ToF-SIMS information could not be reconstructed in 3D following classical procedures. Indeed, its initial topography and its composition of materials with different sputter rates distorted the ToF-SIMS images. Through the combined ToF-SIMS and AFM protocol, a sputter rate map was determined for each sputter cycle. They were used to transform the sputter time into sputter depth providing then the 3D chemical visualization of the sample with accurate depth scale. Furthermore, the methodology provided overlays of the chemical information over topographical surfaces, which in turn were used to analyze the surface characteristics and the evolution of the topography during the sputtering.

CHAPTER IV detailed how the protocol to create sputter rate maps was used to investigate the artefacts produced when nanostructures are analyzed using ToF-SIMS. The ToF-SIMS analysis of nanostructures may not be straightforward because of limited lateral resolution and even when it is not a limitation, phenomena such as shadowing effect may be encountered. This chapter used the ToF-SIMS and AFM combined methodology to detect sputtering artefacts and to study the most suitable analysis conditions to reduce them. The influence of primary energy and ion beam orientation on the artefacts development were studied for a nano-patterned sample. However, difficulties came when a non-structured sample was analyzed. The sample consisted on nano-cracks without a former orientation hampering the optimization of the ToF-SIMS analysis conditions. The AFM topographical profiles were used to corroborate the conclusions extracted from the ToF-SIMS chemical analysis. They showed the existence of a shadowing effect altering the depth profiles and the judgment about the sample. A realistic understanding of the sample as well as the study of the visible cracks were then possible through the analysis of the topographical data.

The ToF-SIMS and AFM are complementary techniques. The correlation of their results, seen as 3D or 2D overlay, may provide the answer to current analytical questions of different applications and fields. The initial step is the adaptation of the ToF-SIMS / AFM combined methodology according to the state-of-the-art queries for that specific application. It may involve the utilization of AFM advanced operation modes.

Cette thèse est accessible à l'adresse : http://theses.insa-lyon.fr/publication/2019LYSEI121/these.pdf
© [M.A. Moreno Villavicencio], [2019], INSA Lyon, tous droits réservés

The implementation of the protocol would provide preliminary results that can be used for its optimization. This process was shown in CHAPTER V for two different applications. The first part of the chapter illustrated how the combined ToF-SIMS and AFM methodology was used in the study of piezoelectric materials. The methodology was adapted to include PFM and KFM analysis. The ToF-SIMS confirmed chemical modification at areas that were previously polarized using the AFM tip. However, it also detected a chemical change at the areas where the AFM scanned without voltage application. The contact force between the tip and sample is believed to damage the surface. The PFM signal of non-ferroelectric samples was also studied. The existence of superficial charges was confirmed through KFM analysis and chemical modification of the areas scanned by AFM was also seen. The overlay of ToF-SIMS / PFM / KFM seems to be the tool for the understanding of PFM signal in non-ferroelectrics. However, further investigation is required to provide a proper conclusion. An alternative procedure to reduce the degradation created during FIB sample preparation was detailed in the second part of this chapter. A particular ToF-SIMS / SCM / SSRM protocol was developed to measure and remove electrical damage of devices. The SCM analyses presented issues when analyzing highly doped samples and devices with a too thick oxide layer. They were overcome by performing SSRM analysis instead. Sputtering in the ToF-SIMS was shown to be effective in removing gallium implantation but secondary damages from the sputtering are still unknown. An optimization of the protocol was proposed for future work.

The combination of these two powerful techniques became a tool for advanced characterization of complex systems and devices. After three years of optimization and evaluation of the protocol for specific objectives, I can see that the adaptation of this methodology using various AFM operation modes opens an unlimited number of applications. I recommend the following work to complement the already started investigations:

(1) An advanced study of topography evolution of vertical interfaces through the alignment of AFM profiles taken before and after ToF-SIMS sputtering:

- The alignment using topography maps is not a straightforward procedure because of the distortion of the interfaces. However, it can be done using the map of an invariant property obtained with advanced AFM operation mode.
- The procedure to obtain sputter rate maps can be completed once the alignment is done.

(2) Continue the study of piezoelectric materials:

- In order to detect an oxygen migration, it is important to assure that the oxygen detected in the depth-profiles is not coming from surface contamination. For this, it is recommended to perform the analysis in-situ and clean the surface until the carbon intensity is low before starting the writing of domains.
- Perform high mass resolution analyses to avoid the convolution of interesting peaks.

Cette thèse est accessible à l'adresse : http://theses.insa-lyon.fr/publication/2019LYSEI121/these.pdf
© [M.A. Moreno Villavicencio], [2019], INSA Lyon, tous droits réservés

- Further analysis of the chemical modification produced by the AFM scan in order to dissociate this effect from the one produced by the switching of domains.

(3) Implementation of the proposed protocol to complete the FIB sample preparation procedure:

- Optimization of the ToF-SIMS analysis conditions to decrease the damage created when removing the gallium implantation from the devices.
- Measurement of the removed depth after ToF-SIMS sputtering.
- Calculation of the impact in the electrical properties of the ToF-SIMS sputtering.

Lastly, as the utilization of the ex-situ or in-situ ToF-SIMS / AFM combined methodology was shown to be very versatile, there may be many other applications that were not mentioned here.

Cette thèse est accessible à l'adresse : http://theses.insa-lyon.fr/publication/2019LYSEI121/these.pdf
© [M.A. Moreno Villavicencio], [2019], INSA Lyon, tous droits réservés

BIBLIOGRAPHY

[1] Bargon, J. (2013) Methods and Materials in Microelectronic Technology. Springer Science & Business Media, .

[2] (n.d.) Early Microelectronics — ETHW.

[3] Courtland, R. (2017) Intel Now Packs 100 Million Transistors in Each Square Millimeter. *IEEE Spectrum: Technology, Engineering, and Science News*.

[4] Flamm, K. (2018) Measuring Moore's Law: Evidence from Price, Cost, and Quality Indexes. National Bureau of Economic Research, Inc, .

[5] Silva Bijit, L. (2003) Microelectronics. *Departamento de Electrónica · Universidad Técnica Federico Santa María*.

[6] Zemin, J. (2010) Accelerate the Development of the Electronics Industry and Meet the Challenges of the New Technological Revolution*. in: J. Zemin (Ed.), Dev. Chinas Inf. Technol. Ind., Academic Press, Singaporepp. 79–83.

[7] Vollrath, J. (n.d.) History Microelectronics. *Hochschule Kempten - Fakultät Elektrotechnik*.

[8] Reuss, R.H., Chalamala, B.R., Moussessian, A., Kane, M.G., Kumar, A., Zhang, D.C., et al. (2005) Macroelectronics: Perspectives on Technology and Applications. *Proceedings of the IEEE*. 93 (7), 1239–1256.

[9] Kraft, M. (n.d.) Microélectronique et microsystèmes - Microélectronique. Analyse et CAO des circuits intégrés. *Université de Liège - Faculté Des Sciences Appliquées*.

[10] Joshi, M., Bhattacharyya, A., and Ali, S.W. (2008) Characterization techniques for nanotechnology applications in textiles. *IJFTR Vol.33(3) [September 2008]*.

[11] Mourdikoudis, S., Pallares, R.M., and Thanh, N.T.K. (2018) Characterization techniques for nanoparticles: comparison and complementarity upon studying nanoparticle properties. *Nanoscale*. 10 (27), 12871–12934.

[12] Khanna, V.K. (2016) Nanocharacterization Techniques. in: V.K. Khanna (Ed.), Integr. Nanoelectron. Nanoscale CMOS Post-CMOS Allied Nanotechnologies, Springer India, New Delhipp. 419–442.

[13] De Rosier, D.J. and Klug, A. (1968) Reconstruction of three dimensional structures from electron micrographs. *Nature*. 217 (5124), 130–134.

[14] Ercius, P., Alaidi, O., Rames, M.J., and Ren, G. (2015) Electron Tomography: A Three-Dimensional Analytic Tool for Hard and Soft Materials Research. *Advanced Materials (Deerfield Beach, Fla.)*. 27 (38), 5638–5663.

[15] Midgley, P.A. and Weyland, M. (2003) 3D electron microscopy in the physical sciences: the development of Z-contrast and EFTEM tomography. *Ultramicroscopy*. 96 (3), 413–431.

Cette thèse est accessible à l'adresse : http://theses.insa-lyon.fr/publication/2019LYSEI121/these.pdf
© [M.A. Moreno Villavicencio], [2019], INSA Lyon, tous droits réservés

[16] Ersen, O., Florea, I., Hirlimann, C., and Pham-Huu, C. (2015) Exploring nanomaterials with 3D electron microscopy. *Materials Today*. 18 (7), 395–408.

[17] Gröner, E. and Hoppe, P. (2006) Automated ion imaging with the NanoSIMS ion microprobe. *Applied Surface Science*. 252 (19), 7148–7151.

[18] Kelly, T.F. and Miller, M.K. (2007) Atom probe tomography. *Review of Scientific Instruments*. 78 (3), 031101.

[19] Miller, M.K. (2012) Atom Probe Tomography: Analysis at the Atomic Level. Springer Science & Business Media, .

[20] (n.d.) Time-Of-Flight Secondary Ion Mass Spectrometry. *EAG Laboratories*.

[21] Leggett, G.J. and Vickerman, J.C. (1991) Chapter 4. Static secondary ion mass spectrometry (SSIMS)? an emerging surface mass spectrometry. *Annual Reports Section "C" (Physical Chemistry)*. 88 77.

[22] Wei, X., Zhao, L., Wang, J., Zeng, Y., and Li, J. (2014) Characterization of nitride-based LED materials and devices using TOF-SIMS: Characterization of LED materials and devices using TOF-SIMS. *Surface and Interface Analysis*. 46 (S1), 299–302.

[23] Shahwan, T. and Erten, H.N. (2009) Sorption studies of Cs+, Ba2+, and Co2+ ions on bentonite using radiotracer, ToF-SIMS, and XRD techniques. *Radiochimica Acta*. 89 (11–12), 799–804.

[24] Rondon, S., Wilkinson, W.R., Proctor, A., Houalla, M., and Hercules, D.M. (1995) Characterization of Mo/C Catalysts by XRD, XPS, and TOF-SIMS. *The Journal of Physical Chemistry*. 99 (45), 16709–16713.

[25] Lu, H.B., Campbell, C.T., Graham, D.J., and Ratner, B.D. (2000) Surface Characterization of Hydroxyapatite and Related Calcium Phosphates by XPS and TOF-SIMS. *Analytical Chemistry*. 72 (13), 2886–2894.

[26] Weng, L.T., Poleunis, C., Bertrand, P., Carlier, V., Sclavons, M., Franquinet, P., et al. (1995) Sizing removal and functionalization of the carbon fiber surface studied by combined TOF SIMS and XPS. *Journal of Adhesion Science and Technology*. 9 (7), 859–871.

[27] Langer, E. (2019) Advanced chemical characterization of organic electronic materials and devices, Université Namur, 2019.

[28] Gazi, E., Dwyer, J., Lockyer, N., Gardner, P., Vickerman, J.C., Miyan, J., et al. (2004) The combined application of FTIR microspectroscopy and ToF-SIMS imaging in the study of prostate cancer. *Faraday Discussions*. 126 (0), 41–59.

[29] Peterson, R.E. and Tyler, B.J. (2003) Surface composition of atmospheric aerosol: individual particle characterization by TOF-SIMS. *Applied Surface Science*. 203–204 751–756.

[30] Wang, Z., Liu, J., Zhou, Y., Neeway, J.J., Schreiber, D.K., Crum, J.V., et al. (2016) Nanoscale imaging of Li and B in nuclear waste glass, a comparison of ToF-SIMS, NanoSIMS, and APT. *Surface and Interface Analysis*. 48 (13), 1392–1401.

Cette thèse est accessible à l'adresse : http://theses.insa-lyon.fr/publication/2019LYSEI121/these.pdf
© [M.A. Moreno Villavicencio], [2019], INSA Lyon, tous droits réservés

[31] Ribeiro, J., DaBoit, K., Flores, D., Kronbauer, M.A., and Silva, L.F.O. (2013) Extensive FE-SEM/EDS, HR-TEM/EDS and ToF-SIMS studies of micron- to nano-particles in anthracite fly ash. *Science of The Total Environment*. 452–453 98–107.

[32] De Wolf, P., Stephenson, R., Trenkler, T., Clarysse, T., Hantschel, T., and Vandervorst, W. (2000) Status and review of two-dimensional carrier and dopant profiling using scanning probe microscopy. *Journal of Vacuum Science & Technology B: Microelectronics and Nanometer Structures Processing, Measurement, and Phenomena*. 18 (1), 361–368.

[33] Teichert, C. and Beinik, I. (2011) Conductive Atomic-Force Microscopy Investigation of Nanostructures in Microelectronics. in: B. Bhushan (Ed.), Scanning Probe Microsc. Nanosci. Nanotechnol. 2, Springer Berlin Heidelberg, Berlin, Heidelbergpp. 691–721.

[34] Tanimoto, M. and Vatel, O. (1996) Kelvin probe force microscopy for characterization of semiconductor devices and processes. *Journal of Vacuum Science & Technology B: Microelectronics and Nanometer Structures Processing, Measurement, and Phenomena*. 14 (2), 1547–1551.

[35] Berger, M. (2008) Atomic Force Microscopy (AFM) - A key tool for nanotechnology. *Nanowerk*.

[36] Wirtz, T., Fleming, Y., Gerard, M., Gysin, U., Glatzel, T., Meyer, E., et al. (2012) Design and performance of a combined secondary ion mass spectrometry-scanning probe microscopy instrument for high sensitivity and high-resolution elemental three-dimensional analysis. *Review of Scientific Instruments*. 83 (6), 063702.

[37] Mick, U., Eichhorn, V., Wortmann, T., Diederichs, C., and Fatikow, S. (2010) Combined nanorobotic AFM/SEM system as novel toolbox for automated hybrid analysis and manipulation of nanoscale objects. in: 2010 IEEE Int. Conf. Robot. Autom., pp. 4088–4093.

[38] Fisher, G.L., Dickinson, M., Bryan, S.R., and Moulder, J. (2008) C60 sputtering of organics: A study using TOF-SIMS, XPS and nanoindentation. *Applied Surface Science*. 255 (4), 819–823.

[39] Iacob, E., Demenev, E., Giubertoni, D., Barozzi, M., Gennaro, S., and Bersani, M. (2013) Development of nano-roughness under SIMS ion sputtering of germanium surfaces: Nano-roughness under SIMS sputtering on germanium surfaces. *Surface and Interface Analysis*. 45 (1), 409–412.

[40] Mouhib, T., Poleunis, C., Wehbe, N., Michels, J.J., Galagan, Y., Houssiau, L., et al. (2013) Molecular depth profiling of organic photovoltaic heterojunction layers by ToF-SIMS: comparative evaluation of three sputtering beams. *The Analyst*. 138 (22), 6801.

[41] Cirlin, E., Vajo, J.J., Doty, R.E., and Hasenberg, T.C. (1991) Ion-induced topography, depth resolution, and ion yield during secondary ion mass spectrometry depth profiling of a GaAs/AlGaAs superlattice: Effects of sample rotation. *Journal of Vacuum Science & Technology A: Vacuum, Surfaces, and Films*. 9 (3), 1395–1401.

[42] Kozole, J., Willingham, D., and Winograd, N. (2008) The effect of incident angle on the C60+ bombardment of molecular solids. *Applied Surface Science*. 255 (4), 1068–1070.

Cette thèse est accessible à l'adresse : http://theses.insa-lyon.fr/publication/2019LYSEI121/these.pdf
© [M.A. Moreno Villavicencio], [2019], INSA Lyon, tous droits réservés

[43] Netcheva, S. and Bertrand, P. (2001) Ion-beam-induced morphology on the surface of thin polymer films at low current density and high ion fluence. *Journal of Polymer Science Part B: Polymer Physics*. 39 (3), 314–325.

[44] Kang, M., Lee, J., and Lee, Y. (2014) Comparison of nanostructured blend homopolymers and diblock copolymers by AFM and TOF-SIMS: Characterization of blend homopolymers and diblock copolymers. *Surface and Interface Analysis*. 46 (S1), 105–109.

[45] Terlier, T. (2015) Analyse par ToF-SIMS de matériaux organiques pour les applications en électronique organique, phdthesis, Université Claude Bernard - Lyon I, 2015.

[46] Lau, Y.-T.R., Weng, L.-T., Ng, K.-M., and Chan, C.-M. (2008) Lamellar orientation on the surface of a polymer determined by ToF-SIMS and AFM. *Applied Surface Science*. 255 (4), 1001–1005.

[47] Bernard, L., Heier, J., Paul, W., and Hug, H.J. (2014) The SFM/ToF-SIMS combination for advanced chemically-resolved analysis at the nanoscale. *Nuclear Instruments and Methods in Physics Research Section B: Beam Interactions with Materials and Atoms*. 339 85–90.

[48] Wendeln, C., Singh, I., Rinnen, S., Schulz, C., F. Arlinghaus, H., A. Burley, G., et al. (2012) Orthogonal, metal-free surface modification by strain-promoted azide– alkyne and nitrile oxide – alkene / alkyne cycloadditions. *Chemical Science*. 3 (8), 2479–2484.

[49] Brison, J., Robinson, M.A., Benoit, D.S.W., Muramoto, S., Stayton, P.S., and Castner, D.G. (2013) TOF-SIMS 3D Imaging of Native and Non-Native Species within HeLa Cells. *Analytical Chemistry*. 85 (22), 10869–10877.

[50] Takeda, S., Fukawa, M., Hayashi, Y., and Matsumoto, K. (1999) Surface OH group governing adsorption properties of metal oxide films. *Thin Solid Films*. 339 (1), 220–224.

[51] Jimenez, M., Delaplace, G., Nuns, N., Bellayer, S., Deresmes, D., Ronse, G., et al. (2013) Toward the understanding of the interfacial dairy fouling deposition and growth mechanisms at a stainless steel surface: A multiscale approach. *Journal of Colloid and Interface Science*. 404 192–200.

[52] Jeong, D.S., Schroeder, H., Breuer, U., and Waser, R. (2008) Characteristic electroforming behavior in Pt/TiO2/Pt resistive switching cells depending on atmosphere. *Journal of Applied Physics*. 104 (12), 123716.

[53] Ke, W., Xiao, C., Wang, C., Saparov, B., Duan, H.-S., Zhao, D., et al. (2016) Employing Lead Thiocyanate Additive to Reduce the Hysteresis and Boost the Fill Factor of Planar Perovskite Solar Cells. *Advanced Materials*. 28 (26), 5214–5221.

[54] Ievlev, A.V., Brown, C.C., Agar, J.C., Velarde, G.A., Martin, L.W., Belianinov, A., et al. (2018) Nanoscale Electrochemical Phenomena of Polarization Switching in Ferroelectrics. *ACS Applied Materials & Interfaces*.

[55] Shin, H.-C. and Song, J.-T. (2011) High resolution 3-D imaging for characteristics of (111)-oriented Pb(Zr0.35Ti0.65)O3 thin film by using time-of-flight secondary ion mass

Cette thèse est accessible à l'adresse : http://theses.insa-lyon.fr/publication/2019LYSEI121/these.pdf
© [M.A. Moreno Villavicencio], [2019], INSA Lyon, tous droits réservés

spectrometry and piezoresponse force microscopy. *Electronic Materials Letters*. 7 (3), 265.

[56] Fu, D., Weng, L.-T., Du, B., Tsui, O.K.C., and Xu, B. (2002) Solventless Polymerization at the Gas–Solid Interface to Form Polymeric Thin Films. *Advanced Materials*. 14 (5), 339–343.

[57] Zhao, F., Wang, C., and Zhan, X. (2018) Morphology Control in Organic Solar Cells. *Advanced Energy Materials*. 8 (28), 1703147.

[58] Hazut, O. and Yerushalmi, R. (2017) Direct Dopant Patterning by a Remote Monolayer Doping Enabled by a Monolayer Fragmentation Study. *Langmuir*. 33 (22), 5371–5377.

[59] Masuda, A., Akitomi, M., Inoue, M., Okuwaki, K., Okugawa, A., Ueno, K., et al. (2016) Microscopic aspects of potential-induced degradation phenomena and their recovery processes for p-type crystalline Si photovoltaic modules. *Current Applied Physics*. 16 (12), 1659–1665.

[60] Lo, Y.-S., Huefner, N.D., Chan, W.S., Stevens, F., Harris, J.M., and Beebe, T.P. (1999) Specific Interactions between Biotin and Avidin Studied by Atomic Force Microscopy Using the Poisson Statistical Analysis Method. *Langmuir*. 15 (4), 1373–1382.

[61] Wucher, A., Cheng, J., and Winograd, N. (2007) Protocols for Three-Dimensional Molecular Imaging Using Mass Spectrometry. *Analytical Chemistry*. 79 (15), 5529–5539.

[62] Jung, S., Lee, N., Choi, M., Lee, J., Cho, E., and Joo, M. (2017) Methodological development of topographic correction in 2D/3D ToF-SIMS images using AFM images. *Applied Surface Science*.

[63] (n.d.) Combined SIMS-SFM Instrument for the 3-Dimensional Chemical Analysis of Nanostructures | Projects | FP7-NMP. *CORDIS | European Commission*.

[64] (n.d.) Metrology for future 3D-technologies | Projects | H2020. *CORDIS | European Commission*.

[65] Ghosal, S., Fallon, S.J., Leighton, T.J., Wheeler, K.E., Kristo, M.J., Hutcheon, I.D., et al. (2008) Imaging and 3D Elemental Characterization of Intact Bacterial Spores by High-Resolution Secondary Ion Mass Spectrometry. *Analytical Chemistry*. 80 (15), 5986–5992.

[66] Wucher, A., Cheng, J., Zheng, L., Willingham, D., and Winograd, N. (2008) Three-dimensional molecular imaging using mass spectrometry and atomic force microscopy. *Applied Surface Science*. 255 (4), 984–986.

[67] Thomson, S.J.J. (1910) LXXXIII. Rays of positive electricity. *The London, Edinburgh, and Dublin Philosophical Magazine and Journal of Science*. 20 (118), 752–767.

[68] Alvarez, R.M. (2002) La espectrometria de masas. Nacimiento, desarrollo, evolucion y aplicaciones modernas. *Anales de La Real Sociedad Espanola de Quimica*.

[69] Sigmund, P. (2012) Elements of Sputtering Theory. in: D. Kanjilal (Ed.), Nanofabrication Ion-Beam Sputtering, Pan Stanford Publishing, pp. 1–40.

Cette thèse est accessible à l'adresse : http://theses.insa-lyon.fr/publication/2019LYSEI121/these.pdf
© [M.A. Moreno Villavicencio], [2019], INSA Lyon, tous droits réservés

[70] Schueler, B.W. (1992) Microscope imaging by time-of-flight secondary ion mass spectrometry. *Microscopy Microanalysis Microstructures*. 3 (2–3), 119–139.

[71] Fjeldsted, J. (2003) Time-of-Flight Mass Spectrometry - Technical Overview, Agilent Technologies.

[72] Oran, U. (2005) Surface Chemical Characterization of Plasma-Chemically Deposited Polymer Films by Time of Flight Static Secondary Ion Mass Spectrometry, Freien Universität Berlin, 2005.

[73] Hofmann, S. (1980) Quantitative depth profiling in surface analysis: A review. *Surface and Interface Analysis*. 2 (4), 148–160.

[74] Vickerman, J.C. and Briggs, D. (2013) ToF-SIMS: Materials Analysis by Mass Spectrometry. IM Publications, .

[75] Grehl, T. (2003) Improvements in TOF-SIMS Instrumentation for Analytical Application and Fundamental Research, Universität Münster, 2003.

[76] Wang, Z., Jin, K., Zhang, Y., Wang, F., and Zhu, Z. (n.d.) ToF-SIMS depth profiling of insulating samples, interlaced mode or non-interlaced mode? *Surface and Interface Analysis*. 46 (S1), 257–260.

[77] Gilmore, I.S. (2013) SIMS of organics—Advances in 2D and 3D imaging and future outlook. *Journal of Vacuum Science & Technology A: Vacuum, Surfaces, and Films*. 31 (5), 050819.

[78] Mao, D., Wucher, A., and Winograd, N. (2010) Molecular Depth Profiling with Cluster Secondary Ion Mass Spectrometry and Wedges. *Analytical Chemistry*. 82 (1), 57–60.

[79] Sodhi, R.N.S. (2004) Time-of-flight secondary ion mass spectrometry (TOF-SIMS):—versatility in chemical and imaging surface analysis. *The Analyst*. 129 (6), 483–487.

[80] Walker, A.V. (2008) Why Is SIMS Underused in Chemical and Biological Analysis? Challenges and Opportunities. *Analytical Chemistry*. 80 (23), 8865–8870.

[81] Bailey, J., Havelund, R., Shard, A.G., Gilmore, I.S., Alexander, M.R., Sharp, J.S., et al. (2015) 3D ToF-SIMS Imaging of Polymer Multilayer Films Using Argon Cluster Sputter Depth Profiling. *ACS Applied Materials & Interfaces*. 7 (4), 2654–2659.

[82] Gorbenko, V. (2015) Caractérisation par faisceaux d'ions d'hétérostructures III-V pour les applications micro et optoélectroniques. Grenoble Alpes, .

[83] Rangarajan, S. and Tyler, B.J. (2006) Topography in secondary ion mass spectroscopy images. *Journal of Vacuum Science & Technology A: Vacuum, Surfaces, and Films*. 24 (5), 1730–1736.

[84] Van Nuffel, S. (2017) Three-dimensional timeof-flight secondary ion mass spectrometry imaging of primary neuronal cell cultures., University of Nottingham, 2017.

[85] Grehl, T., Möllers, R., and Niehuis, E. (2003) Low energy dual beam depth profiling: influence of sputter and analysis beam parameters on profile performance using TOF-SIMS. *Applied Surface Science*. 203–204 277–280.

Cette thèse est accessible à l'adresse : http://theses.insa-lyon.fr/publication/2019LYSEI121/these.pdf
© [M.A. Moreno Villavicencio], [2019], INSA Lyon, tous droits réservés

[86] Cheng, J., Wucher, A., and Winograd, N. (2006) Molecular Depth Profiling with Cluster Ion Beams. *The Journal of Physical Chemistry B*. 110 (16), 8329–8336.

[87] Winograd, N. (2003) Prospects for imaging TOF-SIMS: from fundamentals to biotechnology. *Applied Surface Science*. 203–204 13–19.

[88] (n.d.) Secondary Ion Mass Spectrometry—a Practical Handbook for Depth Profiling and Bulk Impurity Analysis Wiley, New York, 1989 - Clegg - 1991 - Surface and Interface Analysis - Wiley Online Library.

[89] Galdikas, A. and Pranıavichıus, L. (2000) Interaction of Ions with Condensed Matter. Nova Science Publishers, Inc., Huntington.

[90] Yamamura, Y., Matsunami, N., and Itoh, N. (1982) A new empirical formula for the sputtering yield. *Radiation Effects*. 68 (3), 83–87.

[91] Yamamura, Y. and Tawara, H. (1996) Energy dependence of ion-induced sputtering yields from monoatomic solids at normal incidence. *Atomic Data and Nuclear Data Tables*. 62 (2), 149–253.

[92] Ono, T., Shibata, K., Kenmotsu, T., Muramoto, T., Li, Z., and Kawamura, T. (2007) Extended incident-angle dependence formula for physical sputtering. *Journal of Nuclear Materials*. 363–365 1266–1271.

[93] Touboul, D., Kollmer, F., Niehuis, E., Brunelle, A., and Laprévote, O. (2005) Improvement of biological time-of-flight-secondary ion mass spectrometry imaging with a bismuth cluster ion source. *Journal of the American Society for Mass Spectrometry*. 16 (10), 1608–1618.

[94] Benninghoven, A. (1994) Surface analysis by Secondary Ion Mass Spectrometry (SIMS). *Surface Science*. 299–300 246–260.

[95] Sigmund, P. and Gras-Marti, A. (1980) Distortion of depth profiles during sputtering. *Nuclear Instruments and Methods*. 168 (1–3), 389–394.

[96] Walls, J.M. (1989) Methods of Surface Analysis: Techniques and Applications. Cambridge University Press, Cambridge.

[97] Malherbe, J.B. (1994) Sputtering of compound semiconductor surfaces. I. Ion-solid interactions and sputtering yields. *Critical Reviews in Solid State and Materials Sciences*. 19 (2), 55–127.

[98] Wittmaack, K. (2012) Mechanism of MCs+ formation in Cs based secondary ion mass spectrometry. *Surface Science*. 606 (3), L18–L21.

[99] Mahoney, C.M., Fahey, A.J., Gillen, G., Xu, C., and Batteas, J.D. (2007) Temperature-Controlled Depth Profiling of Poly(methyl methacrylate) Using Cluster Secondary Ion Mass Spectrometry. 2. Investigation of Sputter-Induced Topography, Chemical Damage, and Depolymerization Effects. *Analytical Chemistry*. 79 (3), 837–845.

[100] DARQUE-CERETTI, E., AUCOUTURIER, M., and LEHUÉDÉ, P. (2015) Spectrométrie de masse d'ions secondaires : SIMS et ToF-SIMS - Procédures d'analyse et performances. *Ref : TIP630WEB - "Techniques d'analyse."*

Cette thèse est accessible à l'adresse : http://theses.insa-lyon.fr/publication/2019LYSEI121/these.pdf
© [M.A. Moreno Villavicencio], [2019], INSA Lyon, tous droits réservés

[101] Py, M. (2012) Study of interfaces and nanometric structures by ToF-SIMS : upon a spatially resolved quantitative analysis, Micro and nanotechnologies/Microelectronics, Université de Grenoble, 2012.

[102] Norris, C.P. (2006) Focus on Surface Science Research. Nova Publishers, .

[103] Kubicek, M., Holzlechner, G., Opitz, A.K., Larisegger, S., Hutter, H., and Fleig, J. (2014) A novel ToF-SIMS operation mode for sub 100 nm lateral resolution: Application and performance. *Applied Surface Science*. 289 (100), 407–416.

[104] Scarazzini, R. (2016) ToF-SIMS characterisation of fragile materials used in microelectronic and microsystem devices : validation and enhancement of the chemical information, phd thesis, Université Grenoble Alpes, 2016.

[105] Yamamoto, Y., Ichiki, K., Ninomiya, S., Seki, T., Aoki, T., and Matsuo, J. (2011) Evaluation of surface damage on organic materials irradiated with Ar cluster ion beam. *AIP Conference Proceedings*. 1321 (1), 298–301.

[106] Binnig, G., Quate, C.F., and Gerber, C. (1986) Atomic Force Microscope. *Physical Review Letters*. 56 (9), 930–933.

[107] RIVOAL, J.-C. and FRÉTIGNY, C. (2005) Microscopie à force atomique (AFM). *Ref : TIP673WEB - "Mesures mécaniques et dimensionnelles."*

[108] SALVAN, F. and THIBAUDAU, F. (1999) Microscopie à sonde locale. *Ref : TIP630WEB - "Techniques d'analyse."*

[109] Rugar, D. and Hansma, P. (1990) ATOMIC FORCE MICROSCOPY. *Physics Today*.

[110] Bhushan, B., Ed. (2010) Springer Handbook of Nanotechnology. 3rd ed. Springer-Verlag, Berlin Heidelberg.

[111] Hantschel, T. (2000) Scanning probes for nanometer scale characterization of semiconductor structures, 2000.

[112] Sadewasser, S. and Glatzel, T., Eds. (2012) Kelvin Probe Force Microscopy: Measuring and Compensating Electrostatic Forces. Springer-Verlag, Berlin Heidelberg.

[113] Eaton, P. and West, P. (2010) Atomic Force Microscopy. Oxford University Press, United States.

[114] Conners, T.E. and Banerjee, S. (1995) Surface Analysis of Paper. CRC Press, .

[115] García, R. and Pérez, R. (2002) Dynamic atomic force microscopy methods. *Surface Science Reports*. 47 (6), 197–301.

[116] (2017) Lock-in Amplifiers. *Zurich Instruments*.

[117] Fairbairn, M.W., Member, S., Rezamoheimani, S.O., and Fleming, A.J. (n.d.) Q Control of an Atomic Force Microscope Microcantilever: A Sensorless Approach. .

[118] Butt, H.-J. and Jaschke, M. (1995) Calculation of thermal noise in atomic force microscopy. 6 1–7.

[119] Morin, J. (2013) Etude de fils semi-conducteurs dopés individuels par techniques locales d'analyse de surface, thesis, Grenoble, 2013.

Cette thèse est accessible à l'adresse : http://theses.insa-lyon.fr/publication/2019LYSEI121/these.pdf
© [M.A. Moreno Villavicencio], [2019], INSA Lyon, tous droits réservés

[120] Stangoni, M.V. (2005) Scanning Probe Techniques for Dopant Profile Characterization, Swiss Federal Institute of Technology Zurich, 2005.

[121] Bugg, C.D. and King, P.J. (1988) Scanning capacitance microscopy. *Journal of Physics E: Scientific Instruments*. 21 (2), 147.

[122] Ciampolini, L. (2001) Scanning Capacitance Microscope Imaging and Modelling, Swiss Federal Institute of Technology Zurich, 2001.

[123] Alvarez, D. (2007) Scanning Spreading Resistance Microscopy for the characterization of advanced silicon devices, IMEC, 2007.

[124] Vilimova, P., Placek, T., and Tokarsky, J. (2015) The application of the scanning spreading resistance microscopy for the measurement of the surface conductivity of polypropylene/graphite composites. in: Czech Republic.

[125] Kholkin, A.L., Kalinin, S.V., Roelofs, A., and Gruverman, A. (2007) Review of Ferroelectric Domain Imaging by Piezoresponse Force Microscopy. in: S. Kalinin, A. Gruverman (Eds.), Scanning Probe Microsc. Electr. Electromechanical Phenom. Nanoscale, Springer New York, New York, NYpp. 173–214.

[126] Morelli, A. (2009) Piezoresponse force microscopy of ferroelectric thin films. s.n., .

[127] Rodriguez, B.J., Callahan, C., Kalinin, S.V., and Proksch, R. (2007) Dual-frequency resonance-tracking atomic force microscopy. *Nanotechnology*. 18 (47), 475504.

[128] Brugère, A. (2011) Cinétique de formation et stabilité des domaines ferroélectriques créés par un Microscope à Force Atomique : étude de films minces monocristallins de LiTaO3 en vue d'applications mémoires, phd thesis, INSA de Lyon, 2011.

[129] Niehuis, E., Moellers, R., Kollmer, F., Arlinghaus, H., Bernard, L., Josef Hug, H., et al. (2014) In-Situ TOF-SIMS and SFM Measurements Providing True 3D Chemical Characterization of Inorganic and Organic Nanostructures. *Microscopy and Microanalysis*. 20 (S3), 2086–2087.

[130] Xie, W. (2017) Transfer characteristics of white light interferometers and confocal microscopes, 2017.

[131] Hagenhoff, B. (2000) High Resolution Surface Analysis by TOF-SIMS. *Microchimica Acta*. 132 (2), 259–271.

[132] McDonnell, L.A., Mize, T.H., Luxembourg, S.L., Koster, S., Eijkel, G.B., Verpoorte, E., et al. (2003) Using Matrix Peaks To Map Topography: Increased Mass Resolution and Enhanced Sensitivity in Chemical Imaging. *Analytical Chemistry*. 75 (17), 4373–4381.

[133] Taylor, A.J., Graham, D.J., and Castner, D.G. (2015) Reconstructing accurate ToF-SIMS depth profiles for organic materials with differential sputter rates. *The Analyst*. 140 (17), 6005–6014.

[134] Wagter, M.L., Clarke, A.H., Taylor, K.F., van der Heide, P.A.W., and McIntyre, N.S. (1997) Topographic Correction of 3D SIMS Images. *Surface and Interface Analysis*. 25 (10), 788–789.

Cette thèse est accessible à l'adresse : http://theses.insa-lyon.fr/publication/2019LYSEI121/these.pdf
© [M.A. Moreno Villavicencio], [2019], INSA Lyon, tous droits réservés

[135] Fletcher, J.S. (2015) Latest applications of 3D ToF-SIMS bio-imaging. *Biointerphases*. 10 (1), 018902.

[136] Fletcher, J.S., Lockyer, N.P., Vaidyanathan, S., and Vickerman, J.C. (2007) TOF-SIMS 3D Biomolecular Imaging of *Xenopus laevis* Oocytes Using Buckminsterfullerene (C_{60}) Primary Ions. *Analytical Chemistry*. 79 (6), 2199–2206.

[137] Breitenstein, D., Rommel, C.E., Möllers, R., Wegener, J., and Hagenhoff, B. (2007) The Chemical Composition of Animal Cells and Their Intracellular Compartments Reconstructed from 3D Mass Spectrometry. *Angewandte Chemie International Edition*. 46 (28), 5332–5335.

[138] Robinson, M.A., Graham, D.J., and Castner, D.G. (2012) ToF-SIMS Depth Profiling of Cells: *z* -Correction, 3D Imaging, and Sputter Rate of Individual NIH/3T3 Fibroblasts. *Analytical Chemistry*. 84 (11), 4880–4885.

[139] Wirtz, T., Fleming, Y., Gysin, U., Glatzel, T., Wegmann, U., Meyer, E., et al. (2013) Combined SIMS-SPM instrument for high sensitivity and high-resolution elemental 3D analysis: Combined SIMS-SPM instrument for high-resolution elemental 3D analysis. *Surface and Interface Analysis*. 45 (1), 513–516.

[140] Graham, D.J., Wilson, J.T., Lai, J.J., Stayton, P.S., and Castner, D.G. (2016) Three-dimensional localization of polymer nanoparticles in cells using ToF-SIMS. *Biointerphases*. 11 (2), 02A304.

[141] Fleming, Y. and Wirtz, T. (2015) High sensitivity and high resolution element 3D analysis by a combined SIMS–SPM instrument. *Beilstein Journal of Nanotechnology*. 6 1091–1099.

[142] Terlier, T., Lee, J., Lee, K., and Lee, Y. (2018) Improvement of the Correlative AFM and ToF-SIMS Approach Using an Empirical Sputter Model for 3D Chemical Characterization. *Analytical Chemistry*.

[143] Moreno, M.A., Mouton, I., Chevalier, N., Barnes, J.-P., Bassani, F., and Gautier, B. (2018) Combined ToF-SIMS and AFM protocol for accurate 3D chemical analysis and data visualization. *Journal of Vacuum Science & Technology B, Nanotechnology and Microelectronics: Materials, Processing, Measurement, and Phenomena*. 36 (3), 03F122.

[144] Koch, S., Ziegler, G., and Hutter, H. (2013) ToF-SIMS measurements with topographic information in combined images. *Analytical and Bioanalytical Chemistry*. 405 (22), 7161–7167.

[145] Fleming, Y., Wirtz, T., Gysin, U., Glatzel, T., Wegmann, U., Meyer, E., et al. (2011) Three dimensional imaging using secondary ion mass spectrometry and atomic force microscopy. *Applied Surface Science*. 258 (4), 1322–1327.

[146] Cipro, R., Baron, T., Martin, M., Moeyaert, J., David, S., Gorbenko, V., et al. (2014) Low defect InGaAs quantum well selectively grown by metal organic chemical vapor deposition on Si(100) 300 mm wafers for next generation non planar devices. *Applied Physics Letters*. 104 (26), 262103.

Cette thèse est accessible à l'adresse : http://theses.insa-lyon.fr/publication/2019LYSEI121/these.pdf
© [M.A. Moreno Villavicencio], [2019], INSA Lyon, tous droits réservés

[147] Martin, M., Caliste, D., Cipro, R., Alcotte, R., Moeyaert, J., David, S., et al. (2016) Toward the III–V/Si co-integration by controlling the biatomic steps on hydrogenated Si(001). *Applied Physics Letters*. 109 (25), 253103.

[148] Seah, M.P. and Nunney, T.S. (2010) Sputtering yields of compounds using argon ions. *Journal of Physics D: Applied Physics*. 43 (25), 253001.

[149] Johannessen, J.S., Spicer, W.E., and Strausser, Y.E. (1976) An Auger analysis of the SiO_2-Si interface. *Journal of Applied Physics*. 47 (7), 3028–3037.

[150] Cheng, J. and Winograd, N. (2005) Depth Profiling of Peptide Films with TOF-SIMS and a C_{60} Probe. *Analytical Chemistry*. 77 (11), 3651–3659.

[151] Muramoto, S., Brison, J., and Castner, D.G. (2012) Exploring the Surface Sensitivity of TOF-Secondary Ion Mass Spectrometry by Measuring the Implantation and Sampling Depths of Bi_n and C_{60} Ions in Organic Films. *Analytical Chemistry*. 84 (1), 365–372.

[152] Kozole, J., Wucher, A., and Winograd, N. (2008) Energy Deposition during Molecular Depth Profiling Experiments with Cluster Ion Beams. *Analytical Chemistry*. 80 (14), 5293–5301.

[153] Iida, S., Miyayama, T., Sanada, N., Suzuki, M., Fisher, G.L., and Bryan, S.R. (2009) Incident Angle Dependence in Polymer TOF-SIMS Depth Profiling with C60 Ion Beams. *E-Journal of Surface Science and Nanotechnology*. 7 878–881.

[154] Makeev, M.A. and Barabási, A.-L. (2004) Effect of surface morphology on the sputtering yields. II. Ion sputtering from rippled surfaces. *Nuclear Instruments and Methods in Physics Research Section B: Beam Interactions with Materials and Atoms*. 222 (3–4), 335–354.

[155] Sarkar, S., Franquet, A., Moussa, A., and Vandervorst, W. (2011) Chemical effects during ripple formation with isobaric ion beams. *Applied Surface Science*. 257 (15), 6424–6428.

[156] Lee, J.L.S., Gilmore, I.S., Seah, M.P., and Fletcher, I.W. (2011) Topography and Field Effects in Secondary Ion Mass Spectrometry – Part I: Conducting Samples. *Journal of The American Society for Mass Spectrometry*. 22 (10), 1718–1728.

[157] Lee, J.L.S., Gilmore, I.S., Fletcher, I.W., and Seah, M.P. (2009) Multivariate image analysis strategies for ToF-SIMS images with topography. *Surface and Interface Analysis*. 41 (8), 653–665.

[158] Lee, J.L.S., Gilmore, I.S., Fletcher, I.W., and Seah, M.P. (2008) Topography and field effects in the quantitative analysis of conductive surfaces using ToF-SIMS. *Applied Surface Science*. 255 (4), 1560–1563.

[159] Wucher, A., Cheng, J., and Winograd, N. (2008) Molecular Depth Profiling Using a C_{60} Cluster Beam: The Role of Impact Energy. *The Journal of Physical Chemistry C*. 112 (42), 16550–16555.

[160] Sigmund, P. (1969) Theory of Sputtering. I. Sputtering Yield of Amorphous and Polycrystalline Targets. *Physical Review*. 184 (2), 383–416.

Cette thèse est accessible à l'adresse : http://theses.insa-lyon.fr/publication/2019LYSEI121/these.pdf
© [M.A. Moreno Villavicencio], [2019], INSA Lyon, tous droits réservés

[161] Fletcher, J.S., Conlan, X.A., Jones, E.A., Biddulph, G., Lockyer, N.P., and Vickerman, J.C. (2006) TOF-SIMS Analysis Using C60. Effect of Impact Energy on Yield and Damage. *Analytical Chemistry*. 78 (6), 1827–1831.

[162] Gorbenko, V., Veillerot, M., Grenier, A., Audoit, G., Hourani, W., Martinez, E., et al. (2015) Chemical depth profiling and 3D reconstruction of III-V heterostructures selectively grown on non-planar Si substrates by MOCVD: Chemical depth profiling and 3D reconstruction of III-V heterostructures selectively grown on non-planar Si substrates by MOCVD. *Physica Status Solidi (RRL) - Rapid Research Letters*. 9 (3), 202–205.

[163] Makeev, M.A. and Barabási, A.-L. (2004) Effect of surface morphology on the sputtering yields. I. Ion sputtering from self-affine surfaces. *Nuclear Instruments and Methods in Physics Research Section B: Beam Interactions with Materials and Atoms*. 222 (3), 316–334.

[164] Fukumoto, N., Mizukami, Y., Yoshikawa, S., and Morita, H. (2008) Investigation of surface morphology of SiC during SIMS analysis. *Applied Surface Science*. 255 (4), 1391–1394.

[165] Zalar, A. (1985) Improved depth resolution by sample rotation during Auger electron spectroscopy depth profiling. *Thin Solid Films*. 124 (3), 223–230.

[166] Sjövall, P., Rading, D., Ray, S., Yang, L., and Shard, A.G. (2010) Sample Cooling or Rotation Improves C_{60} Organic Depth Profiles of Multilayered Reference Samples: Results from a VAMAS Interlaboratory Study. *The Journal of Physical Chemistry B*. 114 (2), 769–774.

[167] Stewart, A.D.G. and Thompson, M.W. (1969) Microtopography of surfaces eroded by ion-bombardment. *Journal of Materials Science*. 4 (1), 56–60.

[168] Sigmund, P. (1973) A mechanism of surface micro-roughening by ion bombardment. *Journal of Materials Science*. 8 (11), 1545–1553.

[169] Kanyandekwe, J., Baines, Y., Richy, J., Favier, S., Leroux, C., Blachier, D., et al. (2019) Impact of growth conditions on AlN/GaN heterostructures with in-situ SiN capping layer. *Journal of Crystal Growth*. 515 48–52.

[170] Matthews, J.W. and Klokholm, E. (1972) Fracture of brittle epitaxial films under the influence of misfit stress. *Materials Research Bulletin*. 7 (3), 213–221.

[171] Uchino, K. (1993) Ceramic Actuators: Principles and Applications. *MRS Bulletin*. 18 (4), 42–48.

[172] Shung, K.K., Cannata, J.M., and Zhou, Q.F. (2007) Piezoelectric materials for high frequency medical imaging applications: A review. *Journal of Electroceramics*. 19 (1), 141–147.

[173] Manbachi, A. and Cobbold, R.S.C. (2011) Development and Application of Piezoelectric Materials for Ultrasound Generation and Detection. *Ultrasound*. 19 (4), 187–196.

[174] Xu, Y. (2013) Ferroelectric Materials and Their Applications. Elsevier, .

Cette thèse est accessible à l'adresse : http://theses.insa-lyon.fr/publication/2019LYSEI121/these.pdf
© [M.A. Moreno Villavicencio], [2019], INSA Lyon, tous droits réservés

[175] Martin, S., Gautier, B., Baboux, N., Gruverman, A., Carretero-Genevrier, A., Gich, M., et al. (2019) Characterizing Ferroelectricity with an Atomic Force Microscopy: An All-Around Technique. in: U. Celano (Ed.), Electr. At. Force Microsc. Nanoelectron., Springer International Publishing, Champp. 173–203.

[176] Borowiak, A.S., Baboux, N., Albertini, D., Vilquin, B., Saint Girons, G., Pelloquin, S., et al. (2014) Electromechanical response of amorphous LaAlO3 thin film probed by scanning probe microscopies. *Applied Physics Letters*. 105 (1), 012906.

[177] Bark, C.W., Sharma, P., Wang, Y., Baek, S.H., Lee, S., Ryu, S., et al. (2012) Switchable Induced Polarization in LaAlO3/SrTiO3 Heterostructures. *Nano Letters*. 12 (4), 1765–1771.

[178] Sharma, P., Ryu, S., Viskadourakis, Z., Paudel, T.R., Lee, H., Panagopoulos, C., et al. (2015) Electromechanics of Ferroelectric-Like Behavior of LaAlO3 Thin Films. *Advanced Functional Materials*.

[179] Guan, Z., Jiang, Z.-Z., Tian, B.-B., Zhu, Y.-P., Xiang, P.-H., Zhong, N., et al. (2017) Identifying intrinsic ferroelectricity of thin film with piezoresponse force microscopy. *AIP Advances*. 7 (9), 095116.

[180] Vasudevan, R.K., Balke, N., Maksymovych, P., Jesse, S., and Kalinin, S.V. (2017) Ferroelectric or non-ferroelectric: Why so many materials exhibit “ferroelectricity” on the nanoscale. *Applied Physics Reviews*. 4 (2), 021302.

[181] Pelloquin, S., Saint-Girons, G., Baboux, N., Albertini, D., Hourani, W., Penuelas, J., et al. (2013) LaAlO3/Si capacitors: Comparison of different molecular beam deposition conditions and their impact on electrical properties. *Journal of Applied Physics*. 113 (3), 034106.

[182] Garrillo, P.A.F. (2018) Development of highly resolved and photo-modulated Kelvin probe microscopy techniques for the study of photovoltaic systems.

[183] Yan, L., Yang, Y., Wang, Z., Xing, Z., Li, J., and Viehland, D. (2009) Review of magnetoelectric perovskite–spinel self-assembled nano-composite thin films. *Journal of Materials Science*. 44 (19), 5080–5094.

[184] Graham, D.J. and Castner, D.G. (2012) Multivariate Analysis of ToF-SIMS Data from Multicomponent Systems: The Why, When, and How. *Biointerphases*. 7 (1), 49.

[185] Mayer, F.L., Stalling, D.L., and Johnson, J.L. (1972) Phthalate Esters as Environmental Contaminants. *Nature*. 238 (5364), 411–413.

[186] Gómez, A., Vila-Fungueiriño, J.M., Moalla, R., Saint-Girons, G., Gázquez, J., Varela, M., et al. (2017) Electric and Mechanical Switching of Ferroelectric and Resistive States in Semiconducting BaTiO3–δ Films on Silicon. *Small*.

[187] Ievlev, A.V., Chyasnavichyus, M., Leonard, D.N., Agar, J.C., Velarde, G.A., Martin, L.W., et al. (2018) Subtractive fabrication of ferroelectric thin films with precisely controlled thickness. *Nanotechnology*. 29 (15), 155302.

[188] Giannuzzi, L.A. and Stevie, F.A. (1999) A review of focused ion beam milling techniques for TEM specimen preparation. *Micron*. 30 (3), 197–204.

Cette thèse est accessible à l'adresse : http://theses.insa-lyon.fr/publication/2019LYSEI121/these.pdf
© [M.A. Moreno Villavicencio], [2019], INSA Lyon, tous droits réservés

[189] Mayer, J., Giannuzzi, L.A., Kamino, T., and Michael, J. (2007) TEM Sample Preparation and FIB-Induced Damage. *MRS Bulletin*. 32 (5), 400–407.

[190] Bassim, N.D., Gregorio, B.T.D., Kilcoyne, A.L.D., Scott, K., Chou, T., Wirick, S., et al. (2012) Minimizing damage during FIB sample preparation of soft materials. *Journal of Microscopy*. 245 (3), 288–301.

[191] Tamura, M., Shukuri, S., Moniwa, M., and Default, M. (1986) Focused ion beam gallium implantation into silicon. *Applied Physics A*. 39 (3), 183–190.

[192] Spoldi, G., Beuer, S., Rommel, M., Yanev, V., Bauer, A.J., and Ryssel, H. (2009) Experimental observation of FIB induced lateral damage on silicon samples. *Microelectronic Engineering*. 86 (4), 548–551.

[193] Brezna, W., Wanzenböck, H., Lugstein, A., Bertagnolli, E., Gornik, E., and Smoliner, J. (2003) Scanning capacitance microscopy investigations of focused ion beam damage in silicon. *Physica E: Low-Dimensional Systems and Nanostructures*. 19 (1), 178–182.

[194] Giannuzzi, L.A. and Stevie, F.A. (2004) Introduction to Focused Ion Beams: Instrumentation, Theory, Techniques and Practice. Springer Science & Business Media, University North Carolina State.

[195] Berghmans, B., Van Daele, B., Geenen, L., Conard, T., Franquet, A., and Vandervorst, W. (2008) Cesium near-surface concentration in low energy, negative mode dynamic SIMS. *Applied Surface Science*. 255 (4), 1316–1319.

[196] Ngo, K.Q., Philipp, P., Kieffer, J., and Wirtz, T. (2012) Cs oxide aggregation in SIMS craters in organic samples for optoelectronic application. *Surface Science*. 606 (15–16), 1244–1251.

Cette thèse est accessible à l'adresse : http://theses.insa-lyon.fr/publication/2019LYSEI121/these.pdf
© [M.A. Moreno Villavicencio], [2019], INSA Lyon, tous droits réservés

APPENDIX

A.1. FORMATION OF Cs^+ AGGREGATES AT THE SAMPLE SURFACE

Figure A. 1 shows the AFM images of the *squares* area described in Figure IV.1. These images were captured after the first interface, GaAs / Si, was reached in the ToF-SIMS depth profile. Some of them showed several spherical bumps at the surface of the SiO_2 patterns that produce the increment of the surface roughness. The diameter of these bumps varies with the sputtering energy, between 250 and 300 nm for 250 eV and between 400 and 500 nm for 500 eV. The bumps were only seen at 2 keV when the sample was rotated. Furthermore, no relationship between the bump density and the sputter energy was found.

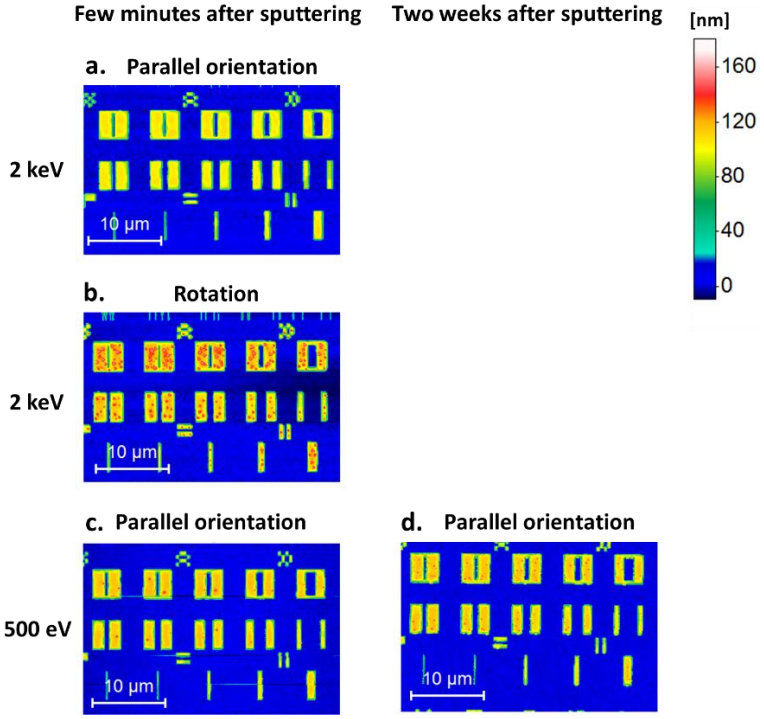

Figure A. 1

AFM topographical images showing the Cs^+ aggregates at the SiO_2 surface. They were captured after sputtering at 2 keV with ion beam a. parallel to the patterns and b. rotating the sample 360°. c. AFM image captured a few minutes after sputtering the sample at 500 eV with ion beam parallel to the lines. d. image captured two weeks later.

The bumps are related to cesium oxides that create clusters at the sample surface. The exact mechanism of formation is unknown but it has been associated with the migration toward the surface of the Cs implanted during the sputtering. These atoms, at the surface, interact with the oxygen to form different oxides: $Cs_{11}O_3$, Cs_2O_2 and CsO_2. [195]

The Cs oxide aggregation was commonly seen at low energy sputtering, below 1 keV. A high energy will implant the Cs ions deeper in the sample inhibiting their migration to the surface. This explains the smooth surface obtained at 2 keV for parallel orientation, Figure A. 1.a.

Cette thèse est accessible à l'adresse : http://theses.insa-lyon.fr/publication/2019LYSEI121/these.pdf
© [M.A. Moreno Villavicencio], [2019], INSA Lyon, tous droits réservés

However, the bumps were still seen by Gorbenko [82] and us when the sample was rotated during the sputtering at a primary energy of 2 keV, Figure A. 1.b.

The formation of Cs aggregates needs the migration of Cs ions and the interaction with oxygen. This may explain the preferred accumulation of these clusters at SiO_2 surfaces. In order to study the evolution of these aggregates after oxygen exposure, AFM images were performed immediately after low-energy ToF-SIMS sputtering, Figure A. 1.c, and 15 days later, Figure A. 1.d. After the two weeks, the aggregates conserved their size but their number increased from about 22 to more than 150.

A similar study was made by Ngo *et al.* [196] to analyze the evolution of the aggregates over time. The size of the aggregates increased with the oxygen exposure for the following two days. After that day, the size decreased to the initial value and 32 days later, the bumps were still observed at the surface.

A.2. TIP CONVOLUTION

The AFM profiles show the sample topography according to the geometry of the tip that scans the surface. Therefore, it is important to choose the tip carefully as a function of the sample and measurement to be performed. Its dimensions and its shape are well specified by the fabricant in order to compare the obtained topography with the tip and conclude about the accuracy of the profiles. However, it is important to keep in mind that the tip shape is probably changing during the analysis due to the wear, contamination or adhesion. Figure A. 2 shows two common aberrations present in the topographical images. In the first example, the radius of the tip does not allow it to reach the bottom of the surface holes. The obtained topography profile of the sample is not accurate and neither is the measured height. The same scan line is repeated in Figure A. 2.b using a tip with smaller radius. The tip reaches the bottom of the hole, however the tip shape, still visible in the edges of the hole, gives the impression that the hole is not rectangular. [113]

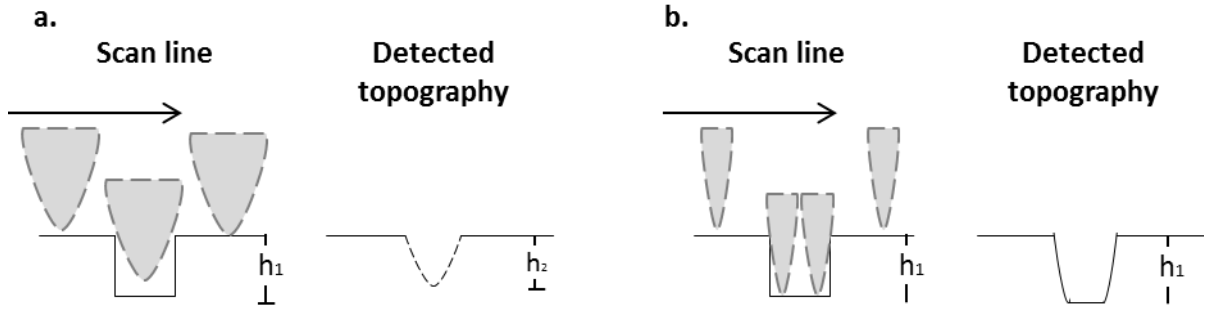

Figure A. 2 Tip convolution in AFM profiles. a. The tip does not reach the bottom of the sample. b. The vertical interfaces adopt the tip shape. [113]

Cette thèse est accessible à l'adresse : http://theses.insa-lyon.fr/publication/2019LYSEI121/these.pdf
© [M.A. Moreno Villavicencio], [2019], INSA Lyon, tous droits réservés

The tip geometry effect would cause the vertical interfaces to have an angle similar to the one that the tip has. However, this is not the case in the profiles presented in Figure A. 3.

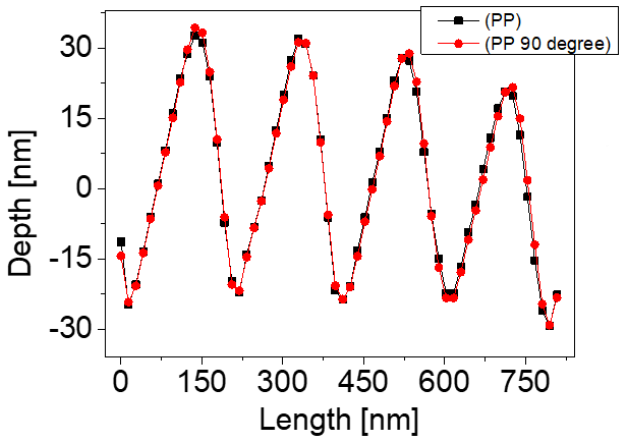

Figure A. 3

AFM profiles of four lines of the sample captured scanning at 0 and 90 degree, black and red respectively. The sample was previously sputtered using the bevel crater approach with a primary beam oriented perpendicular to the sample lines.

Cette thèse est accessible à l'adresse : http://theses.insa-lyon.fr/publication/2019LYSEI121/these.pdf
© [M.A. Moreno Villavicencio], [2019], INSA Lyon, tous droits réservés

Cette thèse est accessible à l'adresse : http://theses.insa-lyon.fr/publication/2019LYSEI121/these.pdf
© [M.A. Moreno Villavicencio], [2019], INSA Lyon, tous droits réservés

RÉSUMÉ ÉTENDU DU MANUSCRIT EN FRANÇAIS

Note : Le lecteur pourra consulter dans le texte principal les figures mentionnées dans ce résumé, ainsi que les références.

Depuis maintenant une dizaine d'année, la technologie des dispositifs et des circuits intégrés évolue rapidement vers le développement de structures tridimensionnelles (3D) complexes fabriquées à l'aide de nouveaux matériaux et procédés aux dimensions nanométriques. La visualisation et l'analyse de ces structures 3D à l'échelle nanométrique constituent un défi de taille pour tous les domaines de la caractérisation et de la métrologie. Parmi les exemples de développement de nouvelles technologies, nous pouvons citer l'auto-assemblage contrôlé par des copolymères à blocs, les transistors FinFET qui constituent l'architecture dominante des dispositifs à microprocesseur, ou encore l'intégration de structures mémoires complexes. Ces évolutions technologiques nécessitent de développer des techniques et des méthodologies qui répondent aux besoins de contrôle dimensionnel, d'analyses chimiques, mécaniques … à l'échelle nanométrique. Cependant, de nombreuses techniques de caractérisation existantes sont aussi à la limite de leurs capacités, et une des solutions envisagées est de les combiner pour dépasser ces limites.

La spectrométrie de masse à temps de vol (ToF-SIMS) est une technique d'analyse qui permet la caractérisation chimique en 3D avec une limite de détection de l'ordre du ppm. Dans cette technique, les ions secondaires émis par la surface (<0.5 nm de profondeur) sont collectés par un spectromètre de masse, puis l'analyse de leur rapport masse sur charge permet de déterminer les groupes fonctionnels, la composition élémentaire et moléculaire de la surface analysée. L'émission d'ions secondaires est obtenue en bombardant la surface de l'échantillon avec un faisceau d'ions primaires [69]. Les ions primaires qui entrent en collision sur la surface avec suffisamment d'énergie permettent de rompre les liaisons chimiques et d'éjecter des molécules et/ou des atomes de la surface. Les particules chargées sont accélérées par le biais d'un champ électrique avant de pénétrer dans l'analyseur de temps de vol (t_{TOF}), qui mesure le temps nécessaire à un ion secondaire pour atteindre le détecteur (Figure II.1.a). Le rapport masse sur charge m/z est calculé à partir de ce temps de vol (Eq. II.1). On obtient ainsi un spectre de masse pour chaque pixel analysé avec une résolution en masse de 10^4 m/dm permettant de distinguer les particules de même masse nominale. Les spectres obtenus permettent de générer des images chimiques. En répétant le processus de pulvérisation décrit précédemment, on réalise l'analyse en profondeur de l'échantillon (Figure II.1.b). Les images chimiques obtenues ont une résolution latérale de l'ordre de 100 nm, ce qui représente une limitation pour répondre aux besoins actuels d'imagerie à l'échelle nanométrique (Figure I.2).

Cette thèse est accessible à l'adresse : http://theses.insa-lyon.fr/publication/2019LYSEI121/these.pdf
© [M.A. Moreno Villavicencio], [2019], INSA Lyon, tous droits réservés

Depuis quelques années, la combinaison du ToF-SIMS avec des techniques d'imagerie à haute résolution spatiale semble être une solution pour dépasser cette limitation.

Parmi les techniques d'imagerie à l'échelle nanométrique, on trouve la microscopie à force atomique (AFM). Cette technique permet de cartographier la topographie de surface avec une résolution latérale de 10 nm et la possibilité d'utiliser des modes de fonctionnement avancés pour sonder les propriétés électriques et mécaniques locales d'un échantillon (Figure I.3). Le principe de l'AFM repose sur la détection des forces d'interaction entre la surface de l'échantillon et une pointe située à quelques nanomètres de hauteur. Depuis de nombreuses années, l'AFM et le ToF-SIMS sont utilisés de manière ex-situ comme techniques d'analyses complémentaires. Cette combinaison présente un intérêt récent pour de nombreux groupes de recherche pour observer et comprendre les mécanismes de pulvérisation à l'échelle nanométrique. Il est à noter qu'un instrument *in-situ* ToF-SIMS et AFM est actuellement disponible sur le marché.

Cette thèse s'inscrit dans le cadre du développement et de l'optimisation de l'analyse combinée AFM et ToF-SIMS. Une méthodologie combinée d'imagerie 3D a été développée (voir Figure II.10). Elle se décline en quatre étapes : (i) la préparation des échantillons, (ii) l'analyse cyclique ToF-SIMS / AFM / profilomètre, (iii) le traitement des données brutes et (iv) la corrélation des données. Les ensembles de données ToF-SIMS d'une part et AFM d'autre part sont obtenus à partir d'une analyse cyclique. Cette méthodologie permet d'obtenir trois résultats principaux : (i) la corrélation de la composition chimique avec la topographie de surface de l'échantillon, et ce à différentes profondeurs, (ii) la cartographie du taux de pulvérisation pour un volume sondé et (iii) une reconstruction et une visualisation 3D des données ToF-SIMS corrigée par la topographie. Ces différents résultats ont été utilisés au cours de cette thèse pour différentes applications.

Cette thèse est accessible à l'adresse : http://theses.insa-lyon.fr/publication/2019LYSEI121/these.pdf
© [M.A. Moreno Villavicencio], [2019], INSA Lyon, tous droits réservés

1. METHODOLOGIE D'ANALYSE COMBINEE TOF-SIMS ET AFM

La méthodologie combinée ToF-SIMS / AFM peut être réalisée de manière *ex-situ* ou *in-situ*. Elle repose sur une analyse cyclique où la topographie de l'échantillon et la profondeur du cratère sont mesurées au début, à la fin et à chaque fois qu'une interface est visualisée dans le profil de profondeur ToF-SIMS. L'interface est définie comme le point où l'intensité du profil associé à un élément chimique diminue jusqu'à 50% de sa valeur maximale. La principale limite de cette méthodologie est que le nombre d'analyses AFM minimum à réaliser dépend du nombre de couches présentes dans l'échantillon. Cependant, il s'agit d'un protocole optimisé pour les structures présentant 2 à 3 interfaces horizontales. Les interruptions de l'analyse ToF-SIMS soulèvent les problèmes de repositionnement, de localisation et de transfert d'échantillon entre les instruments. Ces différents éléments ont été pris en compte dans le développement de la méthodologie.

Les conditions d'analyse, par AFM et par ToF-SIMS, dépendent de l'échantillon à analyser. Voici quelques points importants à prendre en compte :

- Une restriction sur la taille de l'échantillon existe pour pouvoir assurer le transfert entre les 2 équipements dans des conditions optimales (capsule de transfert sous vide ou sous gaz neutre). La taille typique est de l'ordre du centimètre. La mise à l'échelle peut être réalisée par clivage lorsque c'est nécessaire.
- Dans le cas où une zone spécifique doit être analysée, celle-ci peut être préalablement identifiée à l'aide d'un microscope optique. Un défaut ou une forme caractéristique proche de la zone d'intérêt peut être utilisé comme point de référence pour la localisation. Dans le cas d'une surface lisse et homogène, des marques visibles optiquement peuvent être réalisées à la surface de l'échantillon en utilisant par exemple une gravure par faisceau d'ions focalisés (FIB).
- Un profil ToF-SIMS en profondeur avec une résolution en masse élevée est recommandé lorsque l'échantillon à analyser est inconnu. Il permet d'identifier les couches et les ions secondaires caractéristiques associées, et d'optimiser les conditions d'analyse, telles que la nature et l'énergie de la source primaire de pulvérisation.
- Une analyse ToF-SIMS à haute résolution latérale est appropriée pour obtenir des images chimiques de bonne qualité. Il est à noter que la résolution latérale du ToF-SIMS est d'environ 100 nm. Les motifs plus petits que cette taille ne sont pas visibles dans les images chimiques.
- Les images ToF-SIMS et AFM ont une grande différence de résolution latérale. Le rapport taille de pixel ToF-SIMS et AFM doit être un nombre entier afin de faciliter le redimensionnement de l'image dans la phase de traitement des données.

Cette thèse est accessible à l'adresse : http://theses.insa-lyon.fr/publication/2019LYSEI121/these.pdf
© [M.A. Moreno Villavicencio], [2019], INSA Lyon, tous droits réservés

- La zone d'analyse doit être identique à chaque cycle de mesure, avec le moins de variation possible. En raison du multiple repositionnement de l'échantillon, on choisit un champ de vue plus grand, pour s'assurer que la zone d'intérêt est bien analysée.

Les données brutes expérimentales obtenues à la fin de cette procédure sont : des empilements d'images chimiques par cycle de pulvérisation obtenus par ToF-SIMS ; une image AFM initiale et finale de la zone d'intérêt ; et enfin une image AFM et un profil de profondeur du cratère pour chaque interface de l'échantillon. Ces données brutes requièrent un traitement spécifique détaillé ci-après.

1.1. TRAITEMENT DES DONNEES BRUTES

Dans cette étape, l'étalonnage en masse, la sélection des pics, l'exportation des données et la création d'empilements sont effectués pour les spectres ToF-SIMS. Des pics d'ions secondaires caractéristiques sont utilisés pour calibrer le rapport m/z. Pour la sélection des pics, il est recommandé de définir une valeur d'intensité minimale et de sélectionner les pics dont l'intensité est supérieure à celle-ci ou de sélectionner manuellement les ions spécifiques à visualiser. Les images chimiques correspondant aux séquences des pics sélectionnés, exportées au format TIFF3D, sont importées dans le logiciel ImageJ afin de générer par élément chimique considéré un empilement d'images au format TIFF.

La profondeur du cratère est extraite à partir des données mesurées par profilométrie optique ou mécanique. Selon l'équipement utilisé, un profil ou une cartographie de surface est obtenue. Dans le premier cas, un ajustement plan est effectué pour identifier correctement le fond du cratère. Dans le deuxième cas, une section est extraite de la cartographie pour évaluer la profondeur moyenne du cratère. Dans les deux cas, la profondeur du cratère est référencée à partir de la surface non pulvérisée.

Le traitement des données brutes AFM comprend deux étapes : la première consiste à remettre à niveau les images brutes, soit de manière planaire soit ligne à ligne. Dans le premier cas, on soustrait un arrière-plan planaire ou polynomial à l'image brute. Cette méthode est à privilégier à l'ordre 1 notamment lorsque cette surface va servir de référence. Cependant, si l'image présente des sauts de lignes, il est nécessaire de réaliser un ajustement polynomial ligne à ligne. La deuxième étape consiste à localiser les données AFM selon leur position en profondeur. Ce processus consiste à (i) définir la zone d'intérêt à partir de laquelle la profondeur du cratère a été évaluée et (ii) à soustraire la profondeur du cratère mesurée, dz, à l'image AFM correspondante. Ces données sont exportées au format txt.

Chaque ensemble de données ToF-SIMS et AFM nécessitent ensuite un alignement et un redimensionnement de la taille des pixels de chaque image. Ce traitement est effectué à l'aide du logiciel ImageJ et du logiciel MATLAB.

Cette thèse est accessible à l'adresse : http://theses.insa-lyon.fr/publication/2019LYSEI121/these.pdf
© [M.A. Moreno Villavicencio], [2019], INSA Lyon, tous droits réservés

1.2. ALIGNEMENT ET REDIMENSIONNEMENT DES DONNEES

Dans le but de corréler des données, il est nécessaire d'uniformiser la taille du pixel pour chaque ensemble de données. Pour rappel, la taille de pixel se déduit en divisant la longueur de la zone analysée par le nombre de pixels défini pour la ligne. En raison de la différence de résolution latérale entre l'AFM et le ToF-SIMS, la taille d'un pixel peut varier jusqu'à un facteur 10.

Deux options sont possibles, soit on conserve la résolution spatiale du ToF-SIMS, et de ce fait on « dégrade » la résolution des images AFM, soit inversement on conserve la résolution de l'AFM et on extrapole les images ToF-SIMS. Comme la résolution spatiale en AFM est bien meilleure (~10 nm), dégrader la résolution de ces images signifie perdre de l'information topographique. Cette option n'est pas à considérer lorsque cette information est critique, comme par exemple si on souhaite corréler la composition chimique et la rugosité de surface.

Le redimensionnement des données nécessite de déterminer le rapport de taille de pixel, que l'on obtient en divisant la taille d'un pixel AFM par la taille d'un pixel en ToF-SIMS, ou vice et versa selon le choix retenu pour le redimensionnement. La fonction *imresize* sous MATLAB est utilisée pour augmenter ou réduire le nombre de pixels avec une méthode *bicubic*, qui consiste en une moyenne pondérée de pixels dans le voisinage le plus proche 4 × 4.

L'alignement des données comprend trois étapes : (i) l'alignement des images AFM, (ii) l'alignement des ensembles de données ToF-SIMS et (iii) enfin l'alignement commun des ensembles de données AFM et ToF-SIMS. Un code d'alignement utilisant des fonctions MATLAB a été spécifiquement développé pour répondre à ce besoin. Il repose sur l'utilisation d'un algorithme de corrélation croisée normalisée (fonction *normxcorr2*). Cet algorithme permet de déterminer la translation (décalage dans les directions x et y) et l'angle de rotation entre chaque image à partir d'une image de référence. La description des paramètres requis par le code est présentée ci-dessous :

(1) Sélection de l'image de référence.
- ToF-SIMS : il est recommandé de prendre comme référence la somme des images chimiques d'un ensemble de données correspondant à l'élément chimique d'intensité la plus élevée.
- AFM : le choix se porte sur une image au contraste élevé associé à des variations de hauteur, et qui présente le moins de rotation possible.
- ToF-SIMS et AFM : pour cet alignement spécifique, il est recommandé de prendre une image AFM car elle présente un contraste mieux défini.

(2) Définition de la plage d'évaluation de l'angle de rotation : il s'agit d'un choix utilisateur qui dépend du degré d'alignement des images. Les angles sont donnés en degrés, dans le sens antihoraire lorsqu'ils sont positifs et dans le sens horaire lorsqu'ils sont négatifs.

Cette thèse est accessible à l'adresse : http://theses.insa-lyon.fr/publication/2019LYSEI121/these.pdf
© [M.A. Moreno Villavicencio], [2019], INSA Lyon, tous droits réservés

(3) Sélection des images à aligner avec l'image de référence.

- ToF-SIMS : chaque image de l'empilement sélectionnée est comparée puis alignée sur l'image de référence. La translation et la rotation déterminées par image dans l'empilement sont également appliquées aux images des autres empilements. Cette opération est réalisable car les images chimiques de chaque élément à une profondeur donnée sont obtenues à partir du même champ de vue.
- AFM : chaque image AFM est alignée individuellement avec celle choisie comme référence.
- ToF-SIMS and AFM images : la somme des images chimiques existant dans l'empilement ToF-SIMS sélectionné est comparée à l'image AFM définie comme référence. La translation et la rotation calculées sont appliquées à toutes les images chimiques de cette empilement spécifique, puis aux images chimiques des autres empilements.

La phase d'alignement des images avec l'image de référence comporte 4 étapes :

(1) L'image à aligner est tout d'abord pivotée à l'aide de la fonction *imrotate* sous MATLAB, selon un des angles définis dans la gamme de rotation. Pour cet angle spécifique, la fonction *normxcorr2* détermine le coefficient de corrélation avec l'image de référence. Plus ce nombre est élevé, meilleure est la corrélation des images. Cette action est répétée pour chaque angle défini dans la gamme de rotation. Pour chaque angle, le coefficient de corrélation et le déplacement associé (vecteur de translation) de l'image sont sauvegardées dans un tableau similaire à celui de la Figure II.16.

(2) A partir du tableau précédent, on extrait la valeur maximale du coefficient de corrélation, ce qui permet de corriger la translation et la rotation de l'image par rapport à l'image de référence. Cette modification correspond à une cross-corrélation optimale.

(3) Ce processus est effectué pour l'ensemble des images, ce qui se traduit par une rotation et une translation de chaque image. Ce processus d'alignement peut être répété plusieurs fois jusqu'à ce que la translation et la rotation obtenues pour chaque image soient nulles, garantissant ainsi une corrélation optimale de chaque image avec l'image de référence. À ce stade, des pixels « vides » peuvent apparaître dans les images afin de conserver le nombre initial de pixels.

(4) Toutes les images, AFM et ToF-SIMS, sont recadrées pour supprimer les pixels vides.

Le processus d'alignement n'est pas toujours simple. En effet, le contraste des images chimiques par exemple peut ne pas être suffisant pour avoir une bonne estimation de la corrélation. Dans ce cas de figure, d'autres traitements peuvent être appliqués tels que l'érosion et/ou la dilatation. L'idée est de remplir automatiquement les espaces vides dans les images chimiques pour amplifier le contraste. Il est également possible d'utiliser une fonction de « détection de contours » pour identifier les motifs présents dans une image pouvant aider à la corrélation.

Cette thèse est accessible à l'adresse : http://theses.insa-lyon.fr/publication/2019LYSEI121/these.pdf
© [M.A. Moreno Villavicencio], [2019], INSA Lyon, tous droits réservés

Ces processus de traitement sont des solutions d'alignement semi-automatique. Dans le cas extrême, où aucune des fonctions ne fournit un résultat satisfaisant, un alignement manuel est à la seule méthode possible [62]. Pour ce faire, l'utilisateur sélectionne plusieurs points dans l'image de référence et identifie les mêmes points dans l'image à aligner. Le programme trouve alors automatiquement la meilleure translation et la meilleure rotation pour superposer ces points de concordance. Cependant, ces marques doivent figurer sur chaque image et cela peut prendre beaucoup de temps lorsqu'il est appliqué à plusieurs empilements chimiques.

1.3. PRINCIPAUX RESULTATS

1.3.1. SUPERPOSITION DE L'INFORMATION CHIMIQUE SUR LA TOPOGRAPHIE DE SURFACE

Cette superposition d'information ToF-SIMS / AFM permet de corréler la composition chimique locale avec la rugosité et la morphologie de surface de l'échantillon. En pratique, la topographie de surface issue de l'image AFM est présentée sur une image en relief sur laquelle chaque élément chimique est différencié par une couleur [47,144,145]. La réalisation de cette superposition, présentée sur la Figure III.5 se détaille comme suit :

(1) Sélection des images chimiques correspondantes à l'image topographique. Il est recommandé à ce stade d'utiliser la somme de quelques images chimiques pour augmenter le contraste. Le nombre d'images chimiques dépend de la profondeur qu'elles représentent. En pratique, trois à cinq images suffisent pour avoir un bon contraste.

(2) Définition de la taille du voxel des matrices 3D utilisées pour la représentation en relief. La taille du voxel dans les directions x,y correspond à la taille d'un pixel définie pour l'image AFM. La hauteur du voxel est fixée à 0.1 nm, ce qui correspond à la résolution en hauteur attendue par AFM.

(3) Conversion des valeurs de hauteur de l'image AFM en nombre de voxels. A ce stade, les résultats sont arrondis à l'entier le plus proche. Si certaines des valeurs sont négatives, on applique un offset pour n'avoir que des valeurs positives.

(4) Création d'une matrice 3D vide par élément chimique à superposer. Les dimensions latérales correspondent aux nombres de pixels de l'image topographique. La 3ème dimension correspond à la valeur de topographie maximale en voxels extraite de la matrice précédente.

(5) Création d'une surface topographique par élément chimique. L'intensité de chaque pixel (x, y) de l'image chimique est positionnée dans la matrice 3D créée précédemment selon les coordonnées topographiques correspondantes (x, y et z en nombre de voxels).

Cette thèse est accessible à l'adresse : http://theses.insa-lyon.fr/publication/2019LYSEI121/these.pdf
© [M.A. Moreno Villavicencio], [2019], INSA Lyon, tous droits réservés

Cette procédure est répétée dans une nouvelle matrice 3D vide pour chaque élément chimique à superposer.

1.3.2. CARTOGRAPHIE DU TAUX DE PULVERISATION

La cartographie du taux de pulvérisation est calculée à l'aide des images AFM capturées avant et après un cycle de pulvérisation, de la profondeur et du temps de pulvérisation correspondants. La Figure III.6 montre un schéma de la procédure permettant d'obtenir ces cartographies en [nm/s], [nm/image chimique], [voxel/image chimique] pour un cycle de pulvérisation. La procédure décrite ci-après est répétée pour chaque cycle de pulvérisation.

(1) Calcul de la profondeur de pulvérisation, pixel par pixel. Une matrice 2D est créée avec les valeurs de différence de hauteur entre l'image AFM supérieure et inférieure. Pour cette opération, les images brutes ont préalablement été ajustée à l'aide de la mesure de profondeur du cratère (voir la section CHAPTER II.4.3.3). La matrice 2D obtenue correspond donc à la cartographie de profondeur pulvérisée pour un cycle donné.
(2) Cartographie du taux de pulvérisation en [nm/s] : la matrice 2D de profondeur pulvérisée est divisée par le temps de pulvérisation de ce cycle.
(3) Cartographie du taux de pulvérisation en [nm/image chimique] : en divisant la profondeur pulvérisée par le nombre d'images chimiques obtenues dans ce cycle de pulvérisation, on obtient une cartographie de la profondeur pulvérisée pour produire une image chimique.
(4) Cartographie du taux de pulvérisation en [voxel/ image chimique] obtenue en divisant la cartographie par la hauteur du voxel, ce qui permet d'estimer le nombre de voxels par image chimique.

Il est à noter que cette approche de cartographie de vitesse de pulvérisation suppose d'avoir dans l'échantillon des interfaces parfaitement verticales ou horizontales. On suppose en effet pixel par pixel un taux de pulvérisation constant en profondeur lors d'un cycle de pulvérisation. Tenant compte de ces hypothèses, cette cartographie de la vitesse de pulvérisation permet d'analyser plus en détail le comportement de l'échantillon pendant un cycle et l'impact des conditions d'analyse.

1.3.3. CORRECTION ET VISUALISATION 3D DES DONNEES CHIMIQUES

La procédure permettant de créer une visualisation 3D des données chimiques est décrite ci-dessous et sur la Figure III.8. Celle-ci se base sur une reconstruction 3D à partir des données de topographie AFM. Les différentes phases sont :

Cette thèse est accessible à l'adresse : http://theses.insa-lyon.fr/publication/2019LYSEI121/these.pdf
© [M.A. Moreno Villavicencio], [2019], INSA Lyon, tous droits réservés

(1) Création du volume total et des sous-volumes correspondants à chaque cycle de pulvérisation. Cette étape est en fait réalisée au moment du traitement des données brutes AFM, lors de la soustraction des profondeurs de cratère aux images AFM correspondantes. Le volume total est délimité par les images AFM initiale et finale, t_0 et t_n, tandis que chaque sous-volume est délimité par les images AFM acquises avant et après un cycle de pulvérisation. Chaque sous-volume fournit un espace dans lequel les intensités en ions secondaires sont insérées.

(2) Conversion des images AFM en valeurs de voxel. Cette étape a été détaillée précédemment dans la procédure de superposition des images ToF-SIMS et AFM. Cette conversion est faite sur l'empilement total des images AFM. A ce stade, les résultats sont arrondis à l'entier le plus proche. Si certaines des valeurs sont négatives, on applique un offset pour n'avoir que des valeurs positives.

(3) Création d'un volume vide par élément chimique, dont les dimensions latérales sont celles définies par le nombre de pixels de l'image chimique et dont la hauteur en nombre de voxels est définie par l'écart maximal de topographie entre les images initiale et finale. Dans cette étape, la taille latérale en nombre de pixels des images topographiques doit être ajustée afin de correspondre au nombre de pixels de l'image chimique.

(4) Remplissage des volumes vides avec les intensités chimiques. Celui-ci est à répéter pour chaque sous-volume défini par le nombre de cycle de pulvérisation. Le positionnement des intensités chimiques s'effectue dans les colonnes définies par les pixels (x, y) de l'image chimique correspondante. L'image AFM initiale (x,y,z en voxels) définit pour chaque pixel (x,y) la position $z_O(x, y)$ (en voxels) à partir de laquelle doit commencer le remplissage. La cartographie de vitesse de pulvérisation en [voxels/image chimique] définit pour chaque pixel (x,y) d'un cycle de pulvérisation le nombre de voxels $N\ (x, y)$ à remplir (Figure III-7). A partir du 1er cycle de pulvérisation et pour chaque image chimique, une boucle assure le remplissage des $N\ (x, y)$ voxels en chaque pixel (x,y) par la valeur d'intensité correspondante et incrémente la position suivante de remplissage selon la relation :

$$z_n(x, y) = z_{n-1}(x, y) + (n - 1) \times N\ (x, y)$$

avec n le numéro de l'image chimique considérée. Cette boucle est répétée pour chaque empilement chimique et pour chaque cycle de pulvérisation. Il est possible d'optimiser le remplissage des $N\ (x, y)$ voxels par interpolation, ce qui permet de lisser les données pour la visualisation.

Cette thèse est accessible à l'adresse : http://theses.insa-lyon.fr/publication/2019LYSEI121/these.pdf
© [M.A. Moreno Villavicencio], [2019], INSA Lyon, tous droits réservés

Une autre approche pour la reconstruction à partir d'images topographiques consiste à utiliser une vitesse de pulvérisation constante pour chaque élément chimique plutôt que la cartographie du taux de pulvérisation. Dans ce cas, on fait l'hypothèse que la vitesse de pulvérisation ne varie pas ni dans la profondeur ni même dans le plan d'imagerie.

Cette approche convient mieux lorsque le temps de reconstruction est très long, si par exemple le nombre de couches de l'échantillon est élevé. La procédure est similaire à celle décrite précédemment, avec de légères différences :

(1) La vitesse de pulvérisation en [nm/s] pour un élément chimique est convertie en [nm/image chimique] en utilisant le temps de pulvérisation utilisé par cycle. Cette vitesse est ensuite convertie en [voxels/image chimique] à l'aide de la profondeur d'un voxel définie par l'utilisateur. La vitesse de pulvérisation en [voxels/image chimique] indique, comme décrit précédemment, le nombre de voxels correspondant par image chimique. Cette valeur est constante pour un élément chimique.
(2) Calcul de la moyenne de la vitesse de pulvérisation exprimée en [voxels/image chimique]. Plusieurs éléments chimiques peuvent être présents à une même position (x, y, z). Chaque élément chimique pouvant avoir une vitesse de pulvérisation différente, on détermine le nombre de voxels à remplir à la position (x, y, z) par la moyenne de la vitesse de pulvérisation des éléments chimiques présents.
(3) Les intensités chimiques sont ensuite repositionnées dans les colonnes du volume corrigé selon la procédure décrite précédemment.

Cette procédure allégée conduit inévitablement à des différences entre le volume reconstruit et l'échantillon réel. Cependant, cette approche permet d'avoir une reconstruction et une visualisation rapide et grossière du volume pulvérisé et de la répartition des éléments chimiques dans ce volume.

Cette thèse est accessible à l'adresse : http://theses.insa-lyon.fr/publication/2019LYSEI121/these.pdf
© [M.A. Moreno Villavicencio], [2019], INSA Lyon, tous droits réservés

2. APPLICATION DE LA METHODOLOGIE COMBINEE AFM – TOF SIMS

Lors d'une analyse standard par ToF-SIMS, le traitement des empilements d'images chimiques peut engendrer des artefacts sur la reconstruction. En effet, n'ayant aucune information sur la topographie de surface initiale, on suppose par défaut que la surface est parfaitement plane (Figure III.1.e). De plus, on ne tient pas compte du fait que la vitesse de pulvérisation peut changer à la fois localement sur l'échantillon mais aussi avec la profondeur sondée. Si l'échantillon présente une variété de matériaux (multicouches par exemple), il faut pouvoir estimer l'évolution de la vitesse de pulvérisation avec la profondeur. Ces facteurs ne sont pas simples à prendre en compte, et les suppositions simples qui sont faites conduisent dans certains cas à une mauvaise interprétation des résultats (Figure III.2) [133,134]. Pour obtenir une reconstruction chimique 3D correcte et plus précise, il faut pouvoir évaluer précisément les dimensions des volumes pulvérisés, en mesurant la topographie de surface et son évolution au cours du temps. Les dimensions latérales sont déterminées par le champ de vue et la hauteur dépend du temps de pulvérisation utilisé.

Ces dernières années, quelques idées d'amélioration ont été proposées pour optimiser la reconstruction et la visualisation 3D des images ToF-SIMS (Figure III.3). Cependant, aucune des méthodologies proposées ne prend en compte précisément les variations latérales et verticales de la vitesse de pulvérisation. Le protocole d'analyse combinée ToF-SIMS et AFM que nous avons mis au point est une adaptation des méthodologies existantes basée sur la correction des données ToF-SIMS à l'aide de mesures de topographie de surface. Cette méthodologie est tout à fait adaptée pour l'analyse de multicouches.

2.1. DESCRIPTION DE L'ECHANTILLON ET CONDITIONS D'ANALYSE

L'échantillon d'étude est une structure à base de GaAs fournie par le laboratoire des technologies de la microéléctronique (CNRS – LTM). Le dépôt de la couche de GaAs est réalisé en phase gazeuse par procédé chimique organométallique (MOCVD) dans des cavités de SiO_2 préalablement lithographiées sur un substrat silicium (100) de 300 mm. Les cavités présentent une sur-gravure d'environ 9 nm par rapport au substrat de silicium visible sur la Figure III.10.a. La couche de SiO_2 a une épaisseur d'environ 167 nm et la couche de GaAs a une épaisseur variable qui dépend du temps de dépôt. La structure analysée est un motif SiO_2 de 20 µm de large que l'on appellera pour la suite « *pacman* ». Une vue optique en vue de dessus est représentée sur la Figure III.10.b. Les dimensions de cette structure facilitent la localisation optique dans les deux instruments.

Cette thèse est accessible à l'adresse : http://theses.insa-lyon.fr/publication/2019LYSEI121/these.pdf
© [M.A. Moreno Villavicencio], [2019], INSA Lyon, tous droits réservés

2.2. DESCRIPTIF EXPERIMENTAL

Un profil complet ToF-SIMS permet d'identifier la présence de deux interfaces dans la profondeur de l'échantillon : une entre la couche de GaAs et le substrat de Si et une autre entre la couche de SiO_2 et le substrat de Si. A partir de profil, la méthodologie de mesures *ex-situ* ToF-SIMS / AFM / profilomètre a été définie (Figure III.11). Le transfert de l'échantillon entre les équipements a été réalisé à l'aide d'une capsule hermétique remplie en azote (surpression d'environ 10 mbar).

(1) Mesure AFM initiale, correspondant au temps t_0: l'image de la topographie de surface permet d'observer une différence de hauteur h_o of 14 nm entre le SiO_2 et le GaAs.
(2) Un premier cycle de pulvérisation, d'une durée de 920 s, couplé à l'analyse ToF-SIMS est réalisé jusqu'à l'observation de la première interface (GaAs / Si).
(3) Mesure AFM correspondant au temps t_1 = 920 s : la différence de hauteur h_1 entre le SiO_2 et le GaAs est de 108 nm. La profondeur du cratère d_1 mesurée par profilométrie de surface optique (3D Plu neox de Sensofar) en mode confocal est estimée à 160 nm.
(4) Un deuxième cycle de pulvérisation ToF-SIMS est effectué jusqu'à la détection de l'interface SiO_2 / Si, ce qui correspond à un temps t_2 = 2350 s.
(5) Mesure AFM correspondant au temps t_2 : la différence de hauteur h_2 évolue très peu, passant de 108 nm à 119 nm. La profondeur du cratère est estimée à 295 nm.
(6) Un troisième cycle de pulvérisation dans le substrat en Si est réalisé jusqu'à un temps t_3 = 2710 s.
(7) Image AFM finale, correspondant au temps t_3 : la différence de hauteur h_3 reste inchangée à 119 nm et la profondeur de cratère final d_3 est mesurée à 356 nm.

En résumé, les données ainsi obtenues à partir de cette analyse sont :

- Quatre images AFM dont la taille de pixel est de 43 nm, qui correspondent aux temps d'analyses t_0 (initial), t_1 (interface GaAs/Si), t_2 (interface SiO_2/Si) et t_3 (final).
- Trois empilements d'images chimiques dont le premier qui contient 92 images, le second 136 images et le 3ème 36 images. Il y a un empilement par élément chimique, à savoir dans notre cas le GaAs, le SiO_2 et le Si. Chaque image chimique a une taille de pixel de 198 nm.
- Les mesures de profondeur du cratère faites après chaque cycle de pulvérisation (d_1, d_2 et d_3). La profondeur du cratère est mesurée entre la surface pulvérisée, sur le GaAs, et la surface de GaAs non pulvérisée.

Cette thèse est accessible à l'adresse : http://theses.insa-lyon.fr/publication/2019LYSEI121/these.pdf
© [M.A. Moreno Villavicencio], [2019], INSA Lyon, tous droits réservés

2.3. SUPERPOSITION TOF-SIMS ET AFM

L'image chimique à superposer sur l'image AFM est obtenue en moyennant typiquement une dizaine d'images à l'interface, ce qui représente une profondeur sondée de quelques nanomètres. Cette moyenne permet d'augmenter le contraste de l'image chimique. Dans le cas de la topographie initiale (finale), les cinq premières (dernières) images de l'empilement sont moyennées.

La taille des pixels sur les images ToF-SIMS est 4.6 fois plus élevée que sur les images AFM. Afin de ne pas perdre la résolution de l'imagerie AFM, chaque image ToF-SIMS est interpolée, passant ainsi de 256 x 256 pixels à 1183 x 1183 pixels (Figure III.13.a).

Les superpositions des images ToF-SIMS et AFM correspondant aux topographies initiale et finale, ainsi que celle de chaque interface, sont illustrées sur la Figure III.15.a-d. Chaque couleur représente un élément chimique ou un matériau : rouge pour le SiO_2, bleu pour le GaAs et vert pour le Si. Le mélange des couleurs illustre la présence de plusieurs éléments aux interfaces, des traces d'ions $GaAs^-$ et SiO_2^- visible également sur l'image STEM (Figure III.10) sont ainsi respectivement visibles à la surface du substrat de Si à la première interface (t_1) et à la deuxième interfaces (t_2). On peut observer que la différence initiale de hauteur entre le GaAs et le SiO_2, augmente significativement après le premier cycle de pulvérisation (de t_0 à t_1) en raison de la différence de vitesse de pulvérisation entre le GaAs et le SiO_2. Par contre, cette différence de hauteur reste stable pour les cycles de pulvérisation suivants, du fait d'une vitesse de pulvérisation similaire entre le Si et le SiO_2.

Si on analyse la rugosité de la surface, on constate qu'initialement celle-ci est cinq fois plus élevée sur la surface de GaAs que sur la surface de SiO_2. Cette différence est clairement visible sur l'image de la Figure III.15.a. La rugosité élevée de la surface de GaAs (typ. 4 nm) est due à la présence de parois d'antiphase dans la couche de GaAs, défauts caractéristiques liés à la croissance d'un matériau polaire sur un substrat non polaire. On observe ensuite une légère augmentation de la rugosité après le premier cycle de pulvérisation, en particulier sur le GaAs (typ. 5 nm). On peut supposer que la non-homogénéité de la pulvérisation ou encore la présence des parois d'antiphase ou de défauts dans la couche sont à l'origine de cette augmentation. Une fois le substrat de Si atteint sur toute la zone d'analyse, la rugosité obtenue est homogène (typ. 1.5 nm).

Les sections obtenues à partir des images AFM renseignent sur l'impact des conditions de pulvérisation sur la topographie. En effet, on observe ainsi un changement notable de la topographie sur le pourtour de la structure *pacman* (Figure III.16). L'effet d'ombrage est notamment bien visible lorsque que l'orientation du faisceau de pulvérisation est perpendiculaire à la structure (Figure III.16.b).

Cette thèse est accessible à l'adresse : http://theses.insa-lyon.fr/publication/2019LYSEI121/these.pdf
© [M.A. Moreno Villavicencio], [2019], INSA Lyon, tous droits réservés

La courbure observée à la jonction entre le SiO_2 et le GaAs au temps t_0 s'atténue progressivement au cours de la pulvérisation lorsque celle-ci est parallèle à la jonction (Figure III.16.c).

2.4. CARTOGRAPHIE DE VITESSE DE PULVERISATION

Une cartographie de la vitesse de pulvérisation est obtenue par cycle de pulvérisation, avec une résolution spatiale définie par la résolution des images AFM. Pour le premier cycle de pulvérisation, la vitesse de pulvérisation du GaAs est environ 2.5 fois supérieure à celle du SiO_2, clairement identifié sur l'histogramme des valeurs de la cartographie : 0.07 ± 0.01 nm/s et 0.17 ± 0.01 nm/s respectivement pour le SiO_2 et le GaAs (Figure III.17.b). La rugosité de la surface de GaAs étant environ 5 fois supérieure à celle du SiO_2. Il en résulte une augmentation d'un facteur de 3.3 de la largeur à mi-hauteur.

La cartographie associée au deuxième cycle de pulvérisation indique des valeurs de taux de pulvérisation similaires pour le Si et le SiO_2, respectivement de 0.08 ± 0.01 nm/s et 0.07 ± 0.01 nm/s (Figure III.17.c). On constate que la vitesse de pulvérisation du SiO_2 est similaire à celle obtenue pour le premier cycle (Figure III.17.c). Par ailleurs, la valeur obtenue sur le Si a été confirmée sur un échantillon de référence en silicium dans les mêmes conditions d'analyse. Il en résulte une vitesse de pulvérisation de 0.08 nm/s ± 0.01 nm/s.

Les vitesses de pulvérisation ont été également estimées à partir des épaisseurs de couche mesurées par STEM (Figure III.10) et du temps de pulvérisation pour chaque cycle ToF-SIMS. Les valeurs trouvées pour les couches de GaAs et de SiO_2 coïncident avec celles estimées à partir des mesures de profondeur par profilomètrie. Le rendement de pulvérisation du GaAs, du SiO_2 et du Si, déterminé à partir de l'équation Eq. II.4, est respectivement de 2.5, 1.5 et 1.5 atomes/ions. Le rapport de rendement de pulvérisation GaAs / SiO_2 est comparable au rapport de 1.7 calculé dans la référence de Seah *et al.* [148], en utilisant comme faisceau de pulvérisation de l'Ar à 500 eV en incidence normale. Seah *et al.* montrent également que le rapport des vitesses de pulvérisation entre le SiO_2 et le Si, pour différentes énergies avec un faisceau de pulvérisation Ar en incidence normale, est toujours proche de 1. Cependant, il est à noter que Py [101] a obtenu un rapport de vitesse de pulvérisation SiO_2 / Si de 1.35 en utilisant une pulvérisation par Cs^+ à 500 eV avec une incidence à 45°.

On observe sur le contour de la structure *pacman* des valeurs de vitesse de pulvérisation différentes de celles trouvées sur la surface, et ce pour les deux cycles d'abrasion. Cette différence s'explique en raison de la topographie initiale et de la grande différence de vitesse de pulvérisation des matériaux à l'interface (SiO_2 / GaAs), mais aussi du fait de l'orientation du faisceau de pulvérisation.

Cette thèse est accessible à l'adresse : http://theses.insa-lyon.fr/publication/2019LYSEI121/these.pdf
© [M.A. Moreno Villavicencio], [2019], INSA Lyon, tous droits réservés

L'effet de la pulvérisation de structures qui présentent des interfaces verticales et horizontales sur l'évolution de leurs dimensions et de la rugosité a été largement étudié [149,150] Cependant, cette méthodologie est un moyen de caractériser plus finement le processus de pulvérisation en présence d'interfaces.

2.5. VISUALISATION 3D DES DONNEES TOF-SIMS CORRIGEES

La visualisation non corrigée des empilements d'images ToF-SIMS correspondant aux ions SiO_2, GaAs et Si respectivement de couleur rouge, bleu et vert est présenté sur la Figure III.18.a. Le défaut visible dans la couche de SiO_2 est lié à un effet de charge lors de la mesure. On observe également un rétrécissement du motif SiO_2 à l'approche de l'interface SiO_2/Si; probablement dû à une pulvérisation non-homogène dans le plan horizontal créant une déformation des images chimiques.

La vue en coupe présentée ne ressemble pas à l'image STEM de la Figure III.10 ni même à la représentation schématique de la Figure III.11. En effet, la méthode de reconstruction de base ToF-SIMS suppose que les parties haute et basse du volume sont planes. La topographie initiale de 14 nm entre le motif de SiO_2 et la surface de GaAs n'est pas pris en compte. D'autre part, les interfaces GaAs / Si et SiO_2 / Si ne sont pas correctement positionnées (différence de hauteur attendue de 9 nm). Avec cette visualisation, il n'est pas possible d'établir une profondeur du volume car elle dépend des vitesses de pulvérisation du matériau, qui ne sont pas calculées.

Pour la visualisation corrigée en 3D, nous faisons le choix de conserver la résolution spatiale des images chimiques. Dans ce cas de figure, les images AFM sont ainsi « dégradées » passant de 512 x 1024 pixels à 111 x 222 pixels (Figure III.13.b), Cette opération dégrade la résolution et donne une impression de contraste plus élevé, et donc une rugosité plus importante.

La Figure III.18.c présente une coupe transversale du volume chimique 3D corrigé, qui prend en compte la topographie initiale et finale de l'échantillon. La taille du voxel a été fixée à 0.1 nm, ce qui correspond à la résolution verticale de l'AFM. Le volume vide observé dans la couche de silicium est une conséquence directe de la différence de vitesse de pulvérisation entre le GaAs et le SiO_2. La topographie initiale de 14 nm entre le GaAs et le SiO_2 évolue jusqu'à une variation de hauteur finale de 119 nm. La couche de SiO_2 d'épaisseur 167 nm ainsi que la marche de 9 nm entre les interfaces GaAs / Si et SiO_2 / Si sont directement comparables à l'image STEM. Le problème de compensation de charge dans la couche de SiO_2 ainsi que le l'oxydation de la surface à chaque fin d'analyse ToF-SIMS se traduit par un effet de bord visible sur la Figure III.18.c.

Cette thèse est accessible à l'adresse : http://theses.insa-lyon.fr/publication/2019LYSEI121/these.pdf
© [M.A. Moreno Villavicencio], [2019], INSA Lyon, tous droits réservés

Les profils ToF-SIMS en profondeur non-corrigé et corrigé en topographie sont représentés sur la Figure III.18 b and d, respectivement. Nous avons choisi les ions $GaAs^-$, SiO_2^- et Si^- comme représentatifs des couches de GaAs, SiO_2 et Si, respectivement. Des discontinuités dans les profils de la Figure III.18.b sont visibles, probablement en raison de l'oxydation, de la contamination et / ou de la modification de la surface induite pendant le transfert de l'échantillon entre les instruments. Même si l'effet reste très faible au regard de la profondeur pulvérisée, il doit être pris en compte dans le cas où le nombre de cycles ToF-SIMS est important ou lorsque les couches analysées sont très minces.

Le profil ToF-SIMS en profondeur correspondant au volume corrigé a été créé en moyennant l'intensité de chaque voxel (x,y) en z et convertissant avec précision le temps de pulvérisation en profondeur. On constate ainsi que l'intensité du GaAs commence à augmenter après celle du SiO_2 mettant en évidence la topographie initiale de 14 nm observée entre la surface de SiO_2 et celle du GaAs. Le signal reste ensuite constant sur environ 154 nm jusqu'à atteindre l'interface GaAs / Si. Pour ce qui est de l'intensité du SiO_2, on observe une augmentation progressive probablement due à un effet de charge. De plus, on voit très clairement que l'interface SiO_2 / Si est moins profonde que celle du GaAs / Si, ce correspondant à la marche de 9 nm observée sur l'image STEM, Figure III.10. Comme l'ion Si^- est également caractéristique de la couche de SiO_2, l'intensité détectée est non-nulle dès le début du profil. Sa valeur maximale est atteinte après la pulvérisation complète de la couche de GaAs et son intensité chute à la fin du profil, à cause du volume non pulvérisé du substrat sous le SiO_2 (Figure III.18.c). Avec ce profil corrigé, la profondeur de chaque couche peut être mesurée et comparée par exemple à des mesures STEM.

Cette thèse est accessible à l'adresse : http://theses.insa-lyon.fr/publication/2019LYSEI121/these.pdf
© [M.A. Moreno Villavicencio], [2019], INSA Lyon, tous droits réservés

3. ÉTUDE DU PROCESSUS DE PULVERISATION SUR DES NANOSTRUCTURES A L'AIDE DE LA METHODOLOGIE COMBINEE AFM/TOF-SIMS

La collecte d'information chimique sur des nanostructures n'est pas simple. Les limites en termes de résolution latérale et de pulvérisation non homogène sont les principaux défis à maîtriser. La résolution latérale du ToF-SIMS est comprise en standard entre 100 nm et quelques microns. Dans la meilleure configuration, il est possible d'atteindre une résolution pouvant aller jusqu'à 50 nm, mais le réglage des paramètres prend beaucoup de temps. On peut ainsi espérer au mieux collecter une information chimique à cette échelle.

Outre la résolution latérale, le processus de pulvérisation varie en fonction de la composition de l'échantillon et des conditions d'analyse. Les espèces d'ions primaires [151], l'angle [152,153], l'énergie et l'orientation du faisceau de pulvérisation, ainsi que l'impact de la rugosité de la surface et de la topographie initiale sont autant de paramètre qui ont été largement étudiés. De ces études, des phénomènes tels que la dégradation de la topographie sous faisceau d'ions [154,155], la modification locale du champ d'extraction ou encore le rendement de pulvérisation amplifié localement, sont observées.

Les artefacts mentionnés ci-dessus, associés au manque de prise en compte de la topographie, entraînent des distorsions importantes et des problèmes d'ombrage dans les images chimiques lors de l'analyse de nanostructures (Figure III.1). Cet effet tend à s'amplifier pour les échantillons qui présentent une forte topographie car les lignes du champ d'extraction sont modifiées et la topographie sert de barrière physique à la collecte des ions [156]. Dans les deux cas, des stratégies d'analyse d'images multivariées ont été développées comme solution de post-analyse afin de déterminer les informations chimiques cachées dans les zones d'ombre [157]. La déformation des lignes de champ d'extraction peut être simulée dans certains cas géométriques simples [132]. Enfin, il est à noter que l'optimisation des paramètres expérimentaux, comme la tension et le délai d'extraction ou encore l'orientation du faisceau, peut permettre de réduire la taille des zones d'ombre [158].

Dans cette première partie, nous avons utilisé le protocole d'analyse combinée ToF-SIMS / AFM pour démontrer et minimiser l'effet de l'orientation du faisceau d'ions primaires et de l'énergie primaire sur la pulvérisation d'échantillons 3D hétérogènes. L'échantillon se compose de motifs «carrés» de SiO_2 dans lesquels du GaAs se trouve confiné comme présenté sur la Figure IV.1. La largeur du confinement varie de 250 nm à 1.2 µm. La surface de GaAs présente des défauts tels que des parois d'anti-phase et une variation de hauteur entre le SiO_2 et le GaAs d'environ 40 nm. Les motifs de SiO_2 ont une profondeur constante d'environ 167 nm. La région a été analysée de manière *ex-situ* comme suit :

Cette thèse est accessible à l'adresse : http://theses.insa-lyon.fr/publication/2019LYSEI121/these.pdf
© [M.A. Moreno Villavicencio], [2019], INSA Lyon, tous droits réservés

(1) Image AFM initiale de la région d'intérêt.
(2) Pulvérisation et profil en profondeur jusqu'à la première interface, GaAs / Si.
(3) Mesure de la profondeur du cratère.
(4) Image AFM finale de la région d'intérêt.

Chaque étude a été réalisée pour deux orientations de faisceau : parallèle et perpendiculaire au motif SiO_2. La direction du faisceau de pulvérisation est indiquée respectivement par des flèches bleue et rouge sur la Figure IV.1. Une étude a également été réalisée lorsque l'échantillon est mis en rotation. Trois énergies de pulvérisation ont été utilisées : 2 keV, 500 eV et 250 eV. Les conditions d'analyse ToF-SIMS et AFM sont décrites en détail dans la version anglaise du manuscrit.

La deuxième partie se focalise sur l'étude des paramètres qui affecte la résolution latérale, l'effet d'ombrage et de la déformation de l'interface. Pour cela, un réseau de lignes de SiO_2 (300 µm de long et environ 100 nm de large) séparées de 120 nm entre elles, ont été analysées. Chaque espace est rempli de GaAs. Ces lignes sont difficiles à observer à cause de la forte topographie créée par les dislocations dans le GaAs (Figure IV.3). Les analyses ont été menées *ex-situ* comme suit :

(1) Image AFM initiale de la région d'intérêt.
(2) Réalisation d'un cratère en biseau permettant d'observer à la fois la couche supérieure et le substrat.
(3) Analyse ToF-SIMS 2D haute résolution.
(4) Mesure de la profondeur du cratère.
(5) Image AFM finale.

3.1. RESULTATS SUR LES MOTIFS CARRES DE SiO_2

Pour la première analyse, la dose d'ion primaire nécessaire pour pulvériser l'échantillon jusqu'à la première interface était trois fois plus élevée à 250 eV qu'à 500 eV et six fois plus à 250 eV qu'à 2 keV (Figure IV.2.a). La dose d'ions dépend directement du courant des ions, qui est influencé par l'énergie des ions primaires. À partir des valeurs de dose d'ions et des mesures de profondeur de cratère, le rendement de pulvérisation pour chaque énergie a été calculé. Les barres d'erreur ont été calculées en utilisant la précision de la mesure de courant ToF-SIMS et la résolution en profondeur du profilomètre optique. Le rendement de pulvérisation est proportionnel à l'énergie primaire mais pas nécessairement de manière linéaire. En fait, le rendement de pulvérisation du GaAs indique que cette couche a été pulvérisée 9 fois plus rapidement à 2 keV qu'à 250 eV et 2.5 fois plus rapidement qu'à 500 eV (Figure IV.2.b) [159–161].

Cette thèse est accessible à l'adresse : http://theses.insa-lyon.fr/publication/2019LYSEI121/these.pdf
© [M.A. Moreno Villavicencio], [2019], INSA Lyon, tous droits réservés

La rugosité de surface mesurée pour un faisceau primaire orienté parallèlement aux motifs est comparable pour les trois énergies (Figure IV.2.c). A 500 eV et 2 keV, la rugosité est comparable quelle que soit l'orientation, perpendiculaire ou parallèle. Si l'on compare ces valeurs aux mesures de rugosité réalisées dans une zone du cratère pulvérisée sans apport de bismuth, on constate que ces valeurs sont comparables à l'exception de l'orientation perpendiculaire à 250 eV, où la rugosité a été évaluée à 1.6 nm au lieu de 2.1 nm. Pour cette orientation, la rugosité de la zone analysée à 250 eV est 50% plus élevée qu'à 500 eV et 2 keV. Une explication de ce comportement est difficile à fournir mais il est probable que l'effet d'ombrage pour cette orientation inhibe la pulvérisation. L'implantation d'ions bismuth est plus importante ce qui rend plus difficile la pulvérisation et crée alors une rugosité de surface élevée. De plus, le faisceau de pulvérisation à basse énergie est plus instable et pas nécessairement de forme bien définie, ce qui peut provoquer une pulvérisation inhomogène et créer de la rugosité.

La rugosité mesurée lorsque l'échantillon est mis en rotation pendant la pulvérisation à 2 keV est presque deux fois supérieure à celles mesurées sans rotation. Ce résultat n'est pas en accord avec la majorité des résultats trouvés dans la littérature qui montrent une diminution de la rugosité de surface et une amélioration de la résolution en profondeur [41,165,166]. Seules les mesures présentées par Gorbenko *et al.* [82] confirme la tendance que nous avons observée. Une cause possible pourrait être liée à la grande réactivité des ions Cs^+ qui s'agglomèrent en surface. Une autre explication pourrait être liée à une pulvérisation non homogène pendant la rotation du fait d'un mauvais alignement du motif à analyser avec l'axe de rotation.

La variation de l'énergie primaire affecte le rendement de pulvérisation, la rugosité et la résolution en profondeur. Un bon compromis est de travailler avec une énergie proche de 500 eV qui limite l'augmentation de la rugosité tout en conservant une bonne performance sur la résolution en profondeur et le rendement de pulvérisation.

Les images chimiques obtenues lors de l'analyse des motifs « carrés » de SiO_2 avec le faisceau d'ions orienté perpendiculairement montrent la présence d'oxygène à l'intérieur de la zone confinée des motifs 1 à 3, au lieu de détecter l'ion caractéristique $GaAs^-$ (voir Figure IV.4.b). La topographie de ces motifs agit comme une barrière physique qui empêche l'impact des ions primaires dans la zone confinée. Lorsque la largeur du confinement augmente (motifs 4 et 5), on constate une légère diminution du signal d'oxygène et la détection de GaAs. Pour l'orientation parallèle, cet effet est moins visible. Par contre, lors de la rotation de l'échantillon, on observe un signal d'intensité intermédiaire lié à une collecte isotrope des ions générés.

Cette thèse est accessible à l'adresse : http://theses.insa-lyon.fr/publication/2019LYSEI121/these.pdf
© [M.A. Moreno Villavicencio], [2019], INSA Lyon, tous droits réservés

La résolution latérale extraite à partir de profils sous SurfaceLab est d'environ 450 nm, 1000 nm et 800 nm respectivement pour les orientations parallèle et perpendiculaire et pour la rotation. Les largeurs des zones confinées de GaAs ont également été estimées à partir de profils extraits des images pour chaque orientation. L'erreur associée à chaque mesure correspond à deux fois la taille d'un pixel de l'image, soit environ 195 nm. Si l'on compare ces largeurs avec celles mesurées par AFM, on constate une correspondance seulement pour le motif 5 (Figure IV.4.c) Les valeurs mesurées sur les autres motifs sont surestimées du fait de la limitation de la résolution latérale imposée par le ToF-SIMS.

La profondeur de pulvérisation a été calculée pour chaque zone confinée (voir Figure IV.5.b). L'erreur associée a été obtenue en mesurant la largeur à mi-hauteur de la distribution des données AFM. L'effet d'ombrage plus important pour l'orientation perpendiculaire se traduit par des profondeurs mesurées plus faibles notamment dans les motifs 1 et 2. Cette différence est clairement visible sur le profil AFM de la Figure IV.5.a (courbe noire). Une différence relative d'environ 10 à 15 nm à l'intérieur des motifs 1 et 2 par rapport au point de référence (voir point bleu) est mesurée. On constate à partir de ces mesures que la taille critique pour l'effet d'ombrage en orientation perpendiculaire est de 500 nm car au-delà la profondeur mesurée n'est pas affectée. Dans le cas d'une orientation parallèle du faisceau d'ions avec les motifs, les profondeurs mesurées sont sensiblement identiques, ce qui confirme l'intérêt de cette orientation pour réduire l'impact lié à l'ombrage géométrique [158].

L'orientation du faisceau ionique a également un impact sur la morphologie des interfaces verticales de l'échantillon. Pour l'orientation perpendiculaire (voir courbe noire de la Figure IV.6.a), on constate une évolution de l'angle des interfaces verticales des motifs, ce qui se traduit par une modification locale du rendement de pulvérisation. Cette évolution est dissymétrique du fait de l'ombrage géométrique. En effet, on observe que l'interface droite, qui reçoit directement les ions primaires, est moins inclinée que l'interface gauche. Pour l'orientation parallèle, on constate un élargissement du motif (voir courbe rouge). Les pentes pour les interfaces droite et gauche sont d'environ 0.12 pour l'orientation parallèle et respectivement de 0.15 et 0.07 pour l'orientation perpendiculaire. Sigmund [168] a mis en évidence l'apparition de sillons lors de l'abrasion d'une zone confinée, comme celui visible en bas à gauche pour l'orientation parallèle. La formation de ces sillons serait due à la tendance des zones proches de l'interface verticale à être pulvérisées plus rapidement que le sommet.

L'évolution de la topographie des interfaces verticales a également été analysée avec une approche d'analyse par cratère biseauté. Les profils AFM obtenus après pulvérisation de la zone des lignes avec le faisceau d'ions perpendiculaire et parallèle aux lignes SiO_2 sont présentés sur la Figure IV.6.b (respectivement courbes noire et rouge).

Cette thèse est accessible à l'adresse : http://theses.insa-lyon.fr/publication/2019LYSEI121/these.pdf
© [M.A. Moreno Villavicencio], [2019], INSA Lyon, tous droits réservés

Pour l'orientation perpendiculaire, on observe comme précédemment une influence de l'ombrage géométrique sur l'inclinaison des interfaces verticales. Des pentes de 0.87 et 0.59 pour l'interface droite et gauche des lignes ont été mesurées. En revanche, les interfaces verticales des motifs de SiO_2 présentent une inclinaison similaire de 1.09 lorsque le faisceau d'ions est orienté parallèlement. La surface de GaAs entre les lignes de SiO_2 est uniquement observable pour l'orientation parallèle.

Il a été démontré avec ces premiers résultats que la pulvérisation de nano-motifs géométriquement bien définis peut être optimisée par l'orientation du faisceau ionique et l'énergie de pulvérisation. Une question demeure cependant : comment évaluer/anticiper les artefacts de pulvérisation lorsqu'un échantillon ne présente pas de motifs homogènes, comme dans le cas de défauts structuraux par exemple ? Les artefacts possibles lors de la pulvérisation de défauts peuvent conduire à une interprétation incorrecte des données 3D ToF-SIMS obtenues. De plus, les conditions d'analyse ne peuvent pas simplement être optimisées pour réduire ces artefacts. Dans ce cas de figure, l'AFM peut être utilisé comme un outil pour appréhender ces artefacts au travers de la mesure topographique de surface.

3.2. ANALYSE D'UN EMPILEMENT SIN/ALN/GAN

Nous illustrons cette problématique par l'analyse d'un empilement AlN / GaN réalisée par MOCVD sur un substrat de silicium de 200 mm (111). Une couche de passivation de 10 nm de SiN a été déposée in-situ sur cet empilement AlN/GaN pour protéger la surface de la dégradation et le stabiliser. L'épaisseur des couches est de 1.6 µm pour le GaN et d'environ 25 nm pour l'AlN (voir Figure IV.7.a). L'échantillon présente en surface des fissures visibles optiquement sur la Figure IV.7.b.

Une analyse chimique standard SIMS a été faite au préalable sur cet empilement pour étudier les différentes interfaces. Les profils obtenus (Figure IV.7.c) ne montre pas d'interface clairement définie entre la couche d'AlN et de GaN attendue à une profondeur d'environ 35 nm. En effet, les intensités de gallium et d'aluminium commencent à augmenter presque simultanément après 5 à 7 nm de pulvérisation. Si on se limite à l'interprétation basique du profil de gallium, il est assez direct de penser que celui-ci a diffusé dans la couche d'AlN sur environ 30 nm. Cette diffusion n'étant pas attendue, il se pose naturellement la question de l'impact des fissures visibles en surface du SiN sur la détection de gallium dans la couche d'AlN. Afin d'approfondir cette première analyse, nous avons réalisé une étude de cet empilement par ToF-SIMS et AFM.

Grâce à la création de deux régions d'intérêt (ROI) sur les images ToF-SIMS, les informations chimiques détectées au niveau des fissures et des grains ont pu être différenciées. L'analyse des fissures a cependant été limitée par la résolution latérale de l'instrument, ce qui se traduit dans ce cas par une contribution du signal des grains dans le ROI correspondant aux fissures.

Cette thèse est accessible à l'adresse : http://theses.insa-lyon.fr/publication/2019LYSEI121/these.pdf
© [M.A. Moreno Villavicencio], [2019], INSA Lyon, tous droits réservés

Les profils de la Figure IV.8.a montrent deux interfaces, le SiN / AlN atteint après 80 s de pulvérisation et l'AlN / GaN atteint après 440 s de pulvérisation. La forte intensité inattendue de $^{71}GaN^-$ dans la couche de SiN est due à l'influence des ions Si_3H^- dans ce pic, expliquant que le comportement de cette partie de la courbe est le même que celui observé pour le SiN^-. Au-delà de la première interface, la contribution des ions Si_3H^- devient insignifiante tandis que l'intensité du $^{71}GaN^-$ augmente et montre un gradient à l'intérieur de la couche d'AlN. La diffusion du gallium précédemment détectée par l'analyse SIMS est confirmée au niveau des grains et des fissures. Une analyse plus fine des profils révèle cependant quelques différences entre la fissure et le grain. En effet, on constate au niveau des fissures que le signal de SiN^- n'est jamais nul, que la diffusion du GaN^- est légèrement décalée vers la droite et une fois la couche de GaN atteinte, l'intensité du 71GaN est plus élevée qu'au niveau des grains. Compte tenu des artefacts possibles lors de la pulvérisation de nano-structures, la possibilité d'un effet d'ombrage géométrique influençant les profils chimiques des deux régions est suspectée.

La Figure IV.8.b montre l'évolution temporelle des images chimiques correspondantes aux ions SiN^-, AlN^- et $^{71}GaN^-$. La première plage de pulvérisation, de 0 à 100 s, correspond à la pulvérisation de la couche SiN. L'image SiN^- montre les fissures avec un contraste plus sombre. La diffusion du gallium dans la couche d'AlN est observée dans la deuxième plage de pulvérisation, de 100 s à 420 s., l'image de $^{71}GaN^-$ n'étant pas entièrement noire. L'image chimique de l'AlN^- a la plus forte intensité mais les ions SiN^- sont toujours détectés dans les fissures. Une fois la couche d'AlN complètement pulvérisée à 420 s, l'image chimique correspondant au $^{71}GaN^-$ montre la plus forte intensité. À ce moment, des ions secondaires de SiN^-, AlN^- et $^{71}GaN^-$ sont détectés dans les fissures. Ces observations combinées à la faible intensité de SiN provenant des fissures sur la première plage de pulvérisation nous a fait considérer un effet d'ombrage géométrique affectant la pulvérisation au niveau des fissures.

Une visualisation chimique 3D non corrigée de l'échantillon est montrée sur la Figure IV.9.a. Celle-ci suggère que l'analyse ToF-SIMS conduit à la formation de fissures profondes jusque dans la couche de GaAs remplies de SiN et d'AlN. Ceci est encore plus visible sur la Figure IV.9.b où la section transversale permet de visualiser uniquement la couche de GaN avec les ions GaN en bleu et les ions SiN en jaune. Cependant, une interprétation précise du profil en profondeur et des images chimiques de cet empilement AlN / GaN nécessite quelques considérations :

- La résolution latérale de cette analyse ToF-SIMS, estimée à plusieurs dizaines de nanomètres, n'assure pas une détection correcte des informations chimiques au niveau des fissures. En effet, la séparation des fissures et des grains dans deux ROI différentes n'est pas une procédure simple et donc, la fiabilité du profil de profondeur n'est pas garantie.

Cette thèse est accessible à l'adresse : http://theses.insa-lyon.fr/publication/2019LYSEI121/these.pdf
© [M.A. Moreno Villavicencio], [2019], INSA Lyon, tous droits réservés

- Trois couches de matériaux différents signifient donc trois taux de pulvérisation différents, non pris en compte dans le profil de profondeur observé sur la Figure IV.8.
- L'existence de nano-fissures à la surface de l'échantillon produit une pulvérisation non homogène qui peut être aggravée par l'existence d'artefacts comme effet d'ombrage géométrique.

La méthodologie combinée ToF-SIMS et AFM a été utilisée pour confirmer l'existence d'un effet d'ombrage géométrique. De plus, les informations fournies par l'AFM ont été utilisées pour déterminer la géométrie des fissures, leur épaisseur et leur orientation, ainsi que leur évolution avec la pulvérisation. Le protocole comportait deux étapes :

(1) Création d'un cratère biseauté ToF-SIMS permettant d'exposer les trois couches.
(2) Réalisation d'une image AFM dans trois zones du cratère correspondantes respectivement à la couche SiN, la couche AlN et la couche GaN.

Pour plus d'informations sur les conditions d'analyse, le lecteur peut se référer à la section CHAPTER IV.2.2.1. De plus, une pulvérisation ToF-SIMS supplémentaire a été réalisée dans le but d'étudier l'évolution de la topographie des fissures. Une image AFM du fond du cratère a été réalisée dans les mêmes conditions que celles décrites précédemment.

Les Figure IV.10.a, b et c montrent les images AFM prises dans les zones du cratère correspondant respectivement aux couches SiN, AlN et GaN. Les profondeurs exactes d'où les images ont été acquises sont inconnues. Cependant, une image ToF-SIMS de l'ensemble du cratère a confirmé que les trois couches étaient bien exposées à la surface. Les fissures sont visibles sur chaque image AFM, leur largeur et leur longueur variant en fonction de la profondeur de l'échantillon. Les fissures présentes dans l'échantillon avant la pulvérisation montrent un bord arrondi (voir la Figure IV.11.a), ce qui suggère une fissuration avant le dépôt de SiN et un remplissage non-homogène pendant le dépôt du SiN des fissures. Cette hypothèse expliquerait l'évolution de la largeur des fissures de 30 à 60 nm dans la couche de SiN et de 80 à 130 nm dans le GaN. La profondeur des fissures augmente de 5 à 15 nm jusqu'à 30 nm après une pulvérisation plus profonde dans l'échantillon. Cependant, la mesure de la profondeur de la fissure présentée sur la Figure IV.10 est sous-estimée du fait de la forme géométrique de la pointe qui ne permet pas d'atteindre le fond de la fissure.

La Figure IV.11.b montre l'image AFM capturée plus profondément dans la couche de GaN après un temps de pulvérisation de quelques minutes. La topographie des fissures évolue au cours de la pulvérisation produisant des bosses en surface. Ce phénomène implique l'existence d'un effet d'ombrage géométrique empêchant la pulvérisation à l'intérieur des fissures. Au début de l'analyse ToF-SIMS, le SiN est détecté dans les grains et les fissures mais avec moins d'intensité.

Cette thèse est accessible à l'adresse : http://theses.insa-lyon.fr/publication/2019LYSEI121/these.pdf
© [M.A. Moreno Villavicencio], [2019], INSA Lyon, tous droits réservés

En raison de la largeur de la fissure, l'effet d'ombrage géométrique produit une diminution du rendement de pulvérisation au niveau des fissures, ce qui se traduit par une intensité plus faible dans les images chimiques (Figure IV.8.b). En poursuivant le profilage, le SiN est complètement pulvérisé des grains. Cependant, comme la pulvérisation au niveau des fissures est retardée, le SiN est toujours détecté. Cette différence de rendement de pulvérisation modifie le bord des fissures, créant progressivement de petites bosses comme celle illustrée sur les Figure IV.10.a et b. Lorsque la couche d'AlN est complètement pulvérisée au niveau des grains, les images chimiques de SiN et d'AlN montrent une intensité résiduelle provenant des fissures, révélateur d'un retard de pulvérisation. Comme la différence de rendement de pulvérisation est toujours présente, les grains se pulvérisent plus rapidement que les fissures, ce qui se traduit par une inversion de topographie, comme le montre la Figure IV.11.b.

En étudiant les profils de la fissure sur la Figure IV.10.c, nous avons remarqué que les interfaces verticales montrent le même effet de modification de la topographie expliqué dans la partie précédente du chapitre. Le faisceau de pulvérisation bombarde l'échantillon du côté gauche, créant une dissymétrie visible sur les interfaces verticales. Ceci est le produit d'une exposition complète de l'interface droite au faisceau de pulvérisation et d'un ombrage géométrique bloquant la pulvérisation normale de l'interface gauche.

Des images STEM et des analyses EDX ont été réalisées sur un échantillon de même composition et dimension que celui détaillé précédemment mais fabriqué avec une pression NH_3 différente. Des fissures superficielles étaient également visibles en surface, avec cependant des largeurs initiales inférieures à 20 nm. L'image STEM de la Figure IV.12.a montre ces fissures de la couche GaN à la surface. Un léger effondrement de la couche de SiN aux endroits où se trouvent les fissures est observé, confirmant le remplissage des fissures avec du SiN, et en cohérence avec les informations extraites des profils AFM et des images chimiques ToF-SIMS. Le SiN pénétrant à l'intérieur des fissures lors du dépôt est également confirmé par l'image EDX du silicium (Figure IV.12.b). On voit que l'interface N/Si n'est pas plane. En effet, aux endroits où se trouvent les fissures, l'image chimique du silicium laisse penser à une diffusion au sein de la couche d'AlN.

L'influence de l'ombrage géométrique sur l'analyse d'un profil en profondeur et d'images chimiques a été montrée. En effet, lors de l'analyse de zones nanométriques, la résolution latérale de ToF-SIMS s'avère être une limitation qui peut être surmontée à l'aide des profils AFM. De plus, l'AFM a été validé comme un outil pour comprendre la pulvérisation de l'échantillon et l'évolution de l'échantillon au cours de l'analyse.

Cette thèse est accessible à l'adresse : http://theses.insa-lyon.fr/publication/2019LYSEI121/these.pdf
© [M.A. Moreno Villavicencio], [2019], INSA Lyon, tous droits réservés

4. ToF-SIMS combine avec les modes AFM electriques

La polyvalence de la technique AFM permet de déterminer simultanément les informations topographiques et des propriétés locales telles que les propriétés mécaniques, électriques, magnétiques, piézoélectriques. Ces informations sont fournies par le biais de cartographie de la zone analysée avec une résolution latérale à l'échelle nanométrique (généralement supérieure à 50 nm). La communauté scientifique a d'abord pensé à corréler les informations chimiques ToF-SIMS avec les informations topographiques classiques de l'AFM mais le développement des modes de fonctionnement avancés de l'AFM ouvre la possibilité de corréler une propriété physique à l'information chimique. Ainsi, nous avons combiné le ToF-SIMS avec les modes AFM avancés tels que le PFM, KFM, SSRM et SCM, pour deux applications différentes.

4.1. Etude de la modification chimique d'echantillons piezoelectriques apres polarisation electrique locale

Les matériaux piézoélectriques ont la capacité de générer une charge électrique lorsqu'ils sont soumis à une sollicitation mécanique. Ils sont largement utilisés comme actionneurs [171], transducteurs, contrôleurs de fréquence [172], récepteurs ultrasoniques [173], etc. La famille piézoélectrique comprend les matériaux ferroélectriques. Ces derniers possèdent une polarisation permanente dans une ou plusieurs directions qui peut être inversée par l'application d'un champ électrique externe. Ils présentent un intérêt pour les applications mémoires, d'affichage et de modulateurs [174]. Tous les matériaux ferroélectriques sont piézoélectriques mais toutes les matériaux piézoélectriques ne sont pas ferroélectriques [128].

L'utilisation de ces matériaux pour les composants électroniques a augmenté ces dernières années. La réduction de taille des dispositifs a amené la nécessité de comprendre et de contrôler leurs propriétés à l'échelle nanométrique. Pour étudier les propriétés ferroélectriques à l'échelle nanométrique, une pointe AFM conductrice peut être utilisée pour appliquer par exemple un champ électrique supérieur au champ coercitif de l'échantillon. Ceci induit, dans un échantillon ferroélectrique, un alignement permanent de la polarisation selon direction du champ électrique. On appelle par la suite ce processus « écriture » locale de domaines. [175]

Nous avons appliqué la méthodologie combinée ToF-SIMS et PFM pour tenter de détecter une éventuelle modification chimique à l'échelle nanométrique après le processus d'écriture.

Cette thèse est accessible à l'adresse : http://theses.insa-lyon.fr/publication/2019LYSEI121/these.pdf
© [M.A. Moreno Villavicencio], [2019], INSA Lyon, tous droits réservés

La méthodologie consiste à écrire des domaines locaux pour chaque échantillon à l'aide d'une pointe AFM et, ensuite, analyser la zone polarisée par ToF-SIMS pour détecter toute modification chimique. Deux échantillons ont été analysés, un ferroélectrique et un non ferroélectrique : $BaTiO_3$ (BTO) et $LaAlO_3$ (LAO) respectivement.

L'échantillon BTO est constitué d'une électrode en $LaNiO_3$ de 10 nm déposée sur un substrat de $SrTiO_3$. Une couche de 100 nm de $BaTiO_3$ (BTO) est déposée sur cet empilement (Figure V.3.a). Les domaines sont écrits avec une force de contact d'environ 95 nN en appliquant une tension sur l'échantillon de ± 3 V. Une analyse PFM a ensuite été effectuée pour deux configurations en appliquant une tension alternative de 500 mV et 250 mV respectivement. Les zones ont été analysées chimiquement en profondeur par ToF-SIMS. Un faisceau primaire de Bi_3^{++} (60 keV, 0.36 nA) a été utilisé avec un temps de cycle de 70 µs. Aucun faisceau de pulvérisation n'a été utilisé pour la première configuration, mais après 20 minutes d'imagerie de la deuxième configuration, un profil de profondeur en mode non entrelacé (analyse de 15 images, pulvérisation 1 image, 1 s de pause) a été effectué. Un faisceau de Cs^+ d'énergie 500 eV a été sélectionné pour pulvériser une surface de 500 µm x 500 µm. Le profil de profondeur a été acquis pendant plus de 17 heures en mode négatif.

La structure LAO est obtenue par le dépôt d'une couche de 3 nm d'épaisseur de $LaAlO_3$ amorphe (LAO) par épitaxie par jet moléculaire sur un substrat de silicium (figure V.2.a). Le dépôt du premier nanomètre est effectué en limitant la pression d'oxygène pour éviter la formation d'oxyde à l'interface LAO/Si. Les deux nanomètres restants sont déposés sous 2×10^{-6} Torr de pression d'oxygène. Plus d'informations sur la fabrication de l'échantillon se trouvent dans la référence [181]. Les domaines ont été écrits avec une force de contact d'environ 95 nN en appliquant une polarisation de pointe de ± 5 V sur un carré de 10 µm x 10 µm (Figure V.2.b) et sur deux carrés de 20 µm x 20 µm (Figure V.2.c). Un troisième processus d '«écriture» a été réalisé en appliquant une tension d'échantillon de ± 9 V sur deux carrés de 15 µm x 15 µm avec une force de contact d'environ 150 nN (Figure V.2.d). La technique KFM a été utilisée pour caractériser la présence de charges en surface et leur évolution dans le temps. De plus, une analyse PFM a été effectuée sur le carré écrit de la troisième analyse en utilisant une tension AC de 5 V. Les zones ont été analysées par ToF-SIMS en utilisant uniquement un faisceau primaire de Bi_3^{++} (60 keV, 0.8 nA). Les analyses ont duré plusieurs heures et ont été réalisées en polarité négative pour la deuxième configuration et en polarité positive pour la troisième configuration.

Cette thèse est accessible à l'adresse : http://theses.insa-lyon.fr/publication/2019LYSEI121/these.pdf
© [M.A. Moreno Villavicencio], [2019], INSA Lyon, tous droits réservés

4.1.1. RESULTATS

Des images de phase PFM sont montrées pour les deux échantillons, le BTO ferroélectrique et le LAO non ferroélectrique, respectivement sur la Figure V.6.b et la Figure V.10.a , f. Les régions balayées « écrites » avec une polarisation positive montrent un déphasage de 180° par rapport aux régions « écrites » avec une tension négative. Plusieurs études dans la littérature d'échantillons non ferroélectriques montrent qu'un signal PFM peut-être détecté (Figure V.1.b-c) [176–178]. L'origine du contraste sur de tels échantillons est encore inconnue, et on propose de l'étudier par ToF-SIMS et AFM. Des hypothèses ont émergé pour expliquer ce comportement : la mobilité ionique qui induit la redistribution des lacunes d'oxygène ou encore l'injection de charges induite par le champ électrique. Nous avons concentré notre étude sur la détermination de la mobilité ionique.

Bark *et al.* [177] ont observé pour une structure LAO une décroissance temporelle des signaux de microscopie PFM et de force électrostatique respectivement après des dizaines de minutes et 3 heures. Les images KFM que nous avons obtenues montrent un contraste potentiel même après 51 h après l'écriture (Figure V.4). Toutes les images KFM montrent une variation de la différence de potentiel de contact (CPD) dans les zones «écrites» (Figure V.5.a, Figure V.6.c). Cela peut être attribué à l'existence de charges superficielles ou à une modification chimique de surface de cette zone. En effet, les images ToF-SIMS de la Figure V.5.b et de la Figure V.6.d montrent des contrastes chimiques sur les zones « écrites » ainsi que sur les zones « non-écrites » mais balayés par la pointe en mode contact. La zone 0 V sur la Figure V.6.d correspond à la zone où la topographie a été mesurée par AFM en mode contact. Ces résultats suggèrent une modification chimique produite par le contact pointe-surface quelle que soit la tension appliquée. Des hypothèses telles que l'élimination de la contamination de la surface avec la pointe AFM pendant le balayage ou des traces de la pointe laissée lors du balayage sont envisagées.

Étant donné que la modification chimique attendue après l'application de la tension est faible, l'interprétation des images chimiques ToF-SIMS n'est pas une procédure simple. Une analyse en composantes principales (ACP) a été réalisée sur les données de la deuxième analyse. Deux pics se révèlent caractéristiques de la zone qui n'a jamais été en contact avec la pointe de l'AFM, le m/z = 149 et le m/z = 182. Ils correspondent respectivement à des fragments de phtalate et de phosphate, bien connus être représentatif de la contamination organique induite par les plastifiants [185]. Ce résultat suggère que la pointe élimine la contamination lorsqu'elle balaye la surface, réduisant le nombre de ces molécules dans les zones « écrites ».

Cette thèse est accessible à l'adresse : http://theses.insa-lyon.fr/publication/2019LYSEI121/these.pdf
© [M.A. Moreno Villavicencio], [2019], INSA Lyon, tous droits réservés

Le signal PFM obtenu à partir de matériaux non ferroélectriques est souvent attribué à la variation du volume molaire produit par la migration ionique telle que la migration de l'oxygène [180]. La migration suspectée consiste en des ions d'oxygène chargés négativement se déplaçant vers l'anode tandis que la cathode attire les lacunes d'oxygène chargées positivement. Les charges, piégées sur ces sites, seraient à l'origine d'un comportement mimant la polarisation. Dans notre cas, une tension positive appliquée à la pointe impliquerait la migration d'ions d'oxygène chargés négativement vers la surface. Ainsi, l'intensité d'oxygène détectée dans les zones polarisées négativement devrait être inférieure à celle détectée dans les zones polarisées positivement. La Figure V.8 montre les résultats de l'ACP des données extraites exclusivement des zones écrites de ± 5 V. Les données et les pics correspondant au carré négatif sont indiquées en jaune, rose et bleu pour une visualisation plus facile. Les trois mêmes gammes que pour l'analyse précédente ont été maintenues. Malheureusement, les composantes principales de la Figure V.8 montrent une concentration plus élevée d'ions oxygène relativement aux données extraites du -5 V. Une explication possible peut être que les lacunes d'oxygène sont présentes à une concentration élevée dans les échantillons fabriqués par épitaxie par jet moléculaire comme c'est le cas pour cette structure. Le stockage prolongé de cet échantillon dans des conditions ambiantes favorise une réoxydation de la surface modifiant la concentration intrinsèque en oxygène de l'échantillon. Cependant, le sujet est toujours ouvert et l'occurrence d'une migration d'oxygène ne peut être confirmée.

D'un autre côté, les résultats ToF-SIMS suggèrent plutôt la migration ionique du lanthane. Les ions de lanthane chargés positivement peuvent être attirés vers la surface polarisée négativement produisant une concentration plus élevée de ces ions dans ces zones. Ce comportement est illustré dans les composantes principales de la Figure V.8. En effet, le pic La^+ est retrouvé majoritairement sur les carrés - 5 V. Comme les ions secondaires de lanthane sont mieux détectés en polarité positive, la détection ToF-SIMS de la troisième analyse a été effectuée en mode positif. La Figure V.9.a montre l'intensité normalisée du lanthane obtenue après avoir calculé la moyenne des trois ensembles de données par carré. Le lanthane a été trouvé à une intensité plus élevée à la surface du carré où une tension de + 9 V a été appliquée à l'échantillon. Cela suggère qu'effectivement, les ions de lanthane chargés positivement migrent vers la surface où la tension négative est appliquée. Le profil de profondeur ToF-SIMS obtenu pour cette analyse est illustré à la Figure V.9.b. L'analyse a été arrêtée trois fois pour optimiser le stockage des données. La discontinuité dans les profils de profondeur coïncide avec le moment où l'analyse a été arrêtée. L'intensité légèrement plus élevée de lanthane détectée dans la zone polarisée positivement est bien présente pendant au moins 28 h d'analyse. L'intensité détectée après ce temps s'approche de celle détectée pour le carré polarisé négativement.

Cette thèse est accessible à l'adresse : http://theses.insa-lyon.fr/publication/2019LYSEI121/these.pdf
© [M.A. Moreno Villavicencio], [2019], INSA Lyon, tous droits réservés

Après avoir attribué le comportement ferroélectrique des échantillons LAO à une migration ionique de lanthane chargés positivement, nous avons analysé les données ToF-SIMS obtenues pour l'échantillon ferroélectrique BTO. Aucune relation n'a été trouvée entre le contraste de la zone en contact avec la pointe AFM sans application de tension et les pics correspondant à la contamination organique, en particulier le phtalate m / z = 149 et le phosphate m / z = 182. On ne peut donc pas supposer que La pointe AFM a éliminé la contamination de la surface pendant le balayage. De plus, aucun signal de migration d'oxygène n'a été trouvé dans notre analyse. L'étude de la migration de l'oxygène n'est pas simple. Les changements chimiques devraient se produire à la surface de l'échantillon où il y a également l'influence des contaminants de surface. Le fait d'effectuer l'analyse ex situ ajoute l'influence de l'oxydation externe, qui doit alors être dissociée de l'oxygène intrinsèque de l'échantillon. Les résultats obtenus pour le BTO n'ont pas permis de tirer une conclusion correcte sur le mécanisme de polarisation. En effet, une optimisation du protocole et des conditions d'analyse est nécessaire. Une liste de recommandations à considérer pour les travaux futurs est présentée dans le document de thèse.

4.2. MESURE ET RECUPERATION DES PROPRIETES ELECTRIQUES D'ECHANTILLONS DOPES PAR TOF-SIMS ET SCM/SSRM

Les techniques de caractérisation à haute résolution spatiale telles que la microscopie électronique à transmission (TEM), la microscopie électronique à balayage (SEM) et la sonde atomique tomographique (APT) sont largement utilisées pour caractériser les dispositifs de l'industrie de la microélectronique à l'échelle nanométrique. Le principal inconvénient de ces techniques reste la préparation des échantillons avant l'analyse. L'une des méthodes la plus utilisée repose sur la préparation par faisceau d'ions focalisés (FIB). Cette technique utilise une source d'ions de métal liquide pour fournir un faisceau d'ions, généralement du Ga^+, qui est accéléré vers une zone souhaitée de la surface de l'échantillon. Les ions bombardent la surface et pulvérisent le matériau, ce qui permet de produire par exemple des échantillons de dimensions typiques de 20 µm x 5 µm avec une épaisseur uniforme de moins de 100 nm en quelques heures. La précision spatiale du FIB de quelques dizaines de nanomètres est précieuse lorsque des zones précises de taille nanométrique sont à analyser. [188]

Cependant, l'interaction des ions primaires (Ga^+) avec les atomes de surface est une source d'artefacts tels que la redéposition d'atomes pulvérisés, l'implantation d'ions primaires et l'amorphisation due au déplacement des atomes dans l'échantillon. Ces conséquences indésirables sont les principaux inconvénients de cette technique de préparation [189].

Cette thèse est accessible à l'adresse : http://theses.insa-lyon.fr/publication/2019LYSEI121/these.pdf
© [M.A. Moreno Villavicencio], [2019], INSA Lyon, tous droits réservés

L'AFM et ses modes électriques, en particulier la SCM (scanning capacitance microscopy) et la SSRM (scanning spreading resistance microscopy) deux techniques utilisées pour cartographier les propriétés électriques, sont utilisées dans cette étude pour évaluer l'impact de cette préparation, et plus précisément la modification des propriétés électriques d'échantillons semi-conducteurs après implantation de gallium. Nous avons adapté la méthodologie combinée ToF-SIMS et AFM dans le but d'utiliser une pulvérisation ToF-SIMS contrôlée pour éliminer les dommages induits par le FIB et voir s'il est possible de restaurer les propriétés électriques initiales.

Des substrats de silicium dopés non structurés (Figure V.11) ont été utilisés pour obtenir des résultats préliminaires et établir un protocole approprié, qui a ensuite été appliqué sur des échantillons de silicium à motifs comportant des zones dopées n et p (Figure V.12). Le protocole ToF-SIMS / SCM combiné consiste à réaliser une image SCM initiale d'une zone déterminée de l'échantillon, implanter du gallium par FIB à différentes énergies sur cette même zone, réaliser à nouveau une image SCM de la zone implantée, pulvériser par ToF-SIMS la zone implantée jusqu'à diminution complète du signal du gallium dans les images chimiques et enfin réaliser une image SCM finale de la zone pulvérisée. Pour des problèmes de sensibilité de mesure, nous avons également réalisés des mesures par SSRM.

4.2.1. RESULTATS

Le développement du protocole combiné ToF-SIMS / SCM / SSRM a commencé avec l'étude d'un substrat de silicium fortement dopé n après irradiation FIB à différentes énergies. Pour rappel, le signal délivré par la SCM est inversement proportionnel au dopage actif : plus le dopage est élevé, plus le signal est faible (voire nul) et vice-versa (voir le comportement de capacité sur la Figure II.6. Dans notre cas d'étude, aucun signal SCM n'a été détecté sur cet échantillon, ce qui nous a amené à réaliser l'analyse par SSRM (Figure V.13.a).

Le contraste observé en SSRM entre les zones implantées et la zone non implantée indique une diminution de la résistance du substrat de silicium après irradiation FIB, ce qui confirme une dégradation des propriétés électriques. L'implantation par FIB a également affecté la zone externe sur laquelle une diminution de la résistance est également observée. Après 112 s de pulvérisation ToF-SIMS (Figure V.13.b), les zones correspondant aux énergies d'implantation de 5 keV et 8 keV montrent une réduction significative du gallium, qui est également constatée sur l'image SSRM par une homogénéisation du contraste entre ces zones. Le gallium implanté à 16 keV et 30 keV est retiré de l'échantillon après 202 s et 303 s de pulvérisation respectivement. À partir de ce moment, l'image de la résistance présente une cartographie électrique équivalente à une zone non-implantée (Figure V.13.c). La différence finale de résistance des zones implantées et non implantées est de 0.5%.

Cette thèse est accessible à l'adresse : http://theses.insa-lyon.fr/publication/2019LYSEI121/these.pdf
© [M.A. Moreno Villavicencio], [2019], INSA Lyon, tous droits réservés

Les profils de résistance montrent une variation sur les bords de la zone implantée, également visible sur les profils de topographie de la Figure V.14. Spoldi *et al.* [192] expliquent ce phénomène par l'amorphisation du silicium et la redéposition des atomes pulvérisés au bord de ces zones. Une légère augmentation de la topographie des zones irradiées est également observée. Celle-ci dépend de l'énergie primaire du FIB (Figure V.14) et est attribuée à l'amorphisation des zones implantées.

Après l'élimination du gallium par pulvérisation ToF-SIMS, le contraste entre les zones implantées et non implantées est à peine visible sur les images SSRM (Figure V.15.a and d). La différence la plus élevée est observée à 30 keV et correspond à 99.6% de la résistance finale mesurée dans la zone non implantée. Il est à noter que les dommages créés par la pulvérisation ToF-SIMS tels que l'amorphisation peuvent être la raison pour laquelle les valeurs finales de résistance ne correspondent pas à la valeur initiale. La dégradation des propriétés électriques des échantillons est également observée sur les zones balayées lors de l'imagerie SSRM (zones plus claires et plus sombres sur les images SSRM finales à 8 keV et 30 keV respectivement). Cela est probablement dû à la force de contact élevée entre la pointe de l'AFM et l'échantillon, qui a été calculée à environ 1.6 µN. Le profil en profondeur ToF-SIMS en fonction de l'énergie d'implantation montre une intensité en silicium similaire quel que soit l'énergie d'implantation utilisée (

Figure V.16). Cependant, le temps nécessaire pour éliminer le signal du gallium augmente avec l'énergie d'implantation, ce qui implique que la profondeur d'implantation du gallium est proportionnelle à l'énergie primaire. En fait, Giannuzzi et Stevie [194] ont montré par simulation que la couche amorphe créée peut être en première approximation supposée comme la couche implantée, elle-même approximée à la valeur de l'énergie primaire du faisceau d'ions.

Ces résultats préliminaires ont permis de valider le protocole d'analyse, que nous avons ensuite testé sur deux échantillons de silicium comportant des zones de dopage n et p de différentes concentrations. Ces zones sont bien identifiées pour les deux échantillons par imagerie SCM (Figure V.17.a et Figure V.18a). Les couleurs foncées (signal négatif) distinguent les zones dopées de type n tandis que les couleurs claires (signal positif) correspondent aux zones de type p. Les zones isolantes ou fortement dopées correspondent à un signal SCM nul.

La zone implantée par FIB est facilement reconnaissable après imagerie SCM car aucun signal n'est détecté (Figure V.17.b et Figure V.18.b). On constate que la zone impactée est plus grande que la région implantée. L'analyse SCM du deuxième échantillon répétée 3 heures après l'implantation par FIB montre un élargissement de la zone où aucun signal n'est détecté. L'imagerie SCM réalisée 9 jours après l'implantation ne permet plus de distinguer les différentes zones. On ne peut écarter à ce stade la dégradation ou la contamination de la surface des échantillons du fait de l'analyse et du stockage à condition ambiante.

Cette thèse est accessible à l'adresse : http://theses.insa-lyon.fr/publication/2019LYSEI121/these.pdf
© [M.A. Moreno Villavicencio], [2019], INSA Lyon, tous droits réservés

Spoldi *et al.* [192,192] ont également remarqué cet effet d'étalement qu'ils expliquent comme étant lié à l'interaction et la diffusion des atomes de gallium avec les atomes de l'échantillon.

Après élimination du gallium à l'aide de la pulvérisation ToF-SIMS (Figure V.17.c-d Figure V.18.c), on récupère un signal SCM de faible intensité pour le premier échantillon (Figure V.17.d). Aucun signal SCM n'est par contre détecté sur le deuxième échantillon (Figure V.18.e). Deux phénomènes peuvent expliquer cette observation : l'absence d'une couche d'oxyde natif, ou du moins de moins bonne qualité, et l'amorphisation induite par la pulvérisation du ToF-SIMS. Ces deux raisons sont réalistes et ne peuvent être dissociées. Pour s'en assurer, nous avons effectué une analyse SSRM, car le contrôle précis de la force de contact permet de passer au travers cette couche amorphisée pour assurer un bon contact électrique (Figure V.17.f et Figure V.18.e). Les images obtenues montrent une variation de la résistance dans les régions dopées de type p pour le premier et permet de distinguer les zones isolantes sur le deuxième échantillon.

La Figure V.18.f montre l'évolution de la topographie de l'échantillon au cours des différentes analyses du protocole. La hauteur augmente après la pulvérisation ToF-SIMS et la forme des motifs est légèrement modifiée après l'implantation par FIB et l'élimination du gallium.

L'établissement d'une méthodologie combinée implique un compromis entre les limites des techniques de caractérisation et l'application finale que l'on souhaite atteindre. Les résultats préliminaires qui ont été présentés dans ce manuscrit ont favorisé les améliorations de la méthodologie. Les limitations qui doivent être prises en compte sont répertoriées dans la version anglaise.

Cette thèse est accessible à l'adresse : http://theses.insa-lyon.fr/publication/2019LYSEI121/these.pdf
© [M.A. Moreno Villavicencio], [2019], INSA Lyon, tous droits réservés

5. PERSPECTIVES

Le ToF-SIMS est une technique de caractérisation puissante qui permet la caractérisation chimique 3D avec des limites de détection de l'ordre du ppm. Malgré les bonnes performances du ToF-SIMS, les informations chimiques obtenues ont une résolution latérale de 150 nm, ce qui n'est pas suffisant pour l'analyse de dispositifs de taille nanométrique. La combinaison avec des techniques de caractérisation à haute résolution latérale a émergé ces dernières années pour surmonter cette limitation. Ce travail de thèse s'est focalisé sur le développement et l'optimisation de la combinaison du ToF-SIMS avec l'AFM.

L'AFM est une technique d'imagerie de résolution nanométrique conçue pour mesurer la topographie de surface grâce à l'interaction d'une sonde nanométrique à la surface de l'échantillon. L'AFM permet de mesurer la topographie et simultanément d'autres propriétés de l'échantillon : cartographie avec des informations électriques, magnétiques, piézoélectriques ou mécaniques de l'échantillon mesurées avec une résolution latérale de quelques nanomètres. On peut ainsi espérer, en combinant ces cartographies à haute résolution avec les informations chimiques, améliorer la résolution du ToF-SIMS.

Le chapitre II (CHAPTER II) présente une méthodologie combinée ToF-SIMS et AFM qui comprend une section expérimentale et une description détaillée des étapes de traitement des données. Le protocole expérimental consiste en une analyse cyclique ToF-SIMS, AFM et profilomètre où la topographie et la profondeur du cratère sont mesurées au début, à la fin et chaque fois qu'une interface est détectée dans le profil de profondeur ToF-SIMS. La deuxième partie de la méthodologie comprend le traitement des données, tout d'abord la mise en forme des données brutes puis le traitement avancé. Trois principaux résultats sont obtenus à partir de la méthodologie proposée : (i) une visualisation 3D ToF-SIMS corrigée de la topographie, (ii) la cartographie de la vitesse de pulvérisation de la zone analysée et (iii) la superposition des informations chimiques avec les données topographiques. Chacun de ces résultats est illustré dans les chapitres suivants.

Le chapitre III (CHAPTER III) présente la problématique associée à l'analyse 3D ToF-SIMS de structures hétérogènes présentant initialement une topographie. Le manque de prise en compte de cette topographie dans la reconstruction des images chimiques crée une distorsion de l'ensemble des données pour la visualisation 3D. L'AFM est utilisé comme un outil pour corriger l'ensemble de données en mesurant la topographie à chaque interface. La méthodologie combinée ToF-SIMS et AFM a été appliquée sur une hétérostructure de type GaAs / SiO_2 dont la reconstruction 3D n'était pas possible selon les procédures classiques. Grâce au protocole combiné ToF-SIMS et AFM, une cartographie de la vitesse de pulvérisation a été déterminée pour chaque cycle de pulvérisation.

Cette thèse est accessible à l'adresse : http://theses.insa-lyon.fr/publication/2019LYSEI121/these.pdf
© [M.A. Moreno Villavicencio], [2019], INSA Lyon, tous droits réservés

Celles-ci ont été utilisés pour convertir le temps de pulvérisation en profondeur de pulvérisation, pour ainsi permettre la visualisation chimique 3D de l'échantillon avec une échelle de profondeur définie. De plus, la méthodologie a fourni des superpositions d'informations chimiques sur les topographies de surface, qui sont utiles pour analyser les caractéristiques de la surface et l'évolution de la topographie pendant la pulvérisation.

Le chapitre IV (CHAPTER IV) détaille comment les cartographies de vitesse de pulvérisation sont utilisées pour étudier les artefacts produits lors de l'analyse ToF-SIMS des nanostructures. La méthodologie combinée ToF-SIMS et AFM a été utilisée pour détecter les artefacts liés à la pulvérisation et pour optimiser les conditions d'analyse. L'influence de l'énergie primaire et l'orientation du faisceau d'ions sur le développement des artefacts a été étudiée sur un échantillon à motifs (GaAs / SiO_2) de taille nanométrique. Les profils topographiques ont été utilisés pour corroborer les conclusions extraites de l'analyse chimique ToF-SIMS, à savoir l'existence d'un effet d'ombrage modifiant les profils de profondeur et plus généralement la morphologie de l'échantillon. Une étude a également été réalisée sur un échantillon à base de GaN présentant des fissures en surface et dont l'analyse SIMS ne permettait pas une bonne interprétation du profil chimique. La combinaison AFM et ToF-SIMS a permis de mesurer la morphologie de ces fissures et étudier leur comportement lors du processus de pulvérisation.

Le chapitre V (CHAPTER V) présente un travail prospectif sur la combinaison du ToF-SIMS avec des modes AFM électriques pour deux applications différentes : l'étude de la polarisation de matériaux piézoélectriques pour la compréhension des mécanismes de diffusion ionique et une étude pour voir comment réduire l'implantation du gallium dans le silicium, issue de la préparation de l'échantillon par FIB, par la technique ToF-SIMS. Dans le premier cas, l'analyse par ToF-SIMS a confirmé une modification chimique dans les zones polarisées à l'aide de la pointe AFM. Il a également été détecté un changement chimique dans les zones imagées par l'AFM, principalement dû au fait que l'imagerie se fait en mode contact ce qui a pour effet d'endommager la surface. Le signal PFM obtenu sur l'échantillon non ferroélectrique de LAO est attribué à l'existence de charges superficielles et à la migration du lanthane. Dans ce cas, l'analyse combinant le ToF-SIMS, la PFM et le KFM semble être une méthode utile pour analyser le(s) mécanisme(s) physique(s) inhérent(s) à la polarisation de ce matériau. Une étude plus approfondie est cependant nécessaire pour certifier les premières conclusions. Dans le deuxième cas, un protocole ToF-SIMS / SCM / SSRM a été utilisé pour mesurer et réduire les dommages structuraux issues de la préparation par FIB. La pulvérisation dans le ToF-SIMS s'est avérée efficace pour éliminer l'implantation de gallium, et retrouver les propriétés électriques initiales de l'échantillon.

Cette thèse est accessible à l'adresse : http://theses.insa-lyon.fr/publication/2019LYSEI121/these.pdf
© [M.A. Moreno Villavicencio], [2019], INSA Lyon, tous droits réservés

En conclusion, la combinaison des techniques ToF-SIMS et AFM s'avère être un outil de caractérisation avancée pour les systèmes et dispositifs complexes. Après ce travail de thèse focalisé sur l'optimisation et l'évaluation du protocole sur des applications spécifiques, on peut constater que l'adaptation de cette méthodologie à l'aide de différents modes AFM ouvre un nombre illimité d'applications. On recommande le travail suivant pour compléter les études :

(1) Une étude avancée de l'évolution de la topographie des interfaces verticales grâce à l'alignement des profils AFM pris avant et après la pulvérisation ToF-SIMS :

- L'alignement à l'aide des images topographiques n'est pas une procédure simple en raison de la distorsion des interfaces. Cependant, cela pourrait être fait en utilisant une cartographie d'une propriété physique obtenue par un mode AFM avancé.
- La procédure pour obtenir les cartographies de vitesse de pulvérisation pourrait être terminée une fois l'alignement effectué.

(2) L'étude des matériaux piézoélectriques :

- Afin de détecter une migration d'oxygène, il est important de s'assurer que l'oxygène détecté dans les profils de profondeur ne provient pas d'une contamination de surface. Pour cela, il est recommandé d'effectuer l'analyse *in-situ* et de nettoyer la surface jusqu'à ce que l'intensité en carbone soit faible avant de commencer l'écriture des domaines.
- Effectuer des analyses à haute résolution de masse pour éviter la convolution de pics intéressants.
- Analyser de manière approfondie la modification chimique produite par le balayage AFM afin de dissocier cet effet de celui produit par la polarisation des domaines.

(3) Mise en œuvre du protocole proposé pour achever la procédure de préparation des échantillons FIB :

- Optimisation des conditions d'analyse ToF-SIMS pour diminuer les dommages créés lors du retrait de l'implantation de gallium des appareils.
- Mesure de l'épaisseur de la couche implantée supprimée après pulvérisation ToF-SIMS.
- Évaluation de l'impact de la pulvérisation ToF-SIMS sur les propriétés électriques.

Cette thèse est accessible à l'adresse : http://theses.insa-lyon.fr/publication/2019LYSEI121/these.pdf
© [M.A. Moreno Villavicencio], [2019], INSA Lyon, tous droits réservés

Cette thèse est accessible à l'adresse : http://theses.insa-lyon.fr/publication/2019LYSEI121/these.pdf
© [M.A. Moreno Villavicencio], [2019], INSA Lyon, tous droits réservés

FOLIO ADMINISTRATIF

THESE DE L'UNIVERSITE DE LYON OPEREE AU SEIN DE L'INSA LYON

NOM : Moreno Villavicencio DATE de SOUTENANCE : 03 / 12 / 2019
Prénoms : Maiglid Andreina

TITRE :
Développement de l'imagerie 3D haute résolution par ToF-SIMS et AFM de dispositifs avancés

NATURE : Doctorat Numéro d'ordre : 2019LYSEI122

Ecole doctorale : Électronique, Électrotechnique et Automatique
Spécialité : Micro et nano technologies

RESUME :
La miniaturisation continue et la complexité des dispositifs poussent les techniques existantes de nano-caractérisation à leurs limites. De ce fait, la combinaison de ces techniques apparait être une solution attrayante pour continuer à fournir une caractérisation précise et exacte. Dans le but de dépasser les verrous existants pour l'imagerie chimique 3D haute résolution à l'échelle nanométrique, nous avons concentré nos recherches sur la création d'un protocole combinant la spectrométrie de masse à ions secondaires de temps de vol (ToF-SIMS) avec la microscopie à force atomique (AFM). Ceci permet entre autre de corréler la composition et la visualisation en 3 dimensions avec des cartographies de topographie ou d'autres propriétés locales fournies par l'AFM. Trois principaux résultats sont obtenus grâce à cette méthodologie : la correction d'un ensemble de données ToF-SIMS pour une visualisation 3D sans artefacts, la cartographie du taux de pulvérisation locale permettant de mettre en évidence les effets liés à la rugosité et la présence d'interfaces verticales et la superposition des informations avancées ToF-SIMS et AFM.
Quatre applications de la méthodologie combinée ToF-SIMS et AFM sont abordées dans cette thèse. La procédure de correction des données ToF-SIMS en 3D a été appliquée sur une structure hétérogène GaAs / SiO2. Les artefacts liés à la pulvérisation, notamment l'effet d'ombrage, ont été étudiés par le biais des cartographies de taux de pulvérisation sur des échantillons avec nano-motifs structurés et non structuré. Enfin, nous avons exploré la combinaison de l'analyse ToF-SIMS avec trois modes avancées de microscopie AFM : piézoélectrique (PFM), capacité (SCM) et conducteur (SSRM). Une première étude a notamment permis d'observer l'évolution et la modification chimique suite à l'application d'une contrainte électrique sur deux film mince piézoélectriques. Une deuxième étude s'est focalisée sur l'impact de l'implantation Ga lors de la préparation d'échantillons par FIB pour voir comment limiter l'effet de l'amorphisation sur la mesure électrique. Les aspects techniques de la méthodologie seront abordés pour chacune de ces applications et les perspectives de cette combinaison seront discutés.

MOTS-CLÉS :
Caractérisation chimique 3D – AFM – ToF-SIMS – PFM – SCM – SSRM corrélation et combinaison de techniques – reconstruction et visualisation 3D – effets d'ombrage – cartographie de vitesse de pulvérisation – overlay ToF-SIMS et AFM.

Laboratoire (s) de recherche :
CEA Grenoble - INL

Directeur de thèse:
* Brice Gautier

Président de jury :
* Didier Leonard

Composition du jury :
* Anouk Galtayries, rapportrice,
* Thierry Conard, rapporteur
* Nathalie Valle, examinatrice
* Sarah Fearns, examinatrice

Cette thèse est accessible à l'adresse : http://theses.insa-lyon.fr/publication/2019LYSEI121/these.pdf
© [M.A. Moreno Villavicencio], [2019], INSA Lyon, tous droits réservés